Max-Planck-Institut
für Meteorologie

MAX-PLANCK-GESELLSCHAFT

Toward Goal-oriented R-adaptive Models in Geophysical Fluid Dynamics using a Generalized Discretization Approach

Werner Bauer

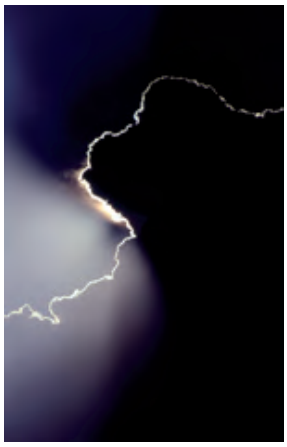

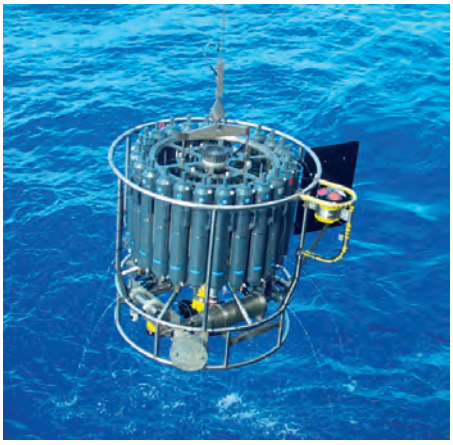

Berichte zur Erdsystemforschung 127/2013

Reports on Earth System Science

Hinweis

Die Berichte zur Erdsystemforschung werden vom Max-Planck-Institut für Meteorologie in Hamburg in unregelmäßiger Abfolge herausgegeben.

Sie enthalten wissenschaftliche und technische Beiträge, inklusive Dissertationen.

Die Beiträge geben nicht notwendigerweise die Auffassung des Instituts wieder.

Die "Berichte zur Erdsystemforschung" führen die vorherigen Reihen "Reports" und "Examensarbeiten" weiter.

Notice

The Reports on Earth System Science are published by the Max Planck Institute for Meteorology in Hamburg. They appear in irregular intervals.

They contain scientific and technical contributions, including Ph. D. theses.

The Reports do not necessarily reflect the opinion of the Institute.

The "Reports on Earth System Science" continue the former "Reports" and "Examensarbeiten" of the Max Planck Institute.

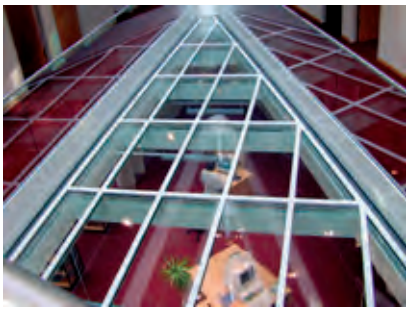

Anschrift / Address

Max-Planck-Institut für Meteorologie
Bundesstrasse 53
20146 Hamburg
Deutschland

Tel.: +49-(0)40-4 11 73-0
Fax: +49-(0)40-4 11 73-298
Web: www.mpimet.mpg.de

Layout:

Bettina Diallo, PR & Grafik

Titelfotos:
vorne:
Christian Klepp - Jochem Marotzke - Christian Klepp
hinten:
Clotilde Dubois - Christian Klepp - Katsumasa Tanaka

Berichte zur Erdsystemforschung 127 2013

Toward Goal-oriented R-adaptive Models in Geophysical Fluid Dynamics using a Generalized Discretization Approach

Werner Bauer

aus Waldkirchen, Deutschland

Hamburg 2013

Reports on Earth System Science 127 2013

ISSN 1614-1199

Werner Bauer
Max-Planck-Institut für Meteorologie
Bundesstrasse 53
20146 Hamburg

Als Dissertation angenommen
vom Department Geowissenschaften der Universität Hamburg

auf Grund der Gutachten von
Prof. Dr. Jörn Behrens
und
Dr. Almut Gassmann

Hamburg, den 10. Juli 2012
Prof. Dr. Jürgen Oßenbrügge
Leiter des Departments für Geowissenschaften

ISSN 1614-1199

Toward Goal-oriented R-adaptive Models in Geophysical Fluid Dynamics using a Generalized Discretization Approach

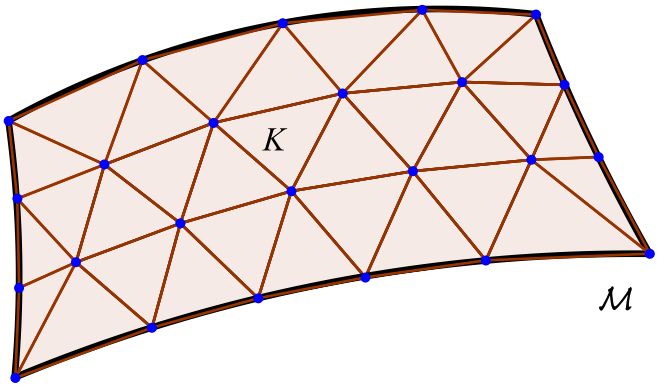

Werner Bauer

Hamburg 2013

Abstract

We propose a generalized discretization procedure for meshes on general polytopes for our new set of invariant equations of geophysical fluid dynamics (GFD) and develop a goal-oriented r-adaptive shallow-water model to accurately simulate the cyclone tracks of an idealized scenario of tropical cyclone interaction.
We introduce an invariant form of the equations based on differential geometry, in which the prognostic variables describing the evolution of the fluid are represented by differential forms. The introduction of additional auxiliary prognostic variables enables to split the invariant equations in topological and metric parts. The result is similar in form to the invariant linear Maxwell's equations. This allows to use concepts of electrodynamics also within fluid dynamics, in particular the discrete exterior calculus. Applying this technique on the topological and metric equations, we obtain a systematic discretization methodology, in which the discrete scheme descends directly from the choice of the topological meshes that approximate the momentum and continuity equations and from the discrete representation of the metric equations. We illustrate this method on a triangular and on a hexagonal C-grid discretization of the linear non-rotating shallow-water equations, for which we study consistency and stability properties for uniform and r-adapted grids.
For the case of rotating fluids, these staggered C-grid schemes require consistent vector reconstructions to adequately represent the Coriolis term. In our form of the invariant equations, the Coriolis term can be represented by means of extrusion, i.e. a flow field swept over a two-dimensional manifold as the Coriolis force acts perpendicularly. We develop a new method for normal vector reconstruction for a hexagonal C-grid scheme out of neighboring tangential vector components, in which the weights are determined by the ability of the tangential components to contribute to the extrusion. For uniform meshes, this reconstruction is stable and adequately represents waves and their dispersion relation. Moreover, in contrast to analogous vector reconstruction schemes from literature, our method does not require the use of the two-dimensional vorticity equation for the derivation and is therefore easier generalizable to three dimensions. In case of non-uniform meshes, we extend our linear model with existing techniques to a nonlinear hexagonal C-grid shallow-water model on r-adapted grid, for which we show stability and proper wave representation.
For this model, we propose a method of goal-oriented grid adaptation for the simulation of geophysical phenomena. By a linear sensitivity analysis for an idealized scenario of two interacting tropical cyclones, we evaluate the contribution of each grid cell to the error in predicting the cyclone tracks and estimate the required local resolution to minimize this error. Using this information when adapting the meshes for the shallow-water runs, we ensure high resolution in regions where the estimated error contributions are high, while using coarser grid cells outside. This leads to a substantial reduction in the number of grid points required to achieve a certain accuracy in the track prediction.
Our new formalism for GFD provides a generalized discretization method to obtain finite difference models on meshes based on general polytopes and allows us to study non-conventional discretization approaches, which contributes to a better understanding of the discrete fluid equations. For the proposed grid adaptation method, the computationally expensive sensitivity analysis and the model runs do not have to be performed by the same model. Following this strategy, the use of efficient models for the sensitivity analysis is a promising first step toward goal-oriented grid adaptation for complex climate models.

Contents

Chapter 1

Introduction

The simulation of many phenomena in geophysical fluid dynamics (GFD) requires, due to scale-interactions, an adequate representation of a large range of scales, for instance, to accurately simulate tropical cyclones (TCs) [30, 59, 63]. However, covering large parts of the scale range by using uniform grids with sufficiently high resolution would imply extremely high computational costs. For simulations for which high resolution is not required over the entire domain, grid adaptation can contribute to high accuracy of the solution while keeping the computational costs as low as possible.

Mainly two approaches are used for grid adaptation in geophysical applications: either new grid points are introduced to increase local resolution (h-adaptivity) and/or grid points are moved to those regions where higher resolution is required (r-adaptivity). Grid adaptation methods can be furthermore categorized as static or dynamic. In dynamic approaches, the grid is adapted to the solution during runtime according to a local refinement criterion, e.g., in [15, 14, 50, 64, 98]. Static adaptation is more frequently used in global atmosphere and ocean models, e.g., in [39, 45, 88, 110, 116]. Here, the grid remains unchanged during the model integration. The locations of high-resolution areas are usually chosen such that they include certain dynamic or orographic features of interest or cover regions in which more accurate predictions are required. For an adequate grid adaptation, application-specific error measures are often more useful in assessing the quality of a numerical solution than global error norms. Goal-oriented adaptivity methods allow for an automatic optimization of the grid for such application-specific error measures. Hereby, the mesh is adapted such that the error with respect to a goal functional is minimized. This goal functional can represent, for example, the error in the TC position. Such grid adaptation approaches are often based on the dual-weighted residual (DWR) method [7, 10, 11, 36].

The discretization methods have to be able to cope with adapted non-uniform grids, for which, in case of r-adaptivity, the geometrical properties of the cells change with adaptation or, in case of h-adaptivity, the topology change because of newly added grid points having possibly hanging nodes. Because the tessellation of the sphere using the icosahedron, e.g., [18, 89, 90], the lat-lon grid or the cubed sphere, e.g., [115, 116], does not lead to a completely smooth grid with uniform cells [49, 103], suitable discretization methods able to cope with this non-uniformity have been studied intensively, e.g. in [46, 89, 88, 102]. It seems natural to combine these discretization schemes suitable for non-uniform meshes with r-adaptive grid refinement. In case of dynamic grid adaptation, the unchanged topology in r-adaptive schemes makes load balancing in parallel computing easier, when compared to h-adaptive approaches.

Discretization schemes that properly represent waves and their dispersion relations

[76, 101] are particularly interesting for geophysical applications. Therefore, staggered grids, in which mass and velocity components are positioned at cell centers and cell edges, respectively, are often used. These finite difference schemes require, however, a reconstruction of the vector field to calculate the Coriolis term. For triangular C-grid models there are several consistent vector reconstructions available, e.g., in [46, 62, 78, 111, 113], mostly based on the low-order Raviart-Thomas (RT0) interpolation functions [84], which are also widely used in finite element models. However, for hexagonal C-grids, such reconstructions are rare and they often represent the waves inadequately [76]. The reason may lie in the fact that, in contrast to triangular cells where all linear reconstructions reduce to the low-order RT0 functions [46], linear reconstructions within a hexagonal cell seem to be not unique and different approaches have been investigated, e.g., in [43, 78, 107, 114]. Nevertheless, Thuburn et al. [102] recently derived a vector reconstruction with proper wave representation on arbitrarily-structured C-grids for shallow-water models. Despite the problem of normal vector reconstruction, an important reason to pursue the development of hexagonal models lies in the fact that they represent the divergence field more accurately than triangular C-grid models do (cf. [43, 112]).

Several attempts have been made to obtain a better geometrical understanding of discretization schemes on general polytopes. For instance, on the basis of finite elements exterior calculus, Arnold et al. [4] proposed for several partial differential equations (PDEs) a formulation using differential forms and exterior calculus and provided a set of stable mixed finite elements that are determined by topological constraints. The invariant form of the equations provides insight into their geometrical structure and allows to transfer algebraic properties of the continuous equation to the discrete level. An invariant formulation for the fluid equations has been introduced by Abraham and Marsden [1]. Using differential forms, the authors derived a general form of the equations on general manifolds for the incompressible and for the barotropic equations within one formulation. A similar invariant formulation is also widely used in computational electrodynamics for Maxwell's equations. The frequently used splitting of the invariant Maxwell's equations in a topological and in a metric part provides a systematic methodology for discretization (cf. [22, 25]).

To summarize, although some available finite difference schemes give stable and consistent discrete equations for geophysical applications, further theoretical investigations are highly desirable. For instance, it is not clear how to generalize the method of Thuburn and Ringler et al. [89, 102] for hexagonal C-grid toward three-dimensional equations, as the derivation relies essentially on the two-dimensional vorticity equation. Furthermore, the finite difference methods often used in geophysical fluid dynamics are usually not based on one general formalism with a strong mathematical background comparable to the finite element method [120]. The generalized formulation of fluid equations using differential form incorporates different coordinate systems and dimension within one set of equations on an arbitrary manifold. It seems thus promising to exploit such general form for the derivation of discrete schemes on arbitrarily-structured polytopes, in order to provide r-adaptive models for the investigation of geophysical problems.

1.1 Objectives of the thesis

In this work we develop a generalized discretization framework for the equations of geophysical fluid dynamics (GFD) and derive suitable finite difference schemes with r-adaptive grid refinement for the shallow-water equations. Moreover, we investigate the issue on how grid adaptation methods can be used to increase the accuracy of model solutions.

In this context, the research questions covering some major challenges in the development and application of an r-adaptive model are:

1. How can we derive suitable finite difference schemes for r-adaptive grid refinement using a generalized discretization approach?
2. Could such general approach provide new knowledge about the equations of GFD? What practical benefit do we gain in the process of discretization?
3. What kind of scenarios in geophysical applications profit from grid adaptation? How do we actually adapt the grid to increase the accuracy of model solutions?

These research questions and, accordingly, the topics in this thesis are ordered in a logical way leading toward an r-adaptive model for geophysical applications. However, every topic is by itself worth to be investigated independently from the others. With respect to the available literature, we suggest for every question an alternative approach, which may be followed in future research leading to a more profound understanding of discrete schemes on general unstructured grids.

1.2 Thesis outline

The thesis consists of three main chapters, each addressing a research question. Chapter 2, 3 and 4 are written in a journal article style and contain individual abstracts, introductions and conclusions, which makes them largely independent to read.

- In **Chapter 2** we introduce a novel formulation for the geophysical fluid equations by splitting them in a topological and in a metric part, which allows a systematic discretization applying the tools of discrete exterior calculus (DEC). Using this discretization method, we derive the triangular and hexagonal C-grid discretizations of the linear non-rotating shallow-water equations and study their consistency and stability properties on uniform and non-uniform grids.
- In **Chapter 3** we develop, on the basis of our invariant formulation, a new method for consistent normal vector reconstruction required for staggered grid schemes, for which we use the tools of DEC to represent the Coriolis term. We extend the linear hexagonal C-grid scheme for rotating fluids toward a nonlinear model on arbitrarily-structured C-grids and perform simulations of nonlinear test cases also for r-adapted grids.
- In **Chapter 4** we demonstrate how efficient r-adapted grids for the prediction of tropical cyclone (TC) tracks can be constructed with the help of goal-oriented error estimates. We perform a linear sensitivity analysis for the scenario of two interacting TCs to estimate the local grid resolution required to minimize an error measure correlated with the cyclone positions. We show how such information can be used to adapt the grid of the nonlinear hexagonal C-grid model such that high accuracy in cyclone track prediction is guaranteed, while significantly reducing the number of degrees of freedom required.

Chapter 4 has been submitted to the Journal "Theoretical and Computational Fluid Dynamics (TCFD)" (Bauer et al. [9]). In Chapter 5 we present a summary, draw some conclusions and present an outlook for future work.

Chapter 2

Discretization of the invariant geophysical fluid equations using discrete exterior calculus

Abstract We introduce a new formulation of the equations of geophysical fluid dynamics (GFD) consisting of sets of topological and metric invariant equations, which allows a systematic discretization by applying the tools of discrete exterior calculus (DEC).
Within the invariant equations, where the form of the equations is invariant under coordinate transformation, the prognostic variables describing the evolution of the fluid are represented by differential forms. By introducing additional auxiliary prognostic variables, we split the geophysical fluid equations in a topological and in a metric part. The resulting set of equations has similar form to the invariant linear Maxwell's equations and allows to use concepts of electrodynamics also within fluid dynamics. Moreover, such formulation enables a systematic discretization according to DEC by using chains and cochains to approximate manifolds and differential forms, respectively. The discrete scheme follows from the choice of the topological meshes (chains) for the momentum and continuity equations and from the discrete representation of the metric equations (Hodge-star operator, interior product). We illustrate that this formulation incorporates several finite difference schemes, for instance, the triangular and the hexagonal C-grid discretization of the non-rotating linear shallow-water equations, for which we study consistency and stability properties for uniform and non-uniform grids.

2.1 Introduction

During the last decades of intensive studies in geophysical fluid dynamics (GFD) on different regimes and scales for several purposes, quite a large variety of different analytic equations and, accordingly, of different discretization schemes has been developed and studied on idealized models, as well as intensively used in numerical weather prediction (NWP) and in climate research. The reason for such variety is manifold. Based on the full Navier-Stokes equations, plenty of different simplified sets of equations such as the barotropic or the shallow-water equations have been derived based on certain approximations, e.g. divergence-free flow, geostrophic balance, etc. Simplified equations allow for an accurate simulation of certain geophysical features (e.g. the track predictions of tropical cyclones in a barotropic model), while reducing the computational costs to a minimum. Furthermore, the analytic system of equations is often modified to meet the specific re-

quirements of the discretization methods; for instance, the vector-invariant form is often used in finite difference schemes [3], the flux-form is often applied for finite volume schemes [67], the formulation of the equations in weak form is essential in finite-element methods [13]. These three major discretization methods may differ according to the set of analytic equations with respect to consistency, to stability and to the representation of waves and of their dispersion relations, which is essential for geophysical applications [76]. In addition, often required are good performance of the discrete scheme and the possibility to use adaptive grids.

Several attempts have been made on the analytic and on the discrete level to unify some of the different equations or schemes and to gain a better understanding on their mutual relations. Major contributions to a better understanding of the different analytic equations valid for different scale regimes, which is based on a scale analysis approach, are achieved by Pedlosky [77] and more recently by Klein et al. [61]. On the level of discrete schemes, Rostand et al. [92] and LeRoux et al. [65, 66] have compared many low-order finite elements and some finite difference schemes concerning stationary wave solutions. A similar comparison, performed for the shallow-water equations on unstructured, staggered grids by Walters et. al. [111] for low-order finite element and finite difference methods, showed very similar behavior of some of these methods.

A promising method to formulate partial differential equations (PDE) in a more general way is the usage of differential geometry. In computational electrodynamics, Maxwell's equations are frequently written in invariant form, in which the prognostic variables are represented by differential forms, e.g. [22, 25]. The invariant form of an equation incorporates by definition all different coordinate systems and different dimensions. Based on this formulation, Bossavit [25] developed a discretization approach called *generalized finite difference (GFD)* for the invariant Maxwell's equations. On the basis of finite elements exterior calculus, Arnold et al. [4] proposed for several PDEs an invariant formulation using methods of differential geometry and exterior calculus. They provided a set of stable mixed finite elements determined by topological and geometrical constraints. An invariant formulation has also been found for the fluid equations by Abraham and Marsden [1]. Using differential geometry, the authors derived a general form of the equations on a general manifold for the incompressible and for the barotropic equations within one formulation. For the invariant fluid equations, Wilson [119] suggested a discretization based on methods of algebraic topology [47].

In this chapter we aim for a better geometrical understanding of the geophysical fluid equations by using the language of differential geometry and contribute to their unification. Based on the invariant fluid equations derived by Abraham and Marsden [1], we formulate the geophysical fluid equations in invariant form, in which the prognostic variables are written in differential forms. Moreover, by introducing additional auxiliary prognostic variables, we suggest a splitting into sets of topological and of metric equations, which leads to a formulation for GFD similar to the invariant Maxwell's equations used in computational electrodynamics, cf. Bossavit [19]. Such formulation allows, in addition, to apply the tools of discrete exterior calculus (DEC) of Desbrun et al. [33].

On the basis of the new formulation, we introduce a systematic discretization approach using DEC, where chains and cochains are used to approximate manifolds and differential forms, respectively. The discrete scheme descends directly from the choice of the topological meshes and from the discrete representation of the metric equations. We assign to every simplex (vertex, edge and face) one degree of freedom. The chains represent the topological meshes used to discretize the momentum and continuity equations. The discrete metric equations, namely the Hodge-star operator connecting the topological meshes

and the discrete representation of the contraction operator, are required to close the system of equations. Hereby, the analytic vector identities of the Helmholtz decomposition are transfered to the discrete level. Our formulation incorporates several finite difference schemes. Thus, a certain choice of the topological meshes and of the metric equations leads to a certain finite different schemes, for instance, a triangular, quadrilateral or hexagonal C-grid schemes. For the triangular and hexagonal C-grid discretization of the non-rotating linear shallow-water equations, we study consistency and stability properties.

This chapter is structured in the following way. In Section 2.2 we summarize the results of Abraham and Marsden [1] for the derivation of Euler's fluid equation in invariant form and present the required definitions. In Section 2.3 we derive the geophysical fluid equations in invariant form and proof that such formulation is well defined. In Section 2.4 we suggest the splitting of the invariant fluid equations in a topological and in a metric part. In Section 2.5 we compare the linear non-rotating fluid equations with the linear Maxwell's equations. In Section 2.6 we present the method of DEC by Desbrun et al. [33], which we apply to the invariant geophysical shallow-water equations in Section 2.7. In Section 2.8 we perform a consistency and stability analysis of the linear non-rotating shallow-water equation with triangular and hexagonal C-grid discretization for both uniform and non-uniform grids. In Section 2.9 we present a summary and draw conclusions.

2.2 Euler's equations in invariant form

In this section we present the fluid equations in invariant form using differential geometry. The invariant form, in which the prognostic variables are written in differential forms, is the basis for our derivation of the invariant geophysical fluid equations presented in the following sections. The definitions and derivations in this section are taken from standard textbooks on differential geometry, in particular from Abraham and Marsden [1]. For more details we refer to textbooks on differential geometry and to Appendix A, where we present a concise derivation of the invariant fluid equations proposed by Abraham and Marsden [1].

2.2.1 Operators of differential geometry to describe fluids

The equations describing the motion of a fluid (fluid equations) are defined on a general n-dimensional manifold $\mathcal{M}$ (n-manifold $\mathcal{M}$).

Differentiable manifolds: Manifolds are an abstraction of surfaces in the Euclidean space [1]. A *differentiable manifold* is a manifold that is locally similar to a linear space in $\mathbb{R}^n$, which allows to use calculus. It is described by a collection of *charts* that is called the *atlas*. Calculations are thereby done within the individual charts with methods from calculus. Assuming on the charts the *compatibility* property, i.e. the transition between charts is differentiable, then calculations done within one chart are valid in any other differentiable chart and thus on the entire manifold. In case the linear space is an Euclidean space with metric, the differentiable manifold has also this metric structure induced by the charts.

On differentiable manifolds exist at every point $p \in \mathcal{M}$ *tangent spaces*, $\mathcal{T}_p\mathcal{M}$, that are real vector spaces in $\mathbb{R}^n$ attached to this point. The elements of the tangent space at point p are called tangent vectors $\vec{X}_p$. The union of all tangential spaces is a $2n$-dimensional manifold called tangent bundle $\mathcal{TM}$ consisting of all pairs of $(p, \vec{X}_p)$. A *Riemannian*

manifold consists of a real differentiable manifold $\mathcal{M}$ in which every tangent space is equipped with an inner product (metric) $\mathbf{g}$ (cf. Appendix A.4).

Examples: $\mathbb{R}^n$ using the identity as chart is a manifold with the tangent space $\mathbb{R}^n$; the sphere $\mathcal{S}^2$ using the stereographic projection is a manifold with the tangent spaces $\mathbb{R}^2$ at every point on the sphere.

Local coordinates representation: A neighborhood $U \subset \mathcal{M}$ of a n-manifold $\mathcal{M}$ around a point $p \in \mathcal{M}$ is assigned by the differentiable charts to the Euclidean space $\mathbb{R}^n$, which allows to represent vectors and differential operators in so called *local coordinates*. On the patch $U \subset \mathcal{M}$ let a point p be represented by local coordinates $p = (x_p^1, \ldots, x_p^n)$ and the patch U with $x = (x^1, \ldots, x^n)$. On a manifold $\mathcal{M}$ one may define a vector $\vec{X}$ as a differential operator [60]

$$\vec{X}_p := \sum_j X_p^j \frac{\partial}{\partial x^j} \ , \tag{2.1}$$

with $\vec{X}_p \in \mathcal{T}_p\mathcal{M}$ and $X_p^j \in \mathbb{R}$. Furthermore, we regard for the coordinate function x^i the linear functional $dx^i : \mathcal{T}_p\mathcal{M} \to \mathbb{R}$ for any vector $\vec{X} \in \mathcal{T}_p\mathcal{M}$ acting in the following way:

$$dx^i(\vec{X}) = \sum_j X^j dx^i(\partial_j) = \sum_j X^j \frac{\partial x^i}{\partial x^j} = \sum_j X^j \delta_{ij} = X^i \ , \tag{2.2}$$

with $\partial_j := \frac{\partial}{\partial x^j}$ and the Kronecker symbol δ_{ij} [60]. Because of $dx^i(\partial_j) = \delta_{ij}$ the linear functionals $(dx^1, ..., dx^n)$ span the dual basis with respect to the basis $(\partial_1, \ldots, \partial_n)$ of $\mathcal{T}_p\mathcal{M}$. Consequently, a one-form (covector) may be defined with $\omega^1 = \omega_1 dx^1 + \ldots \omega_n dx^n$.

Vector fields and differential forms: A *vector field* $\vec{X}$ on $\mathcal{M}$ is a differentiable mapping $\vec{X} : \mathcal{M} \to \mathcal{T}\mathcal{M}$ such that $\vec{X}_p \in \mathcal{T}_p\mathcal{M}$ for all $p \in \mathcal{M}$. In other words, a vector field assigns to each point of $\mathcal{M}$ a vector based on that point. The set of all C^∞ vector fields on $\mathcal{M}$ is denoted with $\mathcal{X}(\mathcal{M})$. A *differential k-form* $\omega^k \in \Omega^k(\mathcal{M})$ is a multi-linear and skew-symmetric map

$$\omega^k : \underbrace{\mathcal{X}(\mathcal{M}) \times \cdots \times \mathcal{X}(\mathcal{M})}_{k-\text{times}} \to C^\infty \ . \tag{2.3}$$

We denote the space of differential k-form with $\Omega^k(\mathcal{M})$. To define differential forms, one usually defines first an exterior algebra and then extend this by charts to differential k-forms, see Appendix A.1.

As an example, we regard the vector field $\vec{u} \in \mathcal{X}(\mathbb{R}^2)$ describing e.g. the velocity of a fluid. A corresponding one-form u, using the inner product $<,>$ defined in Appendix A.4, can be defined by

$$u :=< \vec{u}, \cdot > \quad \text{for any} \quad \vec{u} \in \mathcal{X}(\mathbb{R}^2) \ . \tag{2.4}$$

We denote $\vec{u}$ as the vector proxy of the one-form $u \in \Omega^1(\mathcal{M})$.

Integration of forms on manifolds: We define the integral of an n-form $\omega^n \in \Omega^n(\mathcal{M})$ on an oriented[1] n-manifold $\mathcal{M}$ by generalizing the results of the $\mathbb{R}^n$ via the charts to $\mathcal{M}$. For a continuous function $f : \mathbb{R}^n \to \mathbb{R}$ with compact support, $\int f dx^1 \ldots dx^n$ is defined by the Riemann integral over any rectangle containing the support of f. Analogously we define an integral for n-forms ω represented in local coordinates by the following definition.

[1] An *orientation* of $\mathcal{M}$ is an equivalence class $[\mu]$ of volume-forms on $\mathcal{M}$. An *oriented* manifold $(\mathcal{M}, [\mu])$ is an orientable (i.e. a volume-form exists) manifold $\mathcal{M}$ together with an orientation [1].

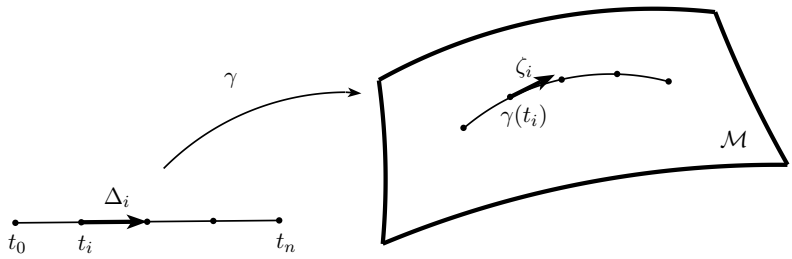

Figure 2.1: Integrating the one-form $\omega^1 \in \Omega^1(\mathcal{M})$ along the curve $\gamma(t) \in \mathcal{M}$.

Definition 2.2.1. Let $U \subset \mathbb{R}^n$ be open and $\omega^n \in \Omega^n(U)$ have compact support. If, relative to the standard basis $(\vec{e}_1, ..., \vec{e}_n)$ of $\mathbb{R}^n$,

$$\omega^n(x) = \omega_{1...n}(x) dx^1 \wedge \cdots \wedge dx^n \ , \tag{2.5}$$

with the components of $\omega_{1...n}(x) = \omega^n(x)(\vec{e}_1, \ldots, \vec{e}_n)$ ($\wedge$ denotes the *wedge* product defined in A.2), then

$$\int_U \omega^n = \int_{\mathbb{R}^n} \omega_{1...n}(x) dx^1 \ldots dx^n \ . \tag{2.6}$$

Using a differentiable atlas, this definition is generalizable to the manifold $\mathcal{M}$. For this definition a local and global change of variable theorem is valid, see Theorem A.2.9 in Appendix A.

Example: We give an example for the integration of a one-form $\omega^1 \in \Omega^1(\mathcal{M})$ along a smooth curve $\gamma : t \in [0,1] \to \mathcal{M}$. We divide the interval $[0,1] \subset \mathbb{R}$ in parts $\Delta_i : t_i \leq t \leq t_{i+1}, t_0 = 0, t_n = 1$. The tangential vectors to curve γ at points t_i are given by $\zeta_i := d\gamma|_{t_i}(\Delta_i) \in \mathcal{T}_{\gamma(t_i)}\mathcal{M}$ [5]. The integral of the one-form ω^1 on the path γ is defined as a limit of Riemann sums, where every sum is the value of ω^1 acting on the tangent vector ζ_i, i.e.

$$\int_\gamma \omega^1 = \lim_{\Delta \to 0} \sum_{i=1}^{n} \omega^1(\zeta_i) \ . \tag{2.7}$$

Figure 2.1 illustrates the integration of the one-form $\omega^1 \in \Omega^1(\mathcal{M})$ along the path $\gamma \in \mathcal{M}$.

Exterior operations on forms: The rate of change of a differential k-form $\omega^k \in \Omega^k(\mathcal{M})$ can be calculated by the *exterior derivative* $\mathbf{d} : \Omega^k(\mathcal{M}) \to \Omega^{k+1}(\mathcal{M})$ that acts on the k-form (cf. Theorem A.2.3 for a more formal definition). In local coordinates the exterior derivative is given by

$$\mathbf{d}\omega^k = \frac{\partial \omega_{i_1 \ldots i_k}}{\partial x^i} dx^i \wedge dx^{i_1} ... \wedge dx^{i_k}, \quad i_1 < ... < i_k \ . \tag{2.8}$$

Examples: The exterior derivative of a function $f \in \Omega^0(\mathbb{R}^2)$ in $\mathbb{R}^2$, i.e. $\mathbf{d}f = \partial_x f dx + \partial_y f dy$, is the total derivative of f. The exterior derivative of a one-form $\omega^1 = \omega_x dx + \omega_y dy \in \Omega^1(\mathbb{R}^2)$ is given by

$$\mathbf{d}\omega^1 = \partial_y \omega_x dy \wedge dx + \partial_x \omega_y dx \wedge dy = (\partial_x \omega_y - \partial_y \omega_x) dx \wedge dy \ .$$

The inverse operation to the exterior derivative is the *interior product* (also called the *contraction operator*) $\mathbf{i} : \Omega^k(\mathcal{M}) \to \Omega^{k-1}(\mathcal{M})$ (cf. Theorem A.2.4 for a more formal definition). The contraction of the k-form $\omega^k \in \Omega(\mathcal{M})$ with $\vec{X} \in \mathcal{X}(\mathcal{M})$ can be written in the form

$$\mathbf{i}_{\vec{X}}\omega^k(\vec{X}_2, ..., \vec{X}_k) = \omega^k(\vec{X}, \vec{X}_2, ..., \vec{X}_k) \ , \tag{2.9}$$

for all vectors $\vec{X}_i \in \mathcal{X}(\mathcal{M}), i = 2, \ldots, k$. The interior product can be evaluated with Lemma 2.2.1, for which the Hodge-star operator $\star$ and the Riemannian lift $\flat$ are required.

Given an inner product $<,>$, there exist a unique relation between a one-form $\omega^1 \in \Omega^1(\mathcal{M})$ and the corresponding vector proxy $\vec{v} \in \mathcal{X}(\mathcal{M})$. This mapping is given by

$$\sharp : \Omega^1(\mathcal{M}) \to \mathcal{X}(\mathcal{M}) \ ; \qquad (\omega^1)^\sharp := \sharp\omega^1 = \sharp < \vec{v}, \cdot >= \vec{v} \ , \tag{2.10}$$

or the inverse operator by

$$\flat : \mathcal{X}(\mathcal{M}) \to \Omega^1(\mathcal{M}) \ ; \qquad \vec{v}^\flat := \flat\vec{v} =< \vec{v} \ , \cdot >= \omega^1 \ . \tag{2.11}$$

We denote in the following both mappings $\flat$ and $\sharp$ as *Riemannian lift*, if there is no danger of confusion. See Definition A.4.1 in Appendix A for a more formal definition.

The *Hodge-star* operator $\star : \Omega^k(\mathcal{M}) \to \Omega^{n-k}(\mathcal{M})$ defined on an n-manifold $\mathcal{M}$ is a unique relation between k-forms and $n-k$-forms. It acts on k-form $\omega^k \in \Omega^k(\mathcal{M})$ in the following way:

$$\bar{\alpha} \wedge \star\bar{\beta} =< \bar{\alpha}, \bar{\beta} > \mu \quad \text{for} \quad \bar{\alpha}, \bar{\beta} \in \Omega^k(\mathcal{M}) \ . \tag{2.12}$$

A general definition and the properties of the Hodge-star operator are given in Prop. A.2.1 in Appendix A.

We illustrate on a two-dimensional example how the Hodge-star operator acts on the covariant basis vectors $dx^i \in \Omega^1(\mathcal{M}), i = 1, 2$: $\star 1 = dx^1 \wedge dx^2$, $\star dx^1 \wedge dx^2 = 1$, $\star dx^1 = dx^2$, $\star dx^2 = -dx^1$.

Lemma 2.2.1. (Hirani [54]) *Let be $\vec{X} \in \mathcal{X}(\mathcal{M})$ a vector field and $\alpha \in \Omega^k(\mathcal{M})$ a k-form on a smooth n-manifold $\mathcal{M}$. Then, the interior product can be computed with the following formula*

$$\mathbf{i}_{\vec{X}}\alpha = (-1)^{k(n-k)} \star (\star\alpha \wedge \vec{X}^\flat) \ . \tag{2.13}$$

Remark. Using this lemma, we find that the invariant equations of Abraham and Marsden [1] are equivalent to Wilson's [119] invariant formulation of the fluid equations for non-rotating flows.

Lie-derivative: Let $\vec{X} \in \mathcal{X}(\mathcal{M})$ be a smooth vector field with local flux φ_t. Then $\vec{X}$ is tangential to $\varphi_t(p)$ at a point $p \in \mathcal{M}$ and one determines the directional derivative, i.e. the change of f with variations in direction of $\vec{X}$, by $\mathcal{L}_{\vec{X}}(f)|_p = \frac{d}{dt}|_{t=0} f(\varphi_t(p))$. $\mathcal{L}_{\vec{X}}$ is called *Lie-derivative*. We present a general definition of the Lie-derivative acting on vector fields $\vec{Y} \in \mathcal{X}(\mathcal{M})$ and on differential forms $\omega \in \Omega(\mathcal{M})$ in Theorem A.2.5 in Appendix A.

2.2.2 Fluid equations on general manifolds $\mathcal{M}$

Based on the above introduced operators acting on differential forms and on vector fields on a Riemannian manifold $\mathcal{M}$, Euler's equations can be written in invariant form, as proposed by Abraham and Marden [1]. For a concise derivation of the invariant Euler's fluid equations see Appendix B.

In contrast to the conventional fluid equations in vector calculus, where the integral form of the balance of momentum does change its form when using different coordinate

systems, the invariant (covariant) fluid equations are invariant under coordinate transformations. More important is, however, that one obtains by such formulation a well-defined notion of an integral on any manifold $\mathcal{M}$. This is not given for vector-valued integrals.

Let the one-form $\vec{u}^\flat \in \Omega^1(\mathcal{M})$ describe the velocity of an ideal fluid (cf. Eq. (B.20)) with the functions for density ρ and pressure p. Then, according to Abraham and Marsden [1], the invariant Euler's equations on a compact n-manifold $\mathcal{M}$ with smooth boundary $\partial\mathcal{M}$ and outward unit normal $\vec{n}$ are given by

$$\begin{aligned} \frac{\partial(\vec{u}^\flat)}{\partial t} + \mathcal{L}_{\vec{u}}(\vec{u}^\flat) - \frac{1}{2}\mathbf{d}(\vec{u}^\flat(\vec{u})) + \frac{1}{\rho}\mathbf{d}p = 0 \ , \\ \frac{\partial(\star\rho)}{\partial t} + \mathbf{d} \star (\rho\vec{u})^\flat = 0 \ , \\ (\vec{u}\cdot\vec{n})da = \mathbf{i}_{\vec{u}}\mu = 0 \quad \text{(boundary condition on } \partial\mathcal{M}) \ , \end{aligned} \tag{2.14}$$

with initial conditions $\vec{u}(x,0) = \vec{u}_0(x)$ and volume-form μ (cf. Appendix A.2). By closing the system of equations according to the principle of energy conservation (cf. Appendix B.3), one obtains either:

1. the incompressible fluid equations by $\star\mathbf{d}\star(\vec{u})^\flat = 0$, or
2. the barotropic fluid equations using the equation of state, $p = \rho^2\frac{\partial\omega}{\partial\rho}$, with the internal energy $w = w(\rho)$ defined in Eq. (B.42).

On the basis of the invariant form of Euler's equations we derive in the following a set of invariant geophysical fluid equations.

2.3 Geophysical fluid equations in invariant form

We introduce a new invariant form of the equations of geophysical fluid dynamics (GFD) on the basis of Euler's fluid equations of Abraham and Marden [1]. To our knowledge such formulation has not been presented in literature for the equations of GFD. To guarantee that this formulation is well-defined, we include a proof that for both two and three dimensions the invariant geophysical fluid equations are equivalent to the corresponding equations written in vector calculus.

To compare the invariant form with conventional vector calculus, we present the equations on a rotating Cartesian coordinate system in $\mathbb{R}^3$ that is positioned on the Earth surface, as frequently done for geophysical applications. On a rotating sphere with angular velocity Ω we approximate the Coriolis effect by the two-form $f_C := f dx\wedge dy \in \Omega^2(\mathcal{M})$. The Coriolis parameter $f = 2\Omega\sin(\varphi)$ reflects the dependency of the Coriolis acceleration on the surface of the sphere with respect to the latitude φ of the fluid element's position (cf. Appendix C.1.2). In case of three dimensions, additional Coriolis effects are present when regarding the entire rotation vector $2\vec{\Omega}\times\vec{u}$. In the following we use the *shallow-atmosphere approximation* (cf. C.1.2) and neglect the vertical effects by setting $2\vec{\Omega}\times\vec{u} \approx f\vec{k}\times\vec{u}$, with $\vec{k} = \vec{e}_3 = (0,0,1)$, as the effects of the Earth rotation in vertical direction are small compared to horizontal effects (cf. Pedlosky [77]).

To take the Coriolis effect into account, we replace in Eq. (2.14) the Lie-derivative $\mathcal{L}_{\vec{u}}$ by an equivalent representation that uses a combination of exterior derivative $\mathbf{d}$ and of interior product $\mathbf{i}_{\vec{u}}$ according to Cartan's formula (B.35). With the representation of the Coriolis term using an interior product, i.e. $\mathbf{i}_{\vec{u}}f$, as shown in detail in Eqn. (2.23) and (2.25), the geophysical fluid equations (Euler's equations for rotating fluids) can be written as presented in the following theorem.

Theorem 2.3.1. *Let $\mathcal{M} \subset \mathbb{R}^n, n = 2, 3$, be a compact n-manifold on a rotating coordinate system with angular velocity Ω and with smooth boundary $\partial\mathcal{M}$ and outward unit normal $\vec{n}$. Let the one-form $\vec{u}^\flat \in \Omega^1(\mathcal{M})$ describe the velocity, the functions ρ the density and p the pressure of an ideal fluid. Using the shallow-atmosphere approximation, the Coriolis effect is represented in the horizontal plane by the two-form $f_C := f dx \wedge dy$. Then, the invariant Euler's equations on a rotating sphere are given by:*

$$\begin{aligned} \frac{\partial \vec{u}^\flat}{\partial t} + \mathbf{i}_{\vec{u}}(\mathbf{d}\vec{u}^\flat + f_C) + \frac{1}{2}\mathbf{d}\mathbf{i}_{\vec{u}}\vec{u}^\flat + \frac{1}{\rho}\mathbf{d}p = 0 \ , \\ \frac{\partial(\star\rho)}{\partial t} + \mathbf{d} \star (\rho\vec{u})^\flat = 0 \ , \\ (\vec{u} \cdot \vec{n})da = \mathbf{i}_{\vec{u}}\mu = 0 \quad (\textit{boundary condition on } \partial\mathcal{M}) \ , \end{aligned} \tag{2.15}$$

with the induced volume element[2] *da on the boundary, with initial conditions $\vec{u}(x, 0) = \vec{u}_0(x)$ and with the energy closure*
(i) for incompressible flows *by $\star\mathbf{d} \star (\vec{u}^\flat) = 0$ or*
(ii) for barotropic flows *by the* equation of state, *$p = \rho^2 \frac{\partial \omega}{\partial \rho}$, with the internal energy $w = w(\rho)$ of Eq.* (B.42).

Remark. The extension of the invariant fluid equations (2.14) by a two-form would also be possible without the restrictions put on $\mathcal{M} \subset \mathbb{R}^3$ in Theorem 2.3.1. Moreover, instead of the Cartesian framework, a more general formulation using spherical coordinates on a rotating sphere (cf. White et al. [117]) would be possible but is not subject of this study. Here, we focus on a representation of the invariant equations comparable to a conventional set of rotating fluid equations, such as those shown in Eq. (C.1).

The proof of Theorem 2.3.1 is based on a comparison of the invariant equations (2.15) to the conventional equations in vector calculus (C.1) for which we require the following two identities.

Lemma 2.3.2. *Let $\mathcal{M} \subset \mathbb{R}^3$ be an n-manifold with inner product $<,>$, basis (e_1, e_2, e_3) and dual basis $(dx, dy, dz) := (dx^1, dx^2, dx^3)$ according to $dx^i(e_j) = \delta_{ij}$. Let the velocity be represented by the one-form $\vec{u}^\flat = u_x dx + u_y dy + u_z dz \in \Omega^1(\mathcal{M})$. Then, the following identity is valid:*

$$\left(\mathbf{i}_{\vec{u}}\mathbf{d}\vec{u}^\flat\right)^\sharp = \vec{\zeta} \times \vec{u} \ , \tag{2.16}$$

with $\vec{\zeta} = \nabla \times \vec{u}$ and with the Riemannian lift $\sharp, \flat$.

Proof. Using Hirani's lemma 2.2.1 the interior product can be evaluated by

$$\mathbf{i}_{\vec{u}}\mathbf{d}\vec{u}^\flat = (-1)^{2(3-2)} \star (\star\mathbf{d}\vec{u}^\flat \wedge \vec{u}^\flat) \ . \tag{2.17}$$

Applying the exterior derivative $\mathbf{d}$ (A.2.3), the Hogde-star $\star$ (A.2.2) and the wedge product

[2] The induced volume element da is the contraction of the volume-form μ with the normal vector $\vec{n}$ on the boundary $\partial\mathcal{M}$, i.e. $da = \mathbf{i}_{\vec{n}}\mu$, cf. [1].

$\wedge$ (A.2) on $\vec{u}^\flat = u_x dx + u_y dy + u_z dz$ it follows:

$$\begin{aligned}
\mathbf{d}\vec{u}^\flat &= (\partial_x u_y - \partial_y u_x)dx \wedge dy + (\partial_x u_z - \partial_z u_x)dx \wedge dz + (\partial_y u_z - \partial_z u_y)dy \wedge dz \ , \\
\star\mathbf{d}\vec{u}^\flat &= (\partial_x u_y - \partial_y u_x)dz - (\partial_x u_z - \partial_z u_x)dy + (\partial_y u_z - \partial_z u_y)dx \ , \\
\star\mathbf{d}\vec{u}^\flat \wedge \vec{u}^\flat &= u_x(\partial_x u_y - \partial_y u_x)dz \wedge dx + u_y(\partial_x u_y - \partial_y u_x)dz \wedge dy \\
&\quad - u_x(\partial_x u_z - \partial_z u_x)dy \wedge dx - u_z(\partial_x u_z - \partial_z u_x)dy \wedge dz \\
&\quad + u_y(\partial_y u_z - \partial_z u_y)dx \wedge dy + u_z(\partial_y u_z - \partial_z u_y)dx \wedge dz \ , \\
\star\left(\star\mathbf{d}\vec{u}^\flat \wedge \vec{u}^\flat\right) &= \big[u_z(\partial_z u_x - \partial_x u_z) - u_y(\partial_x u_y - \partial_y u_x)\big]dx \\
&\quad + \big[u_x(\partial_x u_y - \partial_y u_x) - u_z(\partial_z u_y - \partial_y u_z)\big]dy \\
&\quad + \big[u_y(\partial_y u_z - \partial_z u_y) - u_x(\partial_z u_x - \partial_x u_z)\big]dz \ .
\end{aligned}$$

On the other hand, we have $\vec{\zeta} \times \vec{u} = (\nabla \times \vec{u}) \times \vec{u}$ in Cartesian coordinates, where $\vec{u} = u_x e_x + u_y e_y + u_z e_z$ is a vector-valued function, i.e.

$$\begin{aligned}
(\nabla \times \vec{u}) \times \vec{u} &= \begin{pmatrix} \partial_y u_z - \partial_z u_y \\ \partial_z u_x - \partial_x u_y \\ \partial_x u_y - \partial_y u_x \end{pmatrix} \times \begin{pmatrix} u_x \\ u_y \\ u_z \end{pmatrix} \\
&= \begin{pmatrix} u_z(\partial_z u_x - \partial_x u_z) - u_y(\partial_x u_y - \partial_y u_x) \\ u_x(\partial_x u_y - \partial_y u_x) - u_z(\partial_z u_y - \partial_y u_z) \\ u_y(\partial_y u_z - \partial_z u_y) - u_x(\partial_z u_x - \partial_x u_z) \end{pmatrix} \ . \qquad (2.18)
\end{aligned}$$

Using the Riemannian lift $\sharp$, the one-form $\star\left(\star\mathbf{d}\vec{u}^\flat \wedge \vec{u}^\flat\right)$ can be represented as a vector array that corresponds to Eq. (2.18). □

Lemma 2.3.3. *Let $\mathcal{M} \subset \mathbb{R}^2$ be an n-manifold with inner product $<,>$, basis (e_1, e_2) and dual basis $(dx, dy) := (dx^1, dx^2)$ according to $dx^i(e_j) = \delta_{ij}$. Let the velocity be represented by the one-form $\vec{u}^\flat = u_x dx + u_y dyz \in \Omega^1(\mathcal{M})$. Then, the following identity is valid:*

$$\left(\mathbf{i}_{\vec{u}}\mathbf{d}\vec{u}^\flat\right)^\sharp = \zeta\vec{k} \times \vec{u} \ , \qquad (2.19)$$

with the Riemannian lift $\sharp, \flat$ and $\vec{k} = \vec{e}_3 = (0, 0, 1)$. ζ is the vertical component of the relative vorticity, i.e. $\zeta = \vec{k} \cdot \vec{\zeta}$ and $\vec{\zeta} = \nabla \times \vec{u}$.

Proof. With Hirani's lemma 2.2.1 we represent the left side of Eq. (2.19) by

$$\mathbf{i}_{\vec{u}}\mathbf{d}\vec{u}^\flat = (-1)^{2(2-2)} \star (\star\mathbf{d}\vec{u}^\flat \wedge \vec{u}^\flat) \ . \qquad (2.20)$$

Applying the exterior derivative $\mathbf{d}$ (A.2.3), the Hogde-star $\star$ (A.2.2) and the wedge product $\wedge$ (A.2) on $\vec{u}^\flat = u_x dx + u_y dy$ it follows:

$$\begin{aligned}
\mathbf{d}\vec{u}^\flat &= (\partial_x u_y - \partial_y u_x)dx \wedge dy \ , \\
\star\mathbf{d}\vec{u}^\flat &= (\partial_x u_y - \partial_y u_x) \ , \\
\star\mathbf{d}\vec{u}^\flat \wedge \vec{u}^\flat &= (\partial_x u_y - \partial_y u_x)(u_x dx + u_y dy) \ , \\
\star(\star\mathbf{d}\vec{u}^\flat \wedge \vec{u}^\flat) &= (\partial_x u_y - \partial_y u_x)(u_x dy - u_y dx) \ .
\end{aligned}$$

The vertical component of the relative vorticity is given by $\zeta := \vec{k} \cdot (\nabla \times \vec{u}) = (\partial_x u_y - \partial_y u_x)$. We find the stated identity if we represent

$$\vec{k} \times \vec{u} = \begin{pmatrix} 0 \\ 0 \\ 1 \end{pmatrix} \times \begin{pmatrix} u_x \\ u_y \\ u_z \end{pmatrix} = \begin{pmatrix} -u_y \\ u_x \\ 0 \end{pmatrix} \qquad (2.21)$$

and if we apply $\sharp$ on $\star(\star\mathbf{d}\vec{u}^\flat \wedge \vec{u}^\flat)$ to represent the one-form in vector components. □

Proof of theorem 2.3.1. Because the sets of equations in Eq. (2.14) and Eq. (2.15) only differ by the nonlinear term $\mathbf{i}_{\vec{u}}(\mathbf{d}\vec{u}^\flat + f_C)$, it is sufficient to proof whether this term is well-defined. The linearity of $\mathbf{i}_{\vec{X}}$ (cf. Theorem A.2.4) allows to separate the Coriolis two-form $f_C = f dx \wedge dy \in \Omega^2(\mathcal{M})$ with Coriolis parameter f from the nonlinear term $\mathbf{i}_{\vec{u}}\mathbf{d}\vec{u}^\flat$. In Lemma 2.3.2 and 2.3.3 we have shown that the nonlinear terms are well-defined for two and three dimensions. It remains to show that the Coriolis term is correctly represented by the contraction of the two-form f_C with the velocity field $\vec{u}$. Using the shallow-atmosphere approximation (C.4), the Coriolis term is represented for both two- and three-dimensional equations by $f\vec{k} \times \vec{u} = (-fu_y, fu_x, 0)$, with $\vec{k} = (0, 0, 1)$. The velocity fields in two and three dimensions are given by $\vec{u} = (u_x, u_y, 0)$ and $\vec{u} = (u_x, u_y, u_x)$, respectively.

In two dimensions, we find $(\mathbf{i}_{\vec{u}} f_C)^\sharp = f\vec{k} \times \vec{u}$ for the two-form $\vec{u}^\flat = u_x dx + u_y dy$. This can be inferred by using Hirani's lemma 2.2.1 and the Riemannian lift $\flat$:

$$\mathbf{i}_{\vec{u}} f_C = (-1)^{2(2-2)} \star (\star f_C \wedge \vec{u}^\flat) = \star(f u_x dx + f u_y dy) = f u_x dy - f u_y dx \ . \tag{2.22}$$

This leads, by linearity of the differential forms, to

$$(\mathbf{i}_{\vec{u}}(\mathbf{d}\vec{u}^\flat + f_C))^\sharp = (\zeta + f)\vec{k} \times \vec{u} \ . \tag{2.23}$$

In three dimension, we find the identity $(\mathbf{i}_{\vec{u}} f_C)^\sharp = f\vec{k} \times \vec{u}$ for the three-form $\vec{u}^\flat = u_x dx + u_y dy + u_z dz$, as shown by

$$\begin{aligned} \mathbf{i}_{\vec{u}} f_C &= (-1)^{2(3-2)} \star (\star f_C \wedge \vec{u}^\flat) = \star(f dz \wedge (u_x dx + u_y dy + u_z dz)) \\ &= \star(f u_x dz \wedge dx + f u_y dz \wedge dy)) = f u_x dy - f u_y dx \ , \end{aligned} \tag{2.24}$$

leading to the nonlinear term

$$(\mathbf{i}_{\vec{u}}(\mathbf{d}\vec{u}^\flat + f_C))^\sharp = (\vec{\zeta} + f\vec{k}\ ) \times \vec{u} \ . \tag{2.25}$$

The identities (2.23) and (2.25) proof that the geophysical fluid equations in invariant form (2.15) are well-defined in two and three dimensions, because these identities show that the invariant equations correspond to the geophysical fluid equations in vector calculus of Eqn. (C.2) and (C.4) of Appendix C.

□

2.4 Topological and metric geophysical fluid equations

Based on the invariant geophysical fluid equations derived in Section 2.3, we introduce a novel formulation that consists in splitting the equations into a set of topological and metric equations. This separation is possible as we introduce auxiliary quantities, denoted with $\widetilde{\cdot}$ in the following. Such splitting has its origin in electrodynamics (see e.g. [19, 25]) but has, to our best knowledge, not been used so far in the formulation of fluid equations. In this section we introduce this formulation for Euler's fluid equations and for the shallow-water equations for rotating fluids and proof its well-definedness on $\mathbb{R}^n, n = 2, 3$.

In order to explore the potential of such formulation, we address two issues in the following sections. First, in Section 2.5, we compare the linear non-rotating equations with the linear Maxwell's equations used in electrodynamics, from which we adopted the idea of splitting the equations in topological and metric parts. Second, in Section 2.6 and 2.7, we use this formulation to discretize the linear shallow-water equations in a systematic way based on algebraic constraints of the computational meshes.

2.4.1 Splitting the fluid equations in topological and metric parts

The invariant geophysical fluid equations describe the fluid's velocity by the one-form $u \in \Omega^1(\mathcal{M})$, and its density and pressure by the functions $\rho, p \in \Omega^0(\mathcal{M})$, respectively, on an n-manifold $\mathcal{M}$. We restrict our investigations to $\mathcal{M} \subset \mathbb{R}^n, n = 2, 3$, on a rotating coordinate system (rotating frame) with angular velocity Ω (cf. Appendix C.1.2).

The quantities u, ρ, p describe the time evolution of the fluid. In order to split the system of equations into topological and metric equations, we introduce two auxiliary quantities for the continuity equation, $\tilde{\rho}, \widetilde{(\rho u)} \in \Omega^1(\mathcal{M})$, that are, for a start, independent of u and of ρ used in the momentum equation. In addition, the velocity field $\vec{v}$ used to evaluate the contraction within the nonlinear Coriolis term is, for a start, independent of u. Consequently, the momentum and continuity equations of (2.15) do not contain operators that require the definition of a metric, thus being purely topological equations. We have, however, five unknowns for two equations, which requires additional constraints to close the system. Therefore, we introduce three additional metric dependent equations. The resulting system is summarized in the following theorem:

Theorem 2.4.1. *Let $\mathcal{M} \subset \mathbb{R}^n, n = 2, 3$, be a compact manifold on a rotating frame with angular velocity Ω and with smooth boundary $\partial\mathcal{M}$. Let the momentum of the fluid be described by $u \in \Omega^1(\mathcal{M})$, $\rho, p \in \Omega^0(\mathcal{M})$ while using the shallow-atmosphere approximation, i.e $f_C = f dx^1 \wedge dx^2 \in \Omega^2(\mathcal{M})$ with the Coriolis parameter $f = 2\Omega \sin(\varphi)$. Let $\vec{v} \in \mathcal{X}(\mathcal{M})$ be an auxiliary vector field. Let the two auxiliary quantities for density $\tilde{\rho} \in \Omega^n(\mathcal{M}), n = 2, 3$, and mass-flux $\widetilde{(\rho u)} \in \Omega^1(\mathcal{M})$ describe the evolution of the density field by the continuity equation.*

Then, the momentum and continuity equations in integral-form with integrations over arbitrary curves c or volume V on $\mathcal{M}$ do not require the definition of a metric, thus are referred to as topological equations *in the following, and are given by:*

$$\int_c \partial_t u + \int_c \mathbf{i}_{\vec{v}}(\mathbf{d}u + f_C) + \int_c \frac{1}{2}\mathbf{d}\mathbf{i}_{\vec{v}} u + \int_c \frac{1}{\rho}\mathbf{d}p = 0 \ , \qquad \int_V \partial_t \tilde{\rho} + \int_{\partial V} \widetilde{(\rho u)} = 0 \ , \quad (2.26)$$

with boundary conditions $\mathbf{i}_{\vec{v}}\mu$, with initial conditions $u(x, 0) = u_0(x)$ and with the energy closure (i) for incompressible flows by $\star\mathbf{d}\star u = 0$ or (ii) for barotropic flows by the equation of state, $p = \rho^2 \frac{\partial \omega}{\partial \rho}$, where $w = w(\rho)$ is the internal energy of Eq. (B.42)*. To close the system of equations, the following three* metric equations *are required:*

$$\star(\rho u) = \widetilde{(\rho u)} \ , \qquad \star\rho = \tilde{\rho} \ , \qquad u^\sharp = \vec{v} \ , \quad (2.27)$$

where $\star$ denotes the Hodge-star operator that connects the differential forms of momentum and continuity equations, and where the Riemannian lift $\sharp$ connects the one-form u with its vector proxy $\vec{v}$.

Proof. We proof that the invariant fluid equations (2.26) and (2.27) are well-defined by showing the equivalence of these equations with the corresponding vector-invariant fluid equations in shallow-atmosphere approximation.

Using Stokes theorem, i.e. $\int_V \mathbf{d}\omega = \int_{\partial V} \omega$ with $\omega \in \Omega^k(\mathcal{M}), k \leq n$ on an n-manifold $\mathcal{M}$, we can omit the integrations over the curves c and the volumes V. The equations in local form are given by:

$$\partial_t u + \mathbf{i}_{u^\sharp}(\mathbf{d}u + f) + \frac{1}{2}\mathbf{d}\mathbf{i}_{u^\sharp} u + \frac{1}{\rho}\mathbf{d}p = 0 \ , \qquad \partial_t \star \rho + \mathbf{d}(\rho u) = 0 \ , \quad (2.28)$$

in which the metric equations $\tilde{\rho} = \star\rho, \widetilde{(\rho u)} = \star(\rho u)$ and $u^\sharp = (< \vec{v}, \cdot >)^\sharp = \vec{v}$ have been inserted. Applying $\star$ on the continuity equation of (2.28) leads to: (i) $\star\star\rho = \rho$ and (ii)

$\star\, \mathbf{d} \star (\rho u) = \mathrm{div}(\rho u)^\sharp$, for which (ii) follows from Prop. B.1.1. Eq. (2.23) and Eq. (2.25) provide a two- and three-dimensional vector representation, respectively, of the nonlinear term $\mathbf{i}_{u^\sharp}(\mathbf{d}u + f_C)$. Furthermore, the pressure term can be represented with Prop. (A.4.3).

We evaluate the interior product $\mathbf{i}_{u^\sharp} u$ using Lemma 2.2.1. In two dimensions with $u = u_x dx + u_y dy$ and $u^\sharp = \vec{v} = u_x \vec{e}_x + u_y \vec{e}_y$, this leads to

$$\mathbf{i}_{\vec{v}} u = (-1)^{1(2-1)} \star (\star u \wedge \vec{v}^\flat) = - \star (u_x dy - u_y dx) \wedge (u_x dx + u_y dy) = (u_x^2 + u_y^2) \star dx \wedge dy \ ,$$

in which $\star dx \wedge dy = 1$. In three dimension with $u = u_x dx + u_y dy + u_y dz$ and $u^\sharp = \vec{v} = u_x \vec{e}_x + u_y \vec{e}_y + u_x \vec{e}_z$, this leads to

$$\begin{aligned} \mathbf{i}_{\vec{v}} u = \star(\star u \wedge \vec{v}^\flat) &= \star(u_x dy \wedge dz + u_y dz \wedge dx + u_z dx \wedge dy) \wedge (u_x dx + u_y dy + u_z dz) \\ &= (u_x^2 + u_y^2 + u_z^2) \star dx \wedge dy \wedge dz \ , \end{aligned} \tag{2.29}$$

with $(-1)^{1(3-1)} = 1$ and $\star dx \wedge dy \wedge dz = 1$. This corresponds to the inner product of the velocity vector $\vec{v}$, i.e. $< \vec{v}, \vec{v} >= \vec{v}^2$ for two or three dimensions. Because the kinetic energy is defined by $\kappa = \frac{1}{2}\vec{v}^2$, all terms in Eq. (2.26) agree with the fluid equations in vector calculus with shallow-atmosphere approximation of (C.2) and (C.4). □

Remark. The interior product of a one-form $u \in \Omega^1(\mathcal{M})$ can also be evaluated using the Riemannian lift $\sharp : \Omega(\mathcal{M}) \to \mathcal{X}(\mathcal{M}),\ u =< \vec{v}, \cdot >\mapsto \vec{v}$. Let be, for instance, $u^\sharp = \vec{v} = u_x \vec{e}_x + u_y \vec{e}_y$ the vector proxy of u in two dimensions. Then it follows:

$$\mathbf{i}_{u^\sharp} u = u(u^\sharp) =< \vec{v}, \vec{v} >=< u_x \vec{e}_x + u_y \vec{e}_y, u_x \vec{e}_x + u_y \vec{e}_y >= u_x^2 + u_y^2 \ ,$$

which agrees with the calculation for the two-dimensional case, $\mathbf{i}_{\vec{v}} u = u_x^2 + u_y^2$, from above. The same argumentation is valid for the three-dimensional case.

2.4.2 Systematic selection of a set of equations

Based on the splitting of the geophysical fluid equations in topological and metric parts, we introduce a systematic way of selecting a set of equations. That is, by the choice of adequate metric equations we find either the linear or nonlinear, either the rotating or non-rotating invariant fluid equations. Because of their invariant form, they are valid for two- and three-dimensional problems. We obtain the following sets of equations:

1. *the non-rotating linear fluid equations* are obtained if we set for the Riemannian lift $\sharp : \Omega^1(\mathcal{M}) \to 0, u^\sharp \mapsto 0$, leading to $i_{u^\sharp} : \Omega^k(\mathcal{M}) \to 0, k = 1, 2$, e.g. the non-rotating linear shallow-water equations (2.33) and (2.34);

2. *the rotating linear fluid equations* are obtained if we set the nonlinear parts to zero, i.e. $\mathbf{i}_{u^\sharp}\mathbf{d}u = 0$ and $\mathbf{d}\mathbf{i}_{u^\sharp} u = 0$, e.g. the rotating linear shallow-water equations (3.1) and (3.2) investigated in Chapter 3;

3. *the non-rotating nonlinear fluid equations* are obtained by setting the Coriolis parameter $f = 0$, e.g. the invariant fluid equations (2.14);

4. *the rotating nonlinear fluid equations* are obtained if all terms are considered, e.g. the full GFD equations (2.26) and (2.27).

This selection process becomes particularly interesting in the process of discretization, as shown in Section 2.6. Assuming one degree of freedom associated to each vertex, edge and face, we show that the discretization of the topological equations is determined by

the choice of the computational mesh. Then, the choice of discrete metric equations, for instance, the discrete Hodge-star operators, determines the discrete scheme.

We investigate such discretization procedure in Section 2.6 on Case 1, the non-rotating linear shallow-water equations (introduced below). In Chapter 3 of this thesis we introduce discretization schemes for Cases 2 and 4.

2.4.3 Topological and metrical shallow-water equations

For the remainder of this thesis, we focus on the shallow-water equations to introduce our concept of discretization. The formulation of the general geophysical fluid equations of Theorem 2.4.1 can also be applied to the shallow-water equations. In Appendix C.2 we introduce the invariant geophysical shallow-water equations, which are the basis for the splitting into topological and metric parts shown in the following.

Corollary 2.4.2. *Let $\mathcal{M} \subset \mathbb{R}^2$ be a compact manifold on a rotating frame with angular velocity Ω and smooth boundary $\partial\mathcal{M}$. The Coriolis force is represented by the two-form $f_C = f dx^1 \wedge dx^2 \in \Omega^2(\mathcal{M})$ with the Coriolis parameter $f = 2\Omega \sin(\varphi)$. Let the momentum of the fluid be described by $u \in \Omega^1(\mathcal{M})$, $h \in \Omega^0(\mathcal{M})$ and let $\vec{v} \in \mathcal{X}(\mathcal{M})$ be an auxiliary vector field. Let the two auxiliary quantities for height $\tilde{h} \in \Omega^2(\mathcal{M})$ and mass-flux $\widetilde{(hu)} \in \Omega^1(\mathcal{M})$ describe the evolution of the density field by the continuity equation. Then, the* topological shallow-water equations *in integral-form are given by:*

$$\int_c \partial_t u + \int_c \mathbf{i}_{\vec{v}}(\mathbf{d}u + f_C) + \int_c \frac{1}{2}\mathbf{d}\mathbf{i}_{\vec{v}}u + \int_c g\mathbf{d}h = 0 \ , \quad \int_V \partial_t \tilde{h} + \int_{\partial V} \widetilde{(hu)} = 0 \ , \tag{2.30}$$

for all c, V with boundary $\mathbf{i}_{\vec{v}}\mu$, with initial conditions $u(x,0) = u_0(x)$ and with the energy closure (i) for incompressible flows by $\star\mathbf{d}\star u = 0$ (cf. Appendix B.3). To close the system of equations, the following metric equations are required:

$$\tilde{h} = \star h \ , \quad \widetilde{(hu)} = \star(hu) \ , \quad u^\sharp = \vec{v} \ , \tag{2.31}$$

with the Hodge-star operator $\star$ and with the Riemannian lift $\sharp$.

Proof. Similarly to the proof of theorem 2.4.1 we reformulate (2.30) and (2.31) to find the well-defined invariant shallow-water equations derived in Appendix C.2. Then, a calculation similar to the proof of theorem 2.3.1 leads to the rotating shallow-water equations in vector calculus form

$$\partial_t \vec{v} + (\zeta + f)\vec{k} \times \vec{v} + \nabla(\frac{1}{2}\vec{v}^2) + g\nabla h = 0 \ , \quad \partial_t h + \nabla \cdot (h\vec{v}) = 0 \ , \tag{2.32}$$

which proves that the shallow-water equations written in topological and metric parts are well-defined. □

The non-rotating linear shallow-water equations: Let the momentum of the fluid be described by the velocity field $u = u_x dx + u_y dy \in \Omega^1(\mathbb{R}^2)$ and by the fluid depth $h \in \Omega^0(\mathbb{R}^2)$ with $h = H + \delta h$, where H is the constant background fluid depth and δh the height variations. Let $\tilde{h} \in \Omega^2(\mathbb{R}^2)$ be an auxiliary height field and $\tilde{u}$ an auxiliary velocity field.

On basis of Corollary 2.4.2, we find the non-rotating linear shallow-water equations, Case 1 of Section 2.4.2, by setting the Riemannian lift to $\sharp : \Omega^1(\mathcal{M}) \to 0, u^\sharp \mapsto 0$ and obtain:

$$\int_c \partial_t u + g\int_c \mathbf{d}h = 0 \ , \qquad \int_V \partial_t \tilde{h} + H\int_V \mathbf{d}\tilde{u} = 0 \ , \tag{2.33}$$

with following metric equations to close the system:

$$\tilde{h} = \star h \ , \quad \tilde{u} = \star u \ . \tag{2.34}$$

This set of linear fluid equations has striking similarity to the linear equations of electrodynamics, introduced below in Eqn. (2.35) and (2.36), if the electric current is $\tilde{j} = 0$.

2.5 Comparison of fluid dynamics and electrodynamics

Our formulation of the non-rotating linear shallow-water equations leads to a set of equations consisting of four independent variables, namely $u, \tilde{u}, h, \tilde{h}$, and of four equations, namely two topological equations (2.33) and two metric equations (2.34). The form of this equations is similar to the linear Maxwell's equations, as discussed in the following.

In the literature the comparison of the two sets of equations is usually based on the similarity of potential vorticity (PV) and electric charges. Thorbe and Bishop [16, 100], for instance, found an analogy between electrostatics and potential vorticity distributions by describing a PV anomaly embedded in a zonally-averaged flow in terms of a nonlinear dielectric medium. An analogy between potential vorticity dynamics and electrodynamics has been established by Schneider et al. [94] to study boundary effects in PV dynamics. More recently, Herbert [51] investigated similarities but also differences between the dynamical PV-related equations and the linear Maxwell's equations.

When regarding the derivations in these references [16, 51, 100, 94], one can infer that the use of vector calculus leads to quite lengthy calculations. The language of differential geometry allows for a more abstract and concise formulation. For instance, for the vorticity $\omega = \mathbf{d}\vec{u}^\flat \in \Omega^2(\mathcal{M})$ one finds the *vorticity-stream equation* given in Eq. (B.59) in Appendix B (cf. also Abraham and Marsden [1]). In this sense, our approach could contribute to a more concise and general comparison of fluid dynamics and electrodynamics using differential geometry.

The following short comparison between the linear shallow-water and Maxwells' equations goes without the use of potential vorticity. We compare purely the form of the equations. Our aim is hereby to use concepts developed for computational electrodynamics for the discretization of the shallow-water equations.

Maxwell's equations in topological and metric parts: The linear Maxwell's equations describe the time evolution of the electric field e and magnetic field b that are caused by a current $\tilde{j}$ within a domain $\mathcal{M}$. Let be $e, \tilde{h} \in \Omega^1(\mathcal{M})$, $b, \tilde{d} \in \Omega^2(\mathcal{M})$ and the current density $\tilde{j} \in \Omega^2(\mathcal{M})$. Then, Maxwell's equations in integral form (Faraday and Ampère laws) are given by

$$\int_f \partial_t b + \int_f \mathbf{d}e = 0 \ , \quad -\int_{\tilde{f}} \partial_t \tilde{d} + \int_{\tilde{f}} \mathbf{d}\tilde{h} = \int_{\tilde{f}} \tilde{j} \ . \tag{2.35}$$

To close the system, we need the following metric equations (constitutive laws):

$$\tilde{d} = \epsilon \star e \ , \qquad b = \mu \star \tilde{h} \ , \tag{2.36}$$

with coefficients ϵ, μ. Here, we use a formulation often applied by Bossavit et al. [19, 20, 21, 22, 23, 24].

To describe the physical measurable fields, electric field e and the magnetic field h, one finds a formulation in two topological equations (2.35) and two metric equations (2.36). As the current $\tilde{j}$ is a function of e [25], the system of equations is closed as

four quantities $e, b, \tilde{d}, \tilde{h}$ are described by four equations. The topological equations, also called *network equations*, are based on conservation laws. These equations purely need topological information and no metric information. The system of equation is closed by the so-called *constitutive laws* (2.36) for which metric information is required.

Fluid dynamics vs electrodynamics: By the splitting of the non-rotating linear shallow-water equations we introduce a formulation very similar to the linear Maxwell's equations. The physical measurable electric and magnetic fields e, b described by Faraday's law (2.35, left) are related to the velocity and height fields u, h in the momentum equation of (2.33). The newly introduced auxiliary values $\tilde{u}, \tilde{h}$ in the continuity equation of (2.33) find their counterparts in the electric displacement and in the auxiliary magnetic fields $\tilde{d}, \tilde{h}$, respectively, described by Ampere's law (2.35, right). However, the dimensions of the equations and fields differ between shallow-water equations and electrodynamics. The momentum and continuity equations are one- and two-dimensional, respectively, whereas in electrodynamics both Faraday's and Ampere's law are two-dimensional. Because of the invariant form of the equations, such difference is not apparent in the form of the equations.

Regarding the rotating linear shallow-water equations, Case 2 of Section 2.4.2, the Coriolis term can be written in invariant form by $(\mathbf{i}_{u^\sharp} f_C)^\sharp = f\vec{k} \times \vec{u}$ (cf. proof of Theorem 2.3.1). A similar representation of the Lorentz force by representing the cross product with an interior product, i.e. $(\mathbf{i}_{\vec{v}} b)^\sharp = \vec{v} \times \vec{B}$, where $\vec{B}$ is the vector proxy of b, has been introduced by Bossavit et al. [27]. However, one has to recognize the difference in the externally prescribed velocity field $\vec{v}$ used to evaluate the Lorentz force, and the vector proxy $u^\sharp$ that has to be calculated by the flow field u itself. The determination of $u^\sharp$ is a nontrivial task, and we will consider this problem in more detail in Chapter 3. In the following we exploit the form similarity of Maxwell's equations and the split form of the shallow-water equations by discretizing the latter using concepts and tools frequently used in computational electrodynamics.

2.6 The method of discrete exterior calculus (DEC)

We introduce a method called discrete exterior calculus (DEC) developed by Hirani [54] and Desbrun and Marsden et al. [32]. Based on exterior calculus and differential geometry (see e.g. [1]), DEC defines the discrete operators on basis of the continuous differential operators and mimics its properties, if possible, also in the discrete case. By this, important properties, for instance, the Hodge decomposition [33] (and its analogous Helmholtz vector decomposition), can be transfered by definition to the discrete level.

All definitions and results presented in this section are taken from Desbrun et al. [33], unless otherwise stated. We first introduce the definitions required to approximate manifolds and differential operators. Such operators are purely topological and are used later (in Sect. 2.7) to discretize the topological equations (2.33). The metric equations (2.34) use the Hodge-star operator and require a metric. We will introduce a discrete diagonal Hodge-star operator at the end of this sections.

Our formulation of the geophysical fluid equations in invariant form including the splitting in topological and metric parts allows to apply the discrete operators of DEC on these equations to discretize them. This is done in Section 2.7 on the basis of the results of this section for the non-rotating linear shallow-water equations (2.33) and (2.34).

2.6.1 Discretization of manifolds by simplices

An n-dimensional manifold $\mathcal{M}$ can be approximated with simplices, i.e. ordered sets of vertices, edges, faces, etc. We use complexes of simplices to discretize the momentum and continuity equations by chains and cochains that are based on simplices and used to discretize the manifolds and differential forms, respectively.

Notation of a simplex: A k-simplex σ_k is the non-degenerate convex hull of $k+1$ geometrically distinct points $v_0, \ldots, v_k \in \mathbb{R}^n$ with $n \geq k$:

$$\sigma_k = \{x \in \mathbb{R}^n \mid x = \sum_{i=0}^{k} \alpha^i v_i \quad \text{with} \quad \alpha^i \geq 0 \text{ and } \sum_{i=0}^{k} \alpha^i = 1\} \ . \tag{2.37}$$

The entities $v_0, \ldots, v_k$ are called the vertices and k the dimension of the k-simplex, which we denote as

$$\sigma_k = \{v_0 v_1 v_2 \ldots v_k\} \ . \tag{2.38}$$

With respect to the ordering of the $k+1$ vertices of a k-simplex, one can assign a local orientation to each element of the mesh. The *orientation*, or(), changes by an odd permutation of the vertices, e.g. if $\text{or}(\{v_0 v_1\}) = 1$ then $\text{or}(\{v_1 v_0\}) = -1$.

Boundary of a Simplex: The notion of a boundary of a simplex is important as it describes the topological relations between different k-simplices. The *boundary* of a k-simplex is the union of $(k-1)$-faces, where $(k-1)$-faces are $(k-1)$-simplices spanned by k vertices taken from a subset of $\{v_0, \ldots v_k\}$.

To find the boundary of a k-simplex, Desbrun et al. [33] defined a boundary operator that returns the signed sum of $(k-1)$-faces with coefficients 1 and -1 for matching or non-matching orientation, respectively. This is summarized in the following definition.

Definition 2.6.1. For the k-simplex, the *boundary operator* ∂ returns the signs sum of $(k-1)$-faces by

$$\partial\{v_0 v_1 \cdots v_k\} = \sum_{j=0}^{k} (-1)^j \{v_0, \cdots, \widehat{v_j}, \cdots, v_k\} \ , \tag{2.39}$$

where $\widehat{v_j}$ means that v_j is missing from the sequence.

With Def. 2.6.1 we find an operator with the property $\partial \circ \partial = 0 \ \forall \sigma_k$, which we illustrate on the simplex $\sigma_2 = \{v_0 v_1 v_2\}$. It follows: $\partial\sigma_2 = \{v_0 v_1\} - \{v_0 v_2\} + \{v_1 v_2\}$, and thus for $\partial\partial\sigma_2 = \partial\{v_0 v_1\} - \partial\{v_0 v_2\} + \partial\{v_1 v_2\} = v_0 - v_1 - v_0 + v_2 + v_1 - v_2 = 0$. This is a general property of the boundary operator ∂ applied on any $\sigma_k, k \leq n$.

Simplicial Complex: A collection K of simplices is called a *simplicial complex* if it satisfies both that (i) every face of each simplex K is in K, and that (ii) the intersection of any two simplices in K is either empty or an entire common face.

Discrete Manifolds: To approximate manifolds, we use simplicial complexes (Fig. 2.2). We define an n-dimensional discrete manifold as an n-dimensional simplicial complex that satisfies the following condition: for each simplex, the union of all occurring n-simplices forms an n-dimensional ball, or, if the simplex is on the boundary, only half of a ball (cf. [33]). Thus, each $(n-1)$-simplex has exactly two adjacent n-simplices or only one if it is a boundary simplex. Figure 2.2 shows a two-dimensional manifold that is approximated by a two-dimensional simplicial mesh.

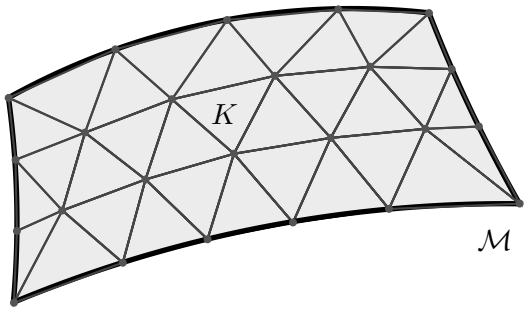

Figure 2.2: An n-dimensional manifold $\mathcal{M}$ is approximated by an n-dimensional simplicial complex K.

2.6.2 Topological operators on discrete manifolds

The notion of chains and cochains will be introduce to find a discrete analog for k-dimensional sub-manifolds and k-form. According to Eq. (2.3) a continuous k-forms is a multi-linear map from the k-spaces of vector fields $\mathcal{X}(M)$ to the space of continuous functions and an integral of a k-form assigns an value to a k-dimensional sub-manifold, according to Definition (2.2.1).

To find a discrete analog to a k-dimensional manifold, we use a k-chain that is a weighted sum of k-simplices with one value for every single simplex.

Definition 2.6.2. A k-chain c of an oriented simplicial complex K is a linear combination of all the k-simplices in K, i.e.

$$c = \sum_{\sigma \in K} c(\sigma) \cdot \sigma \ , \tag{2.40}$$

where $c(\sigma) \in \mathbb{R}$. The set of k-chains is denoted by C_k. We indicate with K^k the set of all k-simplices in K with cardinality $|K^k|$. Because there is one number for each k-simplex, the k-chain can be stored as a vector array of dimension $|K^k|$.

Analogously to k-forms acting on k-dimensional sets, we define k-cochains acting on k-chains in the following way:

Definition 2.6.3. A k-cochain ω is the dual of a k-chain, i.e. ω is a linear mapping that takes k-chains to real numbers by

$$\omega : C_k \to \mathbb{R} \ , \quad c \mapsto \omega(c) \ . \tag{2.41}$$

The set of k-cochains is denoted by C^k and is the dual space to C_k. As a chain c is a linear combination of simplices, a cochain returns a linear combination of values, such as:

$$\omega(c) = \int_{\sum_i c_i \sigma_i} \omega = \sum_i c_i \int_{\sigma_i} \omega = \sum_i c_i \omega[i] \ , \tag{2.42}$$

with $\omega[i] := \int_{\sigma_i} \omega$. As the k-simplices form a basis for the vector space C_k, we only need to know the mapping of vectors in this basis. Hence, $\omega[i]$ uniquely determines ω and is moreover a *discrete* representation of ω on a discrete manifold (cf. [33]).

A vector representation of the k-cochain ω^k can be established when regarding how ω^k acts on chains c_k that are represented as a vector with dimension $|K^k|$. By definition the linear operator $\omega(c)$ returns a scalar in $\mathbb{R}$. This can be seen as the inner product

$\omega^k \cdot \sigma_k$, where the vector ω^k has the same length as c_k. If we regard c_k as column vectors, then the row vector $(\omega^k)^t$ represents an $\mathbb{R}$-linear mapping and $\omega(c)$ becomes the matrix multiplication of $(\omega^k)^t$ with c_k.

Boundary operator on chains: The boundary operator ∂_k of Definition 2.6.1 applied to a k-simplex returns a $(k-1)$-chain with coefficients $0, -1, 1$. Based on the linearity property, ∂ can also be applied to chains. The boundary operator is thus a linear mapping from the space of k-simplices into the space of $(k-1)$-simplices. This map can be represented as a matrix with dimension $|K^{k-1}| \times |K^k|$ that acts on chains represented as arrays with dimension $|K^k|$. This matrix is sparse and contains, similarly to the boundary of simplices, only entries with $0, -1, 1$. The operators ∂_k differ with respect to the dimension of the simplex they act upon. As it becomes clear, based on the dimension of the simplex, which ∂_k is meant, we simply drop the index k when there is no ambiguity.

Discrete exterior derivative: Based on the definitions of chains and cochains the *discrete exterior derivative* $\mathbf{d}$ can be defined via Stokes' theorem[3]:

$$\int_\sigma \mathbf{d}\omega = \int_{\partial\sigma} \omega \ , \tag{2.43}$$

in which the discrete exterior derivative $\mathbf{d} : \omega^k \to \omega^{k+1}$ applied to an arbitrary k-cochain ω^k is evaluated on an arbitrary simplex σ^{k+1}.

Frequently, the integration is denoted as pairing of cochains and chains, i.e. $\int_\sigma \omega =: < \omega, \sigma >$. Thus, Eq. (2.43) can be written as $< \mathbf{d}\omega, \sigma > = < \omega, \partial\sigma >$, where the boundary operator has been applied to σ. Thus, $\mathbf{d}$ is the adjoint of the boundary operator ∂ and is also called coboundary operator. Based on the duality of ∂ and $\mathbf{d}$, we find $\partial\partial = \mathbf{dd} = 0$, which can easily be inferred by applying the notation of paring and exploiting the duality property of both operators.

By definition, the discrete exterior derivative $\mathbf{d}$ of (2.43) is a linear mapping of the space of k-cochain K^k into the space of $k+1$-cochain K^{k+1}. An adequate representation is thus a matrix with dimension $|K^{k+1}| \times |K^k|$. Based on the duality properties of ∂ and $\mathbf{d}$ and by exploiting the notation of pairing we can write:

$$\int_{\partial c} \omega = < \omega, \partial c > = \omega^t(\partial c) = (\omega^t \partial)c = (\partial^t \omega)^t c = < \partial^t \omega, c > = \int_c \partial^t \omega \ . \tag{2.44}$$

Based on Stokes' theorem (2.43) and on the fact that $\mathbf{d}$ is the adjoint operator of ∂, the matrix $\mathbf{d}$ equals ∂^t that is the transposed of the boundary operator ∂. Hereby, we use Stokes' theorem to convert an integral over a k-dimensional set into a boundary integral of a $(k-1)$-dimensional boundary to find adequate discrete analogs to the continuous differential operators.

Chain and cochain complexes and its properties: A *chain complex* is a sequence of linear spaces connected by a linear operator l with the property $l \cdot l = 0$, e.g. the boundary and coboundary operators with $\partial\partial = \mathbf{dd} = 0$. The chain complex for the linear spaces C_k in three dimensions based on the boundary operator ∂ can be illustrated with the following diagram:

$$0 \longrightarrow C_3 \xrightarrow{\partial_3} C_2 \xrightarrow{\partial_2} C_1 \xrightarrow{\partial_1} C_0 \longrightarrow 0 \ . \tag{2.45}$$

[3]This theorem states in terms of differential forms vector identities equivalent to curl, divergence and Green's theorem [1].

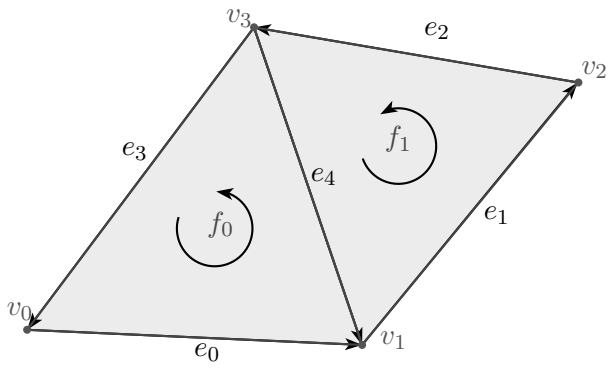

Figure 2.3: Discrete manifold with nodes v_i, edges e_i and faces f_i. The arrows indicate the intrinsic orientation of the edges and faces. The relative orientation of edges to vertices and of faces to edges is given by the coincidence matrix $\mathbf{G}$ and $\mathbf{R}$, respectively.

As the discrete exterior derivative $\mathbf{d}$ is the adjoint of ∂, the cochain complex for the linear spaces C^k in three dimensions is given by

$$0 \longleftarrow C^3 \xleftarrow{\mathbf{d}_2} C^2 \xleftarrow{\mathbf{d}_1} C^1 \xleftarrow{\mathbf{d}_0} C^0 \longleftarrow 0 \,. \tag{2.46}$$

Such chain and cochain complexes are illustrated in Figure 2.4.

2.6.3 Example on two-dimensional topological meshes

We present in the following on two-dimensional primal and dual meshes concrete realizations of chains, cochains, boundary and coboundary operators, and present their implementation as vectors arrays and matrices. We will require these results, in particular the topological differential operators that are analogs to gradient, curl and divergence operators, in the next section in order to discretize the shallow-water equations.

In accordance with the notation for simplices of Eq. (2.37) and with the boundary operator of Def. 2.6.1, we calculate the boundary operator ∂_2 for the faces $f_0 = \{v_0 v_1 v_3\}$ and $f_1 = \{v_1 v_2 v_3\}$ of Fig. 2.3 by

$$\begin{aligned} \partial_2^0 f_0 &= \{v_0 v_1\} - \{v_0 v_3\} + \{v_1 v_3\} = \{e_0\} - \{-e_3\} + \{-e_4\} \,, \\ \partial_2^1 f_1 &= \{v_1 v_2\} - \{v_1 v_3\} + \{v_2 v_3\} = \{e_1\} - \{-e_4\} + \{+e_2\} \,, \end{aligned} \tag{2.47}$$

where the arrows indicate the intrinsic orientation of the edges. The signs of the simplices of (2.47) written as a column vector can be identified with the boundary operator $\partial_2^i, i = 0, 1$, corresponding to face f_i, i.e. the boundary operator for f_0 is $\partial_2^0 = (1, 0, 0, 1, -1)^t$, and for f_1 it is $\partial_2^1 = (0, 1, 1, 0, 1)^t$.

Analogously, the operator $\partial_1^i, i = 0, \ldots, 4$, acts on edges e_i, e.g. on $e_0 = \{v_0 v_1\}$ with $\partial_1^0 e_0 = v_1 - v_0$ or on $e_4 = -\{v_1 v_3\}$ with $\partial_1^4 e_4 = v_1 - v_3$, and gives corresponding coefficient vectors $(-1, 1, 0, 0)^t$ or $(0, 1, 0, -1)^t$, respectively.

The chains and cochains are stored as column vectors, and, according to Eq. (2.44), the transposed cochain vectors then act on the chains by matrix multiplication. Thus, by arranging the coefficients of the chains column-wise within matrices, we find the boundary operators for the entire domain as coefficient matrices[4] by $\partial_2 = (\partial_2^k)_{k=1,\ldots,|K^f|}$ and $\partial_1 =$

[4]For instance, the boundary chains ∂_1 are represented as column vectors with coefficients $0, -1, 1$ of the basis $(e_1, ..., e_4)$ spanning the vector space C_1 of one-chains.

$(\partial_1^k)_{k=1,\dots,|K^e|}$, i.e.

$$\partial_2 = \begin{pmatrix} 1 & 0 \\ 0 & 1 \\ 0 & 1 \\ 1 & 0 \\ -1 & 1 \end{pmatrix}, \qquad \partial_1 = \begin{pmatrix} -1 & 0 & 0 & 1 & 0 \\ 1 & -1 & 0 & 0 & 1 \\ 0 & 1 & -1 & 0 & 0 \\ 0 & 0 & 1 & -1 & -1 \end{pmatrix}, \tag{2.48}$$

where $\partial_2 \in M(|K^e| \times |K^f|)$ and $\partial_1 \in M(|K^v| \times |K^e|)$ are so-called *coincidence matrices* and where $|K^f|, |K^e|$ and $|K^v|$ are the numbers of faces, edges and nodes, respectively, of the simplicial complex of Fig. 2.3 that tessellate the manifold.

According to Eq. (2.44), the discrete exterior derivatives are given by the transposed of the boundary operators, i.e. $\mathbf{d}_1 = \partial_2^t$ and $\mathbf{d}_0 = \partial_1^t$. The change in the indexing comes from the fact that both, the boundary and coboundary operators get the index from the simplex σ^k they acting on (cf. (2.45) and (2.46)). Thus, the exterior derivatives can be represented as:

$$\mathbf{d}_1 = \begin{pmatrix} 1 & 0 & 0 & 1 & -1 \\ 0 & 1 & 1 & 0 & 1 \end{pmatrix}, \qquad \mathbf{d}_0 = \begin{pmatrix} -1 & 1 & 0 & 0 \\ 0 & -1 & 1 & 0 \\ 0 & 0 & -1 & 1 \\ 1 & 0 & 0 & -1 \\ 0 & 1 & 0 & -1 \end{pmatrix}, \tag{2.49}$$

with the coincidence matrices $\mathbf{d}_1 \in M(|K^f| \times |K^e|)$ and $\mathbf{d}_0 \in M(|K^e| \times |K^v|)$.

We define $\mathbf{F} = (f_1, \dots, f_{|K^f|})^t$, $\mathbf{E} = (e_1, \dots, e_{|K^e|})^t$ and $\mathbf{N} = (v_1, \dots, v_{|K^v|})^t$ as basis vectors that span the vector space of two-chains, one-chains and 0-chains, respectively. For our example in Fig. 2.3 there is $\mathbf{N} = (v_0, \dots, v_3)^t$, $\mathbf{E} = (e_0, \dots, e_4)^t$ and $\mathbf{F} = (f_0, f_1)^t$. Then,

$$\mathrm{grad}(\mathbf{E})^\flat \backsimeq \mathbf{d}_0\mathbf{N} = \begin{pmatrix} -v_0 + v_1 \\ -v_1 + v_2 \\ -v_2 + v_3 \\ +v_0 - v_3 \\ +v_1 - v_3 \end{pmatrix}, \qquad \mathrm{curl}(\mathbf{F})^\flat \backsimeq \mathbf{d}_1\mathbf{E} = \begin{pmatrix} e_0 + e_3 - e_4 \\ e_1 + e_2 + e_4 \end{pmatrix}. \tag{2.50}$$

The exterior derivative $\mathbf{d}_0$ and $\mathbf{d}_1$ are operators that are applied by matrix multiplication to the basis vectors $\mathbf{N}$ and $\mathbf{E}$, respectively. Every entry of $\mathbf{d}_0\mathbf{N}$ corresponds to exactly one edge e_k with boundary $\partial_1^k e_k$, and every entry of $\mathbf{d}_1\mathbf{E}$ corresponds to exactly one face with boundary $\partial_2^k f_k$. Therefore, the vectors $\mathrm{grad}(\mathbf{E})$ and $\mathrm{curl}(\mathbf{F})$, obtained by using the Riemannian lift in (2.50), can be identified with a second order gradient and a first order curl operator, respectively (cf. Sections 2.7 and 2.8).

The property $\mathbf{dd} = 0$ of the exterior derivative also transfers to the discrete differential operators (2.50), i.e. $\mathbf{d}_1\mathbf{d}_0\mathbf{N} = 0$, as it can be inferred by simple calculations. Thus, the cochains C^k together with the discrete exterior derivative $\mathbf{d}_k$ fulfill the necessary conditions for a cochain complex (2.46).

For the two-dimensional simplicial mesh of Fig. 2.3, denoted in the following as *primal mesh*, there exists no boundary operator $\mathbf{d}_2$. Therefore, there is no topological divergence operator that describes the changes in fluxes over the cell boundaries of the primal mesh. However, on the dual mesh (definition is given below) a topological divergence operator exists, as derived in the following.

Exterior derivate on the dual mesh: The definition of the dual exterior derivative requires the definition of a *dual mesh*. Based on a triangulation of an n-manifold, we associate to every k-simplex a dual $(n-k)$-cell. Thus, for $n=2$ we associate to a vertex a dual two-cell, to an edge a dual edge and to a face a dual vertex (cf. Fig. 2.4). The number of dual $(n-k)$-cells is, by construction, equal to that of primal k-simplices. The set of dual cells is called cell complex and it is not necessarily a simplicial complex [33].

Based on the inherent properties of a primal simplicial complex, the dual mesh inherits several properties. For instance, on the basis of the primal exterior derivative $\mathbf{d}^{\text{primal}}$, the dual exterior derivative $\mathbf{d}^{\text{dual}}$ can be defined according to Desbrun et al. [33] by

$$\mathbf{d}_{n-k}^{\text{dual}} = (-1)^k (\mathbf{d}_{k-1}^{\text{primal}})^t \ , \tag{2.51}$$

for all $k \leq n$, where $(\cdot)^t$ denotes the transposed matrix.

Following the two-dimensional example of Fig. 2.3 with the primal exterior derivatives $\mathbf{d}_k^{\text{primal}} = \mathbf{d}_k$ defined in Eq. (2.51), we find for $k=1$ the dual exterior derivative $\mathbf{d}_1^{\text{dual}}$ that acts on edges by

$$\mathbf{d}_1^{\text{dual}} = (-1)(\mathbf{d}_0)^t = (-1) \begin{pmatrix} -1 & 0 & 0 & 1 & 0 \\ 1 & -1 & 0 & 0 & 1 \\ 0 & 1 & -1 & 0 & 0 \\ 0 & 0 & 1 & -1 & -1 \end{pmatrix} \in M(|K^v| \times |K^e|) \ . \tag{2.52}$$

Now, let $\mathbf{d}_1^{\text{dual}}$ act on $\mathbf{E} = (e_1, \ldots, e_{|K^e|})^t$, with $|K^e| = 5$ and let be $\mathbf{N} = (v_1, \ldots, v_{|K^v|})^t$ with $|K^v| = 4$ such that

$$\begin{pmatrix} \text{div}(v_o) \\ \text{div}(v_1) \\ \text{div}(v_2) \\ \text{div}(v_3) \end{pmatrix}^\flat = \text{div}(\mathbf{N})^\flat \backsimeq \mathbf{d}_1^{\text{dual}} \mathbf{E} = - \begin{pmatrix} -e_0 + e_3 \\ e_0 - e_1 + e_4 \\ e_1 - e_2 \\ e_2 - e_3 - e_4 \end{pmatrix} . \tag{2.53}$$

Every entry of $\mathbf{d}_1^{\text{dual}}\mathbf{E}$ corresponds to exactly one vertex v including all adjacent edges signed according to their orientation. The vector $\text{div}(\mathbf{N})$, obtained by using the Riemannian lift in (2.53), can thus be identified with a divergence operator positioned at vertices v (cf. Sect. 2.7). This operator is second order accurate on uniform meshes and between first and second order accurate on non-uniform meshes, as shown by a consistency analysis in Section 2.8.

In the following, we denote the coincidence matrix of the dual mesh $\mathbf{d}_1^{\text{dual}}$ with $\mathbf{D}^{\text{dual}}$ and $\mathbf{d}_0, \mathbf{d}_1$, of the primal mesh with $\mathbf{G}, \mathbf{R}$, respectively. In order to evaluate the relative orientation of vertices, edges and faces we use these coincidence matrices. For instance, we find for the vertices-to-edge relation for edge $e = \{v_1, v_2\}$ and for the edge-to-face relation with face $f = \{v_1, v_2, v_3\}$ and edges $e_1 = \{v_1, v_2\}, e_2 = \{v_2, v_3\}, e_3 = \{v_3, v_1\}$ the following signs:

$$\mathbf{G}_e^{v_1} = -1 \ , \quad \mathbf{G}_e^{v_2} = 1 \ , \quad \mathbf{R}_f^{e_1} = 1 \ , \quad \mathbf{R}_f^{e_2} = 1 \ , \quad \mathbf{R}_f^{e_3} = 1 \ , \tag{2.54}$$

as indicated by the arrows in Figure 2.3.

In three dimensions, we find with $\mathbf{d}_0$, $\mathbf{d}_1$ and $\mathbf{d}_2$ the topological gradient, curl and divergence operators, respectively. These operators fulfill the cochain properties $\mathbf{d}_2\mathbf{d}_1\mathbf{E} = 0$ and $\mathbf{d}_1\mathbf{d}_0\mathbf{N} = 0$. By Eq. (2.51), this is also true for the dual exterior derivatives. Therefore, the properties of a cochain complex and of the coboundary operators, i.e. $\mathbf{dd} = 0$, transfer to the corresponding discrete differential operators. Hence, the important vector calculus properties $\nabla \times \nabla = 0$ and $\nabla \cdot \nabla \times = 0$ in $\mathbb{R}^3$ are fulfilled (see more in [33]).

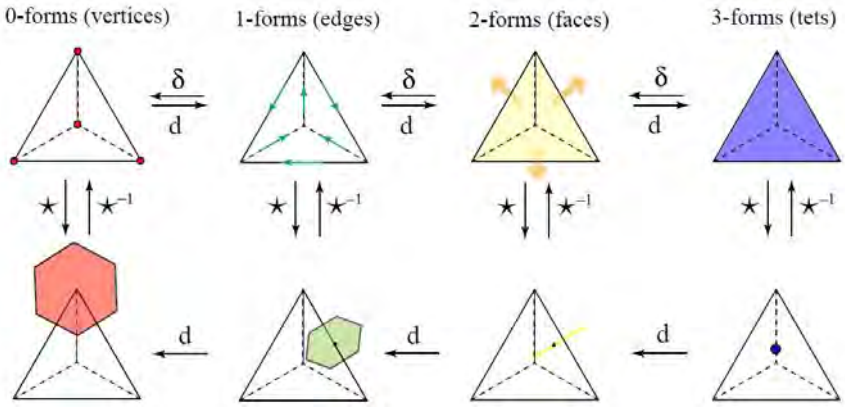

Figure 2.4: Illustration of the diagonal Hodge-star operator $\star_k$, $k = 1, 2, 3$, taken from Desbrun et al. [33].

2.6.4 Metric dependent operators on manifolds

The topology and the coincidence matrix $\mathbf{d}_1^{\text{dual}}$ of the dual topological mesh are defined via the primal topological mesh without using a metric. Hereby, only the neighborhood relationships and the orientations of the simplices are required. However, to determine the actual dual mesh, i.e. the position of the dual vertices, the dual edges that connect those vertices, and the dual faces that are spanned by dual edges, as well as the dual edge length and dual cell sizes, we require a discrete Hodge-star operator $\star$. The Hodge-star connects the primal and dual mesh with each other and assigns to the dual simplices their geometrical and metric properties.

We require a discrete representation of the Hodge-star operator introduced in Proposition A.2.1. The definition of the discrete Hodge-star operator is not unique, as the connection between primal and dual mesh may be realized in different ways, which, in turn, may lead to different properties of the discrete schemes. In the following we introduce two examples of different Hodge-star operators. However, several different possibilities exist, as studied, for instance, in computational electrodynamics [23].

The discrete diagonal Hodge-star operator: Following Desbrun et al. [33], we introduce a discrete diagonal Hodge-star operator $\star$ that connects the two-dimensional primal and dual topological meshes by the following diagonal matrices:

$$\star_0 = \frac{|v^*|}{|v|}, \quad \star_1 = \frac{|e^*|}{|e|}, \quad \star_2 = \frac{|f^*|}{|f|}, \tag{2.55}$$

where v, e, f denote vertices, edges and faces, respectively, and where $*$ means Voronoi dual. $|\cdot|$ denotes the length or the area of the corresponding edges or faces. Figure 2.4 illustrates the connection between primal and dual simplices via the Hodge-star operator (2.55) and shows the simplicial complex of the primal and dual meshes with the corresponding boundary and coboundary operators.

This diagonal Hodge-star operator is used for the remainder of this thesis. By this choice, we decide to use a staggered C-grid on a hexagonal or triangular mesh. Using the definitions introduced in this section, in particular the coincidence matrices $\mathbf{d}_0, \mathbf{d}_1$ and $\mathbf{d}_1^{\text{dual}}$, we derive in Section 2.7 for both meshes the discretized non-rotating linear shallow-water equations.

A non-diagonal Hodge-star operator: In principle, our method enables to use different Hodge-star operators of different complexity connecting the topological meshes. In the following we present a non-diagonal Hodge-star operator (also called Galerkin Hodge-star) introduced by Bossavit [25] for computational electrodynamics on tetrahedral meshes.

The key idea is to use a barycentric dual mesh. On the basis of Whitney interpolation functions ω^e (see e.g. Eq. (3.12)) and their property as partition of unity (see discussion after Eq. (3.10)), Bossavit [25] has shown the following identity:

$$\sum_{e' \in \mathcal{E}} \int_D \epsilon \omega^e(x) \cdot \omega^{e'}(x) e' = \int_D \epsilon \omega^e(x) \,. \tag{2.56}$$

The terms $\int_D \epsilon \omega^e(x) \cdot \omega^{e'}(x)$ on the left hand side can be summarized to a non-diagonal matrix, the Hodge-star operator $\star_\epsilon^{ee'}$, where only off-diagonal elements e' adjacent to edge e contribute with weight ϵ to the sum. The integral over the domain D on the right hand side equals the fraction of the dual area $\tilde{e}$ lying within the tetrahedron T, $\tilde{e}_T$, weighted with ϵ_T, i.e. $\int_T \epsilon \omega^e(x) = \epsilon_T \tilde{e}_T$ [25]. It follows for the non-diagonal Hodge-star

$$\sum_{e' \in \mathcal{E}} \star_\epsilon^{ee'} e' = \sum_T \epsilon_T \tilde{e}_T \,, \tag{2.57}$$

where ϵ_T is uniform in each individual tetrahedron. As one uses Whitney interpolation functions, the dual vertices, dual edges and dual faces are those of a barycentric dual mesh.

As discussed in Section 2.5, the non-rotating linear shallow-water equations and the linear Maxwell's equations have similar form. Thus, it would be interesting to investigate whether such operator leads also in the case of linear shallow-water equations to a stable system. However, we postpone further investigation using this non-diagonal Hodge-star operator to future work.

2.7 Discretization of the non-rotating linear shallow-water equations

We apply the method of DEC on the invariant non-rotating linear shallow-water equations split into topological and metric parts (2.33) to discretize them in a systematic way. As introduced in the previous section, the framework of DEC provides for a certain choice of primal topological mesh its dual topological mesh and the corresponding boundary and coboundary operators that are independent of a metric. The topological meshes are connected via metric dependent discrete Hodge-star operators. The latter are not unique and different choices lead to different discrete schemes. We introduce in the following two schemes, namely the triangular and hexagonal C-grid scheme, obtained by a certain choice of topological meshes and of the discrete Hodge-star operator.

The topological mesh has been introduced as a simplicial complex, a collection of simplices, to approximate the manifold. This simplicial complex is denoted as primal topological mesh in the following, and the dual cell complex, induced by the primal mesh as explained in the previous section, as dual topological mesh. Hereby, we use the diagonal Hodge-star operator (2.55) to obtain a dual mesh based on circumcenters.

The choices made so far involve both the triangular and hexagonal C-grid schemes. The two schemes differ, however, by the position of the degrees of freedom (DoF) for mass and velocity points. One obtains a hexagonal C-grid scheme if the mass points are at the vertices and the tangential velocity components are at the triangular midpoints. In contrast, a triangular C-grid scheme is given if mass points are in the circumcenters of the

triangles and if the normal velocity components are on the intersection of triangular and hexagonal cell edges.

In the following we introduce a method to obtain the DoF on the meshes by integrating the discrete k-cochains over chains. Hereby, we restrict our method to one DoF per simplex, i.e. for every node, edge, face or cell, we assign exactly one DoF, similar to the method of general finite differences (GFD) of Bossavit [25]. Using Stokes Theorem (2.43), our approach provides hereby automatically the discrete differential operators.

Discretization by integrating k-cochains over k-chains

The continuous shallow-water equations in integral form (2.33) must hold for all curves c and all areas A, which leads to an infinite number of equations in the continuous case. In the discretization step one assumes that the equations should hold only for a *finite number* of one-chains and two-chains used to approximate c and A, respectively, and that the k-forms are approximated by k-cochains.

Continuous equations: If we assume for the non-rotating linear shallow-water equations (2.33) that the integrals over the k-chains in the topological equations are time independent, i.e. $c(t) = c_0,\ A(t) = A_0\ \forall t$ – thus switching from the Lagrangian to the Eulerian picture in describing fluid motions – we obtain the following continuous system of equations

$$\partial_t \int_{c_0} u + g \int_{c_0} \mathbf{d}h = 0\,, \qquad \partial_t \int_{A_0} \tilde{h} + H \int_{A_0} \mathbf{d}\tilde{u} = 0\,, \qquad \forall c_0, A_0\,, \tag{2.58}$$

with the velocity one-forms $u, \tilde{u} \in \omega^1(\mathbb{R}^2)$, height and auxiliary height $h \in \Omega^0(\mathbb{R}^2)$ and $\tilde{h} \in \Omega^2(\mathbb{R}^2)$, respectively, and with background height H. The following metric equations close the system:

$$\tilde{h} = \star h\,, \quad \tilde{u} = \star u\,. \tag{2.59}$$

Discrete momentum equation: To obtain from Eq. (2.58) the discrete momentum equation, we approximate the continuous curve c_0 by the one-chain $c_0 \approx \sum_e e$, where e denote the edges of the primal topological mesh. The integral of the one-form u along the edge e is given by $u_e := \int_e u$. Thus, u_e is the DoF associated to edge e of the cochain that approximates u by $u \approx \sum_e u_e$. The integration along e for the second term including the exterior derivative $\mathbf{d}$ can be evaluated by using Stokes theorem (2.43), which translates the exterior derivative in a boundary integral, i.e. $\int_e \mathbf{d}h = \int_{\partial e} h$. Thus, we find for the sum over the edges $e = \{v_i, v_j\}$ the discrete momentum equation

$$\partial_t \sum_e u_e + g \sum_e h_{v_j} - h_{v_i} = 0\,, \tag{2.60}$$

with $\partial e = v_j - v_i$ according to the boundary operator of Def. (2.6.1).

By linearity it is sufficient to investigate the momentum equation for every single edge. Using the definitions introduced in the previous section, the momentum equation can be written in the following matrix form

$$\partial_t \mathbf{u} + g\mathbf{G}\,\mathbf{h} = 0\,, \tag{2.61}$$

where $\mathbf{u} = \{u_{e_i}, i = 1, \ldots, |K^e|\}$ is an array of size $|K^e|$ for the velocities at the edges, $\mathbf{h} = \{h_{v_1}, \ldots, h_{v_{|K^v|}}\}$ is an array of size $|K^v|$ for the height points at the vertices, and

where the exterior derivative is represented by the coincident matrix $\mathbf{G} \in M(|K^e| \times |K^v|)$ of Eq. (2.49).

If l_e is the length of e, then $\overline{u}_e := 1/l_e \int_e u$ is the *edge averaged velocity* positioned at the edge midpoint, thus $u_e = l_e \overline{u}_e$. For every edge e, we find the discrete momentum equation

$$\partial_t \overline{u}_e + g \underbrace{\frac{h_{v_2} - h_{v_1}}{l_e}}_{=\mathrm{grad}^{\mathrm{t}}{}_e(h_v)} = 0\,. \tag{2.62}$$

The relative orientation of edges to their boundaries is contained in $\mathbf{G}$. The amendment with the metric information allows to identify in Eq. (2.62) the finite difference gradient operator $\mathrm{grad}^{\mathrm{t}}{}_e$ that is tangential to the triangular edges and positioned at edge midpoints.

Discrete continuity equation: To discretize the continuity equation of Eq. (2.58), we approximate the area A_0 by the two-chain $A_0 \approx \sum_f f$, where f denotes the cells (hexagons) of the dual topological mesh. The integral of the two-form $\tilde{h} \in \Omega^2(\mathbb{R}^2)$ over the face f is given by $\tilde{h}_f := \int_f \tilde{h}$. $\tilde{h}_f$ is the DoF associated to the face f of the two-cochain that approximates $\tilde{h}$ by $\tilde{h} \approx \sum_f \tilde{h}_f$. To discretize the second term by integrating over f, we use Stokes theorem (2.43) to translate the exterior derivative $\mathbf{d}$ in a boundary integral, i.e. $\int_f \mathbf{d}\tilde{u} = \int_{\partial f} \tilde{u}$. Thus, we find for the sum over the cells f the discrete continuity equation

$$\partial_t \sum_f \tilde{h}_f + H \sum_f \tilde{u}_{\partial f} = 0\,, \quad \tilde{u}_{\partial f} := \int_{\partial f} \tilde{u}\,, \tag{2.63}$$

where ∂f is the cell boundary of f, which can be approximated by a sum of cell edges e_i^{dual}, i.e. $\partial f \approx \sum_i e_i^{\mathrm{dual}}, i = 1, \ldots, \#\text{cell edges}$, and therefore $\tilde{u}_{\partial f} \approx \sum_i \tilde{u}_{e_i^{\mathrm{dual}}}$.

By linearity it is sufficient to study the continuity equation for every single face f. Using the results from the previous section, we write the discrete continuity equation in the following matrix form

$$\partial_t \tilde{\mathbf{h}} + H \cdot \mathbf{D}^{\mathrm{dual}} \tilde{\mathbf{u}} = 0\,, \tag{2.64}$$

where $\tilde{\mathbf{h}} = \{\tilde{h}_{f_i}, i = 1, \ldots, |K^f|\}$ is an array of size $|K^f|$ for face averaged heights, $\tilde{\mathbf{u}} = \{\tilde{u}_{e_i^{\mathrm{dual}}}, i = 1, \ldots, |K^e|\}$ is an array of size $|K^e|$ for the velocities at dual edges e_i^{dual} and where the exterior derivative is represented by the coincidence matrix for the dual mesh $\mathbf{D}^{\mathrm{dual}} \in M(|K^v| \times |K^e|)$ of Eq. (2.52).

Discrete metric equations: With Eqn. (2.60) and (2.63) we have two equations for four unknowns, $u, \tilde{u}, h, \tilde{h}$. We close the system of equations using the discrete Hodge-star operator (2.55) that serves as discretization of Eq. (2.59) and find a relation between u, h and the auxiliary fields $\tilde{u}, \tilde{h}$ by

$$\tilde{h}_f = \star_0 h_v = \frac{A_f}{1} \cdot h_v\,, \qquad \tilde{u}_{e_i^{\mathrm{dual}}} = \star_1 u_{e_i} = \frac{d_{e_i}}{l_{e_i}} u_{e_i} = d_{e_i} \underbrace{\frac{1}{l_{e_i}} \int_{e_i} u}_{=\overline{u}_{e_i}}\,, \tag{2.65}$$

where d_{e_i} denotes the length of the edges e_i^{dual} that are dual to the primal edges e_i and where A_f denotes the size of the dual cell. Substituting $\tilde{h}_f$ and $\tilde{u}_{\partial f}$ in Eq. (2.63), the discrete continuity equation for every cell f on the dual mesh is given by

$$\partial_t h_v + H \cdot \underbrace{\frac{1}{A_f} \sum_{i=1}^{\#\text{edges}} (\pm) d_{e_i} \overline{u}_{e_i}}_{=\mathrm{div}_v(\overline{u}_e)} = 0\,, \tag{2.66}$$

where the sign $\pm$ is determined by the coincidence matrix $\mathbf{d}_1^{\text{dual}}$ of Eq. (2.52) and describes the orientation of edge e_i with respect to the vertex v. In combination with the metric information given by the discrete Hodge-star operator, the sum on the left hand side of Eq. (2.66) gives the divergence of the velocity field at vertices v, denoted with $\text{div}_v(\cdot)$.

Hexagonal C-grid scheme: To summarize, the discretized equations (2.62) and (2.66) for the non-rotating linear shallow-water equations correspond to a staggered hexagonal C-grid discretization. Hereby, the time evolution of the vector arrays $\mathbf{u}$ for the normal velocity components at the hexagonal cell edges and $\mathbf{h}$ for the height points at the hexagonal cell centers are described by the following system of equations written in matrix form:

$$\partial_t \mathbf{u} + g\,\mathbf{G}\mathbf{h} = 0\,, \quad \partial_t \tilde{\mathbf{h}} + H \cdot \mathbf{D}^{\text{dual}} \tilde{\mathbf{u}} = 0\,, \tag{2.67}$$

and the discrete metric equations:

$$\tilde{\mathbf{h}} = \star_0 \mathbf{h} = \frac{A_f}{1}\mathbf{h}\,, \qquad \tilde{\mathbf{u}} = \star_1 \mathbf{u} = \frac{d_e}{l_e}\mathbf{u}\,, \tag{2.68}$$

with the coincidence matrices $\mathbf{G}$ and $\mathbf{D}^{\text{dual}}$ that correspond to the discrete *gradient* and discrete *dual divergence* operators, respectively.

Triangular C-grid scheme: In case the momentum equation (2.58) is integrated over the dual edges e^{dual} of the dual topological mesh, i.e. $c_0 \approx \sum_{e^{\text{dual}}} e^{\text{dual}}$, one obtains, analogously to the derivations from above, for every dual edge with length d_e the following discrete momentum equation

$$\partial_t \overline{u}_{e^{\text{dual}}} + g \underbrace{\frac{h_{cc_j} - h_{cc_i}}{d_e}}_{=\text{grad}^{\text{n}}{}_e(h_{cc})} = 0\,, \tag{2.69}$$

with $\overline{u}_{e^{\text{dual}}} := 1/d_e \int_{e^{\text{dual}}} u$, which is the edge averaged velocity normal to the triangle edge. cc stands for a triangles' circumcenter. The boundary for the edge $e^{\text{dual}} = \{cc_i, cc_j\}$ is given by $\partial e^{\text{dual}} = cc_j - cc_i$ and is required to evaluate the exterior derivative in (2.58) using Stokes theorem (2.43). Using Eq. (2.51) to determine the corresponding coincidence matrix, the orientation of the dual edges to the triangles' circumcenters can be calculated. As indicated in Eq. (2.69), one finds the finite difference normal gradient operator $\text{grad}^{\text{n}}{}_e$ that is normal to the triangle edge e.

The continuity equation (2.58) is integrated over the primal topological mesh, i.e. over triangle faces f^{tri} with $A_0 \approx \sum_{f^{\text{tri}}} f^{\text{tri}}$. We find for every single triangular cell the discrete continuity equation

$$\partial_t h_{cc} + H \cdot \underbrace{\frac{1}{A_{f^{\text{tri}}}} \sum_{i=1}^{\#\text{edges}} (\pm) d_{e_i} \overline{u}_{e_i^{\text{dual}}}}_{=\text{div}_{cc}(\overline{u}_{e^{\text{dual}}})} = 0\,, \tag{2.70}$$

where h_{cc} are the height points at the triangles circumcenters. $A_{f^{\text{tri}}}$ denote the triangular cell area. The sign $\pm$ is determined by the coincidence matrix $\mathbf{d}_1$ of Eq. (2.50) and describes the orientation of the dual edge e^{dual} with respect to the triangular cell center cc. Including the metric information, the sum on the right hand side of Eq. (2.70) gives the divergence operator on the triangular cell centers, denoted with div_{cc}.

Because of the duality of the primal and dual topological meshes, which is based on the definition of the dual mesh (cf. Sect. 2.6.3), the triangular and the hexagonal C-grid

schemes are dual to each other. That is, for a given scheme, one obtains the dual scheme by exchanging with each other the primal and dual meshes, on which one integrates the momentum and continuity equations (see calculations above).

In this sense, also the discrete differential operators are dual, namely, the divergence operator in one model is the curl operator in the dual model and vice versa. For instance, the divergence operator div_{cc} of the triangular scheme coincides with the curl operator, denoted with curl_{cc} in the following, of the hexagonal scheme. The latter fact has already been discussed for an ICON shallow-water model by Bonaventura et al. [18].

2.8 Consistency and stability of the discrete schemes

We investigate the triangular and hexagonal C-grid discretization of the non-rotating linear shallow-water equations derived in the previous section concerning their consistency properties and we study the truncation errors of the differential operators. Furthermore, we investigate also stability for the schemes, as both conditions are required to obtain convergence. Fundamental theorems of numerical analysis are the Dahlquist's equivalence theorem for ordinary differential equations or the Lax's equivalence theorem for partial differential equations. Both theorems state that a method converges if and only if it is consistent and stable [13, 67].

On the basis of an truncation error analysis, where all required functions and operators are represented as Taylor series, we study the order of accuracy of the schemes, in particular of the discrete differential operators. In addition, we investigate the stability by an eigenvalue analysis of the linear algebraic system. To underpin our theoretical results some numerical experiments are performed.

2.8.1 Consistency properties and truncation errors

Given a partial differential equation (PDE) $Pu = f$ and a corresponding discrete scheme obtained by finite difference approximations denoted with $P_{\Delta t,\Delta x} v = f$, we say that the finite difference scheme is *consistent* with the PDE if for any smooth function $\phi(x,t)$ the following limit exists:

$$P\phi - P_{\Delta t,\Delta x}\phi \to 0 \quad \text{as} \quad \Delta t, \Delta x \to 0 \ , \tag{2.71}$$

i.e. if the discrete scheme agrees with the continuous PDE in case of $\Delta x, \Delta t \to 0$. In the following we investigate whether the triangular and/or the hexagonal discrete scheme from above share this property.

The discrete momentum equation: We first consider the discrete momentum equation (2.62), where the edge averaged velocity is represented by $\overline{u}_e := 1/l_e \int_e u$ with $u = u_x dx + u_y dy \in \Omega^1(\mathbb{R}^2)$ and where the height field is given by h_v at the vertices v. Without restriction of generality, let the edge $e = \{x_1 < 0, x_2 \geq 0\}$ be represented by two points on the x-axis around a midpoint at $x = 0$ such that $l_e = (x_2 - x_1) =: \Delta x = (\Delta x_+ + \Delta x_-); \Delta x_+ := x_2, \Delta x_- := -x_1$. Using Def. 2.2.1, we find for the averaged velocity in the limit $\Delta x \to 0$:

$$\overline{u}_e := \frac{1}{\Delta x}\int_{x_1}^{x_2} u_x dx = \frac{(u_x(x_2)x_2 - u_x(x_1)x_1)}{\Delta x} = \frac{(u_x(x_2)\Delta x_+ + u_x(x_1)\Delta x_-)}{\Delta x} \xrightarrow{\Delta x \to 0} u_x|_0 \ ,$$

where $u_x|_0$ gives the x-coordinate of the one-form at the edge midpoint $x = 0$. The same argumentation is valid for the averaged velocities $\overline{u}_{e^{\mathrm{dual}}}$ of Eq. (2.69) on dual (hexagonal) edges, i.e. $\overline{u}_{e^{\mathrm{dual}}} \xrightarrow{\Delta x \to 0} u_x|_0$.

Next, we expand the height field h along the x-axis around midpoint $x = 0$ into a Taylor series and evaluate it on edge e, i.e.

$$h_{\Delta x_\pm} = h_0 \pm \frac{\partial h}{\partial x}\Big|_0 \Delta x_\pm + \frac{1}{2}\frac{\partial^2 h}{\partial x^2}\Big|_0 \Delta x_\pm^2 \pm \frac{1}{6}\frac{\partial^3 h}{\partial x^3}\Big|_0 \Delta x_\pm^3 + O(\Delta x^4)\ . \tag{2.72}$$

The substitution of the expanded height field (2.72) in Eq. (2.62) leads to

$$\begin{aligned}
&\partial_t \overline{u}_e + g\frac{h_{\Delta x_+} - h_{\Delta x_-}}{\Delta x} = 0\ ,\\
&\partial_t \overline{u}_e + g\Big[\frac{\partial h}{\partial x}\Big|_0 \frac{\Delta x_+ + \Delta x_-}{\Delta x} + \frac{1}{2}\frac{\partial^2 h}{\partial x^2}\Big|_0 \frac{\Delta x_+^2 - \Delta x_-^2}{\Delta x} + \frac{1}{6}\frac{\partial^3 h}{\partial x^3}\Big|_0 \frac{\Delta x_+^3 + \Delta x_-^3}{\Delta x} + O(\Delta x^3)\Big] = 0,\\
&\Rightarrow\ \partial_t \overline{u}_e + g\Big[\frac{\partial h}{\partial x}\Big|_0 + O(\Delta x^i)\Big] = 0\ , \quad \text{with } \begin{cases} i = 1 \text{ if } \Delta x_+ \neq \Delta x_- \\ i = 2 \text{ if } \Delta x_+ = \Delta x_- \end{cases}\ .
\end{aligned} \tag{2.73}$$

Expanding h along the dual edges e^{dual} similarly to the Taylor series (2.72) and substituting it in Eq. (2.69), we find that both triangular and hexagonal schemes have the same expanded momentum equation (2.73).

We deduce from Eq. (2.73) the order of accuracy of the tangential gradient ($\text{grad}^{\text{t}}{}_e$ in (2.62)) and of the normal gradient ($\text{grad}^{\text{n}}{}_e$ in (2.69)). On uniform grids both operators have second order accuracy because the edge midpoint bisects the primal (triangular) edge e and the dual (hexagonal) edge e^{dual}. In case of non-uniform grids the primal edge is still bisected by the dual edge maintaining the second order accuracy of $\text{grad}^{\text{t}}{}_e$. However, the normal gradient has only first order accuracy, as the dual edge is in general not bisected by the primal edge leading to $\Delta x_+ \neq \Delta x_-$, which is a consequence of the construction of the dual (hexagonal) meshes using circumcenters (cf. Fig. 4.1).

In order to show consistency, we have to show that the discrete scheme agrees with the continuous scheme as indicate in Eq. (2.71). With the assumption on edge e (or e^{dual} in case of the triangular scheme) being parallel to the x-axis, the continuous momentum equation becomes

$$\frac{\partial u_x}{\partial t} + g\frac{\partial h}{\partial x} = 0\,. \tag{2.74}$$

Using the notation of Eq. (2.71), we investigate the limit of the semi-discrete equation $P_{\Delta x}$ of Eq. (2.73) toward the continuous equation P of (2.74) by

$$P_{\Delta x}\phi_{\Delta x} - P\phi = \frac{\partial}{\partial t}u_x|_0 + g\frac{\partial h}{\partial x}\Big|_0 + O(\Delta x^i)\ \ - \frac{\partial}{\partial t}u_x - g\frac{\partial h}{\partial x} = O(\Delta x^i) \text{ for } i = 1, 2. \tag{2.75}$$

Therefore, we find for the limit $\Delta x \to 0$:

$$\tau = P_{\Delta x}\phi_{\Delta x} - P\phi = O(\Delta x^i) \xrightarrow{\Delta x \to 0} 0 \quad \text{for } i = 1, 2, \tag{2.76}$$

which shows that $P_{\Delta x}$ is consistent with P as the truncation error vanishes when the grid spacing goes to zero. This is true for both triangular and hexagonal schemes for uniform and non-uniform meshes.

The discrete continuity equation: Next, we study the consistency properties of the discrete continuity equation (2.66). We expand the continuous function for the height h around vertex point v and evaluate it at a distance of Δx around v, i.e. $h(x_v + \Delta x) = h_v + h'|_v \Delta x + O(\Delta x^2)$. Using again the notation of Eq. (2.71), we find for the truncation error

$$\tau = P_{\Delta x}\phi_{\Delta x} - P\phi = \partial_t h_v + H\text{div}_v(\overline{u}_e) - \partial_t h - H\nabla \cdot \vec{u}\ . \tag{2.77}$$

The error contribution by $\partial_t h_v - \partial_t h = \partial_t h_v - \partial_t h_v + O(\Delta x)$ vanishes for $\Delta x \to 0$. Therefore, the investigation of the consistency properties of the discrete continuity equation reduces to the investigation of the consistency and truncation error of the divergence operator div_v. The same is true for the discrete continuity equation of the triangular scheme and for its divergence operator div_{cc} of Eq. (2.70).

Truncation error of the divergence operator on hexagons: We investigate the truncation error of the divergence operator defined in Eq. (2.66). Hereby, we rely on the result of Heikes and Randall [49] who have performed a truncation error analysis for the Laplace operator on hexagonal meshes. The authors investigated the Laplace operator that have been defined by Gauss theorem on a twisted icosahedral grid (cf. [48]). As we will see, the results obtained for the Laplace operator are also valid for the flux-divergence operator for hexagonal cells defined in Eq. (2.66).

Following Heikes and Randall [49] the discrete divergence operator at vertex v can be written as

$$\nabla \cdot \vec{u}|_v = \lim_{\Delta x \to 0} \frac{1}{A_{\Delta x}} \sum_i^{\#\text{faces}} \int_{d_{e_i,\Delta x}} \underbrace{\vec{u} \cdot \vec{n}}_{=:u_n^i} dl \ , \tag{2.78}$$

where u_n^i is the normal velocity component[5] to the hexagonal cell edges e_i^{dual}. $A_{\Delta x}$ is the size and $d_{e_i,\Delta x}$ is the edge length of the hexagon with $d_{e_i,\Delta x}, A_{\Delta x} \to 0$ if $\Delta x \to 0$. In case the line integrals are approximated by one DoF per edge with $u_n^i = \overline{u}_{e_i}$, this formulation agrees with our definition of the divergence operator in Eq. (2.66). Assuming that one knows u_n^i along the entire side $d_{e_i,\Delta x}$, one can expand such function into a Taylor series. Analogously to [49], we expand this function around the edge midpoint and take into account that on non-uniform grids there exist a discrepancy $r_{\Delta x}^i := \frac{m_{\Delta x}^i - x_{\Delta x}^i}{d_{e_i,\Delta x}}$ between the edge midpoint $m_{\Delta x}^i$ and the intersection point of primal and dual edge denoted with $x_{\Delta x}^i$. Consequently, when expressing the cell area $A_{\Delta x} = c \cdot (d_{e_i,\Delta x})^2$ with some constant c, we find similarly to [49]

$$\nabla \cdot \vec{u}|_v = \lim_{\Delta x \to 0} \sum_i^{\#\text{faces}} \left\{ \frac{u_n^i|_{x_{\Delta x}^i}}{d_{e_i,\Delta x}} + r_{\Delta x}^i (u_n^i)'|_{x_{\Delta x}^i} + \frac{1}{2} d_{e_i,\Delta x} (r_{\Delta x}^i)^2 (u_n^i)''|_{x_{\Delta x}^i} + \dots \right\}. \tag{2.79}$$

For uniform grids, in which $r_{\Delta x}^i = 0$, the truncation error τ vanishes in the limit of $\Delta x \to 0$ leading to a consistent divergence operator and, by Eq. (2.77), to a consistent discrete continuity equation. For non-uniform grids, there is in general $r_{\Delta x}^i \neq 0$. However, we require that $r_{\Delta x}^i \xrightarrow{\Delta x \to 0} 0$, which is in general not fulfilled. Heikes and Randell [49] suggested a grid optimization method in order to minimize the value $r_{\Delta x}^i$. When increasing the grid resolution in the grid generation process, newly introduced DoF are positioned such that a cost functional defined as the sum of $(r_{\Delta x}^i)^4$ at all cell edges is minimized. On such grids, the authors achieved even in the L^∞-norm consistency for the Laplace operator.

Truncation error of the curl operator on triangles: We use the ideas of Heikes and Randell [49] to evaluate the truncation error of the curl operator of Eq. (2.70), which corresponds to the divergence operator on triangular meshes. Analogously to Eq. (2.78),

[5] In [49]: u_n^i equals $\frac{\partial \alpha}{\partial n}$ for a function α.

we write for the curl operator at triangle cell centers *cc*:

$$\nabla \times \vec{u}|_{cc} = \lim_{\Delta x \to 0} \frac{1}{A_{\Delta x}} \sum_{i}^{\#\text{faces}} \int_{l_{e_i,\Delta x}} \underbrace{\vec{u} \cdot \vec{t}}_{=:u_t^i} dl \,, \tag{2.80}$$

where u_t^i is the tangential velocity component to the triangular edges e_i. $A_{\Delta x}$ is the size and $l_{e_i,\Delta x}$ is the edge length of the triangle with $l_{e_i,\Delta x}, A_{\Delta x} \to 0$ if $\Delta x \to 0$. The expansion of Eq. (2.80) in Taylor series analogously to Eq. (2.78) leads to a truncation error analogously to Eq. (2.79), including the dependency on the intersection point of primal and dual edges $r^i_{\Delta x}$. However, in case of the curl operator, the positions of u_t^i always coincide with the triangles' edge midpoints by construction of Delaunay/Voronoi grids leading to $r^i_{\Delta x} = 0$ for all meshes. The truncation error of the curl operator is therefore independent of whether we use uniform or non-uniform grids.

2.8.2 Numerical tests on consistency on uniform and non-uniform grids

The truncation error analysis performed in the previous section can be summarized as following. On uniform meshes, all differential operators are consistent and hence also the triangular and hexagonal C-grid schemes. However, on non-uniform grids that are not optimized according to Heikes and Randall [49], the inconsistency of the divergence operator leads to an inconsistent hexagonal scheme. This inconsistency also occurs for the triangular model on non-uniform grids in case the curl operator is required, because the triangular curl operator coincides with its dual hexagonal divergence operator (see discussion at the end of Sect. 2.7).

This raises the question on how severe this inconsistency affects the quality of the solutions. Therefore, we perform numerical tests, analogously to [49, 104], to investigate the truncation errors of all differential operators introduced in the previous section, i.e. $\text{grad}^{\text{t}}{}_e, \text{grad}^{\text{n}}{}_e, \text{div}_v$ and curl_{cc}, and of the Laplace operator introduced further below.

We measure the truncation error as a function of resolution for uniform and non-uniform grids with respect to the error measure L_1, L_2 and L_∞:

$$\begin{aligned}
L_1: &\quad ||x^{\text{approx}} - x^{\text{true}}||_1 := \frac{1}{A_\Omega} \sum_{i \in \mathcal{N}} A_i |x_i^{\text{approx}} - x_i^{\text{true}}| \,, \\
L_2: &\quad ||x^{\text{approx}} - x^{\text{true}}||_2 := \Big[\frac{1}{A_\Omega} \sum_{i \in \mathcal{N}} A_i (x_i^{\text{approx}} - x_i^{\text{true}})^2 \Big]^{1/2} \,, \\
L_\infty: &\quad ||x^{\text{approx}} - x^{\text{true}}||_\infty := \max\{|x_i^{\text{approx}} - x_i^{\text{true}}|, \forall i \in \mathcal{N}\} \,,
\end{aligned} \tag{2.81}$$

where $A_\Omega := \sum_i A_i$ is the total area of the domain Ω, A_i the area of a cell, $x_i^{\text{approx}}, x_i^{\text{true}}$ are the calculated and the true solution at cell i, respectively.

In the following, we compare analytic solutions with numerically calculated ones. To this end, we define analogously to Tomita et al. [104]:

$$\alpha(x,y) = \sin(c \cdot x) \;\text{ with } c := \frac{2\pi k}{L_x} \,, \tag{2.82}$$

$$\beta(x,y) = \cos(c_1 \cdot x) \cdot \cos(c_2 \cdot y)^4, \;\; \text{with } c_1 := \frac{2\pi m}{L_x}, \; c_2 := \frac{2\pi n}{L_y} \,, \tag{2.83}$$

where k, m, n are arbitrary integers and L_x, L_y are the domain lengths in x and y-direction, respectively. For the analytic first and second partial derivatives we find:

$$\frac{\partial \alpha}{\partial x} = c\cos(cx), \qquad \frac{\partial \beta}{\partial x} = -c_1 \sin(c_1 x)\cos(c_2 y)^4, \qquad \frac{\partial \beta}{\partial y} = -4c_2 \cos(c_1 x)\cos(c_2 y)^3 \sin(c_2 y),$$

$$\frac{\partial^2\beta}{\partial x^2} = -c_1^2\cos(c_1x)\cos(c_2y)^4,\ \frac{\partial^2\beta}{\partial y^2} = 12c_2^2\cos(c_1x)\cos(c_2y)^2\sin(c_2y)^2 - 4c_2^2\cos(c_1x)\cos(c_2y)^4.$$

These partial derivatives are evaluated at the vertices, the edge midpoints or the triangle cell centers, denoted with $\cdot_v, \cdot_e, \cdot_{cc}$, respectively, and are combined such that the analytic gradient, divergence, curl and Laplace operators are represented. The numerically calculated values are then compared to the point-wise analytic solutions using (2.81).

For the calculation of the numerical values in order to determine the operators' order of accuracy, we use the discrete differential operators on uniform and non-uniform grids for different resolution, which are similar to those shown in Figure 3.13. How to construct such non-uniform (r-adapted) grids is topic of Chapter 4.

The gradient operator: We calculate for the normal gradient $\text{grad}^{\text{n}}{}_e$ of Eq. (2.69), for the tangential gradient $\text{grad}^{\text{t}}{}_e$ of Eq. (2.62) and for the full gradient $\text{grad}_e(\beta) := \text{grad}^{\text{t}}{}_e(\beta_v) + \text{grad}^{\text{n}}{}_e(\beta_{cc})$, all positioned at edge midpoints e, the truncation errors τ by using the following analytic solution:

$$\nabla\beta = \left(\frac{\partial\beta}{\partial x}, \frac{\partial\beta}{\partial y}\right), \tag{2.84}$$

with β of Eq. (2.83), $m = 4$ and $n = 2$. The full gradient $\text{grad}_e(\beta)$ can be directly compared with the analytic solution. To test the tangential and normal gradients on consistency, we project the analytic solution onto the tangential and normal direction of the triangular edges, respectively.

The results are shown in Fig. 2.5 for the three different norms. As expected from the truncation error analysis (cf. Eq. (2.73)), the tangential gradient is always second order, also on non-uniform grids, because of $\Delta x_+ = \Delta x_-$. Indeed, the tangential gradient operator has second order accuracy (a slope of -2) on uniform and non-uniform meshes. For the normal gradient on non-uniform grids there is in general $\Delta x_+ \neq \Delta x_-$, which leads to a decrease in the order of accuracy between first and second order. This behavior is visible in the plots for non-uniform meshes (right), where for higher resolution all three error norms bend upwards, indicating a loss of accuracy. The same behavior is shared by the full gradient operator, inheriting this property from the normal gradient operator.

The hexagonal curl operator: The triangular divergence operator of Eq. (2.70) is, by the duality property, the hexagonal curl operator curl_{cc}. For this operator, positioned at the triangle cell centers cc, we determine the truncation error τ by using the following analytic solution:

$$\vec{k}\cdot\nabla\times(\alpha\nabla\beta) = \frac{\partial\alpha}{\partial x}\frac{\partial\beta}{\partial x}, \tag{2.85}$$

with $\vec{k} = (0,0,1)$, β of Eq. (2.83) with $m = 4$ and $n = 2$ and α of Eq. (2.82) with $k = 1$. This analytic solution is compared to the numerical result of $\text{curl}_{cc}(\alpha_e\text{grad}^{\text{t}}{}_e(\beta_v))$. As $\text{grad}^{\text{t}}{}_e$ is second order on both uniform and non-uniform grids, a comparison of the order of convergence of the curl operator between uniform and non-uniform grids is possible.

Figure 2.6 illustrates the truncation error for the curl operator for all three norm on uniform and non-uniform grids. As theoretically expected, the truncation error is independent of the deformation of the grid. For both uniform and non-uniform meshes the curl operator is of first order accuracy.

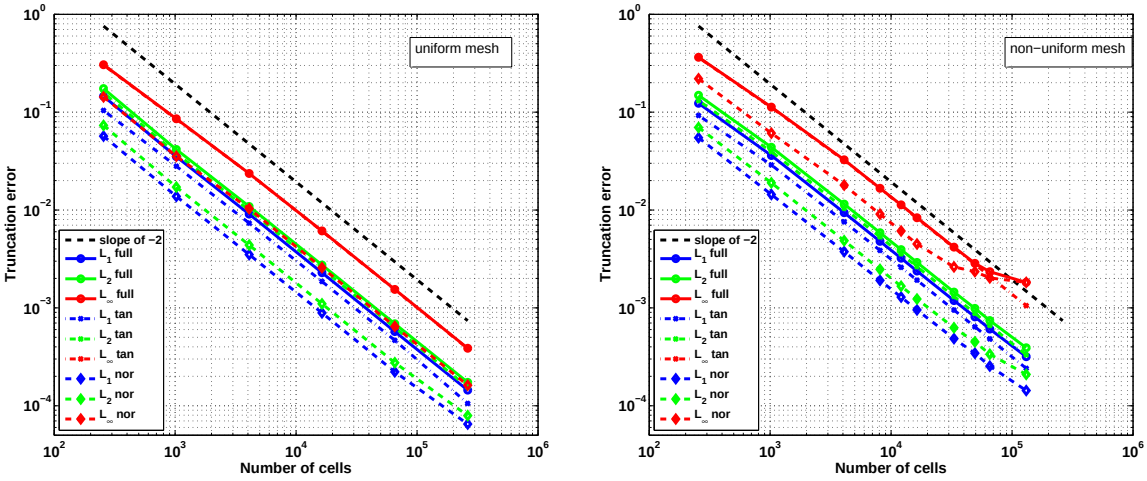

Figure 2.5: Truncation errors in the L_1, L_2, L_∞-norm of the full gradient (full), of the normal gradient (nor) and of the tangential gradient (tan) on uniform (left) and on non-uniform (right) meshes.

The hexagonal divergence operator: We determine for the divergence operator of Eq. (2.66), positioned at hexagonal cell centers v, the truncation error τ by using the following analytic solution:

$$\nabla \cdot (\alpha \nabla \beta) = \frac{\partial \alpha}{\partial x}\frac{\partial \beta}{\partial y} + \alpha(\nabla^2 \beta)\,, \tag{2.86}$$

using β of Eq. (2.83), with $m = 4$, $n = 2$ and α of Eq. (2.82) with $k = 1$. This analytic solution is compared with the discrete solution of $\mathrm{div}_v(\alpha_e \cdot \mathrm{grad}^{\mathrm{t}}{}_e(\beta_v))$.

Figure 2.7 (left) illustrates the truncation errors for the three different norms. The divergence operator has second order accuracy on uniform grids. On non-uniform grids with low resolution up to approximately 128^2 cells, the operator shows almost second order accuracy. For non-uniform meshes with larger resolution, the accuracy, however, drops significantly leading even to an inconsistent operator, indicated by the upward bending of the curves. This inconsistency can be explained theoretically by Eq. (2.79), because with increasing grid resolution our adapted meshes show increased values for $r^i_{\Delta x} \neq 0$. By the duality of the differential operators, these properties are shared by the triangular curl operator.

Consistency of the Laplace operator: We investigate the consistency property of the discrete Laplace operator at vertices v that is a combination of the above introduced divergence and gradient operators, i.e. $\nabla^2_v(\cdot) = \mathrm{div}_v \circ \mathrm{grad}^{\mathrm{t}}{}_e(\cdot)$. We determine the truncation error τ of the discrete Laplace operator by using the following analytic solution:

$$\nabla^2 \beta\,, \tag{2.87}$$

using β of Eq. (2.83) with $m = 4$ and $n = 2$. We calculate the numerical Laplace operator with $\nabla^2_v(\beta_v)$ and compare it with the analytic solution. Moreover, a comparison of the analytic solutions of (2.86) and (2.87) suggest that Laplace and divergence operators should behave similarly because the first term on the right hand side of (2.86) is comparably small.

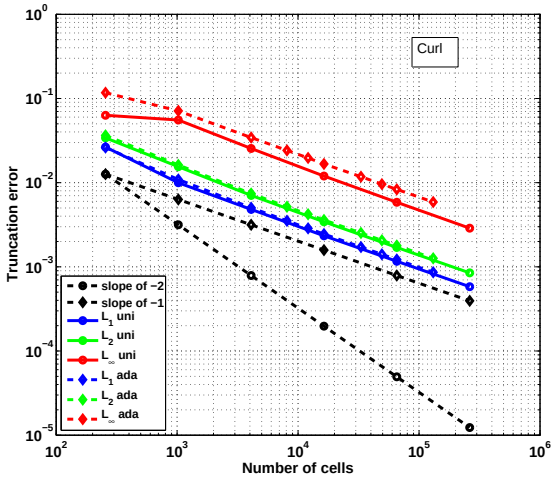

Figure 2.6: Truncation errors in the L_1, L_2, L_∞-norm of the curl operator on uniform (solid lines) and non-uniform (dashed lines) grids.

Figure 2.7 (right) illustrates the truncation errors in the three norms of the discrete Laplace operator applied on the function β_v for uniform and non-uniform grids. The truncation errors and the (in)consistency properties agree very well with those of the divergence operator applied to the function $\alpha\nabla\beta$, shown in Fig. 2.7 (left). This can be expected as the influence of the second term on the right hand side of Eq. (2.86) is one order of magnitude larger than the first term, leading to the similar truncation errors of Laplace and divergence operators.

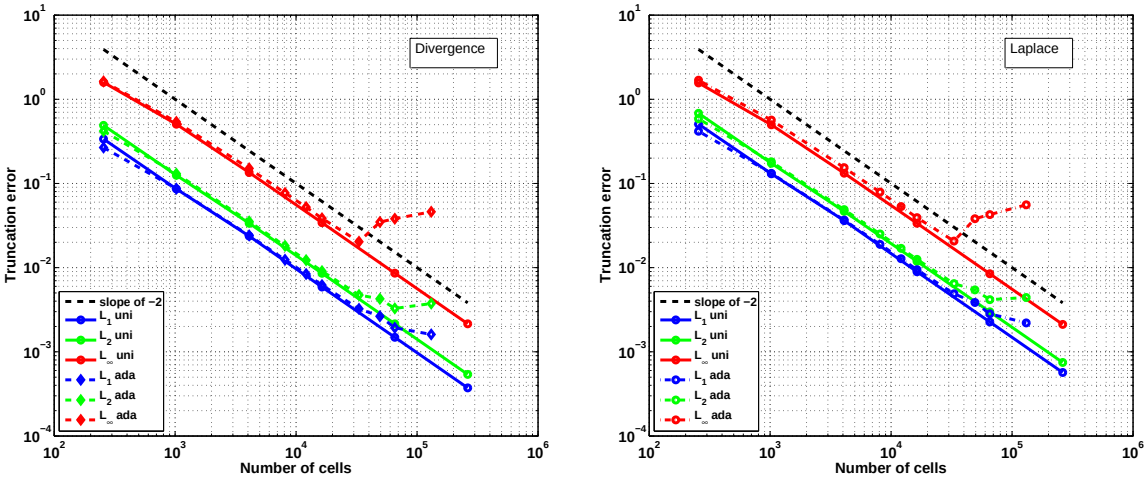

Figure 2.7: Truncation errors in the L_1, L_2, L_∞-norm of the divergence operator (left) and of the Laplace operator (right) on uniform (solid) and non-uniform (dashed) grids.

2.8.3 Stability and symmetry for the non-rotating linear schemes

Finally, we study the stability properties of the hexagonal C-grid scheme. Based on the method developed by Espelid et al. [37] we investigate the eigenvalues of the propagation

matrix of the semi-discretized equations. By this we evaluate whether there exist real eigenvalues that cause instabilities.

The method by Espelid et al. [37] has been used to develop stable shallow-water models with varying background depth (see for instance [46, 105]). We will apply this method in Chapter 3 to put constraints on the vector reconstruction in order to obtain a stable model. Here, we use the method to investigate the eigenvalues of the system matrix of the hexagonal scheme to discuss its stability properties. The same argumentation is valid for the triangular scheme, as presented by Ham et al. [46].

Matrix formulation of the discrete linear shallow-water equations

For the following stability analysis it is useful to present the non-rotating linear shallow-water equations in matrix form. Given $\overline{\mathbf{u}}_\mathbf{e}$ the vector of all edge velocities $\overline{u}_e$ and $\mathbf{h_v}$ the vector of all surface elevations h_v, the set of linear equations can be written in matrix form:

$$\frac{\partial}{\partial t}\begin{bmatrix} \overline{\mathbf{u}}_\mathbf{e} \\ \mathbf{h_v} \end{bmatrix} = \begin{bmatrix} 0 & G \\ D & 0 \end{bmatrix}\begin{bmatrix} \overline{\mathbf{u}}_\mathbf{e} \\ \mathbf{h_v} \end{bmatrix}, \tag{2.88}$$

with $G := \frac{g}{l_e}\mathbf{G}$ of Eq. (2.62) and $D := \frac{Hd_e}{A_c}\mathbf{D}^{\text{dual}}$ of Eq. (2.66). g is the gravity, l_e the triangular edge length and d_e its dual edge length (hexagonal cell edge), H is the background height and A_c is the area of the hexagonal cell. The system matrix shall be denoted with $\mathbf{A}$. We denote the solution vector with

$$\mathbf{s}(t) = \begin{pmatrix} \overline{\mathbf{u}}_\mathbf{e}(t) \\ \mathbf{h_v}(t) \end{pmatrix}; \tag{2.89}$$

then, the non-rotating semi-discrete, i.e. only discretized in space, shallow-water equations are given by

$$\frac{d}{dt}\mathbf{s}(t) = (\mathbf{A}+\mathbf{F})\mathbf{s}(t)\ , \tag{2.90}$$

where $\mathbf{A}+\mathbf{F}$ is the propagation matrix. Matrix $\mathbf{F}$ contains terms with the Coriolis parameter f. In Chapter 3 we investigate also terms with $f \neq 0$, but here we focus on the non-rotating equations by setting $\mathbf{F} = 0$.

We investigate the eigenvalues of the semi-discretized equations. Let $\mathbf{z}$ be an eigenvector of $\mathbf{A}$ with eigenvalue λ, i.e. $\mathbf{Az} = \lambda\mathbf{z}$. If the initial value is $\mathbf{s}(0) = \mathbf{z}$, than the solution of Eq. (2.90) is

$$\mathbf{s}(t) = e^{\lambda t}\mathbf{z}\ . \tag{2.91}$$

The continuous equation describes a system that conserves energy. To guarantee this also for the discrete scheme, all eigenvalues λ of the propagation matrices must be purely imaginary. If this holds, no growing and damping modes exist and the system is stable. This property is shared by *skew-symmetric* matrices and *similar to skew-symmetric* matrices (cf. [105]). In contrast, if the propagation matrices contain symmetric parts, growing and damping computational modes exist.

The scaling matrix [46] for the system (2.88) can be written as

$$\mathbf{D} = \begin{bmatrix} D_p & 0 \\ 0 & D_c \end{bmatrix}, \tag{2.92}$$

with $(D_p)_{ii} = Hd_{e_i}l_{e_i}$ and $(D_c)_{ii} = gA_{c_i}$, where the size of $\mathbf{D}$ is equal to the size of $\mathbf{A}$. Applying $\mathbf{D}$ on $\mathbf{A}$ gives the following matrix

$$\mathbf{DA} = \begin{bmatrix} 0 & \pm Hd_{e_i}l_{e_i}\cdot g\frac{1}{l_{e_i}} \\ \mp gA_{c_k}\cdot\frac{Hd_{e_j}}{A_{c_k}} & 0 \end{bmatrix}. \tag{2.93}$$

DA is skew-symmetric and the matrix **A** is sign skew symmetric, i.e. for $a_{ii} = 0 \forall i, a_{ij}a_{ji} < 0$ if $i \neq j$ and $a_{ij} \neq 0$. Consequently, the system is stable, because the system matrix **A** has purely imaginary eigenvalues and does not support growing or damping modes. This is valid for both uniform and non-uniform grids.

We verify this theoretical results by using the MATLAB eigenvalue function to determine the eigenvalues of **A** for a uniform and a non-uniform grid with 32^2 cells on a domain of 5000 km $\times$4330 km (shown in Figure 3.13). Figure 2.8 illustrates the real and the imaginary parts of the eigenvalues of **A** for the uniform (left) and the non-uniform (right) grid. In both cases, the real parts of the eigenvalues are smaller than real$\lambda < 10^{-11}$. This verifies that for any grid the method is stable. This is true also for the triangular C-grid scheme introduced in the previous section, as shown by Ham et al. [46].

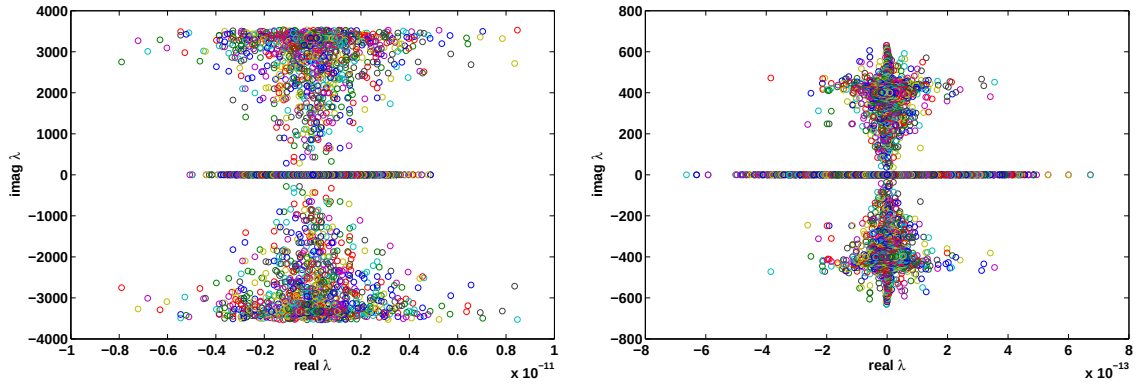

Figure 2.8: Eigenvalues λ of the propagation matrix **A** for 32^2 cells on a uniform grid (left) and a non-uniform grid (right) shown in Fig. 3.13.

2.9 Summary and conclusions

The equations of geophysical fluid dynamics (GFD) written in vector-invariant form remain unchanged using different vector representations, but their form differs with different dimensions, because of the change in the Coriolis term. Differential geometry allows for a more general formulation of the equations of GFD. We have introduced an invariant form of these equations including the Coriolis term by using differential forms for the prognostic variables. This formulation is based on Abraham and Marsden [1].

Furthermore, we have developed an alternative invariant form by splitting the GFD equations into topological and metric parts, which we could achieve by introducing auxiliary prognostic variables. Such formulation is similar to the invariant Maxwell's equations frequently used in computational electrodynamics (CED) [27]. In the literature the comparison of the two sets of equations is usually based on the similarity of potential vorticity and electric charge [51, 94, 100]. In contrast, we have compared purely the form of the invariant equations and have applied for the discretization of the fluid equations concepts used in CED, in particular we used the method of discrete exterior calculus (DEC).

The invariant form, including the splitting of the equations, enables a systematic discretization method by applying chains and cochains to approximate manifolds and differential forms, respectively, while assigning to every simplex (vertex, edge and face) one degree of freedom. The chains represent the topological meshes used to discretize the momentum and continuity equations. The discrete metric equations, namely the Hodge-star

operator connecting the topological meshes and the discrete representation of the contraction operator, are required to close the system of equations. The discrete scheme then follows directly from the choice of the topological meshes and of the discrete representation of the metric equations.

In formulating the invariant GFD equations in topological and metric parts, similarly to Bossavit et al. [27], we were able to apply the method of DEC of Desbrun et al. [33] and found a systematic discretization approach of the equations of GFD that incorporates several finite difference schemes. We have illustrated that a certain choice of the topological meshes and of the discrete operators, in particular of the Hodge-star operator, leads to a certain finite difference scheme. On the example of the non-rotating linear shallow-water equations, we have derived, by applying our discretization method, the triangular and hexagonal C-grid schemes.

As these schemes are employed in the following chapters, we have performed numerical tests concerning consistency and stability for uniform and non-uniform grids. For both uniform and strongly deformed grids, the triangular and hexagonal models are stable. Neither growing nor decreasing energy modes are present, because all eigenvalues of the system matrices are purely imaginary. The consistency investigation for the schemes reduces to the corresponding properties of the discrete differential operators. We have shown that all operators are consistent with second order accuracy (except those defined on triangles, having first order accuracy) on uniform grids, whereas, on non-uniform grids, the order in accuracy decreases (except for those defined on triangles, keeping first order accuracy), which may be caused by strongly deformed grid cells (cf. Chapter 4).

On the basis of the framework introduced in this chapter including the diagonal Hodge-star operator, we study in the following chapter the representation of the linear Coriolis term. We introduce an adequate representation of the contraction operator (interior product) and of the Riemannian lift connecting one-form with its corresponding vector proxies.

As future work, one may investigate different Hodge-star operators leading to different schemes. The diagonal barycentric Hodge-star operator connecting primal and dual mesh via the barycentric coordinates instead of the triangles' circumcenters would allow for stronger grid deformation as the barycenters always lie within their triangles' boundaries unlike the circumcenters. This may lead to different consistency and stability properties, or even to unstable schemes (cf. Ham et al. [46]). Moreover, one could use a non-diagonal Hodge-star operator that connects one primal with several dual edges, for instance the Galerkin Hodge-star operator introduced by Bossavit [27] used in CED. A systematic investigation on which Hodge-star operator that gives a stable scheme in CED would also give a stable scheme in GFD could provide a more solid understanding in the mutual relations of the different set of equations and may suggest useful tools and methods to discretize the equations of GFD.

Based on the similarity of the formulations of CED and GFD, a generalization of our method toward higher order discretization schemes by using more degrees of freedom per simplex seems also possible. Bossavit [27] introduced first steps in such direction by using higher-order Whitney interpolation functions. Consequently, our reformulation of the geophysical fluid equations provides both a generalization of the discretization method and the possibility to use well-known concepts of other disciplines, while providing a deeper geometrical understanding of the geophysical fluid equations.

Chapter 3

Consistent vector reconstruction scheme based on exterior calculus

Abstract We present a consistent low-order vector reconstruction scheme based on the representation of the Coriolis term by means of exterior calculus for a linear hexagonal C-grid shallow-water model for rotating fluids. On rotating fluids the Coriolis force acts perpendicularly to the flow field causing this field to be swept over a two-dimensional manifold that is called extrusion. The concept of extrusion can be used in exterior calculus to represent the Coriolis term. Based on extrusion, we develop a method for normal vector reconstruction out of neighboring tangential vector components, in which the weights are determined by the ability of the tangential vector component to contribute to the extrusion. Using this approach we can successfully determine weights on a uniform grid to obtain a stable model that adequately represents the geostrophic modes. In contrast, spurious geostrophic modes emerge in case low-order Raviart-Thomas (RT0) interpolations (suitable for triangular C-grids) are used for normal vector reconstruction for hexagonal C-grids, as our study reveals. Our normal vector reconstruction based on extrusion does not require, unlike analogous vector reconstruction schemes for uniform meshes from literature, the use of the two-dimensional vorticity equation for the derivation and is therefore easier generalizable to three dimensions. In case of non-uniform meshes, we extend our linear model with existing techniques to a nonlinear hexagonal C-grid shallow-water model on r-adapted grid, for which we show stability and proper wave representation on nonlinear test cases.

3.1 Introduction

The simulation of many phenomena in geophysical fluid dynamics requires an adequate representation of a broad range of scales. For simulations where high resolution is not required over the entire domain, grid adaptation methods can contribute to high accuracy of the solution while keeping the computational costs as low as possible. Among others, mainly two approaches are frequently used in geophysical applications: either new grid points are introduced to increase local resolution (h-adaptivity) or grid points are moved to regions where higher resolution is required (r-adaptivity). In any case, the discretization schemes have to be able to cope with non-uniform grids, for which, in case of r-adaptivity, the geometrical properties of the cells change with adaptation or, in case of h-adaptivity, the topology changes because of the added grid points.

The choice of suitable discretization schemes depends on the problem to be investigated. Of particular interest in geophysical applications is the proper representation of

waves and of their dispersion relations [76, 101]. As, in particular, staggered C-grids do properly represent the wave dispersion relations, the staggering of mass and velocity components is mostly used in simulations of geophysical fluids on different grid types, for instance on quadrilateral, triangular and hexagonal meshes.

In order to find a smooth tessellation of the sphere while avoiding the pole problem of lat-lon grids, triangular or hexagonal meshes based on the icosahedron are often investigated [18, 89, 90]. However, in none of the approaches like lat-lon, cubed sphere, triangular and hexagonal tessellation of the sphere (e.g. Weller et al. [115, 116]), one obtains a completely smooth mesh with uniform grid cells [49, 103]. Therefore, discretization methods that are able to cope with the non-uniformity of the grids have been studied intensively, e.g. in [46, 89, 88, 102]. A combination of a discretization scheme suitable for non-uniform grid with r-adaptive grid refinement seems thus natural. In addition, the unchanged topology of r-adapted grids makes load balancing in parallel computing easier (compared to h-adaptivity) when the grid is adapted during runtime (dynamic grid adaptation).

The major difficulty with staggered finite difference schemes is to find a vector reconstruction that leads to a consistent and stable model with proper wave representation. Discretization methods for non-uniform grids have been widely investigated for triangular and quadrilateral meshes. For triangular C-grid models there are several consistent reconstruction methods (e.g. [62, 78, 111, 113]) that are mostly based on the low-order Raviart-Thomas (RT0) interpolation [84]. These methods are also widely used in finite element modeling. Hereby consistent means that a linear vector field is exactly represented by the reconstruction method (cf. Ham et al. [46]).

For hexagonal models, however, such reconstructions are rare (apart from [89, 102]). This is probably due to the fact that linear reconstructions within a hexagonal cell seem to be not unique, in contrast to triangular cells, where all linear reconstructions reduce to the low-order RT0 functions [46]. Methods suitable for triangular models are not automatically suitable for hexagonal models, as we confirm in this chapter. In order to find suitable normal vector reconstructions to obtain a stable model with proper representation of the geostrophic modes, one may put some constraint on the equations. As an example, by enforcing the geostrophic modes to be stationary, Thuburn et al. [102] found a suitable normal vector reconstruction scheme for arbitrarily-structured C-grids.

Despite the problem of normal vector reconstruction, an important reason to pursue the development of hexagonal models lies in their advantage of representing the divergence field more accurately than triangular models, because in the latter case the discrete divergence operator has only first order accuracy (cf. Chapter 2). In addition, the velocity field is underrepresented on such grids, which may lead to a checkerboard pattern in the divergence (cf. Gassmann [43]). This effect becomes even more pronounced when extending the shallow-water model to a three-dimensional hydrostatic model [112].

In this chapter we suggest an approach to find an adequate normal vector reconstruction for hexagonal C-grid models on non-uniform meshes. Our approach differs from the literature, in particular from the method proposed by Thuburn et al. [102], in which the derivation of the weights for the vector reconstruction relies essentially on the two-dimensional vorticity equation. We do not put a similar constraint on the equation. Instead, we rely on the invariant form of the geophysical fluid equations introduced in Chapter 2. In particular, we represent the Coriolis term by the concept of extrusion. The Coriolis force acting perpendicularly on the flow field causes this flow field to be swept over a two-dimensional manifold that is called the extrusion. Based on extrusion, we develop a method for normal vector reconstruction out of neighboring tangential vector components where the weights are determined by the ability of the tangential vector component to

contribute to the extrusion.

The concept of extrusion has been developed in several studies [27, 75] to represent vector fields on arbitrary meshes. In these studies extrusion has been used, for instance, for advection schemes [52, 75] or to represent the Lorentz force in computational electrodynamics [25]. To our knowledge, we use extrusion in a novel way, namely to reconstruct velocity values in a staggered grid environment, in particular, for a hexagonal C-grid. We show how the concept of extrusion can be used to determine the weights of a vector reconstruction such that the model is consistent, stable, and represents the geostrophic modes adequately. We perform several numerical tests to verify these properties.

Having found an adequate formulation that equals for uniform grids the method proposed by Thuburn et al. [102], we extend this hexagonal C-grid shallow-water model by the normal vector reconstruction scheme of Thuburn et al. [102] and by the nonlinear terms proposed by Ringler et al. [89] for arbitrarily-structured C-grids. This enables us to investigate nonlinear phenomena with r-adapted grids, as done in Chapter 4. In order to show stability and proper representation of the geostrophic balance, we perform in this chapter numerical tests on nonlinear scenarios.

This chapter is structured in the following way. In Section 3.2 we introduce the shallow-water equations in invariant form for rotating fluids and represent the Coriolis term by means of extrusion. Conventional vector reconstructions are then introduced and it is shown in numerical experiments that such reconstructions suitable for triangular models are in general not suited for hexagonal models because some spurious geostrophic modes may arise. In Section 3.3 we present the normal vector reconstruction based on extrusion for a hexagonal C-grid discretization of the rotating linear shallow-water equations. In Section 3.4 we extend the linear shallow-water model to a nonlinear model using techniques from literature and present the numerical results for some nonlinear test cases. In Section 3.5 we summarize the results and draw conclusions.

3.2 The rotating linear shallow-water equations

We aim at a discrete representation of the linear shallow-water equations in a rotating coordinate system (rotating frame). As introduced in Chapter 2, the discretization is done by integrating the invariant equations over chains. In this section, we deal with the Coriolis effect that occurs in case of rotating fluids. We present a discretization of the Coriolis term based on the tools developed in Chapter 2 and on the representation of the interior product on meshes by the concept of *extrusion* introduced in this Chapter.

3.2.1 The equations in invariant form

Using the selection mechanism of section 2.4.2 for the invariant form of the equations, we may choose the linear shallow-water equations on a rotating frame. Let be $\mathcal{M} \subset \mathbb{R}^2$ and $u : \mathcal{X}(\mathcal{M}) \to \mathbb{R}$ with $u = u_x dx + u_y dy \in \Omega^1(\mathcal{M})$ a one-form describing the velocity field. The function $h \in \Omega^0(\mathcal{M})$ describes the variation of the height field around a mean value H. The two-form $f_C := f dx \wedge dy \in \Omega^2(\mathcal{M})$ represents the Coriolis term with Coriolis parameter f. We set the nonlinear terms to zero. The interior product $\mathbf{i}_{\vec{v}} : \Omega^k(\mathcal{M}) \to \Omega^{k-1}(\mathcal{M})$ acts thus only on the two-form f_C, where $\vec{v}$ is an auxiliary vector field being determined in the following. This reduces the full shallow-water equations (2.30) and (2.31) to:

$$\int_c \partial_t u + \int_c \mathbf{i}_{\vec{v}} f_C + g \int_c \mathbf{d} h = 0 \ , \qquad \int_V \partial_t \tilde{h} + H \int_V \mathbf{d} \tilde{u} = 0 \ , \quad \forall c, V, \tag{3.1}$$

with the following metric equations to close the system:

$$\tilde{h} = \star h \ , \quad \tilde{u} = \star u \ , \quad u^\sharp = \vec{v} \ . \tag{3.2}$$

The metric-dependent operator $\sharp : u \to \vec{v}$ (cf. Def. A.4.1) connects the one-form $u \in \Omega^1(\mathcal{M})$ with the corresponding vector proxy $\vec{v}$ and the Hodge-star operator $\star$ (cf. Proposition A.2.1) connects the topological equations.

Analogously to Sect. 2.7 we restrict our investigation to the discrete diagonal Hodge-star operator (2.55), although other choices are also possible in case of the rotating equations. By linearity, only the Coriolis term $\int_c \mathbf{i}_{\vec{v}} f_C$ remains to be investigated as the other terms agree with those in Sect. 2.7. We denote the discretized Coriolis term with $\mathbf{I}(\vec{u}, f)$. It will be thoroughly investigated in the following sections. In the notation introduced in Chapter 2 we can write the semi-discretized equations by

$$\partial_t \mathbf{u} + \mathbf{I}(\vec{u}, f) + g\mathbf{G}\,\mathbf{h} = 0 \ , \qquad \partial_t \tilde{\mathbf{h}} + H \cdot \mathbf{D}^{\text{dual}} \tilde{\mathbf{u}} = 0 \ , \tag{3.3}$$

with the discrete Hodge-star operator (2.55) for a Delaunay/Voronoi dual grid,

$$\tilde{\mathbf{h}} = \star_0 \mathbf{h} \ , \quad \tilde{\mathbf{u}} = \star_1 \mathbf{u} \ , \tag{3.4}$$

where $\mathbf{h}$ and $\tilde{\mathbf{h}}$ are the discrete 0-form and two-form describing the height and the auxiliary height fields, respectively. $\mathbf{u}$ and $\tilde{\mathbf{u}}$ are discrete one-forms to describe the velocity and the auxiliary velocity fields, respectively. $\mathbf{G}$ and $\mathbf{D}^{\text{dual}}$ are the discrete *gradient* and *divergence* operators, respectively, defined in Chapter 2.

3.2.2 The linear Coriolis term and its discretization

In this section we tackle the problem of discretizing the Coriolis term $\int_c \mathbf{i}_{\vec{v}} f_C$. As shown in the proof to Theorem 2.3.1 the integrand of the Coriolis term corresponds to the linear term of Eq. (2.23), i.e. for $u^\sharp = \vec{v}$, there follows

$$(\mathbf{i}_{\vec{v}} f_C)^\sharp = f\vec{k} \times \vec{v} \ . \tag{3.5}$$

This equation illustrates how the Coriolis force acts on the velocity field of the fluid. In case of a rotating frame, in which the Coriolis parameter $f \neq 0$, the Coriolis force acts perpendicularly to the flow field causing this field to be swept over a two-dimensional manifold called extrusion. We represent in our approach the Coriolis term by means of extrusion and use the tools of discrete exterior calculus (DEC) [33] to find a discrete representation.

From (3.5) we can infer that the discretization problem is twofold, i.e. we have to find a discrete representation of Riemannian lift $\sharp$ and of the interior product $\mathbf{i}_{\vec{v}} : \Omega^k(\mathcal{M}) \to \Omega^{k-1}(\mathcal{M})$. However, as both operators are independent form each other, we elaborate how the operators can be discretized separately, and how they combine finally to the discrete Coriolis term.

Representation of the interior product: According to Eq. (3.5), the invariant form allows to interpret the Coriolis term as the contraction of the two-form f_C along the one-dimensional surface c by the vector field $\vec{v}$. In order to clearly distinguish between the interior product and the Riemannian lift $\sharp$, we start with the definition of the interior product of a general k-form using a general vector field $\vec{X}$ that is not necessarily connected via $\sharp$ to the prognostic variable $u \in \Omega^1(\mathcal{M})$.

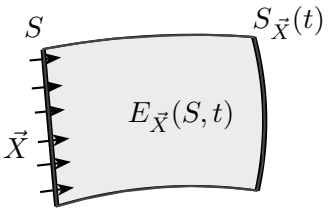

Figure 3.1: Extrusion $E_{\vec{X}}(S,t)$ of a surface S by the vector field $\vec{X}$ (see text).

For a representation of the interior product we choose the concept of extrusion [27, 52], in particular, we use the definition proposed by Mullen et al. [75]. Let $\mathcal{M}$ be an n-dimensional smooth manifold and $\vec{X}$ a smooth vector field on the manifold. Let S be a k-dimensional sub-manifold on $\mathcal{M}$ with $k < n$. The vector field gives rise to a flow $\varphi : \mathcal{M} \times \mathbb{R} \to \mathcal{M}$ such that $\varphi(\varphi(S,t),s) = (\varphi(S,s+t))$, $\varphi(S,0) = S$, $\forall s,t \in \mathbb{R}$, which is a one-parameter group. If S is carried by the flow φ for a time t, then we denote this sub-manifold with $S_{\vec{X}}(t) := \varphi(S,t)$, i.e. the image of S under the mapping φ. The advection of S over the time t to the final position $S_{\vec{X}}(t)$ is a $(k+1)$-dimensional sub-manifold called *extrusion* $E_{\vec{X}}(S,t)$, and written formally as

$$E_{\vec{X}}(S,t) = \bigcup_{\tau \in [0,t]} S_{\vec{X}}(\tau) \ . \tag{3.6}$$

One can assign an orientation to $E_{\vec{X}}(S,t)$ and its boundary ∂E (cf. [75, 52]). Figure 3.1 illustrates the extrusion of a one-manifold S by a vector field $\vec{X}$.

Let $\omega \in \Omega^{k+1}(\mathcal{M})$ be a $(k+1)$-form and S a k-dimensional sub-manifold. By the notion of extrusion, we define the contraction of the $(k+1)$-form by the vector field $\vec{X} \in \mathcal{X}(\mathcal{M})$, i.e. $\mathbf{i}_{\vec{X}} : \Omega^{k+1}(\mathcal{M}) \to \Omega^k(\mathcal{M})$, according to Bossavit [27]:

$$< \mathbf{i}_{\vec{X}}\omega, S >= \lim_{t \to 0} \frac{< \omega, E_{\vec{X}}(S,t) >}{t} \ . \tag{3.7}$$

With this definition we find a possibility to represent the interior product on a mesh.

Representation of the extrusion on a mesh: According to Bossavit [27], the extrusion $E_{\vec{X}}(S,t)$ can be represented as a chain. Recall the definition of a chain in Chapter 2, where we write for a k-chain ch^k over the mesh m for a simplicial complex $\mathcal{S}_m^k$:

$$ch^k = \sum_{s \in \mathcal{S}_m^k} \alpha_s s \ , \quad ch^k \in \mathcal{C}H^k(m) \ , \quad \alpha_s := \int_s \omega^s \ , \tag{3.8}$$

where $\mathcal{C}H^k(m)$ is the set of k-chains on the mesh m. The coefficients α_s of the cells are determined by integration of the s-form ω^s over the simplex s, i.e. $< \omega, s >:= \int_s \omega^s$. Thus α_s describes the DoF associated to this cell. Following this idea, the extrusion can be approximated by a weighted sum over all cells c by

$$E_{\vec{X}}(S,t) \approx \sum_{c \in \mathcal{C}} \int_{E_{\vec{X}}(S,t)} \omega^c c \ , \tag{3.9}$$

where $\mathcal{C}$ denotes the set of all cells. By the definition of a chain (Eq. (3.8)) the weights are given by

$$\int_{E_{\vec{X}}(S,t)} \omega^c =< \omega^c, E_{\vec{X}}(S,t) > \ , \tag{3.10}$$

where ω^c is a two-form associated to cell c, thus $\omega = \sum_{c\in\mathcal{C}} \omega^c c$. To guarantee that Eq. (3.9) properly represents the extruded manifold $E_{\vec{X}}(S,t)$ by weighted face elements, the interpolation function ω^c has to be a partition of unity [27], i.e. $\sum_{c\in\mathcal{C}} c >< \omega^c(x) = 1$, which is a projection operator to obtain a representation of any surface S in the basis of the faces c of the mesh. This is similar to the representation of a scalar value by hat functions based on the partition of unity $\sum_{n\in\mathcal{N}} n >< \omega^n(x) = 1$ for the nodes n of a mesh.

Whitney interpolation functions have the property of partition of unity [27]. Based on the barycentric coordinates λ, these functions are linear interpolations suitable for triangles (Fig. 3.3 right) similar to the linear RT0 interpolation functions (Fig. 3.3 left). Whitney interpolation functions allow to approximate differential k-forms by discrete linear k-forms. For a tetrahedral mesh in n-dimensions, the Whitney forms can be presented for the nodes n, edges e and cells c in vector proxy form by:

$$\omega^n = \lambda_n \ , \tag{3.11}$$

$$\omega^e = \lambda_l \nabla\lambda_m - \lambda_m \nabla\lambda_l \ , \tag{3.12}$$

$$\omega^c = 2(\lambda_l \nabla\lambda_m \times \nabla\lambda_k + \lambda_m \nabla\lambda_k \times \nabla\lambda_l + \lambda_k \nabla\lambda_l \times \nabla\lambda_m) \ . \tag{3.13}$$

Also higher dimensional Whitney k-forms ($k \leq n$) exist (cf. [26, 53]). For all simplices, the Whitney interpolation functions provide a partition of unity, i.e. $\sum_k k >< \omega^k(x) = 1$, as required for Eq. (3.9).

In two-dimensions, there is $\omega^c = \pm 1$, where the orientation of every face has to be taken into account (cf. Chapter 2). Therefore, the partition of unity reduces to the properties $\int_{c'} \omega^c = \delta_{cc'}$ or if $c_1 + c_2 = c, c_1, c_2 \in c$, then $\int_{c_1} \omega^c + \int_{c_2} \omega^c = 1$. This property will be important when we represent the extrusion on the underlying mesh in Sect. 3.3.2.

According to Eq. (3.10), the weights of the extrusion represented as chain in Eq. (3.9) are determined by the projection of the extrusion onto the underlying cells c. Let us assume that the one-dimensional manifold S can be approximated by $S \approx \sum_e e$. Then, Eq. (3.7) reduces by linearity to the sum of cell contributions along e to

$$< \mathbf{i}_{\vec{X}} \omega^c, e >= \lim_{t\to 0} \frac{< \omega^c, E_{\vec{X}}(e,t) >}{t} \ . \tag{3.14}$$

Given a vector field $\vec{X}$ and using the Whitney interpolation function ω^c as approximation of the two-form ω, Eq. (3.14) allows for a cell-wise representation of the interior product by setting the time to a finite value, for instance $t = 1$. This, in turn, enables us to represent Eq. (3.14) by a projection of the extrusion onto the mesh, which corresponds to a representation as chain according to Eq. (3.10).

Under the assumption that the velocity field $\vec{X}$ is given and with a representation of the extrusion on the mesh – either by the representation in Sect. 3.3.2 or following Bossavit [27] – the interior product can be evaluated. The next step is to look whether a suitable discrete Riemannian lift $\sharp$ exists that is required to evaluate the Coriolis term of Eq. (3.5) under the condition $u^\sharp = \vec{v}$.

Representation of the Riemannian lift on staggered C-grids: The invariant form of the fluid equations (3.1) and (3.2) requires to connect the one-form u that describes the velocity of the fluid with its corresponding vector field $\vec{v}$ uniquely by the Riemannian lift $\sharp$. When defining an inner product $<,>$ the unique relation between u and $\vec{v}$ can easily be found in the continuous case with $\sharp : u =< \vec{v}, \cdot >\to \vec{v}$ (cf. Appendix A).

In the discrete case a point-wise definition of $\sharp$ is possible, if there is a point-wise definition of the inner product available, and, in addition, if the velocity components are

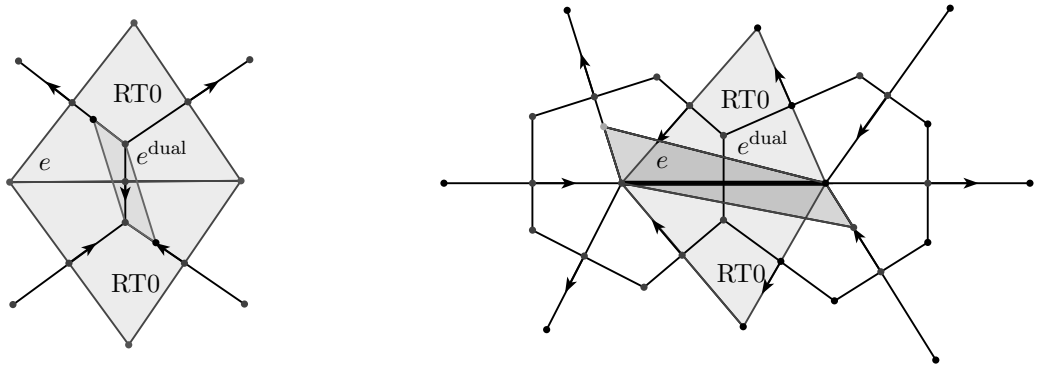

Figure 3.2: Continuity properties of the extrusion caused by a smooth RT0 reconstructed velocity field for a triangular (left) and a hexagonal C-grid scheme (right).

collocated at these points, as in the case of *A-grids*. Then, there is a unique relation between the components u_x, u_y of the one-form u and the velocity field $\vec{v}$, which in turn allows to evaluate the Coriolis term at this points according to Eq. (3.5).

In the example elaborated in Chapter 2, the choices for the primal and dual grids and the corresponding Hodge-star operator resulted in a discretization based on the triangular and hexagonal C-grid staggering. In case of *staggered C-grids* the velocity components are positioned at the cell edges and not collocated at some grid points. This does not allow for a point-wise definition of the $\sharp$ operator because there exist no points on the grid where both vector components are located. Using vector reconstructions, for instance, the Raviart-Thomas interpolation [84] or the Whitney interpolation [26], one may reconstruct at every point the second vector component to obtain the full velocity field.

The pointwise and the full velocity fields allow to define a unique $\sharp$ operator in order to associate the interpolated velocity field $\vec{v}$ with the corresponding linear discrete form u. Moreover, it allows to evaluate the Coriolis term of Eq. (3.5) without employing the definition of extrusion in Eq. (3.14). However, we explain on the basis of the definition of the interior product of Eq. (3.14) why such an approach can fail in case of a hexagonal model

Continuity property of the extrusion: The extrusion of an edge by a vector field $\vec{X}$ generates an area that has to be projected onto the underlying mesh. The extrusion $E_{\vec{X}}(S,t)$ caused by a vector field $\vec{X}$ have to be smooth, i.e. small changes in the velocity field in all directions must not lead to jumps of the extruded manifold. This can only be guaranteed if all velocity components of those edges that are connected via the vertex points to the extruded edge e contribute to the extrusion and finally to the vector reconstruction.

Figure 3.2 illustrates two different examples of the extrusion by adjacent velocities. The RT0 vector reconstruction leads to a smooth linear vector field within the two triangles adjacent to triangle edge e (indicated in light gray). In case of triangular schemes (left), the normal velocity components of the triangles causes the hexagonal edge e^{dual} to be extruded. The smooth velocity field causes a smooth extrusion of e^{dual} (dark gray) if it stays inside the triangles. However, in case of the hexagonal scheme (right) where the tangential velocity components of the triangular edges causes the extrusion of e, discontinuities occur if the extrusion lies outside the two triangles with the smooth RT0 vector field, because the RT0

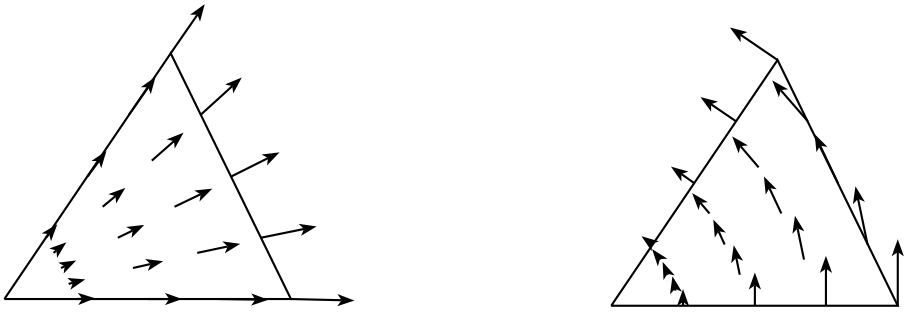

Figure 3.3: Linear Raviart-Thomas (left) and Whitney interpolation function of Eq. (3.12) (right) – shown only for one of the three triangle edges. At the midpoint of edges the other two interpolation function of the adjacent edges are zero by construction.

reconstruction does not consider all velocity components from the triangles adjacent to the vertices of e.

In the literature several approaches that are based on the RT0 functions for the tangential vector reconstruction of triangular schemes have been investigated (e.g. in [18, 44]). In the following, we use a method for triangular schemes proposed by Ham et al. [46], but for normal vector reconstruction of a hexagonal C-grid. This transfer is based on results by Perot et al. [79], who have compared several low-order face and edge elements. However, on the basis of the discussion about continuity of the extruded manifold shown in Fig. 3.2, we expect that using the RT0 vector reconstruction in case of hexagonal C-grids may lead to problems.

Therefore, we proceed as following. First, we introduce RT0 vector reconstructions for both triangular and hexagonal models and we study consistency, stability and the representation of geostrophic balance. Then, in Sect. 3.3, we extend the stencil for the normal vector reconstruction in the hexagonal case in order to avoid the discontinuities of the extrusion.

3.2.3 Consistent RT0 vector reconstruction on triangles

We propose a normal vector reconstruction scheme on the basis of the RT0 basis functions, where we use results of Ham et al. [46] for tangential RT0 vector reconstruction and of Perot et al. [79]. In the following, we denote this method with *normal RT0 vector reconstruction*.

General linear interpolation fields for triangles: Mainly two linear interpolation fields that provide full velocity information at every triangle point $\vec{x}$ are used for triangles. The lowest order Raviart-Thomas elements (RT0) [79, 84] are used to uniquely reconstruct the full velocity field by three basis functions that are weighted by the normal velocity values $v^{\mathrm{no}}_{e_i}, v^{\mathrm{no}}_{e_j}, v^{\mathrm{no}}_{e_k}$. The velocity at location $\vec{x}$ is given by

$$\vec{u}(\vec{x}) = \sum_{j=1}^{N_e} v^{\mathrm{no}}_{e_j} \vec{\Psi}_{e_j} \ , \quad \vec{\Psi}_{e_j} = \frac{\vec{x} - \vec{x}_{e_j s}}{2A_c/l_{e_j}} \ , \tag{3.15}$$

where N_e is the number of element sides. $\vec{\Psi}_{e_j}$ are the basis functions, with A_c for cell area, l_{e_j} for the length of edge e_j and $\vec{x}_{e_j s}$ for the position of the node s opposite to edge e_j.

By definition of the basis functions, the normal velocity components between neighboring triangles are continuous. In Fig. 3.3 (left), one of the three weighted linear basis functions is shown.

Another linear interpolation is based on the Whitney edge-element of Eq. (3.12) (cf. [25, 79]). Analogously to the RT0 vector reconstruction, the full velocity field is reconstructed by the linear combination of three basis functions $\vec{\omega}_{ij}$, the Whitney edge-elements (shown in Fig. 3.3 (right)), weighted by the tangential velocity values $v_{ij}^{\mathrm{tg}}, v_{jk}^{\mathrm{tg}}, v_{ki}^{\mathrm{tg}}$. We find the velocity at location $\vec{x}$ by

$$\vec{u}(\vec{x}) = v_{ij}^{\mathrm{tg}}\vec{\omega}^{ij} + v_{jk}^{\mathrm{tg}}\vec{\omega}^{jk} + v_{ki}^{\mathrm{tg}}\vec{\omega}^{ki} \ , \quad \vec{\omega}^{ij} = \lambda_i(\vec{x})\nabla\lambda_j - \lambda_j(\vec{x})\nabla\lambda_i \ . \tag{3.16}$$

Let $\vec{p}_{jk} = p_k - p_j$ and $\vec{p}_{jk}^{\perp}$ be the orthogonal vector to $\vec{p}_{jk}$ generated by simply rotating $\vec{p}_{jk}$ by $\pi/2$, then we can represent $\nabla\lambda_i = \frac{\vec{p}_{jk}^{\perp}}{2|t_{ijk}|}$. Here, the tangential velocity components between neighboring triangles are continuous.

Normal RT0 vector reconstruction: We propose a normal RT0 vector reconstruction for hexagonal schemes that is based on the tangential RT0 vector reconstruction suggested by Ham et al. [46] for triangular models. On the basis of the results of Perot et al. [78, 79] we transfer the tangential into a normal vector reconstruction. It is suitable to reconstruct the full velocity at the triangles' circumcenters.

Investigating first-order edge-elements (Whitney edge-elements), Perot et al. [79] proposed a vector reconstruction scheme that is based on Stokes theorem – analogously to reconstruction methods for face elements based on Gauss theorem. Assuming constant vorticity in every cell, constant tangential velocity along the triangle edges e with length l_e and a linear velocity field, while using the tangential velocity components $\overline{u}_e := 1/l_e \int_e u$ (cf. Eq. (2.62)), the full velocity field at the circumcenters cc can be determined by the linear interpolation formula

$$\vec{u}_c^{cc} = \sum_{\mathrm{j}=1}^{N_e} \pm \left(\vec{x}_{e_j}^{cc} - \vec{x}_c^{cc}\right) \overline{u}_{e_j} l_{e_j} \ , \tag{3.17}$$

where $\vec{x}_c^{cc}$ denotes the circumcenter of a triangle c, $\vec{x}_{e_j}^{cc}$ the edges' midpoints and where $\pm$ indicates counterclockwise integration around the edges with respect to the tangential vector $\vec{t}_e$. We put the origin at the point cc which allows to substitute the position vectors by $\vec{n}_e \Delta x_e^{cc} = (\vec{x}_e^{cc} - \vec{x}_c^{cc})$, where $\vec{n}_e$ is the normal unit vector. We find

$$\vec{u}_c^{cc} = \frac{1}{A_c}\left(\overline{u}_{e_i}\Delta x_{e_i}^{cc} l_{e_i}\vec{n}_{e_i} + \overline{u}_{e_j}\Delta x_{e_j}^{cc} l_{e_j}\vec{n}_{e_j} + \overline{u}_{e_k}\Delta x_{e_k}^{cc} l_{e_k}\vec{n}_{e_k}\right) \ . \tag{3.18}$$

This equation agrees with the reconstruction method for triangular schemes proposed by Ham et al. [46] to obtain the full velocity component at cc out of normal velocity components. Therefore, we proceed for the next steps according to their derivations.

To find the reconstructed normal values we project the full vector $\vec{u}_c^{cc}$ onto the normal direction of the corresponding edges, i.e. for edge e_i it follows

$$u_{e_i}^{\mathrm{no}} = \frac{\overline{u}_{e_j}\Delta x_{e_j}^{cc} l_{e_j}}{A_c}\vec{n}_{e_j}\cdot\vec{t}_{e_i} + \frac{\overline{u}_{e_k}\Delta x_{e_k}^{cc} l_{e_k}}{A_c}\vec{n}_{e_k}\cdot\vec{t}_{e_i} \ , \tag{3.19}$$

and analogous equations for edges e_j and e_k. For Whitney edge-elements only the tangential values are continuous, whereas the normal components are in general not continuous (vise-versa for RT0 elements). Thus, some averaging is necessary:

$$\overline{u_{e_i}^{\mathrm{no}}} = \gamma_{e_i}^a u_{e_i}^{\mathrm{no}}|_a + \gamma_{e_i}^b u_{e_i}^{\mathrm{no}}|_b \ , \tag{3.20}$$

where $\gamma^a_{e_i}, \gamma^b_{e_i}$ denote the weights and where a, b denote the triangles adjacent to edge e_i. These weights have to obey certain conditions that we will investigate in the following.

On the basis of Eq. (3.19) with the weights of Eq. (3.20) we have introduced a vector reconstruction for hexagonal C-grid schemes. We will denote this reconstruction as *normal RT0 vector reconstruction*. The similarity with the tangential RT0 reconstruction of Ham et al. [46] suggests to proceed analogously to their derivation of the weights for triangular schemes.

Stability conditions on the weights: The weights γ^a_e, γ^b_e of Eq. (3.20) have to be such that the Coriolis term does not contribute to the kinetic energy. In order to find the corresponding constraint on these weights we investigate analogously to Sect. 2.8.3 the properties of the system matrix $\mathbf{S}$, which consists of the linear part $\mathbf{A}$ investigated in Chapter 2 and of the Coriolis part $\mathbf{F}$ to be investigated in the following (see more about this method in Espelid et al. [37] and Ham et al. [46]).

Let $\mathbf{A}$ be the system matrix of Eq. (2.88) that is similar to a skew-symmetric matrix (sign-skew-symmetric), i.e. by applying the scaling matrix $\mathbf{D}$ of Eq. (2.92) on the matrix $\mathbf{A}$, the latter becomes skew-symmetric. The fact that $\mathbf{A}$ fulfills these properties guarantees that there are only purely imaginary eigenvalues without growing or descending energy modes leading to a stable system. The scaling matrix introduced in Eq. (2.92) is

$$\mathbf{D} = \begin{bmatrix} D_p & 0 \\ 0 & D_c \end{bmatrix} , \tag{3.21}$$

with $(D_p)_{ii} = H d_{e_i} l_{e_i}$ and $(D_c)_{ii} = g A_{a_i}$, with g for gravity, H for the background fluid depth, l_e for the triangular and d_e for the hexagonal edge length and A_a for the size of the hexagonal cell a. Hereby, the size of $\mathbf{D}$ is equal to the size of $\mathbf{A}$. The following matrix F^a multiplied with f for cell a is a sub-matrix of the Coriolis matrix $\mathbf{F}$:

$$F^a = \begin{bmatrix} 0 & \gamma^a_{e_i} \frac{\Delta x^a_{e_j} l_{e_j}}{A_a} \vec{n}_{e_j} \cdot \vec{t}_{e_i} & \gamma^a_{e_i} \frac{\Delta x^a_{e_k} l_{e_k}}{A_a} \vec{n}_{e_k} \cdot \vec{t}_{e_i} \\ \gamma^a_{e_j} \frac{\Delta x^a_{e_i} l_{e_i}}{A_a} \vec{n}_{e_i} \cdot \vec{t}_{e_j} & 0 & \gamma^a_{e_j} \frac{\Delta x^a_{e_k} l_{e_k}}{A_a} \vec{n}_{e_k} \cdot \vec{t}_{e_j} \\ \gamma^a_{e_k} \frac{\Delta x^a_{e_i} l_{e_i}}{A_a} \vec{n}_{e_i} \cdot \vec{t}_{e_k} & \gamma^a_{e_k} \frac{\Delta x^a_{e_j} l_{e_j}}{A_a} \vec{n}_{e_j} \cdot \vec{t}_{e_k} & 0 \end{bmatrix} , \tag{3.22}$$

with $\Delta x^a_e := \Delta x^{cc}_e|_a$. To obtain a skew symmetric matrix $\mathbf{DF}$, the following equations have to hold

$$H d_{e_i} l_{e_i} \gamma^a_{e_i} \frac{\Delta x^a_{e_j} l_{e_j}}{A_a} \vec{n}_{e_j} \cdot \vec{t}_{e_i} = -H d_{e_j} l_{e_j} \gamma^a_{e_j} \frac{\Delta x^a_{e_i} l_{e_i}}{A_a} \vec{n}_{e_i} \cdot \vec{t}_{e_j} , \tag{3.23}$$

$$H d_{e_i} l_{e_i} \gamma^a_{e_i} \frac{\Delta x^a_{e_k} l_{e_k}}{A_a} \vec{n}_{e_k} \cdot \vec{t}_{e_i} = -H d_{e_k} l_{e_k} \gamma^a_{e_k} \frac{\Delta x^a_{e_i} l_{e_i}}{A_a} \vec{n}_{e_i} \cdot \vec{t}_{e_k} , \tag{3.24}$$

$$H d_{e_k} l_{e_k} \gamma^a_{e_k} \frac{\Delta x^a_{e_i} l_{e_i}}{A_a} \vec{n}_{e_i} \cdot \vec{t}_{e_k} = -H d_{e_j} l_{e_j} \gamma^a_{e_j} \frac{\Delta x^a_{e_k} l_{e_k}}{A_a} \vec{n}_{e_k} \cdot \vec{t}_{e_i} . \tag{3.25}$$

Hereby, the identities $\vec{n}_{e_i} \cdot \vec{t}_{e_j} = -\vec{n}_{e_j} \cdot \vec{t}_{e_i}$ and similar ones for the other pairs e_i, e_k and e_j, e_k hold. One possibility to guarantee equality for all equations is to take the weights

$$\gamma^a_{e_i} = \frac{\Delta x^a_{e_i}}{d_{e_i}} , \tag{3.26}$$

and analogous weights for e_j and e_k, where we assume a constant bottom topography H (cf. [46, 62] for varying H). With $\Delta x^a_{e_i} + \Delta x^b_{e_i} = d_{e_i}$, the weights sum up to one, i.e. $\gamma^a_{e_i} + \gamma^b_{e_i} = \frac{\Delta x^a_{e_i}}{d_{e_i}} + \frac{\Delta x^b_{e_i}}{d_{e_i}} = 1$, which is also fulfilled for the weights of edges e_j and e_k.

The upper block of the scaling matrix, $(D_p)_{ii} = Hd_{e_i}l_{e_i}$, coincides with the upper block matrix of the triangular scheme of Ham et al. [46] leading to the fact that the therein introduced tangential RT0 vector reconstruction equals our normal RT0 vector reconstruction of Eq. (3.19). Both schemes should thus show similar properties concerning consistency and stability.

In the following section we numerically test consistency and stability for both the tangential RT0 reconstruction for triangular schemes and the normal RT0 vector reconstruction for hexagonal schemes. Moreover, we study whether these schemes maintain geostrophic balance on both uniform and non-uniform grids. We expect for both schemes similar behavior on stability and consistency. However, when using the normal RT0 vector reconstruction of Eq. (3.19) in the hexagonal scheme, we expect problems to arise based on the discontinuous extrusion (cf. discussion to Fig. 3.2).

3.2.4 Numerical results of the normal RT0 vector reconstruction

We investigate in this section convergence – consistency and stability – and geostrophic balance of the discrete scheme consisting of the linear parts derived in Chapter 2 and of the vector reconstruction of Eq. (3.19). For the linear parts, such an investigation has already been performed in Chapter 2. Therefore, we focus here on a comparison between the normal and the tangential RT0 vector reconstructions.

Matrix representation: Let be $\overline{\mathbf{u}}_\mathbf{e}$ the vector of all edge velocities $\overline{u}_e$ and $\mathbf{h_v}$ the vector of all surface elevations h_v. We use the linear parts of Eq. (2.88) and extend it by the linear Coriolis term including the normal RT0 vector reconstruction of Eq. (3.19) to obtain a discrete representation of the linear rotating shallow-water equations (3.3) in matrix form. According to Eq. (2.88), the system matrix for the linear non-rotating equations is given by

$$\mathbf{A} = \begin{bmatrix} 0 & G \\ D & 0 \end{bmatrix} , \tag{3.27}$$

with $G := \frac{g}{l_e}\mathbf{G}$ of Eq. (2.62) and $D := \frac{Hd_e}{A_c}\mathbf{D}^{\text{dual}}$ of Eq. (2.66). The *semi-discrete* form of the rotating linear shallow-water equations in matrix formulation is given by

$$\frac{\partial}{\partial t}\begin{bmatrix} \overline{\mathbf{u}}_\mathbf{e} \\ \mathbf{h_v} \end{bmatrix} = \begin{bmatrix} F & G \\ D & 0 \end{bmatrix}\begin{bmatrix} \overline{\mathbf{u}}_\mathbf{e} \\ \mathbf{h_v} \end{bmatrix} , \tag{3.28}$$

with $F = f\mathbf{F}$ of Eq. (3.22). We denote this matrix as extended system matrix $\mathbf{A} + \mathbf{F}$, in which the Coriolis matrix $\mathbf{F}$ is extended with zeros to match the dimension of $\mathbf{A}$.

According to Ham et al. [46], the tangential RT0 vector reconstruction used for the triangular model is consistent and stable for uniform and non-uniform grids. In the following we investigate whether this is also valid for the hexagonal C-grid discretization of the rotating linear shallow-water equations using the normal RT0 vector reconstruction (3.19) for the Coriolis term and the linear parts derived in Section 2.7.

Consistency: In the following we test consistency for this scheme with system matrix $\mathbf{A} + \mathbf{F}$. With respect to Eq. (3.28) the semi-discrete momentum equation per edge $e = \{v_1, v_2\}$ is given by

$$\partial_t \overline{u}_e + f \cdot \overline{u_e^{\text{no}}} + g\frac{h_{v_2} - h_{v_1}}{l_e} = 0 , \tag{3.29}$$

with $\overline{u_e^{\text{no}}} = \text{Rec}^{\text{RT0}}{}_{t\to n}(\overline{u}_e)$, where $\text{Rec}^{\text{RT0}}{}_{t\to n}$ denotes the normal RT0 vector reconstruction of (3.19) and (3.20) with weights (3.26). To show consistency of the momentum

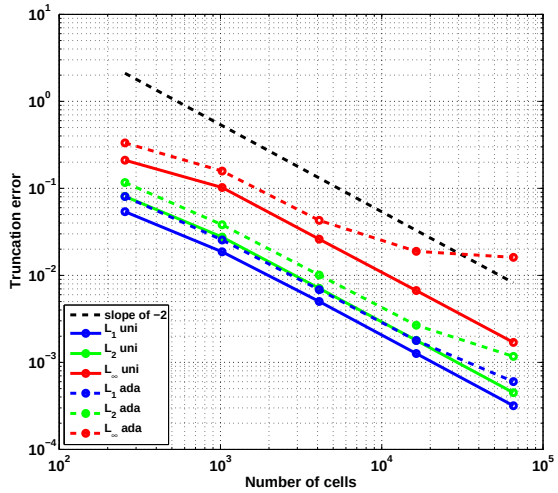

Figure 3.4: Truncation errors in the L_1, L_2, L_∞-norm of the normal RT0 vector reconstruction $\mathrm{Rec}^{\mathrm{RT0}}{}_{t\to n}$ for uniform grids (solid) and for non-uniform grids (dashed lines) similar to the meshes in Fig. 3.13.

equation (3.29), it is sufficient by linearity to show consistency for $\mathrm{Rec}^{\mathrm{RT0}}{}_{t\to n}$, because for the remainder parts this has already been studied in Sect. 2.8.

Analogously to Sect. 2.8.2, we investigate whether the vector reconstruction $\mathrm{Rec}^{\mathrm{RT0}}{}_{t\to n}$ is consistent and converges with increasing resolution toward the true solution. We take the analytic vector field

$$\vec{v} = \alpha \nabla \beta = \alpha \left(\frac{\partial \beta}{\partial x}, \frac{\partial \beta}{\partial y} \right) \ , \tag{3.30}$$

with the analytic values given in Eqn. (2.82) and (2.83) and the corresponding derivations. For the numerical calculation, we project the analytic vector $\vec{v}$ onto the tangential direction $\vec{t}_e$ of edge e, i.e. $v_e^{\mathrm{tg}} = \vec{v} \cdot \vec{t}_e$. To obtain the normal vector coefficient v_e^{no} to edge e we use the vector reconstruction, i.e. $v_e^{\mathrm{no}} = \mathrm{Rec}^{\mathrm{RT0}}{}_{t\to n}(v_e^{\mathrm{tg}})$. The numerically reconstructed vector $\vec{v}_e^{\mathrm{Rec}} = v_e^{\mathrm{tg}} \cdot \vec{t}_e + v_e^{\mathrm{no}} \cdot \vec{n}_e$ is then compared to the analytic vector $\vec{v}|_e$ evaluated at edge midpoints. With respect to the error measures L_1, L_2, L_∞ defined in (2.81), the truncation error

$$\tau_e^{\mathrm{Rec}} = \vec{v}_e^{\mathrm{Rec}} - \vec{v}|_e \tag{3.31}$$

gives information about the consistency properties of the vector reconstruction method.

Figure 3.4 shows the consistency property of $\mathrm{Rec}^{\mathrm{RT0}}{}_{t\to n}$ with respect to the error norms L_1, L_2, L_∞ for uniform and non-uniform grids similar to the meshes shown in Fig. 3.13. On uniform grids the normal RT0 vector reconstruction scheme has second order accuracy in all three norms. On non-uniform grids, the vector reconstruction is almost second order accurate for lower numbers of grid cells. However, with increasing resolution the order of convergence decreases, in particular in the L_∞-norm. This may lie in the fact that our grid adaptation process, presented in Chapter 4, constructs grids in which some grid cells are possibly strongly stretched. The problem of deformed cells increases with resolution, which may lead to the decrease in accuracy (cf. Chapter 4).

Stability: In order to investigate stability we analyze the properties of the system matrix $\mathbf{A} + \mathbf{F}$ of Eq. (3.28) analogously to Sect. 2.8.3. Let $\mathbf{z}$ be an eigenvector of $\mathbf{A} + \mathbf{F}$ with

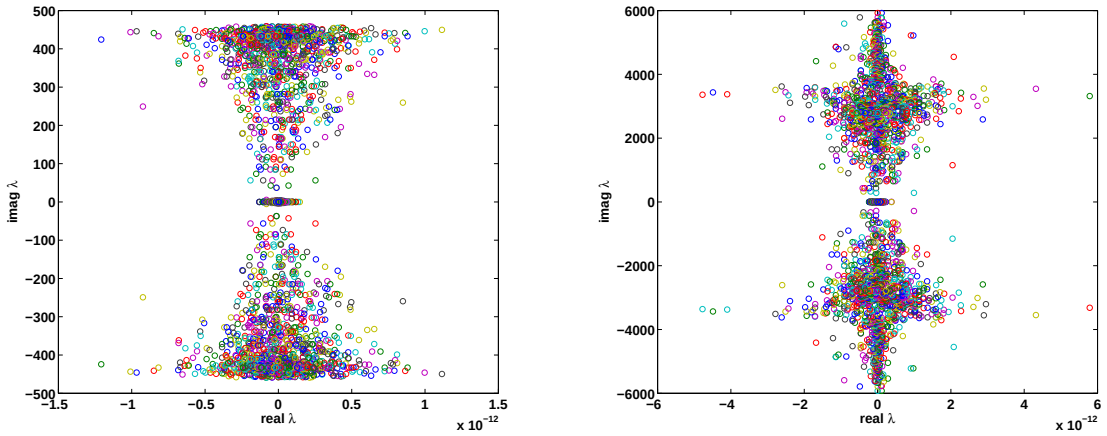

Figure 3.5: Eigenvalues λ of the propagation matrix $\mathbf{A}+\mathbf{F}$ including the linear Coriolis term for 32^2 grid cells on a uniform grid (left) and on a non-uniform grid (right) shown in Fig. 3.13.

eigenvalue λ, i.e. $(\mathbf{A}+\mathbf{F})\mathbf{z} = \lambda\mathbf{z}$. With initial values $\mathbf{s}(0) = \mathbf{z}$, the solutions to the linear rotating equations are

$$\mathbf{s}(t) = e^{\lambda t}\mathbf{z} \ . \tag{3.32}$$

Therefore, only purely imaginary eigenvalues guarantee a stable model as only those lead to solutions $\mathbf{s}(t)$ that neither grow nor decrease with time. Calculating the eigenvalues by using the MATLAB eigenvalue function delivers the required information.

Figure 3.5 shows the eigenvalues of $\mathbf{A}+\mathbf{F}$ for uniform and non-uniform grids. As we can infer from this figure, the extended system with $\mathbf{A}+\mathbf{F}$ has solutions $\mathbf{s}(t)$ with purely imaginary eigenvalues λ with real parts real$\lambda < 10^{-12}$ on both uniform and non-uniform grids. The system have thus no growing nor decreasing solutions and is therefore stable.

Concerning consistency (Fig. 3.4) and stability (Fig. 3.5), we can conclude for the system $\mathbf{A}+\mathbf{F}$ that the normal RT0 vector reconstruction (3.19) is consistent and leads to a stable model, in agreement to the tangential RT0 vector reconstruction for the triangular model of Ham et al. [46].

Tests on geostrophic balance: The Coriolis term influences linearly the solutions of the shallow-water equations as we infer from Eq. (3.1). In the following, we perform test cases where an adequate representation of the Coriolis term is expected to be essential, namely in vorticity dominated scenarios. On such scenarios, we study for uniform grids, whether the hexagonal/triangular C-grid scheme with normal/tangential RT0 vector reconstruction properly represents the geostrophic balance.

We use the version of a triangular shallow-water model introduced in Giorgetta et al. [44] that agrees with the model of Ham et al. [46] on a uniform grid including the tangential RT0 vector reconstruction. From the results of Ham and colleagues and our results introduced above, both reconstructions provide consistent vector reconstructions (Fig. 3.4) and stable schemes (Fig. 3.5) for uniform and non-uniform grids.

To study whether the schemes maintain the geostrophic balance, we use a test case introduced in Giorgetta et al. [44]. We initialize the height distribution by

$$h(x,y,0) = H_0 - H'\left[e^{-\frac{1}{2}({x'_1}^2+{y'_1}^2)} + e^{-\frac{1}{2}({x'_2}^2+{y'_2}^2)} - \frac{4\pi\sigma_x\sigma_y}{L_xL_y}\right] \ , \tag{3.33}$$

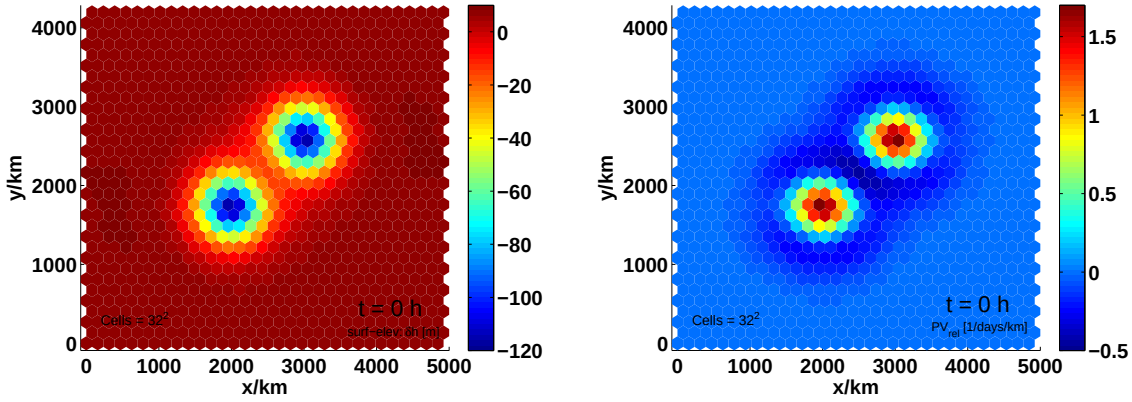

Figure 3.6: Initial surface elevation [m] (left) and initial potential vorticity distribution [1/days/km] (right) for a uniform grid with 32^2 cells on a domain with double periodic boundaries.

with

$$x'_{1,2} = \frac{L_x}{\pi\sigma_x}\sin\left(\frac{\pi}{L_x}(x - x_{c_{1,2}})\right), \quad y'_{1,2} = \frac{L_y}{\pi\sigma_y}\sin\left(\frac{\pi}{L_y}(y - y_{c_{1,2}})\right). \tag{3.34}$$

The centers of the vortices and σ are given by

$$\begin{aligned} x_{c_1} &= (\frac{1}{2} - o)L_x\,, \quad x_{c_2} = (\frac{1}{2} + o)L_x\,, \quad \sigma_x = \frac{3}{40}L_x\,, \\ y_{c_1} &= (\frac{1}{2} - o)L_y\,, \quad y_{c_2} = (\frac{1}{2} + o)L_y\,, \quad \sigma_y = \frac{3}{40}L_y\,. \end{aligned} \tag{3.35}$$

Analogously to Giorgetta et al. [44] we take the height distribution $h_0 = H + \delta h_0$ over a domain of 5000 km $\times$ 4330 km with double periodic boundaries and the parameters of $o = 0.1$ and $H' = 75$ m. We initialize the velocity distribution for the hexagonal model by imposing geostrophic balance:

$$\vec{v} = -\frac{g}{f}\nabla h \xrightarrow{discretized} v_e^{\mathrm{tg}}(0) = -\frac{g}{f}\mathrm{grad}^{\mathrm{n}}{}_e\,(h_{cc}(0))\,, \tag{3.36}$$

where g is the gravity and f is the Coriolis parameter. h_{cc} is the height field sampled at the triangular cell centers cc, $\mathrm{grad}^{\mathrm{n}}{}_e$ is the gradient operator of (2.69) and v_e^{tg} the prognostic tangential velocity values. Figure 3.6 illustrates the initial surface elevation (left) and the initial vorticity distribution (right) on a grid with 32^2 cells, in which the potential vorticity q is determined by the tangential velocities, i.e. $q = \nabla \times \vec{v} \xrightarrow{disc.} q_v = \mathrm{curl}_{cc}(v_e^{\mathrm{tg}})$. We perform low resolution runs in order to test the maintaining of geostrophic balance. As our experiments have shown, low resolution favors the growth of spurious geostrophic modes, if present.

In Fig. 3.7 we compare the ability of the different schemes to maintain the geostrophic balance. In principle, both the height distribution and the initially balanced vorticity distribution should not change during the integration time. In Fig. 3.7 A and B we present the height and vorticity distribution after 10 days for the triangular and in C and D for the hexagonal model on a uniform grid with 32^2 vertices. The triangular model maintains the geostrophic balance. For the hexagonal version, using the normal RT0 vector reconstruction of Eq. (3.19), appears a hexagonal pattern that spoils the vortex

distribution. The balance is thus not maintained as some *spurious geostrophic modes* emerge (see discussion below). The negative surface elevation decreases significantly for both schemes. This is caused by the linearized continuity equation, as we conclude from the fact that the use of the nonlinear continuity equation avoids such decrease (cf. the height field after an integration of 100 days using the nonlinear equations in Fig. 3.14). In order to understand the occurrence of the spurious geostrophic modes, we compare in the following the representation of the wave dispersion relation for both triangular and hexagonal C-grids.

Wave representation and dispersion relation: Let us regard the linear rotating shallow-water equations (3.1). Written in vector calculus, the equations take the form:

$$\partial_t \vec{v} + f\vec{k} \times \vec{v} + g\nabla h = 0 \ , \quad \partial_t h + H\nabla \cdot \vec{v} = 0 \ , \tag{3.37}$$

where $\vec{v}$ denotes the fluid velocity, h the surface elevation with background height H, g the gravity and f the Coriolis parameter. According to an analysis of LeRoux et al. [65] with the assumption of wave solutions $(u, v, h) = (u_0, v_0, h_0)e^{i(kx+ly)}$ – subindex 0 indicates the initial conditions, k and l are wave numbers along the Cartesian coordinates x and y – inserted into Eq. (3.37), one obtains the following frequencies in the continuous case:

$$\nu_{\text{gst}} = 0 \ , \quad \nu_{gi} = \pm\sqrt{f^2 + gH(k^2 + l^2)} \ , \tag{3.38}$$

where ν_{gst} relates to the geostrophic and ν_{gi} relates to the two branches of the gravity-inertia wave solutions.

Among others, Nickovic et al. [76] investigated the discrete wave frequencies of a hexagonal C-grid model that coincides with our scheme. The authors found that the gravity-inertia waves are well presented. However, the discrete representation of the geostrophic waves have non-zero frequencies (cf. [76, 101]) that are called *spurious geostrophic modes*. These frequencies develop in time and spoils the geostrophic balance of Fig. 3.7 C and D.

In the triangular case, the low-order RT0 vector reconstruction introduced in Eq. (3.19) has been used. In LeRoux et al. [65, 66], the wave spectra of several finite element pairs for the shallow-water equations have been studied. Among those, the finite element pair (RT0 -P0) that corresponds to the triangular model used for our experiments. The authors found for this pair that the geostrophic waves frequencies are zero, i.e. $\nu_{gst} = 0$, leading to the stationarity of the geostrophic modes. In this case, the geostrophic balance is adequately satisfied, cf. Fig. 3.7 A and B.

The triangular C-grid discretization of the shallow-water equations thus properly represent the geostrophic modes. However, as theoretically elaborated by Gassmann [43], it supports a checkerboard pattern in the divergence field. Numerical experiments performed therein or by Wan [112] for the triangular C-grid discretization of the shallow-water equations confirm this analysis.

Discussion of the numerical results: Both normal and tangential RT0 vector reconstruction schemes give consistent and stable models on uniform grids, but the models differ strongly concerning geostrophic balance. In particular, the hexagonal scheme has non-stationary geostrophic wave solutions $\nu_{\text{gst}} \neq 0$ leading to spurious geostrophic modes that destroy the geostrophic balance. In contrast, the triangular model with geostrophic modes with zero frequency maintains the geostrophic balance.

As discussed in Section 3.2.2 the discrete representations of the extrusion on the triangular and hexagonal models differ. In case of triangular models, the continuous extrusion

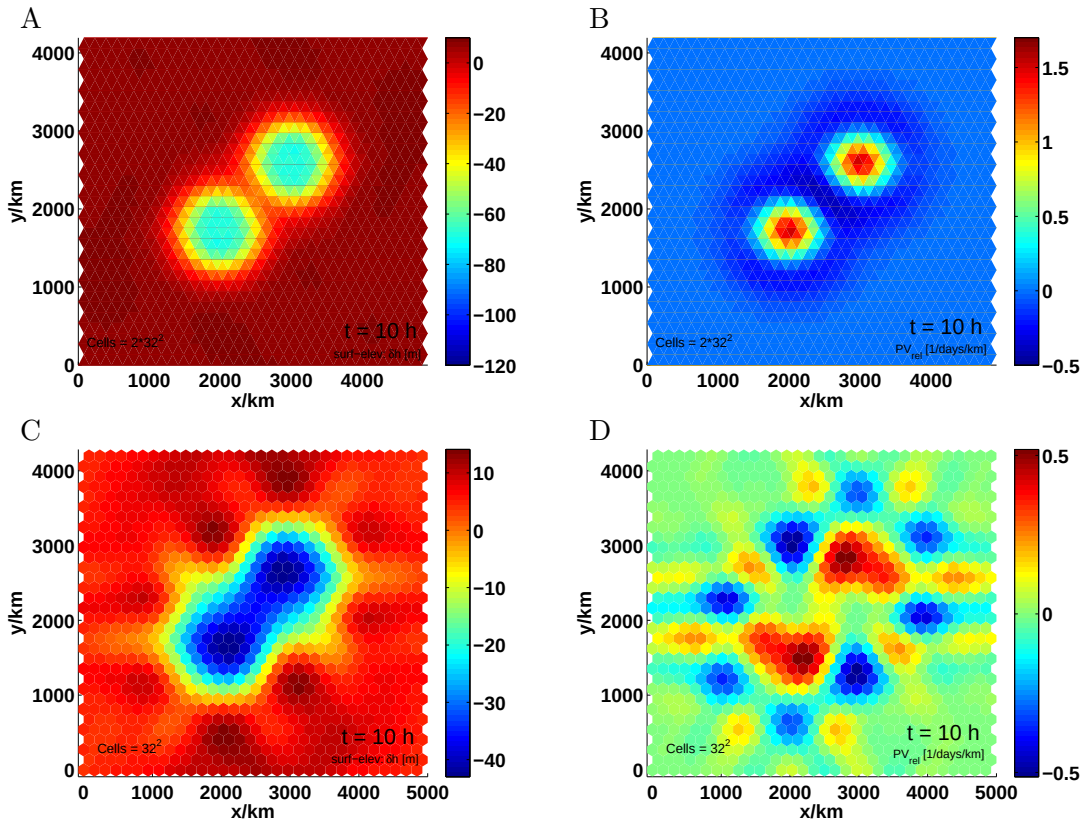

Figure 3.7: Surface elevation [m] (left) and vorticity distribution [1/days/km] (right) after a model integration of 10 days for the triangular model (A and B) with tangential RT0 vector reconstruction and for the hexagonal model (C and D) with normal RT0 vector reconstruction. In the latter case spurious geostrophic modes (visible as hexagonal pattern) occur. Please notice the modified color bars in C and D.

(Fig. 3.2 left) is caused by the hexagonal edges e_{dual} being swept over an area, where the full RT0 reconstructed vector field is smooth. In contrast, using the same smooth RT0 vector field, the extruded triangular edge e may partly lie outside the area of the two triangles defining the RT0 vector field. This may lead to jumps in the extrusion (Fig. 3.2 right). A study on whether a theoretically solid connection between a proper wave representation and the continuity properties of extrusion can be established has to be postponed, however, to future work.

The question arises whether we can avoid the development of the spurious modes by extending the stencil for the vector reconstruction such that we obtain a smooth extrusion for the triangular edge e. Examples in literature, e.g. Nickovic et al. [76] and Thuburn et al. [101], reveal that an extended stencil for normal vector reconstruction with equal weights, for instance in Perot [78] and Wang et al. [113], can also lead to spurious geostrophic modes.

To obtain a continuous value for the extrusion of the vertices of edge e in any direction that is consistent with the geometrical properties of extrusion, all connected velocities have to be taken into account. Thus, the normal velocity component has to be a weighted sum of all tangential velocity components of edges e' adjacent to the vertices of edge e. According to the idea of extrusion, the weights represent the influence of the tangential velocity component to contribute to the extrusion of edge e. In the following section we derive a normal vector reconstruction under the conditions of continuous extrusion.

3.3 Normal vector reconstruction based on extrusion

In this section we develop a method for normal vector reconstruction based on the idea of representing the Coriolis term by means of extrusion, which puts geometrical constraints on the derivation of the normal velocity components. The reconstructed velocity field will lead to a smooth extrusion of the triangular edges in any direction. The extrusion is hereby caused by a smooth velocity field positioned at the vertices of the triangular edges e. This is similar to the case of the tangential RT0 reconstruction, in which a smooth velocity field at the circumcenters causes a smooth extrusion of the hexagonal edges e^{dual} (cf. Fig. 3.2 left).

We proceed as follows. First, we explain how a nodal velocity field can be represented on a general mesh as a linear one-chain. On the basis of such one-chain, the normal vector reconstruction can be represented as a weighted sum, where the weights are determined by the ability of every single edge to contribute to the total extrusion.

3.3.1 Nodal vector representation

In order to represent a known vector field $\vec{v}(x)$, where x denotes the position vector, on an underlying mesh, one can use the concept of chains, as introduced in Bossavit [27]. Positioning the discrete vector field at the vertices by $\mathbf{v_n}$ and using barycentric coordinates for linear interpolation, one can represent the linear vector field by

$$\vec{v}(x) \approx \sum_{n\in\mathcal{N}} \lambda^n(x)\mathbf{v_n} \ , \tag{3.39}$$

where $\lambda^n(x)$ are the barycentric coordinates associated to the nodes n with support within the corresponding triangles. Using the nodal velocity components in Cartesian coordinates it is possible to represent those also as edge values, i.e. the Cartesian coordinates associated to the basis $(\vec{e}_x, \vec{e}_y)$ are projected to the edges adjacent to node n. We denote those values with v_e^n. To represent the vector, two edges that are not parallel are enough. However, in order to present any vector $\vec{v}$ and $-\vec{v}$, the information of the projection of $\vec{v}$ on all edges is required (cf. Bossavit [28]). Knowing $v_e^n e$, one is able to represent $\mathbf{v_n}$ in terms of the edges e by

$$\mathbf{v_n} \approx \sum_{e\in\mathcal{E}} \mathbf{G}_e^n v_e^n e \ , \tag{3.40}$$

where $\mathbf{G}_e^n$ is the incident matrix of Chapter 2 and $e = l_e \cdot \vec{t}_e$ stands for the edge vector with length l_e and unit vector $\vec{t}_e$ tangent to e. Combining this two equations, we find an expression for the vector-valued velocity field as a position dependent, affine in x, one-chain by

$$\vec{v}(x) \approx \sum_{n\in\mathcal{N}} \sum_{e\in\mathcal{E}} \lambda^n(x)\mathbf{G}_e^n v_e^n e \ . \tag{3.41}$$

Figure 3.8 shows how the nodal velocity values are interpolated by barycentric coordinates to obtain a continuous vector field, affine in x.

We use the concept of extrusion, to our best knowledge for the first time here, in order to determine the weights of a vector reconstruction. Studies in literature [27, 52, 75] use this concepts to represent known vector fields and calculate the influence on the acceleration along the triangle edges. We differ from such approaches in the sense that the values v_e^n are unknown in our study.

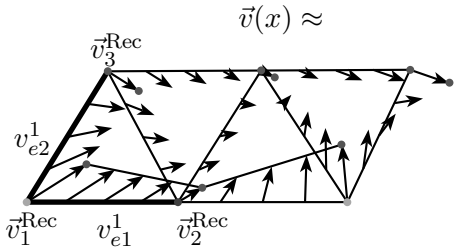

Figure 3.8: Vector representation with nodal values $\vec{v}_n^{\text{Rec}}$ at the vertex points n on a triangular mesh with barycentric coordinates. The edge values v_e^n for the linear one-chain are indicated with bold triangular edges.

General nodal vector reconstructions: Based on the vector representation for a linear affine vector field on a mesh of Eqn. (3.40) and (3.41), we derive the following vector reconstruction. We substitute in Eq. (3.41) the known values for v_e^n (2 DoF) with the weighted tangential velocity components $v_{e'}^{\text{tg}}$ of all edges e' adjacent to node n, i.e.

$$\vec{v}_n^{\text{Rec}} \approx \sum_{e' \in \mathcal{E}} \mathbf{G}_{e'}^n \mathrm{w}_{ee'} v_{e'}^{\text{tg}} e' \ , \tag{3.42}$$

where the properties of the weights $\mathrm{w}_{ee'}$ are discussed further below. Hence, the affine one-chain with weights is given by

$$\vec{v}(x) \approx \sum_{n \in \mathcal{N}} \sum_{e' \in \mathcal{E}} \lambda^n(x) \mathbf{G}_{e'}^n \mathrm{w}_{ee'} v_{e'}^{\text{tg}} e' \ . \tag{3.43}$$

By this approach we do not recover the values for v_e^n of Eq. (3.41). Instead, we aim to reconstruct the normal velocity value at edge midpoint e that is consistent with extrusion. Clearly, the vector reconstruction of Eq. (3.43) is not unique. Different weights $\mathrm{w}_{ee'}$ can be used to find the nodal reconstructed full vector $\vec{v}_n^{\text{Rec}}$, (as, for instance, in Wang et al. [113] and Perot et al. [78]). However, such reconstruction may lead to a scheme that shows spurious geostrophic modes (cf. Thuburn [101]).

We have to specify in more detail the requirements the reconstruction scheme should satisfy. When considering Eq. (3.7) we can derive additional constraints, for instance, that the weights should properly represent the extrusion of a manifold S and thus the acceleration along S.

3.3.2 Determining the weights by the extrusion of manifolds

In this section we introduce our idea to determine weights $w_{ee'}$ for normal vector reconstruction by the concept of extrusion, i.e. the sought-after vector field is an affine in x one-chain that acts on k-dimensional simplices to extrude these to $(k+1)$-dimensional simplices. Therefore, we first represent the extrusion by a weighted linear combination of contributions of edges e' adjacent to edge e to the total extrusion of e that leads to an acceleration of the fluid along e. Then, we show that the weights $w_{ee'}$ that determine the contributions of the different edges to the total extrusion coincide with the weights of our ansatz for a normal vector reconstruction.

The linear discrete interior product defined by extrusion

We use the concept of extrusion of Eq. (3.7) to determine the influence of different edges e' on the extrusion and thus to the Coriolis acceleration along edge e. For every single

edge e adjacent to node n, we define the interior product via the extrusion of Eq. (3.14) by

$$\mathrm{I}(e, \lambda^n e', c) := \lim_{t \to 0} \frac{< \omega^c, E_{\lambda^n e'}(e,t) >}{t} \ , \tag{3.44}$$

with $\mathrm{I}(e, \lambda^n e', c) = 0$ if $e = e'$, $\partial e \cap \partial e' = \varnothing$ or $\partial c \cap e = \varnothing$, where ω^c is the Whitney interpolation function of Eq. (3.13). Hereby, the barycentric coordinate $\lambda^n(x)$ linearly interpolates between the nodes of e to obtain a linear vector field $\vec{X} = \lambda^n(x)e'$ that extrudes e (cf. Fig. 3.9).

The interior product of Eq. (3.44) is linear in all three arguments. This is based on the definition of the extrusion – a manifold that is spanned by the linear extrusion of a surface S during the time t and by its projection to the underlying mesh – and on the fact that ω^c is continuous on the domain. For discontinuous forms ω^c, the linearity in e' is in general not fulfilled (cf. Heumann and Hiptmair [52]). The Coriolis two-form $f_C = f dx \wedge dy \in \Omega^2(\mathcal{M})$ has constant Coriolis parameter f and its discrete representation using Whitney-forms ω^c is continuous on the entire domain and given by $\mathbf{f}_C = \sum_f f \omega^f$.

The linear interior product: To determine the weights for the vector reconstruction, the weights will be determined by the ability of every single edge to contribute to the total extrusion of the edge e, i.e. analogously to the linear ansatz of Eq. (3.43) we set for the interior product for $n \in \partial e \cap \partial e'$:

$$\mathbf{I}(\vec{v}, \mathbf{f}_C)_e = \frac{1}{c^n_{\mathrm{norm}}} \mathrm{I}(e, \sum_{n,e',c} \lambda^n \mathbf{G}^n_{e'} v^{\mathrm{tg}}_{e'} e', \mathbf{f}_C) = \sum_{n,e',c} \frac{\mathrm{I}(e, \lambda^n e', c) \mathbf{G}^n_{e'}}{c^n_{\mathrm{norm}}} v^{\mathrm{tg}}_{e'} f \ , \tag{3.45}$$

which corresponds to the Coriolis term $\int_e \mathbf{i}_{\vec{v}} f_C \approx \mathbf{I}(\vec{v}, \mathbf{f}_C)_e$ of Eq. (3.3). In Eq. (3.45), all adjacent edges to node n can contribute to the extrusion of the manifold. To obtain a consistent formulation, the sum of extrusions should never be larger than over the area caused by the vector field itself (cf. Fig. 3.9). To guarantee this, we normalize every edges' contribution to the total extrusion by a constant c^n_{norm}. We define the weights for the contribution of a single edge to the entire extrusion by

$$w^n_{ee'} := \frac{\mathrm{I}(e, \lambda^n e', c) \mathbf{G}^n_{e'}}{c^n_{\mathrm{norm}}} \ , \tag{3.46}$$

with the normalizing constant

$$c^n_{\mathrm{norm}} = \sum_{e', c|_{e \in \partial c}} \mathrm{I}(e, \lambda^n e', c) \ , \tag{3.47}$$

where we sum over all edges e' and over the cells c adjacent to edge e, i.e $c|_{e \in \partial c}$.

Representation of the interior product on the mesh: In order to derive the weights of Eq. (3.46), a concrete representation of the definition of the interior product (3.44) on the mesh is required. Let us assume that $\vec{v}$ is such that during $t = 1$ the edge e_1 is extruded by e_2 such that it coincides with the cell a, thus $\vec{v} = l_{e_2}/t \cdot \vec{t}_{e_2}$. Then, node $n = 1$ is advected during $t = 1$ along e_2 by the length $\vec{v}(x) \cdot t = l_{e_2}/t \cdot \vec{t}_{e_2} \cdot t = e_2$ with $\vec{t}_{e_2} = e_2/l_{e_2}$. Therefore, there is $\vec{v}(x)|_{e_2} = e_2$ and we find for the linear vector field within cell a

$$\vec{v}(x)|_a = \lambda^1_a(x) e_2 \ . \tag{3.48}$$

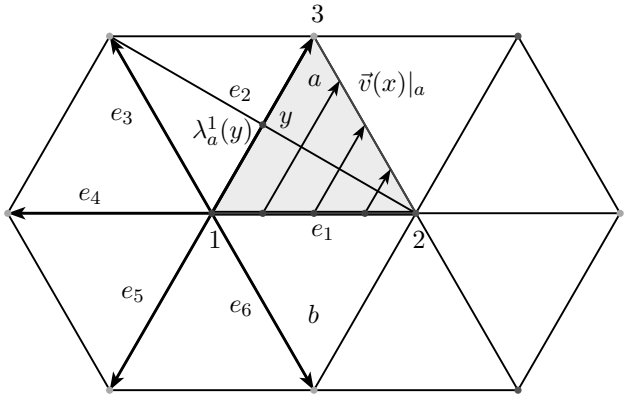

Figure 3.9: Contribution of every edge $e_i, i = 2, ..., 6$, adjacent to node $n = 1$, to the total extrusion caused by the vector field $\vec{v}(x)|_a \approx \lambda_a^1(x)e_2$ within triangle a that acts on e_1 (with $\vec{v}(x)|_b \approx \lambda_b^1(x)e_6$ within triangle b).

Here, $\lambda_a^1(x)$ is the barycentric coordinate of triangle a associated to vertex $n = 1$. Figure 3.9 illustrates this vector field. For the barycentric coordinate follows $\lambda_a^1(x(n = 1)) = 1$ and $\lambda_a^1(x(n = 2)) = 0$. Therefore, $\vec{v}(x)|_a$ is a linear vector field within the triangle.

Now the question arises, how strong every single tangential velocity component $v_{e_i}^{\text{tg}}$ associated to edge e_i can contribute to the extrusion of e_1 caused by the prescribed velocity field of Eq. (3.48) during the time $t = 1$. e_i denotes all edges adjacent to node $n = 1$, except edge e_1. The relative orientation and the direction of the edges e_i with respect to edge e_1 lead to different contributions to the extrusion of e_1. To determine the weights $w_{e_1 e_i}$ by the pure geometrical influence of edge e_i on the extrusion of e_1, we set the absolute velocity values of edge e_i equal to the absolute value of Eq. (3.48), i.e. $|v_{e_i}^{\text{tg}}| = |\vec{v}(x)|_a|$. Thus, during the time $t = 1$, $v_{e_i}^{\text{tg}}$ extrudes node $n = 1$ the distance $l_{e_i} = l_{e_2}$, whereas the remaining edges should not contribute to the extrusion, i.e $v_{e_j}^{\text{tg}} = 0 \forall j \neq i$. Consequently, the velocity $v_{e_i}^{\text{tg}}$ of edge e_i that extrudes e_1 can be written as

$$v_{e_i}^{\text{tg}}(x) = \lambda_a^1(x)e_i = \lambda_a^1(x) l_{e_i} \vec{t}_{e_i} \ , \tag{3.49}$$

where $l_{e_i} = l_{e_2}$ has to be fulfilled. Thus, the right hand side of Eq. (3.45) is reduced to one term, i.e.

$$\mathbf{I}(\vec{v}(x)|_a, \mathbf{f}_C)_e = \frac{\mathrm{I}(e, \lambda_a^1(x)e_i, a)\mathbf{G}_{e_i}^n}{c_{\text{norm}}^n} f \ . \tag{3.50}$$

With the definition of the interior product $\mathrm{I}(,,)$ via extrusion and by the projection of the extrusion on the underlying mesh, cf. Eq. (3.44), we see different influences of different edges e_i. Taking $i = 2$, for instance, the extruded manifold $v_{e_2}^{\text{tg}}(x)$ equals those of $\vec{v}(x)|_a$, which leads to $\mathrm{I}(,,) = 1$. However, for $i = 3$ the extruded manifold projected on the underlying mesh leads to a weight with $\mathrm{I}(,,) < 1$, but also in this case the normalizing constant guarantees the equality in Eq. (3.50).

In the following, we represent the values $\mathrm{I}(e, \lambda^n e', c)$ of Eq. (3.44) on a two-dimensional triangular mesh more quantitatively. We have to take two possible cases into consideration:

1. With the coincident matrices[1] of Chapter 2 and for $n \in \partial e \cap \partial e'$ there is:

$$\text{i) for } e, e' \in \partial c: \ \mathrm{I}(e, \lambda^n e', c) = \mathbf{R}_c^e \ , \tag{3.51}$$

$$\text{ii) for all } c' \neq c: \ \mathrm{I}(e, \lambda^n e', c') = 0 \ . \tag{3.52}$$

[1] In Chapter 2 we denoted cells with f instead of c to be consistent with literature (cf. Bossavit [25]).

The fact that the extrusion of e by e' for $t = 1$ is exactly c leads to i) and from $< \omega^c, c' >= 0$ follows ii).

2. For $n \in \partial e \cap \partial e'$, $e \in \partial c$ and $e' \notin \partial c$, there is:

$$\mathrm{I}(e, \lambda^n e', c) = \lambda^{c-e}(y)\mathbf{R}_c^e \ , \tag{3.53}$$

where y is the intersection point of the edge opposite to node n of the triangle spanned by e and e' with one edge of the boundary ∂c. There follows $\lambda^{c-e}(y) = \lambda^k(y)$ when defining $\lambda^e = \lambda^i + \lambda^j$ for edge $e = \{i, j\}$ and $\lambda^c = \lambda^i + \lambda^j + \lambda^k$ for cell $c = \{i, j, k\}$ (cf. Bossavit [25, 27]). This definition takes the orientation of the tangential vector $\vec{t}_{e'}$ of every extruding edge e' with respect to the normal direction $\vec{n}_e$ of the extruded edge e into account.

With the representation of $\mathrm{I}(e, e', c)$ on the mesh we can calculate the weights $w_{ee'}$ in Eq. (3.46). According to the definition of the interior product in Eq. (3.45), these weights determine how strong every single edge contributes by pure geometrical factors to the acceleration along edge e.

Connection between extrusion and normal vector reconstruction

Based on the weights $w_{ee'}$ describing the edges' contribution to the total extrusion and on the formulation of a vector field as a one-chain, defined in Eq. (3.43), we present in the following a normal vector reconstruction scheme.

In the above derivation, an edge velocity may have any direction, only its contribution to the extrusion is included in the corresponding weight. According to the definition of extrusion, the same extrusion is caused by the normal vector component emanating form the projection of the edge velocity to the normal direction. In Eq. (3.43) the velocity $\vec{v}$ is presented as a one-chain by the edge vectors $e' = l_{e'}\vec{t}_{e'}$. Integrations of the one-form $u \in \Omega^1(\mathcal{M})$ of Eq. (3.1) along curves c with lengths l_c give the components of a one-chain, i.e. $\int_c u = l_c \overline{u}_c$, where $\overline{u}_c$ describe the averaged velocity components. Therefore, we can interpret the terms $\int_{e'} v_{e'}^{\mathrm{tg}} \vec{t}_{e'} = v_{e'}^{\mathrm{tg}} l_{e'}$ as coefficients associated to edges e' of the velocity one-chain of the invariant fluid equations. Analogously, we interpret the coefficients $v_e^{\mathrm{no}} e^{\mathrm{dual}}$, i.e. the product of the reconstructed *normal velocity component* v_e^{no} and of the dual edge e^{dual} with edge length d_e, as the coefficient of a velocity one-chain associated to e^{dual}. Consequently, we approximate the extruding velocity field $\vec{v}(x)|_e^{\mathrm{Extr}}$ acting on edge e by

$$\vec{v}(x)|_e^{\mathrm{Extr}} \approx v_e^{\mathrm{no}} e^{\mathrm{dual}} = (v_e^{\mathrm{no}} d_e)\vec{n}_e \ . \tag{3.54}$$

In our derivation of the weights, the directions of the edges described by $\vec{t}_{e'}$ and $\vec{n}_e$ are only important for the magnitude of the extrusion, as only the extrusion contributes to the Coriolis acceleration along e. The different influence of the direction of every single edge e is taken into account by the weights (cf. calculation in Eq. (3.68)). Based on this knowledge, we can reformulate Eq. (3.43) by associating $\vec{v}$ as extruding velocity field, i.e. $\vec{v} = \vec{v}(x)|_e^{\mathrm{Extr}}$, and projecting it onto the normal edge direction $\vec{n}_e$ in the following way:

$$(v_e^{\mathrm{no}} d_e)\vec{n}_e \cdot \vec{n}_e = \sum_{n \in \mathcal{N}} \sum_{e' \in \mathcal{E}} \lambda^n(x) \mathbf{G}_{e'}^n \mathrm{w}_{ee'} \vec{n}_e \cdot \vec{t}_{e'} (v_{e'}^{\mathrm{tg}} l_{e'}) \ . \tag{3.55}$$

With the coefficients of Eq. (3.46) we substitute here $\lambda^n(x)\mathbf{G}_{e'}^n \mathrm{w}_{ee'} \vec{n}_e \cdot \vec{t}_{e'}$ by $w_{ee'}^n$. The normal vector reconstruction to edge e' using all edges adjacent to the vertices of edge e can be calculated with

$$v_e^{\mathrm{no}} d_e = \sum_{n \in \mathcal{N}, e' \in E(n(e))} w_{ee'}^n v_{e'}^{\mathrm{tg}} l_{e'} \ , \tag{3.56}$$

where $E(n(e))$ stands for the set of all edges that are connected to the two nodes $n(e)$. Such reconstruction has already been suggested in the literature, for instance by Arakawa and Lamb [3] or more recently by Thuburn [101]. This is of advantage for our investigation, as we intend to compare it later with the method for arbitrarily-structured C-grids developed by Thuburn and Ringler et al. [89, 102].

The extrusion caused by v_e^{no} is a weighted linear combination of extrusions caused by the edge velocities adjacent to edge e. Therefore, the weights are derived by the influence that the different edges have on the extrusion and thus on the acceleration represented by the interior product $\mathbf{i}_{\vec{u}} \approx \mathbf{I}(\vec{u}, \cdot)$.

In the following we show that the normal vector reconstruction of Eq. (3.56) is indeed a reasonable choice. In addition, we find an additional constraint to be imposed onto the weights for the sake of stability.

Stability requirements for the normal vector reconstruction: The weights $w^n_{ee'}$ for the normal vector reconstruction of Eq. (3.56) have to be such that the model is stable. Analogously to Eq. (3.22), we investigate stability by investigating the eigenvalues of the system matrix $\mathbf{A} + \mathbf{F}$ and its properties concerning skew-symmetry.

With respect to the normal vector reconstruction of Eq. (3.56), the *extended Coriolis matrix* at a single vertex n is given by

$$F_n^{\mathrm{extend}} = \begin{bmatrix} 0 & \frac{l_{e_2}}{d_{e_1}} w^n_{e_1 e_2} & \frac{l_{e_3}}{d_{e_1}} w^n_{e_1 e_3} & \dots \\ \frac{l_{e_1}}{d_{e_2}} w^n_{e_2 e_1} & 0 & \frac{l_{e_3}}{d_{e_2}} w^n_{e_2 e_3} & \dots \\ \frac{l_{e_1}}{d_{e_3}} w^n_{e_3 e_1} & \frac{l_{e_2}}{d_{e_3}} w^n_{e_3 e_2} & 0 & \dots \\ \dots & \dots & \dots & 0 \end{bmatrix} , \tag{3.57}$$

where the five edges $e_i, i = 2, ..., 6$, are connected to edge e_1 via vertex $n = 1$ (cf. Fig. 3.9). Analogously to the derivation of the weights of Eq. (3.26), the weights $w^n_{ee'}$ have to be chosen such that the matrix $\mathbf{DF}^{\mathrm{extend}}$ is skew-symmetric, where $\mathbf{F}^{\mathrm{extend}}$ denotes the extended Coriolis matrix including all vertices. Thus, the following equations

$$H d_{e_i} l_{e_i} \frac{l_{e_j}}{d_{e_i}} w^n_{e_i e_j} = -H d_{e_j} l_{e_j} \frac{l_{e_i}}{d_{e_j}} w^n_{e_j e_i} \tag{3.58}$$

have to hold for all e_i, e_j and for all vertices n. Therefore, the weights have to satisfy the antisymmetric condition

$$\forall e_i, e_j \in E(n): \quad w^n_{e_i e_j} = -w^n_{e_j e_i} , \quad w^n_{e_i e_i} = 0 . \tag{3.59}$$

If the weights $w^n_{e_i e_j}$ fulfill these requirements, the model is stable. These weights have no unit, as we can infer from Eq. (3.58). Thus, even on non-uniform grids, antisymmetric weights ensure stability, which justifies *a posteriori* the ansatz for the normal vector reconstruction of Eq. (3.56).

3.3.3 Determine the weights for a uniform hexagonal mesh

As an example, we derive the weights (3.46) for a uniform hexagonal mesh. We regard, for instance, edge e_2 as edge that extrudes e_1, and we denote such edge as *extruding edge*. Let the tangential velocity be $v^{\mathrm{tg}}_{e_2}$, the extruding velocity is thus $v^{\mathrm{tg}}_{e_2} = \lambda^1_a(x) e_2$. During the time $t = 1$ the edge e is extruded to the area that coincides with the triangle a. By

Eq. (3.46) and with the representation of the interior product on the mesh by Eqn. (3.51) and (3.52) we find the weight

$$w_{12}^1 = \frac{1}{c_{\text{norm}}^1}\mathrm{I}(e_1, \lambda^1 e_2, a)\mathbf{G}_{e_2}^1 = \frac{1}{c_{\text{norm}}^1}\mathbf{R}_a^{e_1}\mathbf{G}_{e_2}^1 = \frac{1}{c_{\text{norm}}^1} \ , \tag{3.60}$$

because $\mathbf{R}_a^{e_1}\mathbf{G}_{e_2}^1 = 1 \cdot 1$, as shown in Eq. (2.54) of Chapter 2. The extruding edge e_3 contributes to the extrusion by Eq. (3.53) with the weight

$$w_{13}^1 = \frac{1}{c_{\text{norm}}^1}\mathrm{I}(e_1, \lambda^1 e_3, a)\mathbf{G}_{e_3}^1 = \frac{1}{c_{\text{norm}}^1}\lambda_a^1(y)\mathbf{R}_a^{e_1}\mathbf{G}_{e_3}^1 = \frac{-1}{2}\frac{1}{c_{\text{norm}}^1} \ , \tag{3.61}$$

with $\mathbf{R}_a^{e_1}\mathbf{G}_{e_3}^1 = 1 \cdot (-1) = -1$ and where y denotes the intersection point of the third edge of the degenerated triangle – spanned by e_1, e_3 – with edge e_2 (cf. Fig. 3.9). On a regular grid it follows $\lambda_a^1(y) = \frac{1}{2}$. Edge e_4 leads to a one-dimensional extruded area of e_1. Thus, a projection onto a two-dimensional area gives zero leading to

$$w_{14}^1 = 0 \ . \tag{3.62}$$

The extrusion of e by edge e_5 differs from that caused by e_3 only in the sense that e is extruded now over triangle b instead of a. This leads to the weight

$$w_{15}^1 = \frac{1}{c_{\text{norm}}^1}\mathrm{I}(e_1, \lambda^1 e_5, b)\mathbf{G}_{e_5}^1 = \frac{1}{c_{\text{norm}}^1}\lambda_b^1(y)\mathbf{R}_b^{e_1}\mathbf{G}_{e_5}^1 = \frac{1}{2}\frac{1}{c_{\text{norm}}^1} \ , \tag{3.63}$$

with $\mathbf{R}_b^{e_1}\mathbf{G}_{e_5}^1 = (-1) \cdot (-1)$. The extrusion caused by edge e_6 corresponds to edge e_2 and we find

$$w_{16}^1 = \frac{1}{c_{\text{norm}}^1}\mathrm{I}(e_1, \lambda^1 e_6, b)\mathbf{G}_{e_6}^1 = \frac{1}{c_{\text{norm}}^1}\mathbf{R}_b^{e_1}\mathbf{G}_{e_6}^1 = \frac{-1}{c_{\text{norm}}^1} \ , \tag{3.64}$$

with $\mathbf{R}_b^{e_1}\mathbf{G}_{e_6}^1 = (-1) \cdot 1$. The normalizing constant can be calculated with definition (3.47):

$$c_{\text{norm}}^1 = \mathrm{I}(e_1, \lambda^1 e_2, a) + \mathrm{I}(e_1, \lambda^1 e_3, a) + \mathrm{I}(e_1, \lambda^1 e_5, b) + \mathrm{I}(e_1, \lambda^1 e_6, b) = 1 + \frac{1}{2} + \frac{1}{2} + 1 = 3 \ , \tag{3.65}$$

which leads to the weights for node $n = 1$:

$$w_{11}^1 = 0, \ w_{12}^1 = \frac{1}{3}, \ w_{13}^1 = -\frac{1}{6}, \ w_{14}^1 = 0, \ w_{15}^1 = \frac{1}{6}, \ w_{16}^1 = -\frac{1}{3} \ . \tag{3.66}$$

Based on the definition of $\mathrm{I}(e, e', c)$ and of the coincident matrices, these weights change sign when permuting the edges e with e'. This is in agreement with the requirement of antisymmetry of the weights $w_{ee'}^n = -w_{e'e}^n$ of Eq. (3.59) in order to obtain stability. A permutation of the edges for weights w_{13}^1 or w_{15}^1 requires a change of the related triangle on which we project the extruded manifold. On regular grids the cells are equal, which guarantees the antisymmetric property. On non-uniform grid, this is in general not fulfilled. The study on how to modify our approach to guarantee antisymmetric weights also on non-uniform grids has to be postponed to future work.

Is the normal vector reconstruction based on extrusion consistent? On the basis of the weights (3.66) for uniform hexagonal grids, we investigate whether the normal vector reconstruction of Eq. (3.56) does properly represents the extrusion and with this also the tangential acceleration along e cause by the Coriolis term.

Let us assume, analogously to the derivation of the weights for the tangential velocities, $v_{e_2}^{\text{tg}} = \frac{l_{e_2}}{t}$ with $t = 1$ and $v_{e_j}^{\text{tg}} = 0 \forall j \neq 2$. According to Eq. (3.56) and to the weights defined

in Eq. (3.46), we find for the normal velocity component at edge midpoint for a uniform mesh:

$$v_{e_1}^{\mathrm{no}} = \frac{1}{3}\frac{l_{e_2}}{d_{e_1}} v_{e_2}^{\mathrm{tg}} \ , \tag{3.67}$$

using $w_{e_1e_2} = 1/3$ of Eq. (3.66). To check consistency of Eq. (3.67), we assume, analogously to $v_{e_2}^{\mathrm{tg}} = \frac{l_{e_2}}{t}$, that $v_{e_1}^{\mathrm{no}} = \frac{d_{e_1}}{2t}$, i.e. during $t = 1$ the normal component $v_{e_1}^{\mathrm{no}}$ extrudes e_1 along that part of the dual edge e_1^{dual} (in direction of $\vec{n}_{e_1}$) that lies within triangle a. Under this assumption, where $e_1^{\mathrm{dual}}/2 = \vec{n}_{e_1} d_{e_1}/2 = \vec{n}_{e_1} v_{e_1}^{\mathrm{no}} \cdot t$, while using Eq. (3.67), it follows for the area of the extruded manifold:

$$\begin{aligned}
\mathrm{I}(e_1, \frac{e_1^{\mathrm{dual}}}{2}, a)|_{n=1} &= \mathrm{I}(e_1, \vec{n}_{e_1} v_{e_1}^{\mathrm{no}} \cdot t, a) = \frac{1}{3}\mathrm{I}(e_1, \vec{n}_{e_1} \vec{t}_{e_2} \underbrace{\vec{t}_{e_2} \frac{l_{e_2}}{d_{e_1}}}_{=2\vec{n}_{e_1}} v_{e_2}^{\mathrm{tg}} \cdot t, a) \\
&= \frac{1}{3}\mathrm{I}(e_1, 2 \underbrace{\vec{n}_{e_1}\vec{n}_{e_1}}_{=1} \vec{t}_{e_2} \underbrace{v_{e_2}^{\mathrm{tg}} \cdot t}_{=l_{e_2}}, a) = \frac{2}{3}\mathrm{I}(e_1, \vec{t}_{e_2} l_{e_2}, a) = \frac{2}{3}\mathrm{I}(e_1, e_2, a) = \frac{2}{3} \ ,
\end{aligned} \tag{3.68}$$

with $\mathrm{I}(e_1, e_2, a) = 1$ of Eq. (3.51). Hereby, the identity $\vec{n}_{e_1} = \cos(30°)\vec{t}_{e_2} = \frac{1}{2}\frac{l_{e_2}}{d_{e_1}}\vec{t}_{e_2}$ describes the projection of the tangential unity vector $\vec{t}_{e_2}$ of edge e_2 onto the normal direction $\vec{n}_{e_1}$ of edge e_1. On the other hand, for $t = 1$ the normal component $v_{e_1}^{\mathrm{no}} = \frac{d_{e_1}}{2t}$ leads to an area of extruded manifold:

$$\mathrm{I}(e_1, \frac{e_1^{\mathrm{dual}}}{2}, a)|_{n=1} = \mathrm{I}(l_{e_1}\vec{t}_{e_1}, \frac{d_{e_1}}{2}\vec{n}_{e_1}, a) = \underbrace{l_{e_1} \cdot \frac{d_{e_1}}{2}}_{2\cdot 1/3} = \frac{2}{3} \ , \tag{3.69}$$

which is a fraction of the area spanned by e_1 and e_1^{dual} that lies within triangle a. As the areas of the extruded manifolds caused directly by $v_{e_1}^{\mathrm{no}} = \frac{d_{e_1}}{2t}$ or via Eq. (3.67) by $v_{e_2}^{\mathrm{tg}} = \frac{l_{e_2}}{t}$ agree, we conclude that Eq. (3.67) consistently describes the normal velocity component by the tangential one.

On a uniform grid the relation $\vec{n}_e = \frac{1}{2}\frac{l_{e'}}{d_e}\vec{t}_{e'}$ is valid for all edges e' that contribute to the normal velocity component of e (in our example e_3, e_5). Thus, for every term in the normal vector reconstruction of Eq. (3.56) the above calculation can be repeated. Using $|w_{e_1e_3}| = |w_{e_1e_5}| = 1/6$, the area of the extruded manifold caused by either e_3 or e_5 is only half the size of $\mathrm{I}(e_1, e_2, a)$. This reflects the fact that the influences of edge e_3 and e_5 have to be weighted, according to Eq. (3.52), by the barycentric coordinate with $\lambda^1(y) = 1/2$. This shows, by linearity, that the weights determined by extrusion reflect reasonably the influence of every single edge to the total extrusion. In agreement with Eq. (3.56), the calculation in Eq. (3.68) shows that the edges' contribution to the total extrusion determines the weights. The edges' direction is hereby included in the ability of the edge to contribute to the extrusion. Consequently, the ansatz in Eq. (3.56) is justified.

In case of a uniform grid, the weights of Eq. (3.59) equal those derived in Thuburn et al. [102]. Thereby, the authors derived a normal vector reconstruction for arbitrarily-structured C-grids by using the two-dimensional vorticity equations, while requiring the geostrophic modes to be stationary. In our approach, we do not put a similar constraint on the equations. Besides the condition on stability (antisymmetric weights), our derivation for a normal vector reconstruction relies on a geometrically adequate representation of the extrusion (and alongside of the Coriolis term). In the following numerical tests we show that such derivation leads to a stable and consistent model with adequate representation of the geostrophic balance.

3.3.4 Numerical results for the normal vector reconstruction based on extrusion

For the hexagonal model with C-grid staggering and for the normal vector reconstruction of Eq. (3.56) we perform numerical tests on consistency, stability and on whether the model maintains geostrophic balance. We repeat the numerical experiments of Sect. 3.2.4 for the new normal vector reconstruction scheme based on extrusion.

On uniform grids, our normal vector reconstruction based on extrusion coincides with the one introduced by Thuburn et al. [101]. For non-uniform grids we rely on the method proposed by Thuburn et al. [102], in which the authors obtained a stable model with stationary geostrophic modes. Therefore, we include in the following tests on consistency and stability for the non-uniform grids shown below in Fig. 3.13 also Thuburn's vector reconstruction.

Consistency: We compare the analytic vector field $\vec{v}|_e$ given in Eq. (3.30) with the numerical solution $\vec{v}_e^{\text{Rec}}$ obtained by projecting the analytic vector field to the tangential direction of the edges and use the vector reconstruction of Eq. (3.56) to find the normal vector values. The truncation error is given by $\tau_e^{\text{Rec}} = \vec{v}_e^{\text{Rec}} - \vec{v}|_e$, analogously to Eq. (3.31).

Figure 3.10 illustrates for both uniform and non-uniform grids the convergence behavior of the truncation error with increasing resolution. For the uniform grid the scheme shows second order convergence. In case of non-uniform grids, the accuracy is almost second order for coarser grids up to 64^2 cells, but decreases with increasing grid resolution. This may be caused by strong stretching of the cells occurring in the grid adaption process, in which some hexagons are almost deformed toward quadrangles (cf. Chapter 4). This leads to a reduction in accuracy, in particular in the L_∞ norm.

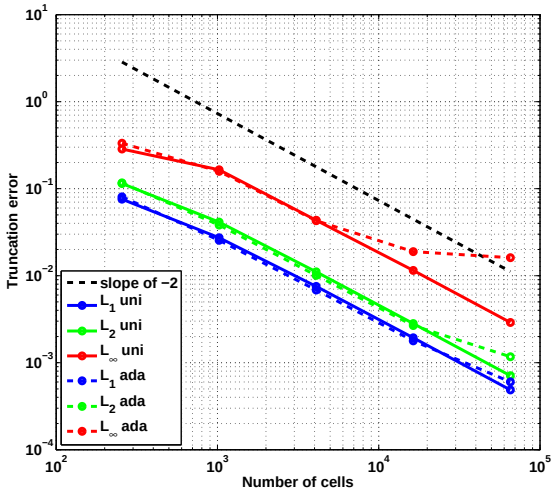

Figure 3.10: Truncation errors in the L_1, L_2, L_∞-norm of the normal vector reconstruction for uniform grids (solid) and for non-uniform grids (Thuburn's method) similar to meshes in Fig. 3.13 (dashed lines).

Stability: The system matrix $\mathbf{F}^{\text{extend}}$ of Eq. (3.57) has to be skew-symmetric. This can only be guaranteed if the weights $w_{ee'}$ satisfy the antisymmetric condition of Eq. (3.59). Our method on a uniform grid fulfills this requirement per construction. The same is

true for the method of Thuburn et al. [102] for both uniform and non-uniform grids. For both grid types, we determine the eigenvalues λ of the system matrix $\mathbf{A} + \mathbf{F}$ using the eigenvalue function of MATLAB. Figure 3.11 shows the results for the eigenvalue analysis for uniform grids (left panel) and non-uniform grids (right panel). For both cases, the real part of the eigenvalues is smaller then real$\lambda < 10^{-11}$. Consequently, the normal vector reconstruction scheme is stable for uniform and non-uniform grids (Thuburn's method), because it shows no growing or decreasing energy modes that cause instabilities.

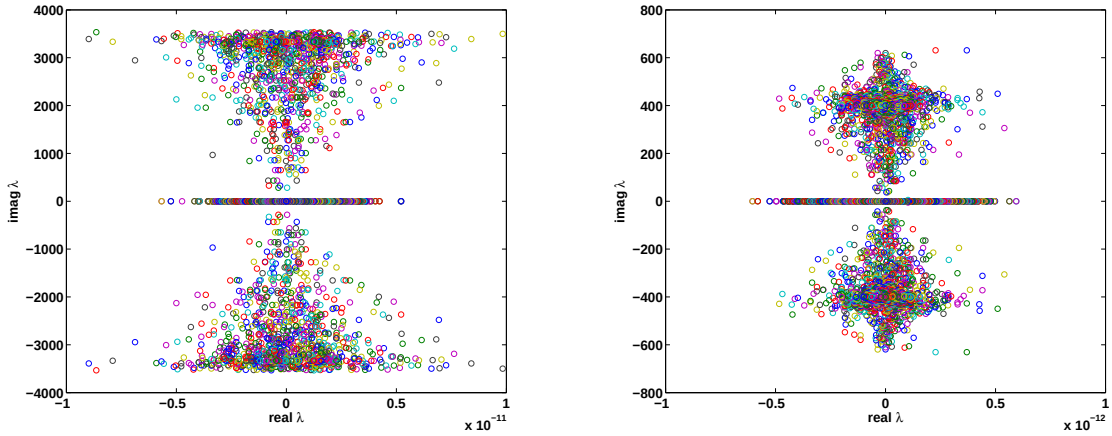

Figure 3.11: Eigenvalues λ of the propagation matrix $\mathbf{S}$ using the normal vector reconstruction for 32^2 grid cells on a uniform grid (left-panel) and on non-uniform grids (Thuburn's method) (right panel).

Test on geostrophic balance: We perform the test case introduced in Sect. 3.2.4 for our normal vector reconstruction scheme based on extrusion to investigate whether the model maintains geostrophic balance. On a uniform grid with 32^2 cells, the vortex distribution shown in Fig. 3.6 should not change during the model integrations. Figure 3.12 shows the results after a model integration of 60 days. The vortex pair remains in balance and no spurious geostrophic modes appear. Our new methods properly represent the Coriolis term on a hexagonal mesh, without the growth of spurious geostrophic modes. This is in contrast to the normal RT0 vector reconstruction scheme (3.19), for which after 10 days the spurious modes are strongly developed (cf. Fig. 3.7 C and D). As in case of the triangular model, the linearized continuity equation leads also in case of the hexagonal model to a decrease in the negative surface elevation of comparable magnitude to the height field shown in Fig. 3.7 A.

Wave representation on hexagonal meshes: The agreement of our scheme for normal vector reconstruction based on extrusion with the one proposed by Thuburn [101] for uniform hexagonal C-grids underpins our approach of using geometrical constraints for vector reconstruction. In addition, we instantly know the wave dispersion relation from investigations in literature. The wave frequencies of the linear shallow-water equations for geostrophic mode ν_{gst} and gravity-inertia modes ν_{gi} are given in Eq. (3.38). Thuburn [101] and more recently Gassmann [43] studied the wave properties, in particular the wave frequencies of geostrophic and gravity-inertia modes for the above discussed hexagonal C-grid discretization of the shallow-water equations on a uniform mesh. They found that this hexagonal C-grid scheme accurately represents the gravity-inertia frequencies of Eq. (3.38)

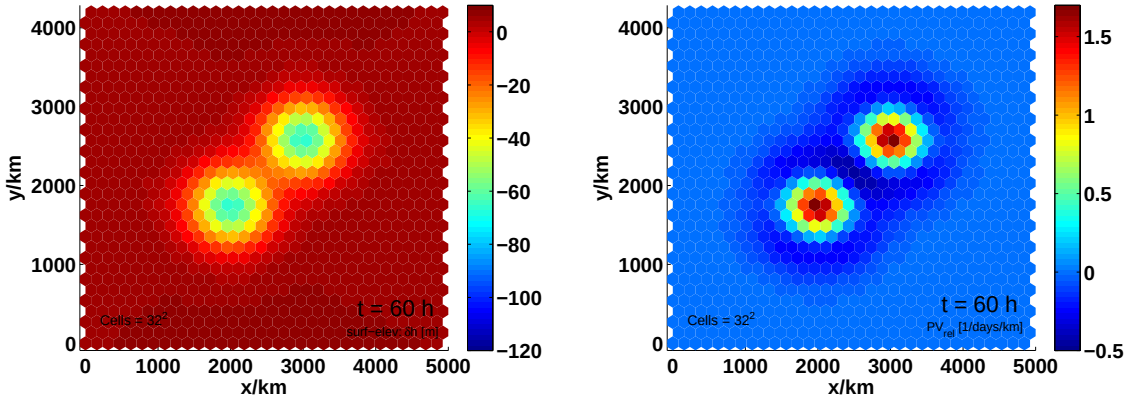

Figure 3.12: Geostrophic balance test case: surface elevation [m] (left) and potential vorticity [1/day/km] (right) after an integration of 60 days using the normal vector reconstruction based on extrusion on uniform grids with 32^2 cells.

in the discrete case. Moreover, this scheme properly represents the geostrophic modes, i.e. $\nu_{gst} \approx 0$. Therefore, no spurious non-zero frequencies for the geostrophic modes occur, unlike the case shown in Fig. 3.7, where the usage of the normal RT0 reconstruction of Eq. (3.19) for a hexagonal C-grid leads to geostrophic modes with non-zero frequencies.

Generalization to non-uniform grids: A generalization for normal vector reconstruction on arbitrarily-structured C-grids has been proposed by Thuburn et al. [102], in which the authors could achieve a stable model with stationary geostrophic modes. Hereby, the weights for vector reconstruction have to be antisymmetric with exchange of the contributing edges also for the non-uniform meshes. This property is shared for uniform meshes also by our approach, as the eigenvalue analysis, shown in Fig. 3.11 (left), of the system matrix Eq. (3.57) confirms. It seems thus possible to generalize our geometrical approach of vector reconstructions also toward non-uniform hexagonal grids. However, as we could not yet succeed in a consistent derivation, we use for the remainder of the thesis the normal vector reconstruction introduced by Thuburn et al. [102] for arbitrarily-structured C-grids. Its consistency and stability properties have been tested already in Fig. 3.10 and Fig. 3.11 (right), respectively.

3.4 The rotating nonlinear shallow-water equations

For the investigation of nonlinear phenomena, for instance, the interaction of tropical cyclones (TCs), also the nonlinear parts of the equations have to be taken into account. The linear parts have already been studied in the previous sections for a hexagonal C-grid model. They ensure a stable and consistent scheme on uniform and non-uniform meshes. Because the linear parts coincide with those used by Ringler et al. [89], we use the therein proposed discretization methods for the nonlinear terms to extend our linear shallow-water model toward a nonlinear hexagonal C-grid shallow-water model for uniform and non-uniform grids. In order to test our implemented scheme concerning consistency, stability, and geostrophic balance, we perform runs for nonlinear test cases.

3.4.1 The nonlinear equations in invariant form

Based on the derivations in Chapter 2, we can write the rotating nonlinear shallow-water equations in invariant form according to Theorem (2.4.1) as

$$\int_c \partial_t u + \int_c \mathbf{i}_{\vec{v}}(\mathbf{d}u + f_C) + \int_c \frac{1}{2}\mathbf{d}\mathbf{i}_{\vec{v}}u + \int_c g\mathbf{d}h = 0 \ , \qquad \int_V \partial_t \tilde{h} + \int_{\partial V} \widetilde{(hu)} = 0 \ , \quad (3.70)$$

in which h instead of ρ has been used to describe the variation of the water height. c and V denote arbitrary curves or volumes on the manifold $\mathcal{M}$, respectively. To close the system of equations, we include the metric equations:

$$\star(hu) = \widetilde{(hu)} \ , \qquad \star h = \tilde{h} \ , \qquad u = \vec{v}^{\flat} \ , \quad (3.71)$$

(cf. Chapter 2 for notation). This general set of equations leads to different discrete schemes dependent on the choice of topological meshes and metric equations.

Based on our method of discretization by integration over chains and cochains, we have already discretized the linear parts in Chapter 2. We investigated a hexagonal C-grid scheme, with circumcenters as dual vertices. With the definitions introduced in Chapter 2 and previously in this chapter, we write the discrete nonlinear shallow-water equations as

$$\partial_t \mathbf{u} + \mathbf{I}(\vec{u}, \mathbf{R}\mathbf{u} + f) + \mathbf{G}\,\mathbf{k} + g\mathbf{G}\,\mathbf{h} = 0 \ , \qquad \partial_t \tilde{\mathbf{h}} + \mathbf{D}^{\mathrm{dual}}\widetilde{(\mathbf{hu})} = 0 \ , \quad (3.72)$$

$$\star_0 \mathbf{h} = \tilde{\mathbf{h}} \ , \quad \star_1(\mathbf{hu}) = \widetilde{(\mathbf{hu})} \ , \quad (3.73)$$

where the nonlinear parts are defined in the following. As previously, $\mathbf{u} = \{u_{e_i}, i = 1, \ldots, |K^e|\}$ with $u_e = \int_e u$ is an array for the velocities at the edges and $\tilde{\mathbf{h}} = \{\tilde{h}_{f_i}, i = 1, \ldots, |K^f|\}$, with $\tilde{h}_f = \int_f \tilde{h}$ and the two-form $\tilde{h}$, is an array for the heights that are averaged over the hexagonal cells f. With $\mathbf{h} = \{h_{v_i}, i = 1, ..., |K^v|\}$ for the heights at v, there follows $\mathbf{G}\,\mathbf{h} \approx \int_e \mathbf{d}h$. The coincident matrices $\mathbf{G}, \mathbf{R}, \mathbf{D}^{\mathrm{dual}}$ (cf. Chapter 2) are discrete analogs of the gradient, curl and divergence operators, respectively.

In the following, only the nonlinear terms in the equations are discussed. $\mathbf{I}(\vec{u}, \mathbf{R}\mathbf{u}+f) \approx \int_e \mathbf{i}_{\vec{u}}\mathbf{d}(u + f_C)$ is the discrete absolute vorticity and $\mathbf{G}\,\mathbf{k} \approx \int_e \frac{1}{2}\mathbf{d}\mathbf{i}_{\vec{u}}u$ is the gradient of the discrete kinetic energy $\mathbf{k} \approx \frac{1}{2}\mathbf{i}_{\vec{u}}\mathrm{u}$. With $\mathbf{D}^{\mathbf{dual}}\widetilde{(\mathbf{hu})} \approx \int_f \mathbf{d}\widetilde{(hu)}$, where $\widetilde{(hu)}$ is a one-form, we approximate the divergence of the mass-flux over cell f by the sum of averaged mass-fluxes over the boundary ∂f.

The discretization of the mass-flux one-form $\widetilde{(hu)}$ is done by averaging the heights h_v to the edge midpoints, i.e. $\overline{h}_{e_i} := 1/2h_{v_1} + 1/2h_{v_2}$ for $v_1, v_2 \in \partial e_i$. Then, the diagonal Hodge-star operator $\star_1$ of (2.55) can be applied to obtain a circumcenter scheme and, according to Eq. (2.66), we result in the following discrete continuity equation:

$$\partial_t h_v + \underbrace{\frac{1}{A_f}\sum_{i=1}^{\#\mathrm{edges}} (\pm) d_{e_i}\overline{h}_{e_i}\overline{u}_{e_i}}_{=\mathrm{div}_v(\overline{h}_e\overline{u}_e)} = 0 \ , \quad (3.74)$$

with $\overline{u}_e = \frac{u_e}{l_e}$ of Eq. (2.62). The signs $\pm$ are determined by the discrete exterior derivative $\mathbf{D}^{\mathbf{dual}}$ of Eq. (2.52) and describe the orientations of edges e with respect to vertices v.

The absolute vorticity $\eta = \vec{k} \cdot \nabla \times \vec{v} + f$ can be discretized at triangle cell centers cc by using the operator curl_{cc} (cf. Eq. (2.70)). Furthermore, the DoF for the height field h_v are averaged with area weighting to the triangle cell centers. Thus, the potential vorticity $q_{cc} = \frac{\eta_{cc}}{h_{cc}}$ is positioned at triangular cell centers. In addition, the thickness flux $F_e = \overline{h_e}\overline{u}_e$

is calculated at edge midpoints. According to Ringler et al. [89], the nonlinear Coriolis term in the energy conserving form for a single edge e is given by

$$\mathbf{I}(\vec{u}, \mathbf{Ru} + f)_e = \frac{1}{l_e}\Big[\sum_{e' \in EVP(e)} w_{ee'} d_{e'} F_{e'} \Big(\frac{\tilde{q}_e + \tilde{q}_{e'}}{2} \Big) \Big] \ , \tag{3.75}$$

where d_e is the hexagonal and l_e the triangular edge length and $EVP(e)$ is the set of all edges e' which are connected to the pair of vertices of edge e and $\tilde{q}_e = \frac{1}{2} \sum_{cc \in CE(e)} q_{cc}$, where $CE(e)$ is the pair of triangle cells that share edge e. The weights $w_{ee'}$ are derived in Thuburn et al. [102] for arbitrarily-structured C-grids and coincide with the weights derived in Eq. (3.66) for uniform meshes.

For the term $\mathbf{G}\,\mathbf{k}$, the discrete kinetic energy $\mathbf{k} \approx \frac{1}{2}\mathbf{i}_{\vec{u}}\mathrm{u}$ can be represented by

$$\mathbf{k} = \frac{1}{A_v} \sum_{e \in EV(v)} \frac{1}{4} A_e \cdot (\overline{u}_e)^2 \ , \tag{3.76}$$

where $EV(v)$ is the set of edges meeting at vertex v, A_v is the hexagonal cell area and $A_e = d_e l_e$ is the area related to edge e (cf. [89]).

An analysis of the convergence properties of this schemes by Ringler et al. [89, 88] reveals second order accuracy on uniform and almost second order accuracy on non-uniform grids, where the shape and size of the grid cells varies only slightly.

To represent the viscosity term, required in the next chapter, we apply the discrete differential operators defined in Eq. (2.62), Eq. (2.66) and Eq. (2.70). We assume for almost all experiments in this thesis a background fluid depth $H = 10\,\mathrm{km}$ leading to small variations of the total depth h. In our model setup, we represented the viscosity term by

$$\begin{aligned} \frac{1}{h}\nu\nabla \cdot (h\nabla\vec{v}) &\approx \nu\nabla \cdot (\nabla\vec{v}) = \nabla(\nabla\vec{v}) - \nabla \times \nabla \times \vec{v} \\ &\approx \mathrm{grad^n}_e \cdot \mathrm{curl}_{cc}(\overline{u}_e) + \mathrm{grad^t}_e \cdot \mathrm{div}_v(\overline{u}_e) \end{aligned} \tag{3.77}$$

where the parameter ν describes the viscosity of the fluid.

3.4.2 Numerical results

On the basis of numerical tests that we perform in the following on the nonlinear rotating shallow-water model, we study whether our model setup performs properly in terms of conservation properties. We investigate cases, in which the non-uniform grids, constructed with the adaptation method introduced in Chapter 4 (grid parameters: $\gamma = 4$, $d = 550\,\mathrm{km}$, $b = 1\%$), are strongly deformed in the sense that a significant amount of the originally hexagonal cells is almost degenerated to quadrangles. We want to assure that the model remains stable also in case of strongly deformed grids. In the following we perform the model integrations on both uniform and non-uniform grids similar to the ones of Fig. 3.13.

Geostrophic balance and conservation properties

In order to investigate the model performance with respect to geostrophic balance, we introduce a test case where one vortex core positioned at the domain center is initialized such that it is in geostrophic balance. When integrating over long time periods with the nonlinear model, the shape of the vortex core should remain in balance even in the case when nonlinear effects are present. A second test case considers two vorticity cores, in which the nonlinear effect will lead to a movement of the two vortices into opposite directions (see nonlinear test cases below).

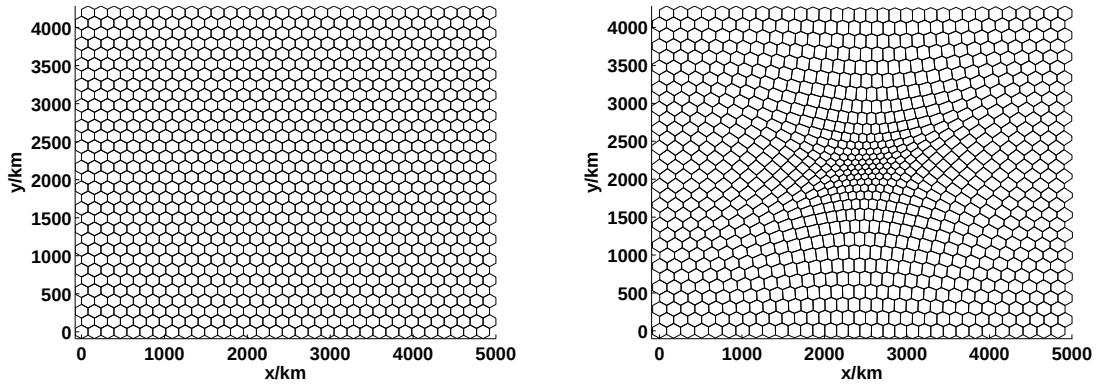

Figure 3.13: Illustration of the computational uniform (left) and non-uniform (right) meshes on a domain of 5000 km $\times$ 4330 km for 32^2 grid cells.

For the experiment of a single vortex core positioned in the center of the domain, we initialize the height field according to Eq. (3.33) on a double periodic f-plane with 5000 km $\times$ 4330 km, where we set $o = 0$ to omit the terms for the second vortex. For the height we set $H = 10\,\text{km}$ and $H' = 75\,\text{m}$. Analogously to Sect. 3.2.4 we initialize the velocity distribution by imposing the geostrophic balance and determine the relative potential vorticity $PV_{\text{rel}} := q - f/h = |\nabla \times \vec{v}|/h$, with Coriolis parameter $f = 6.147 \cdot 10^{-5} s^{-1}$, which corresponds to a latitude of 25°. In order to guarantee nonlinear balance we recalculate the surface elevation $h - H$ with the nonlinear balance equation (4.19). The initial surface elevation $h - H$ and the relative potential vorticity are illustrated in Figure 3.14 A and D, respectively. We perform model integrations of 100 days on uniform and non-uniform grids that are similar to those illustrated in Fig. 3.13, but use 64^2 grid cells.

Figure 3.14 illustrates the results for the model integration on uniform (B and E) and non-uniform grids (C and F). After a model integration of 100 days on a uniform mesh, the surface elevation (B) and the potential vorticity distribution (E) are relatively similar to the initial conditions. The expected conservation of the geostrophic balance is very well met. However, for the non-uniform mesh (C and F), the strongly stretched cells influences the results significantly. As the vortex is partly positioned in regions where the grid is strongly stretched, containing cells with varying sizes, the initial PV_{rel} distribution is strongly smeared out over the whole domain after an integration of 100 days. The negative surface evaluation does not stay within the domain center, it even crosses the periodic domain boundary during the integration time. The irregularly deformed cells lead to an effective acceleration of the vortex core away from the center. However, the model remains stable and, for shorter integration times of up to 40 days, the balance is sufficiently well maintained, as we can infer from the energy and enstrophy properties.

We diagnose the *energy* according to

$$E = 1/2 \int_{\Omega} (h|\vec{v}|^2 + gh) d\mathbf{x} \ . \tag{3.78}$$

Based on the definition of the *absolute potential vorticity*, with $PV = (\nabla \times \vec{v} + f)/h$, we can define the *potential enstrophy* as

$$\epsilon = 1/2 \int_{\Omega} h(PV)^2 d\mathbf{x} \ . \tag{3.79}$$

Analytically, the quantities E, PV, ϵ are conserved in shallow-water equations. Our numerical scheme should thus conserve the discrete analogs of these conservative quantities.

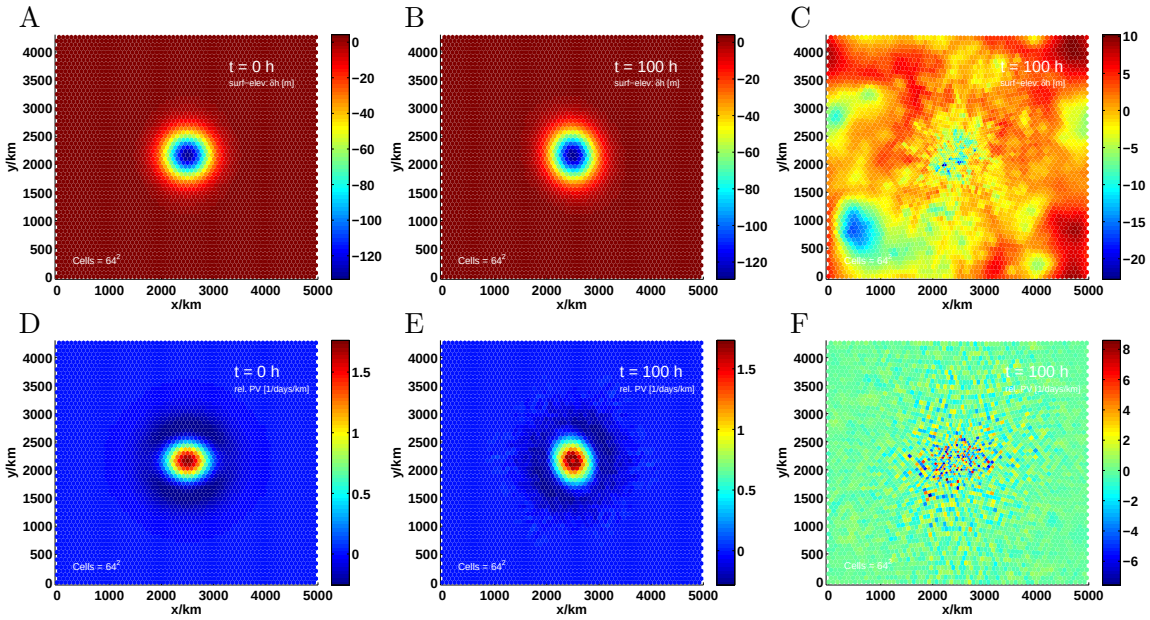

Figure 3.14: Test case for geostrophic balance. (A and D): initial surface elevation [m] $h - H$ and relative potential vorticity [1/days/km], respectively. Surface elevation and relative potential vorticity calculated on the uniform grid (B and D, respectively) and on the non-uniform grid (C and F, respectively) with 64^2 cells similar to those in Fig. 3.13.

We evaluate the solution concerning relative error in total energy, $(E - E_0)/E_0$, relative error in potential enstrophy, $(\epsilon - \epsilon_0)/\epsilon_0$ and relative error in relative potential vorticity $(PV - PV_0)/PV_0$.

Figure 3.15 illustrates the energy, potential enstrophy and potential vorticity evolution for an integration of 100 days for the uniform (upper row) and for the non-uniform grid (middle, lower row) with 64^2 cells similar to those in Fig. 3.13. For the uniform mesh (upper row), the relative energy decreases constantly with time. As we use a leap-frog scheme for time discretization, this loss in energy is mainly caused by the Asselin-filter needed to keep the time scheme stable, because this filter acts like a diffusion. However, the magnitude in energy loss is small, i.e. in the order of 10^{-8}. For the potential vorticity and potential enstrophy, the conservation properties are not as good as for the energy, but still in the order of 10^{-4} or 10^{-5} for the relative enstrophy error (middle column) and relative potential vorticity error (right column). For the non-uniform meshes (middle and lower rows) and during the first 40 days, the energy is quite well conserved within an error of about 10^{-8}. During that time, both potential enstrophy and potential vorticity are also quite well conserved. Figure 3.15 (lower row) shows the order of the relative error during the first 40 days for the non-uniform grid with a relative error of about 10^{-3} for ϵ and of 10^{-5} for PV_{rel}. Up to 40 days of integration, the vortex is properly represented on the mesh. Later, however, the vortex does not maintain in balance and is distributed over the entire domain, which may lead in a redistribution of energy of the large scale flow into small scales. This, in turn, may cause a drop in energy and an increase in potential enstrophy.

The results show that strongly deformed cells lying in the region where the vortex is positioned, can compromise on the long run the balanced flow (see more about a reasonable choice of r-adapted (non-uniform) grids in Chapter 4).

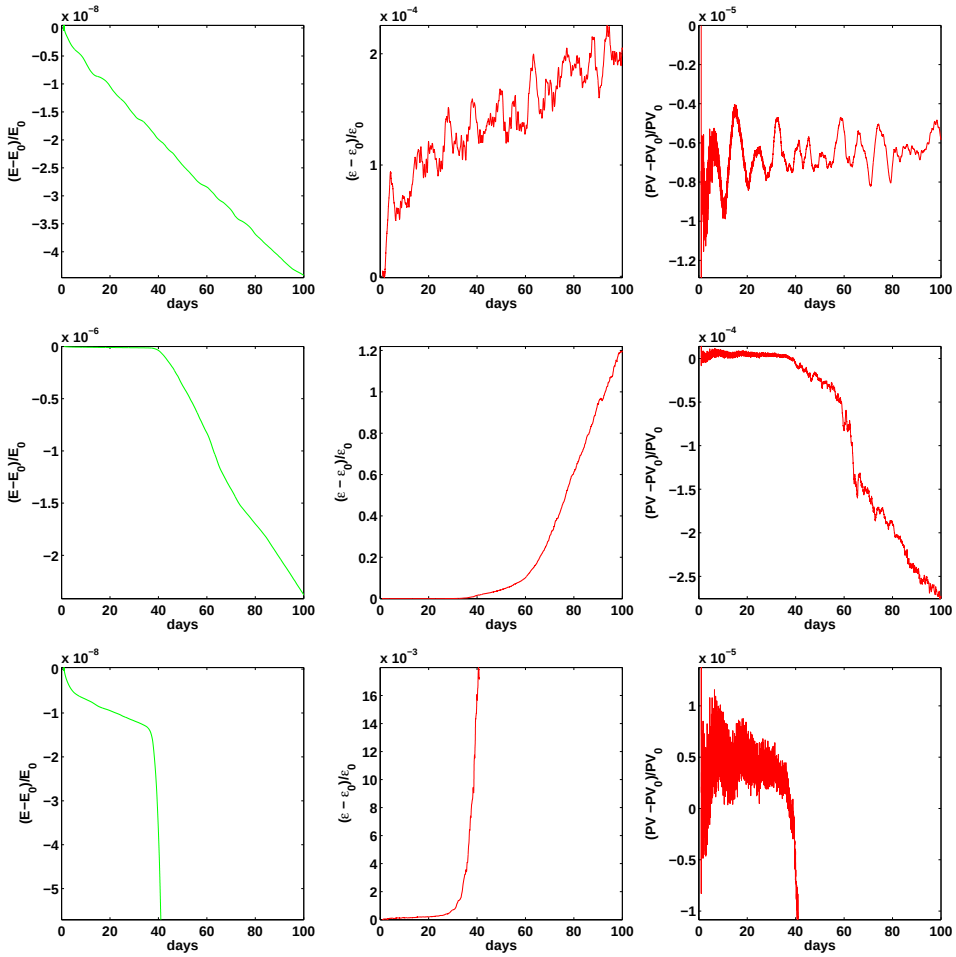

Figure 3.15: Relative errors in energy (left column), relative potential enstrophy (middle column) and potential vorticity (right column) for an integration of 100 days on the uniform hexagonal mesh (upper row) and the non-uniform hexagonal mesh (middle and lower rows) with 64^2 cells. The order of errors for the non-uniform mesh for the first 40 days of integration is shown in the lower row using modified y-axis scales.

Vortex pair interaction and shear flow evolution

For the test cases of vortex pair interaction and of shear flow evolution we compare our hexagonal C-grid shallow-water model with a version of the triangular C-grid model introduced in Giorgetta et al. [44] that uses the differential operators and the tangential RT0 vector reconstruction discussed in Chapter 2. For the implementation of the nonlinear parts, see the derivations in Giorgetta et al. [44]. For both models we use a leap-frog time discretization with Asselin-filter $\alpha = 0.03$ in order to reduce the differences between the models to the differences in the spatial discretizations. We aim at a qualitative comparison of the model solutions between the triangular and the hexagonal schemes to assure that the nonlinear parts, implemented in our setup, perform well.

Vortex pair interaction: The test case of vortex pair interaction has already been introduced in Sect. 3.2.4, in particular in Eq. (3.33), where the initial surface elevation is given (see also [85, 86, 99]). Based on the height distribution, the initialization for the relative potential vorticity PV_{rel} field is done by first ensuring geostrophic balance for

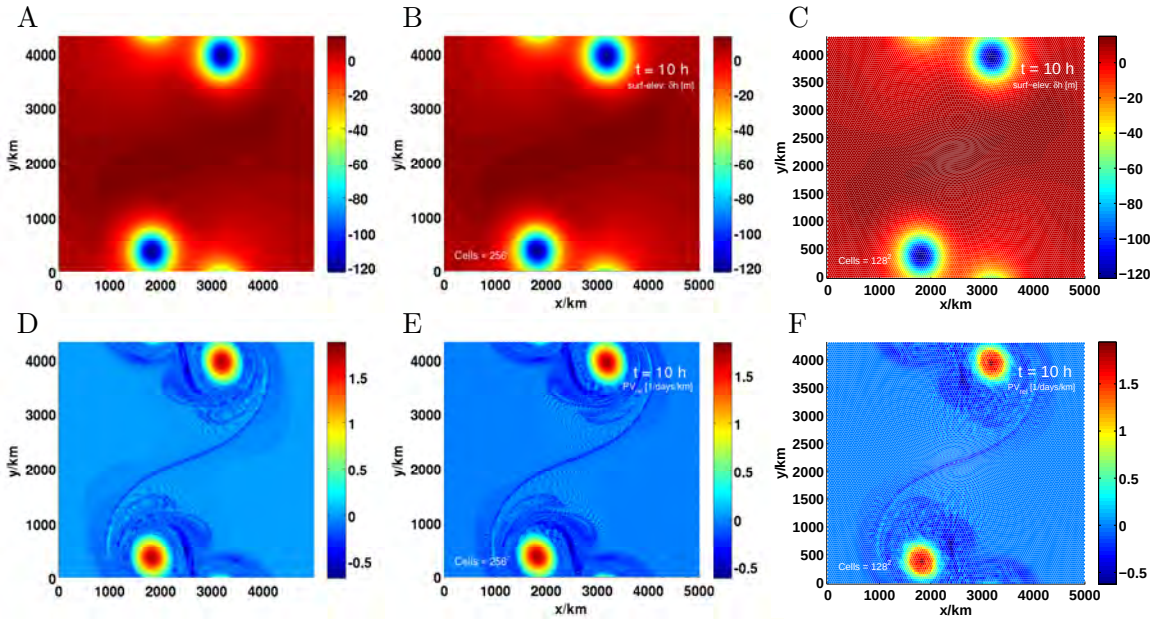

Figure 3.16: Vortex pair interaction for 10 days of integration. (A and D): solutions of the triangular model for surface elevation [m] $h - H$ and relative potential vorticity [1/days/km], respectively. (B, C, E, F): solutions of the hexagonal model for surface elevation and relative potential vorticity calculated on the uniform grid (B and D, respectively) and on the non-uniform grid (C and F, respectively).

the velocity field and then recalculating the surface elevation $h - H$ with the nonlinear balance equation (4.19). In this section effects caused by nonlinear interactions are taken into account by using the nonlinear equations.

The time evolution of two interacting co-rotating vortices is studied in the inviscid case over an integration time of 10 days. For the surface elevation of Eq. (3.33) we take the parameters $H_0 = 10\,\text{km}$, $H' = 75\,\text{m}$ and $o = 0.1$ on a double periodic domain with $5000\,\text{km} \times 4330\,\text{km}$ and $f = 6.147 \cdot 10^{-5} s^{-1}$, which corresponds to a latitude of 25° (cf. Fig. 3.6 for the initialization on a grid with 32^2 cells). In this experiment we use 256^2 cells in order to minimize the errors caused by a too low grid resolution and in order to compare our results with those of Giorgetta et al. [44].

For the uniform triangular grid we use $2 * 256^2$ triangles corresponding to 256^2 vertices, which coincides with the number of vertices of the hexagonal mesh with 256^2 cells. Both meshes are thus comparable in terms of computational costs and not directly by resolution. We use the same number of prognostic velocity components, as in both cases the number of edges are similar. However, both grids differ in the number of prognostic values for the surface elevation, namely $2 * 256^2$ for the triangular and 256^2 for the hexagonal model, which corresponds to the respective number of cells. In addition, we compare the results calculated with the hexagonal model on the uniform grid with 256^2 cells and on the non-uniform grid with 128^2 cells similar to those shown in Fig. 3.13, since in this case the size of the cells of the uniform grid and of the cells within the high resolution region of the non-uniform grid agree.

Figure 3.16 illustrates the results for an integration of 10 days for the triangular mesh (A and D) and for the hexagonal uniform (B and E) and non-uniform (C and F) meshes. The upper row shows the surface elevation, the lower row the relative potential vorticity. The results for the triangular and hexagonal models are very similar. The end positions

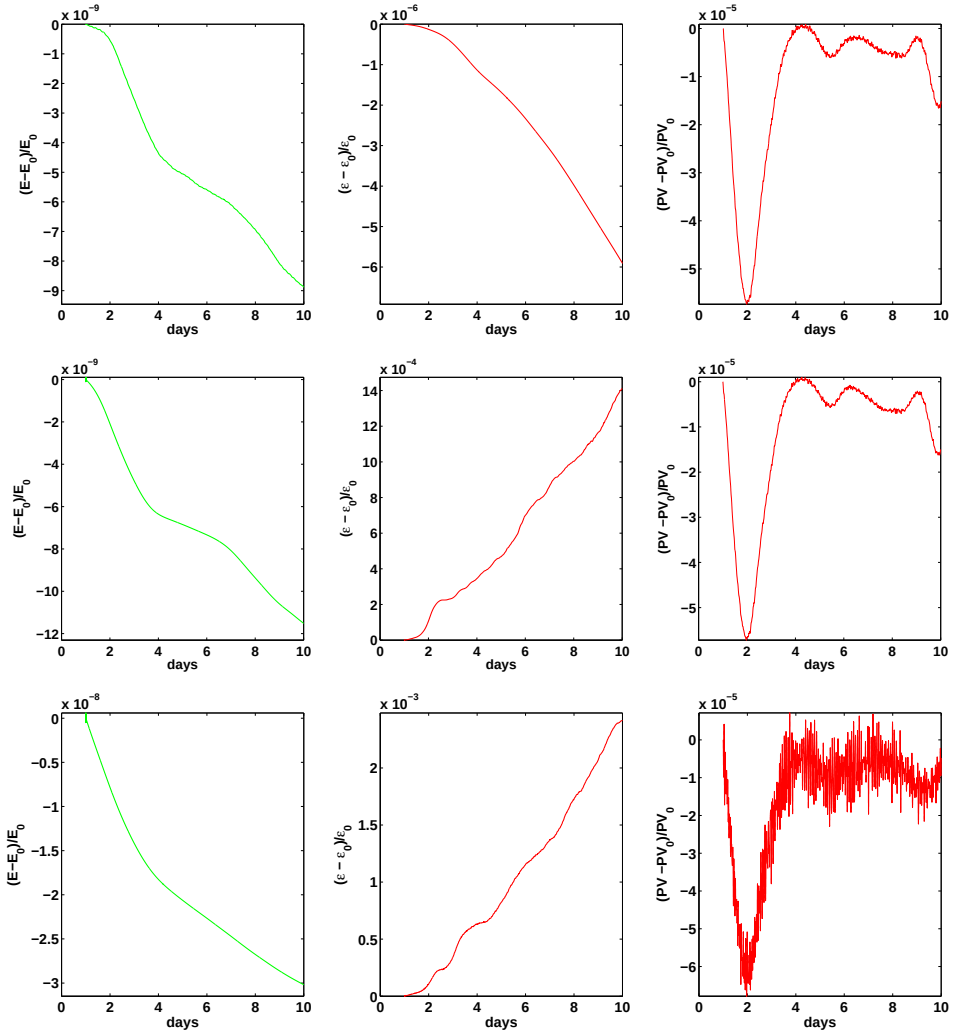

Figure 3.17: Vortex pair interaction: relative errors in energy (left column), potential enstrophy (middle column) and potential vorticity (right column), for the triangular model with $2 * 256^2$ cells (upper row), for the hexagonal model on the uniform grid with 256^2 cells (middle row) and on the non-uniform grid with 128^2 cells (lower row).

of the vortices and of the negative surface elevations are quite similar in both triangle and hexagonal model, although the shape of the vortex cores differs slightly. The intensities of the vortex cores and of the negative surface elevations agree also very well. The results for the strongly stretched grid (C and F) are also very similar to those of the uniform triangular and hexagonal grids. The shape of the vortex cores is very similar to cases B and E, although the grid shows strong deformations in the area of vorticity interaction. The end positions of the two vortices agree quite well for all three different grid types.

The good performance of the non-uniform grid also in case of strong cell deformation is in agreement with the test case on geostrophic balance, for which during an integration time of up to 40 days the results are sufficiently close to the uniform runs. Here, with a integration of 10 days we stay within a regime, where the potential vorticity is properly represented also on the strongly deformed grid.

Figure 3.17 shows relative errors of energy E (left column), potential enstrophy ϵ (middle column) and potential vorticity PV_{rel} (right column) of the solutions calculated on

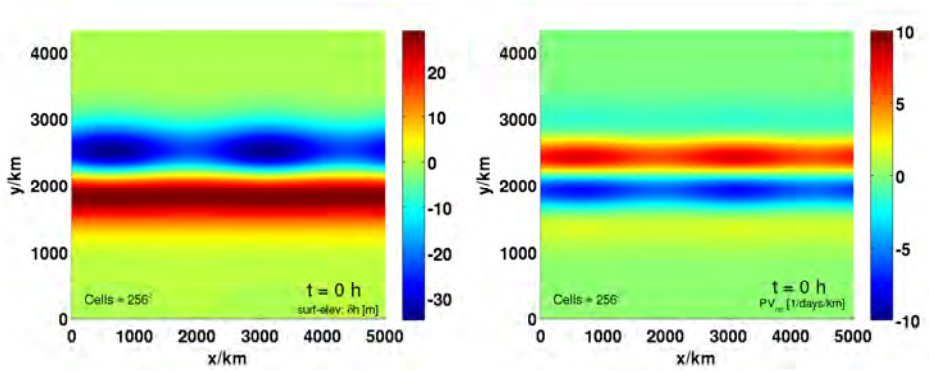

Figure 3.18: Test case for shear flow evolution: initial surface elevation $h - H$ [m] (left) and relative potential vorticity [1/day/km] (right) on a hexagonal grid with 256^2 cells.

the triangular uniform mesh (upper row) and on the hexagonal uniform (middle row) and non-uniform meshes (lower row) for an integration of 10 days. For such short integration period, the energy conservation is for all three model configurations in the order of 10^{-8}. In case of the non-uniform grid, the potential enstrophy and potential vorticity are worse conserved staying within the order of 10^{-3} and 10^{-4}, respectively. This is one order of magnitude worse than in the uniform hexagonal case. The best results are obtained by the triangular model. This is not surprising, as the numerical scheme conserves those quantities by construction (cf. [44]).

Shear flow evolution: For the test case of shear flow evolution we proceed for initialization as done in the previous experiments, namely we prescribe the surface elevation, solve the geostrophic balance to obtain the velocity field and then solve the nonlinear balance equation (4.19) to obtain the balanced surface elevation. The prescribed surface elevation is given by

$$h(x, y, 0) = H_0 - H' \frac{y''}{\sigma_y} e^{-\frac{y'^2}{2\sigma_y^2} + \frac{1}{2}} \left(1 + \kappa \sin\left(\frac{2\pi x'}{\lambda_x}\right)\right) , \tag{3.80}$$

with $\lambda_x = \frac{1}{2}$, $\sigma_y = \frac{1}{12}$, $\kappa = 0.1$ and

$$x' = \frac{x}{L_x} , \quad y' = \frac{1}{\pi} \sin\left(\frac{\pi}{L_y}\left(y - \frac{L_y}{2}\right)\right) , \quad y'' = \frac{1}{2\pi} \sin\left(\frac{2\pi}{L_y}\left(y - \frac{L_y}{2}\right)\right) . \tag{3.81}$$

We refer to Giorgetta et al. [44] to learn more about the characteristics of this flow. Analogously to the authors, we set the initial conditions for $H_0 = 1076\,\text{km}$ and $H' = 30\,\text{m}$, to obtain an inviscid flow in quasi-geostrophic regime. In Fig. 3.18 the initial surface elevation (left) and the potential vorticity (right) are shown for a uniform hexagonal mesh with 256^2 cells.

Analogously to the investigation of the vortex pair interaction, we compare solutions calculated on the triangular uniform grid using $2 * 256^2$ cells with the hexagonal uniform (256^2 cells) and the hexagonal non-uniform (128^2 cells) grid, described in detail previously. We integrate up to 10 days: within this time scale the evolving instabilities consisting of two couples of counter-rotating vortices are already very advanced and the evolving vorticity filaments have already reached scales beyond the spatial resolution (cf. Giorgetta et al. [44]).

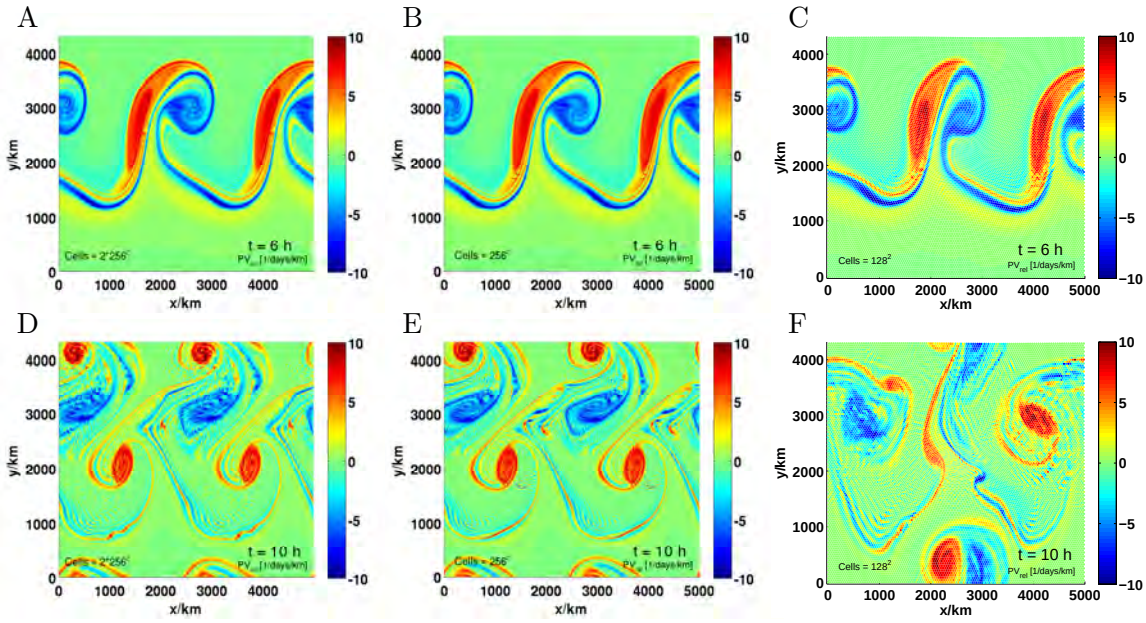

Figure 3.19: Shear flow evolution integrated over 10 days. (A and D): solutions of the triangular model for relative potential vorticity [1/days/km] for day 6 and day 10, respectively. (B, C, E, F): solutions of the hexagonal model for relative potential vorticity calculated on the uniform grid for day 6 and 10 (B and D, respectively) and on the non-uniform grid for day 6 and 10 (C and F, respectively).

Figure 3.19 illustrates the results of the model integration for the triangular mesh (A and D) and for the hexagonal uniform (B and E) and non-uniform meshes (C and F). As in the case of vortex pair interaction, the results of the uniform triangular and hexagonal models are qualitatively very similar. Only in the case of the non-uniform grid a significant difference is visible. The evolution of the two counter-rotating vortex pairs has a different speed in vertical direction leading to a different distance from the domain center. In addition, much more small-scale features have been evolved that are beyond spatial resolution. For this test case, the difference between uniform and non-uniform grids is more pronounced than in case of the vortex pair interaction of Fig. 3.16. The reason for this discrepancy may lie in the deformed grid cells that cause disturbances of different magnitude on the shear flow and may therefore influence the time at which the instabilities, in form of the two couples of counter-rotating vortices, are triggered.

Figure 3.20 illustrates that for short integration times up to 5 days the errors in relative energy (left column), relative potential enstrophy (middle column) and relative potential vorticity (right column) are very similar to those presented for the vortex pair interaction. From day 5 on, the potential enstrophy strongly increases for uniform (middle row) and for non-uniform grids (lower row) on the hexagonal scheme, whereas the triangular scheme (upper row) conserves the potential enstrophy with an accuracy of 10^{-4}. However, all simulations on the three different grids give comparable results concerning energy and potential vorticity properties.

3.5 Conclusions

The usage of staggered C-grids for geophysical applications is in particular favorable for an adequate representation of waves and of their dispersion relations. However, the stag-

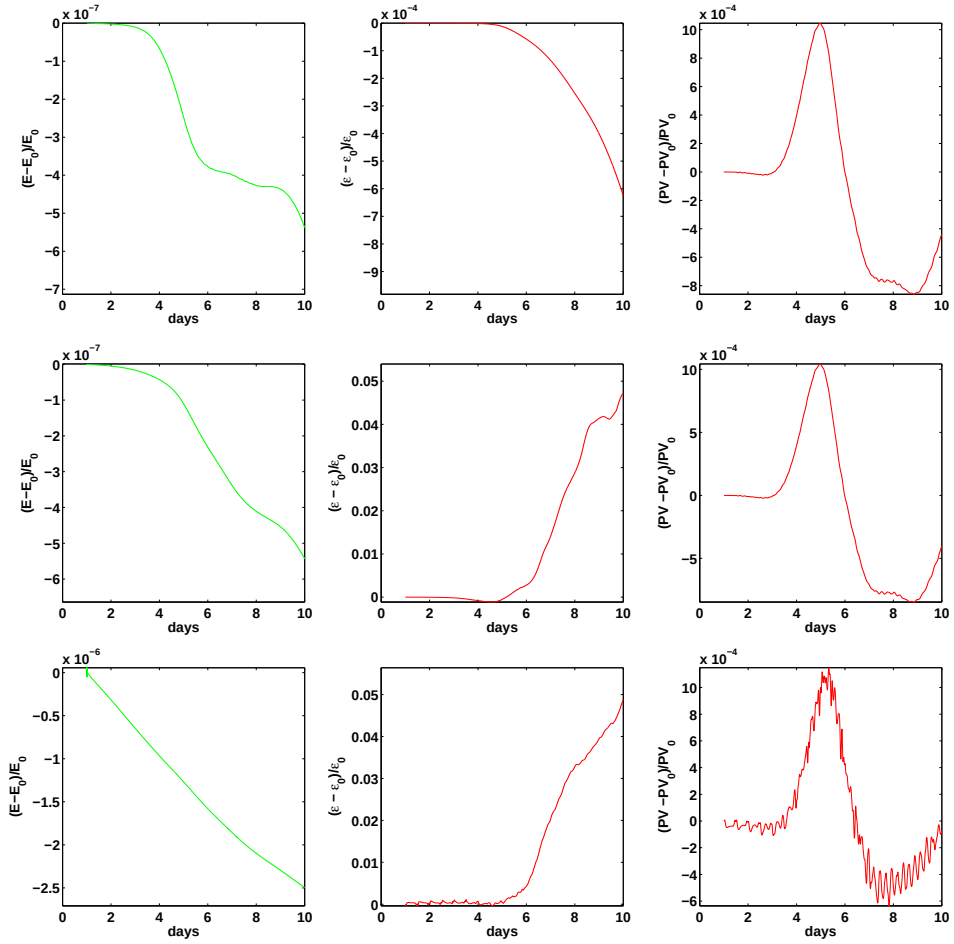

Figure 3.20: Shear flow evolution: relative errors in energy (left column), potential enstrophy (middle column) and potential vorticity (right column), for the triangular model with $2 * 256^2$ cells (upper row), for the hexagonal model on the uniform grid with 256^2 cells (middle row) and on the non-uniform grid with 128^2 cells (lower row).

gering of mass points and velocity components requires to reconstruct the missing vector components to represent the Coriolis term. In particular, for hexagonal C-grid models on non-uniform meshes this is more difficult than for triangular ones. All linear tangential vector reconstructions for triangular cells reduce to the low-order Raviart-Thomas interpolation [46]. In contrast, there seems to be no similar unique linear normal vector field reconstruction for hexagonal cells.

In order to find a suitable vector reconstruction for hexagonal models, one may put some constraints on the momentum equations to derive normal vector components that lead to a stable scheme with proper wave representation. A normal vector reconstruction for arbitrarily-structured C-grids has been successfully presented in Thuburn et al. [102]. Using the two-dimensional vorticity equation, the authors have derived weights for normal vector reconstruction out of tangential components for the hexagonal C-grid discretization of the linear shallow-water equations. These weights ensure stability of the model and lead to stationary geostrophic modes similar to the continuous equations.

We do not restrict our momentum equation to the two-dimensional case. Based on the invariant form of the geophysical fluid equations derived in Chapter 2, we have represented instead the Coriolis term by means of exterior calculus and, in particular, by the

concept of extrusion. Based on extrusion, we have introduced a method for normal vector reconstruction out of neighboring tangential vector components, in which the weights are determined by the ability of the tangential vector components to contribute to the extrusion.

We have derived a normal vector reconstruction scheme with weights that guarantee stability and lead to an adequate wave representation without spurious geostrophic modes on uniform grids. The vector reconstruction agrees on uniform meshes with the method introduced by Thuburn et al. [102]. This agreement underpins our strategy of using geometrical constraints on the equations to derive the weights. For both approaches, the weights have to be antisymmetric with exchange of the contributing edges for uniform and non-uniform meshes to guarantee stability. Our method provides such weights for uniform meshes as an eigenvalue analysis of the system matrix has confirmed. Using the constraint of antisymmetric weights, it seems very likely that our approach can also be generalized to non-uniform grids.

Furthermore, we have shown that a vector reconstruction based on the Raviart-Thomas interpolation suitable for triangular models may lead to spurious geostrophic modes in the hexagonal case, although the model is consistent and stable. Hereby, the continuity properties of the extrusion may give information about the differences in using RT0 interpolations for triangular and for hexagonal models and about the size of the stencil required to guarantee continuous representation of the extrusion on the mesh. In case of triangular cells, the RT0 interpolation led to a tangential vector field causing a smooth extrusion. In contrast, when using the RT0 interpolation for normal vector reconstruction, the extrusion was discontinuous. A smooth extrusion can be achieved with a larger stencil using more neighboring velocity components. Our normal vector reconstruction method fulfills such continuity requirement.

To proceed toward a nonlinear hexagonal C-grid shallow-water model with the ability of grid adaptation, we used the general weights for normal vector reconstruction for arbitrarily-structured C-grids by Thuburn et al. [102] and extended our model setup by the nonlinear parts for the same kind of non-uniform meshes by Ringler et al. [89]. In order to guarantee a proper model performance including grid adaptation also within our software environment, we performed several nonlinear test cases on uniform and on strongly deformed grids. We have shown stability, consistency and proper representation of the geostrophic balance and of the geostrophic modes.

In addition, a comparison to the triangular shallow-water version of ICON on a uniform grid, introduced by Giorgetta et al. [44], has been performed. Both models performed very similar in most cases except for the potential enstrophy conservation, for which the triangular model performed better. However, as thoroughly elaborated in Wan [112] and theoretically elaborated in Gassmann [43], the triangular shallow-water model shows a checkerboard pattern in the divergence field. Moreover, the models differ in the wave representation and their dispersion relation [43].

Lastly, the usage of methods of exterior calculus to discretize the invariant equations seems to be a promising approach in the sense that it can provide new insight into the properties of staggered grid schemes and into the geometrical nature of the Coriolis term and of its behavior on the mesh. A generalized discretization method for the equations of GFD on meshes based on general polytopes could help to find, for instance, a consistent and stable scheme on a barycentric mesh, higher order schemes or vector reconstruction schemes for three-dimensional models. For the latter, the method of exterior calculus, which is by definition independent of the dimension, is particularly suitable.

Chapter 4

Simulation of tropical-cyclone-like vortices in shallow-water ICON-hex using goal-oriented r-adaptivity

Abstract We demonstrate how efficient r-adapted grids for the prediction of tropical cyclone (TC) tracks can be constructed with the help of goal-oriented error estimates. The binary interaction of TCs in a barotropic model is used as a test case. We perform a linear sensitivity analysis for this problem to evaluate the contribution of each grid cell to an error measure correlated with the cyclone positions. This information allows us to estimate the local grid resolution required to minimize the TC position error. An algorithm involving the solution of a Poisson problem is employed to compute how grid points should be moved such that the desired local resolution is achieved. A hexagonal shallow-water version of the next-generation numerical weather prediction and climate model ICON is used to perform model runs on these adapted grids. The results show that for adequately chosen grid adaptation parameters, the accuracy of the track prediction can be maintained even when a coarser grid is used in regions for which the estimated error contribution is low. Accurate track predictions are obtained only when a grid with high resolution consisting of cells with nearly constant size and regular shape covers the part of the domain where the estimated error contribution is large. The number of grid points required to achieve a certain accuracy in the track prediction can be decreased substantially with our approach. [1]

4.1 Introduction

The adequate representation of tropical cyclones (TCs) in numerical weather prediction (NWP) models and climate models is a challenging problem. One of the main difficulties is related to the multiscale nature of these storms. Processes in the inner core of a TC proceed on convective scales, determine the intensity evolution and thus the influence of the storm on the large-scale flow [35]. The large-scale flow causes the advection of the TC [55] and thus influences its environment, which in turn affects the processes in the inner core (cf. [73]). Due to these scale-interactions, a large range of scales has to be included

[1] This chapter has been submitted to the Journal of Theoretical and Computational Fluid Dynamics (TCFD) as Bauer et al. [9].

to model TCs adequately. NWP and climate models cover only a part of this scale range and rely on parameterizations to model processes on subgrid scales. The representation of TCs in climate models and the quality of TC forecasts in NWP could be improved by resolving a larger range of scales. However, using uniform grids with sufficiently high resolution for this purpose would lead to extremely high computational cost.

A promising solution for this problem is to adapt the grid such that the resolution is high only where it is required to resolve essential features. In the rest of the domain a lower grid resolution is used, thus making the overall computational costs affordable. Grid adaptation methods can be categorized as static or dynamic approaches. In methods using dynamic adaptation the grid is adapted to the solution during runtime according to a local refinement criterion. This method is, however, not yet used operationally in atmospheric and ocean applications (except for the OMEGA model [6, 29]), but has been investigated for idealized models in several studies (e.g. [14, 15, 50, 64, 98]). Static grid refinement approaches are more frequently used in global atmosphere and ocean models (e.g. in [8, 39, 45, 87, 88, 110, 116]), for which the grid remains unchanged during the model integration. The locations of high-resolution areas are usually chosen such that they include certain atmospheric or orographic features of interest or cover regions in which predictions with higher accuracy are required. Outside of this high-resolution regions the error might be high and, consequently, also errors measured in some global error norms. Based on such refined grids, several global shallow-water models (e.g. [31, 88, 98, 116]) have been investigated with the standard test set of Williamson et al. [118], in particular with test cases 2 and 5 described therein. The numerical results of these investigations have been summarized by Ringler et al. [88]. The authors observe that the global error of the solution depends on the resolution of the coarse mesh regions. Investigating the test case of baroclinic instability [58], where the storm-track region is within a highly resolved northern hemisphere, Jablonowski et al. [57] confirmed that also in such case the global error is determined by the globally coarsest grid cells. However, higher resolution at the regions of storm-tracks can slow down the error growth when the baroclinic wave contributes to the error. A suitable local error norm confined to the highly resolved storm-track region shows with increasing local resolution in this region a decreasing error.

Often application-specific error measures are more useful in assessing the quality of a numerical solution than a global error. For tropical cyclones, errors in the cyclone position and the cyclone intensity are such important error measures. Goal-oriented adaptivity methods allow for an automatic optimization of the grid for cyclone track prediction. In this approach the grid is adapted such that the error with respect to a goal functional, which represents, for instance, the error in the TC position, is minimized. These methods, e.g. the dual-weighted residual (DWR) method [7, 10, 11, 36], are often based on a posteriori error estimators that allow to assign to every cell a local contribution to the estimated error in the goal functional. The error distribution is used to control the grid adaptation process towards efficient grids that minimize the estimated error.

In this manuscript we present a method for goal-oriented static grid adaptation for a hexagonal C-grid shallow-water model. This model is based on ICON (ICOsahedral Non-hydrostatic model), the next generation numerical weather prediction and general circulation model, developed in cooperation with the Max Planck Institute for Meteorology and the German Weather Service [18, 112]. In the following, we refer to this model version as ICON-hex shallow-water.

We use the interaction of two tropical cyclones in a barotropic model as a test case for grid adaptation. Binary TC interaction is a process for which the track prediction is known to be difficult [30, 59]. The high sensitivity of the solution with respect to the

initial conditions for this problem is also found in strongly idealized models, in which the intensity evolution is not modeled adequately. Consequently, we focus on the track prediction and use the error in the final vortex position as an error norm.

In our approach the grid is adapted by moving grid points to regions where higher resolution is required, a method generally known as r-adaptivity. We use the discretization scheme of Ringler et al. [89] that shows conservation of mass, energy and potential vorticity [88]. However, for this numerical scheme there is, to our knowledge, no adequate goal-oriented error estimator available. In recent literature [82, 83] an automatic differentiation tool has been applied on a triangular C-grid ICON shallow-water model to derive an adjoint model which allows the estimation of the error of the solution with respect to a goal functional. As the triangular C-grid model shows grid scale noise [112], which can be avoided by using a hexagonal C-grid model [43, 110], the latter has been chosen for this study. In addition, such choice makes a comparison with the results of Ringler et al. [88, 89] easier.

In order to allow goal-oriented grid adaptivity within the ICON-hex model, we adopt the following approach as an intermediate step until an adequate error estimator is available for this model. We estimate the error distribution with a goal-oriented error estimator that is implemented in the finite element package HiFlow^3 [2]. The error information contains the discretization error weighted by the dual solution. The dual solution represents the sensitivity of the goal functional with respect to perturbations of the solution (independent of the discretization). We assume that for our test scenario, the discretization errors of the HiFlow^3 finite element discretization are sufficiently well correlated with the discretization errors of the ICON-hex discretization such that the indicated errors are meaningful for adapting the ICON-hex grid. Cellwise error indicators calculated based on the finite element model are then used to define an adequate monitor function that controls the r-adaptive grid optimization of the ICON-hex model. In this step, it must be ensured, that the deformation of the cells is not too strong. Several parameters control the grid adaptation and we investigate their impact on the grid quality and the resulting accuracy in track prediction.

The paper is structured in the following way. In Sect. 4.2 we introduce the ICON-hex shallow-water model. In Sect. 4.3 our method of goal-oriented r-adaptivity for the ICON-hex model is presented in detail and the connection between the error distribution of the finite element model and the grid adaptation of the ICON-hex model is established. In Sect. 4.4 we introduce the scenario of binary tropical-cyclone-like vortex interaction as a test case for the proposed adaptive method. In Sect. 4.5 we present and discuss the numerical results. In Sect. 4.6 we present a summary and conclusion.

4.2 The hexagonal C-grid shallow-water model ICON-hex

Within the framework of ICON [18, 43, 90], we develop ICON-hex, a shallow-water model with static grid adaptation. Based on a suitable discretization scheme of Thuburn et al. [102] and Ringler et al. [89], the geophysical shallow-water equations are discretized by using the hexagonal C-grid staggering. The discretization scheme allows for an r-adaptive grid refinement, i.e. grid points are moved to regions where higher resolution is required.

As no grid points are added and thus the neighborhood relations do not change, only geometric properties as cell sizes or edge lengths of the adapted grid have to be recalculated in order to update the operators. Such unvarying topology eases the problem of load-balancing in parallel computing, which may be advantageous in particular for models with dynamic grid adaptation.

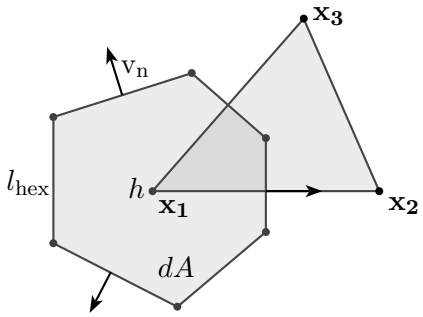

Figure 4.1: Position of the prognostic variables fluid depth h and normal velocity component $\mathrm{v_n}$ on the grid. l_{hex} and dA denote edge lengths and cell areas of the hexagonal cells, respectively. With $\mathbf{x_i} \in \Omega, i = 1, 2, 3$, we denote the triangular vertex points that are moved during the grid adaptation process (cf. Sect. 4.3.4).

4.2.1 The continuous equations

As basic system of equations we use the nonlinear geophysical shallow-water equations, written in vector-invariant form:

$$\begin{aligned} \frac{\partial \mathbf{v}}{\partial t} &= -(\zeta + f)\mathbf{k} \times \mathbf{v} - \nabla(\frac{1}{2}\mathbf{v}^2) - g\nabla h - \nu\nabla \cdot (\nabla \mathbf{v}) \ , \\ \frac{\partial h}{\partial t} &= -\nabla \cdot (h\mathbf{v}) \ , \end{aligned} \tag{4.1}$$

where $\mathbf{v} = (v_x, v_y, 0)$ is the velocity vector, h is the fluid depth, $\zeta = \mathbf{k} \cdot \nabla \times \mathbf{v}$ is the vorticity, f is the Coriolis parameter, $\mathbf{k} = (0, 0, 1)$, $\nabla = (\partial_x, \partial_y, 0)$, ν is the viscosity and g the gravity.

4.2.2 Discretization in space and time

The ICON-hex model provides discrete approximations for the differential operators of Eq. (4.1) according to the definitions in Chapter 2.7 for a grid based on the Voronoi-Delaunay tessellation of the computational domain Ω. The prognostic variables fluid depth h and normal component $\mathrm{v_n}$ of the velocity $\mathbf{v}$ are positioned at the Voronoi cell centers, in the following denoted with $\mathbf{x}$, and at the intersection of hexagonal and triangular cell edges, respectively (cf. Fig. 4.1). This hexagonal C-grid staggering allows for favorable wave dispersion relations. However, the C-grid staggering requires a reconstruction of the missing tangential velocity component in order to determine the Coriolis-term in Eq. (4.1). In this study, we exploit the reconstruction and interpolation methods suggested by Thuburn et al. [102] and Ringler et al. [89].

For the time discretization, we use a leap-frog scheme with an Asselin-filter coefficient $\alpha = 0.03$. The diffusion introduced by this filter is small compared to the diffusion caused by the viscosity for the investigated scenario (cf. Sect. 4.4).

The definitions of the differential operators [18, 90] and of the reconstruction and interpolation methods [89, 102] guarantee conservation of mass, total energy, potential vorticity and geostrophic balance for the spatial semi-discretization even on an r-refined grid [88]. However, with increasingly deformed grid cells we expect a decrease in the order of the operators.

For this combined finite difference and finite volume method there exists to our knowledge no goal-oriented error estimator. Therefore, we suggest a method that allows, despite the lack of an error estimator, a goal-oriented grid adaptation in ICON-hex.

4.3 Goal-oriented r-adaptivity for the ICON-hex model

The goal-oriented adaptive methods investigated in this study allow to construct efficient discretizations by grid adaptation for the determination of certain physical quantities of interest definable as functionals, in this context denoted as *goal functionals*.

In the following, we present an *a posteriori error estimator* based on which each grid cell's contribution to the error in the goal functional can be quantified. This calculation requires information about the sensitivity of the functional with respect to perturbations, which is given by a dual problem. The error estimator is described in the context of an abstract parabolic problem and an adequate finite element discretization.

Based on such error estimates, an adequate *monitor function* that controls the r-adaptive grid refinement can be defined. The aim is to adapt the ICON-hex grid such that the error in the quantity of interest is minimized for shallow-water runs. In the following, we introduce the necessary steps in more detail.

4.3.1 Goal-oriented error estimation

The error estimator presented in this section requires solutions that are Galerkin approximations. In case of time-dependent problems, space-time finite element methods provide adequate discretizations. Consider the following initial value problem in the domain $\Omega \subset \mathbb{R}^2$ and the time horizon $(0,T)$ given as variational formulation: Find $u \in W := \{u \in L^2(0,T;V) \,|\, \partial_t u \in L^2(0,T;V^*)\}$ such that

$$\rho(u,\varphi) := \int_0^T \big((\partial_t u, \varphi)_\Omega + a(u,\varphi)\big)\, dt + (u(0) - u_0, \varphi(0))_\Omega = 0, \tag{4.2}$$

for all $\varphi \in L := L^2(0,T;V)$. Here, $a : V \times V \to \mathbb{R}$ denotes a continuous operator on the Hilbert space V with dual space V^*, and $(a,b)_\Omega := \int_\Omega a \cdot b\, dx$ denotes the inner product on the space of square-integrable functions on Ω, i.e. $L^2(\Omega)$. Details about existence and uniqueness of solutions as well as details on the related function spaces can be found, for instance, in [120]. The operator $a(\cdot,\cdot)$ and the function spaces W and L can be chosen such that problem (4.2) represents, for instance, the time-dependent two-dimensional Navier-Stokes equations. A discrete approximate solution of problem (4.2) can be calculated by replacing the function spaces W and L by finite dimensional subspaces $L_h \subset L$ and $W_h \subset W$. To this end, a space-time mesh with a partitioning of the interval $(0,T)$ in N_{time} sub-intervals and a triangulation of the domain Ω consisting of N_{space} cells is assumed. The discrete functions are defined as piecewise polynomials.

Let the user-defined *goal functional* be denoted by J, then $J(u)$ denotes the quantity of interest. The sensitivity of the goal functional with respect to perturbations of u can be determined by a dual problem, which is defined as linearization of (4.2) – referred to as *primal problem* in this context – and depends on the solution u and on the goal functional J: Find $z \in W$ such that

$$\rho_u^*(z,\varphi) := \int_0^T \Big(-\big(\partial_t z, \varphi\big)_\Omega + a_u^*(z,\varphi)_\Omega \Big)\, dt + \big(z(T), \varphi(T)\big)_\Omega = J'(u)\varphi\,, \tag{4.3}$$

for all $\varphi \in L$. $a_u^*(z,\cdot)_\Omega$ denotes the adjoint of the linearization of $a(\cdot,z)$, evaluated at u. $J'(u)\varphi$ denotes the directional derivative of J at u in direction φ. The negative sign of

$\partial_t z$ indicates that the dual problem is posed backward in time, with initial condition at time $t = T$, which depends on the goal functional. An approximate solution $z_h \in W_h$ of problem (4.3) can be calculated using the same finite dimensional spaces W_h and L_h as before.

Since we choose different trial space W_h and test space L_h, the discrete variational problems (4.2) and (4.3) belong to the class of Petrov-Galerkin methods. For an approximate solution $u_h \in W_h$ of the primal problem, the error with respect to the goal functional J can be estimated by [10]:

$$J(u)-J(u_h) \approx E(u_h) := \frac{1}{2}\Big(\rho(u_h, Z+z_h-I_h(Z+z_h))+\rho^*_{u_h}(z_h, U-u_h-I_h(U-u_h))\Big). \quad (4.4)$$

Here, $I_h : W \to L_h$ denotes an interpolation operator that maps into the discrete space of the test functions. The functions $U, Z \in W$ denote approximations of the exact primal and dual solutions u and z, respectively. We defined these approximations by a projection of the calculated solutions u_h and z_h into a finite element space of higher order by patch-wise interpolation, cf. [7].

The error estimation $E(u_h)$ is defined in terms of the residuals $\rho(\cdot,\cdot)$ and $\rho^*_{u_h}(\cdot,\cdot)$, which represent integrals in space and time. These can equivalently be formulated as sum of space-time integrals over all cells in the space-time mesh. By the triangle inequality, error indicators $\eta_{ij} \geq 0$ that denote the contribution of cell $j \in \{1, \ldots, N_{space}\}$ in the time interval $i \in \{1, \ldots, N_{time}\}$ of the time partitioning can be introduced by

$$E(u_h) \leq \sum_{i=1}^{N_{time}} \sum_{j=1}^{N_{space}} \eta_{ij}. \quad (4.5)$$

Further details on the calculation of these error indicators can be found in [10]. Since the adapted grid should be fixed in time, only the maximal error contribution over time for each of the N_{space} grid cells is of interest. This leads to the final error indicators

$$\eta_j := \max_{i=1}^{N_{time}} \eta_{ij}, \quad j = 1, \ldots, N_{space}. \quad (4.6)$$

Based on these error indicators, we describe in the following how a monitor function that controls the r-adaptive grid optimization can be defined.

4.3.2 Definition of the monitor function

For a numerical scheme that is of second order in space on a uniform grid, the error $\epsilon \propto l^2$ is proportional to the squared grid length. The scheme used for the ICON-hex shallow-water model shows this property.

When investigating global flow phenomena with adapted grids, the error is determined by the grid length of the coarsest cells, as shown by Ringler et al. [88]. Local errors might be distributed with the flow field across long distances. Increasing the resolution only in certain grid areas would therefore not reduce the global error.

In contrast, when investigating *non-global* phenomena with localized features, as for instance the scenario of binary TC interaction (see Sect. 4.4), we expect more accurate solutions when using adequately adapted grids. For the estimated local error contributions, denoted by ϵ_{est} in the following, we assume $\epsilon_{\text{est}} = c l_{\text{est}}^2$, where l_{est} is the grid length of the uniform grid that is used in the error estimation process. c is an unknown factor independent of l_{est} that will cancel out in the following argumentation.

The adaptation of an initially uniform grid in correspondence to the local errors aims at an equal distribution of the local error contributions and a reduction of the error in the goal functional. When the local error has to be reduced below $\epsilon_{\text{target}} = c l_{\text{target}}^2$, the corresponding grid length l_{target} is related to the estimated local error ϵ_{est} by

$$l_{\text{target}} = l_{\text{est}} \sqrt{\frac{\epsilon_{\text{target}}}{\epsilon_{\text{est}}}} \ . \tag{4.7}$$

To estimate the local error contributions ϵ_{est} of the single cells of a uniform ICON-hex grid, we interpolate the error indicators η_j from the grid cells of the finite element discretization to the ICON-hex grid cells. The interpolated error indicators are denoted with $\eta(\mathbf{x})$, where $\mathbf{x} \in \Omega$ are coordinates of the cell centers (see Fig. 4.1).

Our grid adaptation method uses a monitor function $f(\mathbf{x})$ that controls the distribution of the size of the grid cells over the entire domain by the relation $f(\mathbf{x}) \propto l_{\text{target}}(\mathbf{x})^2, \forall\, \mathbf{x} \in \Omega$ (cf. Eqn. (4.13) and (4.14) further below). If we assume to constrain the local error contributions below a globally valid error threshold ϵ_{target}, we find the desired relation between error indicators and the monitor function by

$$f(\mathbf{x}) \propto \frac{1}{\eta(\mathbf{x})}, \qquad \forall\, \mathbf{x} \in \Omega. \tag{4.8}$$

In general, $\eta(\mathbf{x})$ contains error information that span over a range too large to be used directly as monitor function. Bounding the error values and smoothing the monitor function are therefore necessary steps as the pure error information can lead to strongly deformed and thus possibly unusable grids.

4.3.3 Bounding and smoothing of the monitor function

Ill-defined geometrical properties on strongly deformed grids: By definition of the Voronoi-Delaunay tessellation, as used in ICON-hex, the cell edges of the hexagonal and triangular grids are always perpendicular to each other. This is due to the fact that the circumcenters of the triangles are vertices of the hexagonal cells also in case of deformed grids. During the grid adaptation, the grid point transformation moves the vertices of the triangular cells (cf. Fig. 4.1). However, problems arise when the circumcenter of a strongly deformed triangle lies outside its own boundaries. This fact translates into ill-defined geometrical properties, for instance negative edge lengths and grid sizes of the hexagonal cells. As the differential operators rely on well-defined geometrical cell properties, numerical simulations cannot be carried out on such grids. In the following we call this geometrical restriction to grids with circumcenters lying within their own triangle boundaries the *grid duality constraint*.

Grids that use the barycenters, instead of the circumcenters, as vertices of the hexagonal cells do not show this limitation. For instance, the finite volume model OLAM [108, 109] is based on such grids. However, as in such case the primal and dual cell edges are in general not perpendicular to each other, the use of these grids demands for a different numerical scheme and is thus not an option for our investigations.

The grid duality constraint imposes, besides the error distribution itself, a second condition on the grid adaptation process. This condition restricts the possibility to adapt the grid in an arbitrary manner. However, strongly deformed grid cells that violate the grid duality constraint can be avoided by limiting the range of cell areas in the grid and by ensuring that cell areas vary smoothly rather than abruptly.

Bounding of the values of the error indicators: To obtain adapted grids that obey the grid duality constraint, the monitor function has to be restricted such that the ratio of the cell area of the uniform grid to the area of the smallest cells of the adapted grid, $dA(\mathbf{x})/\min_{\mathbf{x}\in\Omega} dA'(\mathbf{x})$ (cf. Eq. (4.14) for notation), does not exceed a constant γ, which we will call the refinement level. Based on Eq. (4.8), this bounding can be accomplished by setting

$$\forall \mathbf{x} \in \Omega: \quad f(\mathbf{x}) := C_{\text{norm}} \cdot \begin{cases} 1/\eta_b & \text{for } \eta(\mathbf{x}) > \eta_b \\ 1/\eta(\mathbf{x}) & \text{for } \eta_b/\gamma \le \eta(\mathbf{x}) \le \eta_b \\ \gamma/\eta_b & \text{for } \eta(\mathbf{x}) < \eta_b/\gamma. \end{cases} \tag{4.9}$$

If A_Ω is the total area of the domain Ω, and $A(\eta_b)$ is the area of the region of Ω where $\eta(\mathbf{x}) > \eta_b$, we can define an *area fraction* $b(\eta_b) := A(\eta_b)/A_\Omega$ that is a monotonically decreasing function of the error bound η_b. According to Eq. (4.9), b is the fraction of the area where the grid will have the finest resolution, with cell sizes that are a factor γ smaller than for the cells of the uniform grid. In the following we specify for all model runs the area fraction b instead of the error bound η_b. The normalization constant, $C_{\text{norm}} > 0$, will be defined further below.

Smoothing of the monitor function: If the error indicators $\eta(\mathbf{x})$ vary strongly on small scales, even the bounded monitor function of Eq. (4.9) may result in grids that violate the grid duality constraint. This problem can be avoided by using a smoothed version of the monitor function, which results in smooth transitions between regions with coarse and fine cells. Smooth transitions and a high homogeneity of the shape of the cells guarantee well-defined geometrical properties.

For this purpose we suggest a smoothing method in two steps. In the first step, for each grid point $\mathbf{x} \in \Omega$ the value of the function $f(\mathbf{x})$ is replaced by the minimum of f within the neighborhood $U_d(\mathbf{x}) := \{\mathbf{x}' \in \Omega \mid \|\mathbf{x}' - \mathbf{x}\|_s \le d\}$ with a *smoothing length* $d \in \mathbb{R}$ in km, i.e.

$$f_{\text{ext}}(\mathbf{x}) := \min_{\mathbf{x}'\in U_d(\mathbf{x})} f\left(\mathbf{x}'\right), \ \forall \mathbf{x} \in \Omega\ . \tag{4.10}$$

Here we use a norm

$$\|\mathbf{x}\|_s := \sqrt{x^2 + s^2 y^2}\ , \tag{4.11}$$

with a scaling factor $s = 2/\sqrt{3} \approx 1.15$ that equals the ratio of the zonal to the meridional sizes of the hexagonal grid cells. Thus, regions with small values of f are extended by the same number of cells in zonal and meridional direction.

In the second step, the extended function is convolved with a Gauss function, i.e.

$$f_{\text{sm}}(\mathbf{x}) = \frac{1}{c_{\text{sm}}} \int_\Omega f_{\text{ext}}(\mathbf{x}')\exp(-\|\mathbf{x}' - \mathbf{x}\|_s^2/d^2)\mathrm{d}\mathbf{x}'\ , \quad c_{\text{sm}} = \int_\Omega \exp(-\|\mathbf{x}'\|_s^2/d^2)\mathrm{d}\mathbf{x}'\ , \tag{4.12}$$

This leads to a smoother monitor function f_{sm} while maintaining the minimum of the original function. Furthermore, the area fraction b to be covered by the finest grid cells changes only slightly due to this smoothing method. In contrast, omitting the step for expanding the function and applying thus only the Gaussian convolution on the original monitor function f would lead to a function with changed minimum f_{rd}. An illustration of the bounding and smoothing method is given in Fig. 4.2.

Compared to approaches in the literature, for instance the mesh generation algorithm based on gradient limited monitor functions of Persson [80], our adaptation method, in which the grid parameters are chosen manually, does not generate automatically high

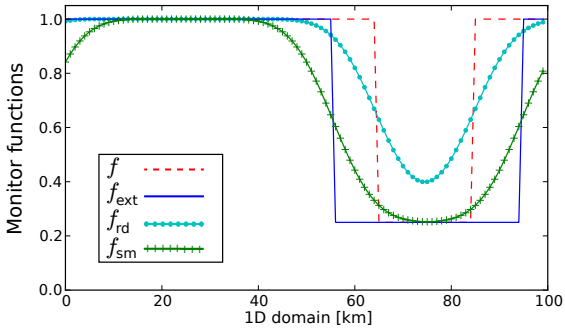

Figure 4.2: The bounding and smoothing method of monitor functions is illustrated on a one-dimensional periodic domain. f denotes the original monitor function, f_{ext} the extended function and f_{sm} the smoothed function. With f_{rd} we denote the monitor function with reduced minimum.

quality grids where the homogeneity of cell shapes and a smooth transition of cell sizes is automatically guaranteed. To obtain nevertheless optimal grids, we address in Sect. 4.5.3 the grid quality issue to find optimal values for area fraction b and smoothing length d.

4.3.4 Grid adaptation controlled by a monitor function

Relation between monitor function and cell size distribution: Let $f \in \mathcal{C}^1(\Omega)$ be a monitor function with (i) $f > 0$ in Ω and (ii) $\int_\Omega (f-1)dA = 0$, where dA is the two-dimensional area measure and $\Omega \subseteq \mathbb{R}^2$ is a bounded domain with smooth boundary. Then, an injective transformation $\phi : \Omega \to \Omega$, which describes the movement of all points $(x, y) \in \Omega$ exists [74, 68], and it is given by

$$\det\nabla\phi(x,y) = f(x,y) \text{ in } \Omega \qquad \text{and} \qquad \phi(x,y) = (x,y) \text{ on } \partial\Omega\,. \tag{4.13}$$

The left-hand side of Eq. (4.13) is the Jacobian determinant J of the mapping ϕ and can be written as

$$J(\phi) = \det\nabla\phi(x,y) = \frac{|dA'(x,y)|}{|dA(x,y)|}, \tag{4.14}$$

where dA' is the image of the area element dA under the mapping ϕ [69]. As $f > 0$ there is also $J(\phi) > 0$.

For the deformation of grids, $dA(\mathbf{x})$ denotes for every grid point $\mathbf{x}$ the cell sizes of the original uniform grid (cf. Fig. 4.1) and $dA'(\mathbf{x})$ the cell sizes after applying the transformation ϕ to the original grid. Taking, for instance, the monitor function $f(\mathbf{x})$ derived in Eq. (4.9), we find, based on Eqn. (4.13) and (4.14), a relation that allows to control the cell size distribution of an adapted grid by a point-wise defined monitor function.

Numerical method for r-adaptation: The grid is adapted by moving the grid points $\mathbf{x}$ in Ω with respect to the monitor function of Eq. (4.9). To guarantee that the monitor function fulfills conditions (i) and (ii), the normalization constant, $C_{\text{norm}} > 0$, must be chosen such that the integral value over the domain equals 1, i.e. $\int_\Omega f(\mathbf{x})\, dA(\mathbf{x}) = 1$. With $\eta_j \geq 0$ (cf. Sect. 4.3.1) and the conditions imposed on $\eta(\mathbf{x})$ by Eq. (4.9), $f > 0$ is also guaranteed.

In order to find the corresponding transformation ϕ, a solution to problem (4.13) has to be found. This can be achieved by an algorithm of Semper and Liao [95] that consists

of two steps. First, the conditions (i) and (ii) on $f(\mathbf{x})$ of Eq. (4.9) guarantee a solution to the following Poisson problem

$$\begin{aligned} -\triangle w(\mathbf{x}) &= f(\mathbf{x}) - 1 \quad \text{in } \Omega\,, \\ \frac{\partial w}{\partial n} &= 0 \quad \text{on } \partial\Omega\,, \end{aligned} \tag{4.15}$$

with $\nu(\mathbf{x}) := -\nabla w(\mathbf{x})$. w is an auxiliary scalar function that is no more needed in the following. The vector function $\nu(\mathbf{x})$ of Eq. (4.15) describes the direction and degree of movement of every grid point $\mathbf{x}$ with respect to the monitor function $f(\mathbf{x})$. The so-called deformation vector $\theta : \Omega \times \mathbb{R} \to \Omega$ can be introduced by

$$\theta(\mathbf{x}, s) := \frac{\nu(\mathbf{x})}{s + (1-s)f(\mathbf{x})}\,, \quad s \in [0,1]. \tag{4.16}$$

Then, for every grid point $\mathbf{x} \in \Omega$ the transformation ϕ can be determined by solving a system of ODEs

$$\frac{d}{ds}\psi(s, \mathbf{x}) = \theta(\psi(s, \mathbf{x}), s), \qquad 0 < s \leq 1, s \in \mathbb{R}, \tag{4.17}$$

with the initial condition $\psi(0, \mathbf{x}) = \mathbf{x}$. The auxiliary function $\psi(s, \mathbf{x}) \in \Omega,\ \forall s \in [0,1]$, moves every grid point $\mathbf{x} = \psi(0, \mathbf{x})$ in steps of increments ds to the desired new position $\psi(1, \mathbf{x})$. Then $\phi(\mathbf{x}) := \psi(1, \mathbf{x})$ defines the desired grid point transformation. To guarantee a smooth transformation, ds has to be reasonably small (for our experiments $ds = 0.1$).

Based on the definition of the monitor function in Eq. (4.9) that fulfills conditions (i) and (ii) of Eq. (4.13), we have thus found a grid point transformation ϕ that adapts the ICON-hex grid with respect to the error indicators η_j provided by the finite element model.

4.4 Binary tropical-cyclone-like vortex experiment

4.4.1 Binary tropical cyclone interaction

When two tropical cyclones come sufficiently close to each other they interact. In the course of the interaction process the circulation of the first vortex advects the second and vice versa. Due to the horizontal shear of the circulations also the structure of the TCs can be modified. These processes may also result in a merger of the cyclones. The binary tropical cyclone interaction often leads to complex tracks [63] and can increase the forecast error significantly [30, 59]. The interaction process was first studied by Fujiwhara [40, 41, 42], who showed in laboratory experiments that two vortices of the same rotation with sufficiently small initial separation approach each other in a spiral orbit and eventually merge. Binary TC interaction was also investigated using idealized models (e.g. [34, 56, 72, 81, 91]). Shin et al. [96] and Holland et al. [56] developed estimates for the maximum initial separation that leads to a merger of the cyclones in a barotropic model. Several studies used vortex profiles with a core of positive relative vorticity surrounded by a ring of negative relative vorticity, mimicking the anticyclonic outflow of tropical cyclones. For these profiles solutions exist, in which two anticyclone-cyclone pairs form and propagate away from each other rapidly [12, 106]. As will be shown below, in such cases the cyclone tracks depend very sensitively on the initial conditions and thus presumably also on numerical errors caused by too coarse grids.

4.4.2 Setup of the test case

In the following we restrict our study to the symmetric case, i.e. the interaction of two identical vortices. We use a vortex defined by [97] with a wind profile resembling the one of a mature tropical cyclone. The tangential wind of the vortex is given by

$$v_{\mathrm{T}}(s) = v_0 \frac{s(1 + (6b/2a)s^4)}{(1 + as^2 + bs^6)^2} \ , \tag{4.18}$$

where $s = r/r_0$. For $a = 0.3398$, $b = 5.377 \times 10^{-4}$, $v_0 = 71.521\,\mathrm{ms}^{-1}$ and $r_0 = 100\,\mathrm{km}$, the maximum wind is $40\,\mathrm{ms}^{-1}$ (at $r = r_0$). The total circulation of this vortex is zero and the relative vorticity is negative for $r > 180\,\mathrm{km}$. As initial condition, two of these vortices are placed 200 km east and west of the center of a domain with a size of 4620 km $\times$ 4000 km. We employ doubly periodic boundary conditions and use the f-plane approximation with a Coriolis parameter $f = 0.62 * 10^{-4} s^{-1}$.

While the velocity or vorticity distribution of the two vortices is sufficient to fully define the initial conditions for non-divergent barotropic models, shallow-water models require, in addition, an initial fluid depth distribution $h_0(\mathbf{x})$. The variation δh_0 of the initial fluid depth distribution $h_0 : \Omega \to \mathbb{R}$ is the solution of the nonlinear balance equation

$$\triangle\,(\delta h_0) = \frac{1}{g} \nabla \cdot \left(-(\zeta_0 + f)\mathbf{k} \times \mathbf{v}_0 - \nabla(\frac{1}{2}\mathbf{v}_0^2) \right) \ , \tag{4.19}$$

derived by applying the divergence-operator $\nabla\cdot$ on both sides of Eq. (4.1) and assuming a divergence-free velocity field. The initial fluid depth is given by adding the variation to a constant background fluid depth H, i.e. $h_0 = H + \delta h_0$. For a sufficient geostrophic adjustment, the fluid depth h of the shallow-water equations of Eq. (4.1) has to be large enough to properly resolve the Rossby deformation radius. To achieve this, we choose a background fluid depth of $H = 10\,\mathrm{km}$ to obtain a Rossby deformation radius of 5096 km that is well resolved also in case of very coarse resolution, e.g. 8^2 cells ($\delta_{\mathrm{cell}} \approx 578\,\mathrm{km}$). For the test problem considered in this study, the variation of the fluid depth δh is small compared to H, so that solutions of non-divergent barotropic and shallow-water models are expected to be very similar.

In order to study the properties of the scenario, we performed high-resolution reference runs on uniform grids with the non-divergent barotropic model HiFlow^3 [2] (the finite element model that provides the error indicators, cf. Sect 4.4.4) with a resolution that corresponds to 1024^2 cells (approximate cell diameter $\delta_{\mathrm{cell}} \approx 4.85\,\mathrm{km}$) and with the shallow-water version of ICON-hex with 1024^2 cells ($\delta_{\mathrm{cell}} \approx 4.5\,\mathrm{km}$). The evolution of the vortices is followed for 4 days. We use a viscosity $\nu = 5000\,m^2/s$, which is sufficient to suppress numerical noise to an acceptable level, in both models.

4.4.3 Nonlinear evolution and sensitivity to initial conditions

For an initial distance of 400 km, i.e. four times the radius of maximum winds, the cyclones are too far apart to allow for a merger, but sufficiently close together for the two negative vorticity regions to overlap (Fig. 4.3, $t = 0$h). During the first 12 hours of the evolution, the zones of positive vorticity forming the vortex cores are strongly deformed and even connected to each other (see Fig. 4.3, $t = 6$h). In the initial phase the fluid with negative vorticity is advected into the regions behind the orbiting positive cores, thereby forming two cyclone-anticyclone pairs (Fig. 4.3, $t \leq 12$h). In each pair the circulation of the cyclone causes an advection of the anticyclone and the circulation of the anticyclone causes an advection of the cyclone in the same direction, leading to a rapid propagation of the pair.

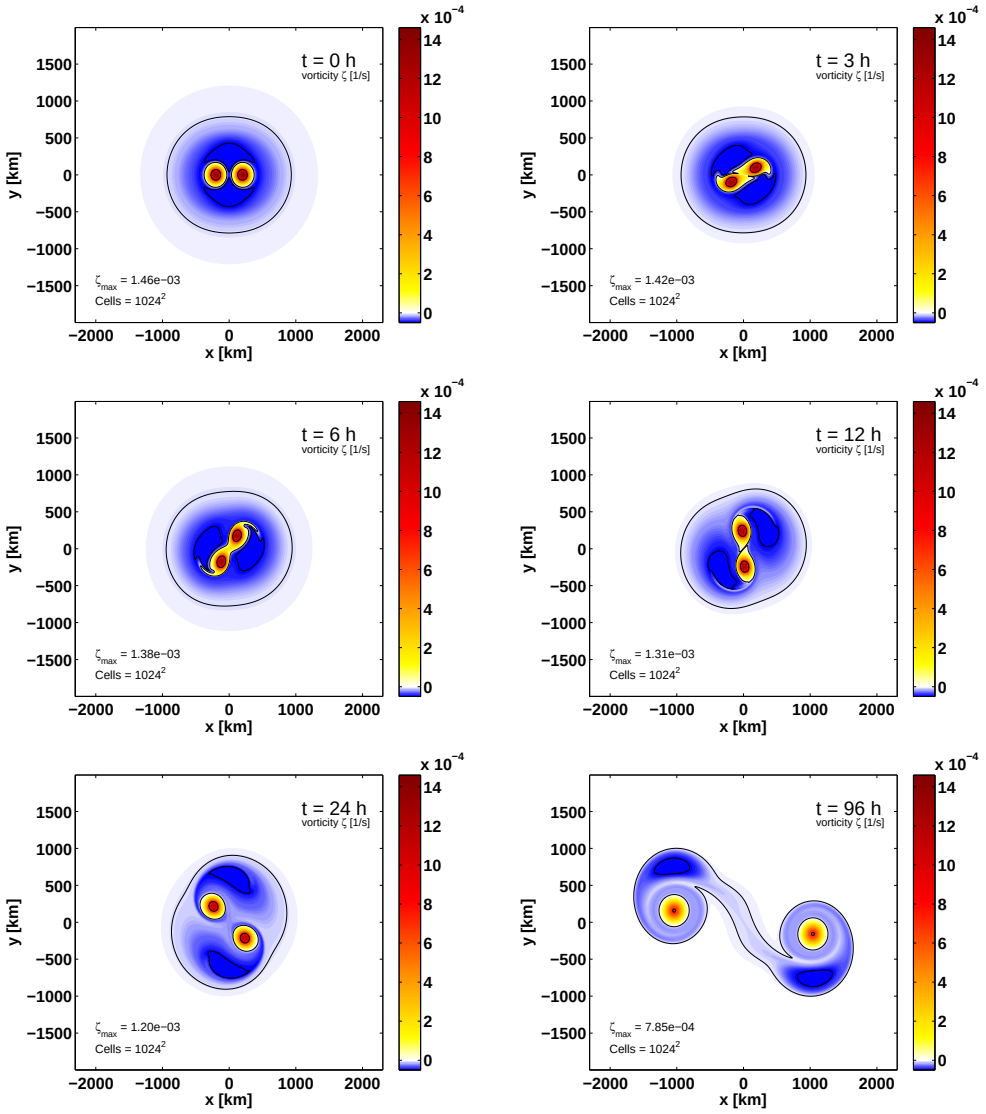

Figure 4.3: Evolution of the vorticity distribution with an initial TC separation of 400 km for a high-resolution ICON-hex shallow-water run with 1024^2 grid cells. The black contour lines denote $\zeta = -5 \times 10^{-5}\mathrm{s}^{-1}$, $\zeta = -5 \times 10^{-6}\mathrm{s}^{-1}$ and $\zeta = 7 \times 10^{-4}\mathrm{s}^{-1}$.

Due to this process, the orbiting motion of the positive cores that dominates the dynamics of the initial phase is replaced by a propagation of the two pairs into opposite directions. After 48 hours, the pairs follow straight tracks, indicating that their mutual influence has become negligible. A similar behavior of interacting vortices has been observed in simulations by Valcke and Verron [106] and in laboratory experiments by Beckers et al. [12].

Additional model runs show that this scenario is very sensitive to variations of the initial separation. If the initial separation is reduced to 390 km, the direction of the cyclone propagation in the final phase changes by 140°. For values below 380 km the solution changes completely and the cyclones merge. The high sensitivity to the initial conditions suggests that there is also a high sensitivity to numerical errors. This is a desirable property for a test case for adaptive methods, as the effect of insufficient resolution, in particular in the initial orbiting phase, should be clearly visible as track errors.

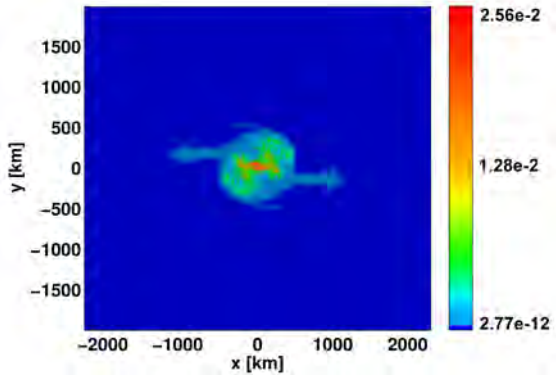

Figure 4.4: Error indicators (Eq. 4.6) corresponding to the goal functional defined in Eq. (4.20) determined by HiFlow^3 on a uniform mesh with 128^2 cells. Blue zones indicate low error contributions, red zones indicate high contributions to the error in the goal functional.

4.4.4 Error estimation using the finite element package HiFlow^3

We performed the goal-oriented error estimation described in Sect. 4.3.1 for the scenario discussed above using a non-divergent barotropic model, implemented in the general-purpose finite element package HiFlow^3 [2]. The discretization in space consists of stable Taylor-Hood elements on a uniform mesh with 128^2 cells. Hence, the cell's diameter is approx. 36 km and the distance between nodal points of the velocity discretization is $\delta_{\text{dof}} \approx 18\,\text{km}$. The time discretization is defined by the cGP(1) method [93], for further details see [10].

The estimation of errors requires the specification of a goal functional. In this study we focus on the correct prediction of the cyclone tracks. Therefore, we use the error in the final cyclone position to quantify the quality of numerical solutions. The cyclone position is characterized by the location of the maximal vorticity. However, the position determined in this way cannot be used directly as goal functional, since the latter must be differentiable. Instead we make use of a smooth functional that is strongly correlated with the position of the cyclones, defined as integrated kinetic energy over the storm cores at the final time T,

$$J(\mathbf{v}) := \int_\Omega \chi(\mathbf{x}, T)\ \|\mathbf{v}(\mathbf{x}, T)\|^2\ \mathrm{d}x\mathrm{d}y, \tag{4.20}$$

where the cores are defined as the regions where the vorticity ζ exceeds half of its maximum value,

$$\chi(\mathbf{x}, t) = \begin{cases} 1\ , & \zeta(\mathbf{x}, t) > 0.5 * \max_{x\in\Omega} \zeta(\mathbf{x}, t) \\ 0\ , & \text{else} \end{cases}. \tag{4.21}$$

The velocity varies strongly within the cyclone cores, and thus for a fixed region selected by χ, J is very sensitive to a displacement of the cyclones. The error indicators η_j computed for this goal functional (Fig. 4.4) thus indicate, which regions of the grid contribute significantly to the position error of the cyclones.

The error indicator distribution is symmetric, since both the initial conditions and the chosen goal functional are symmetric. The zones with the highest error contributions (red) are located between the initial positions of the two storms. This indicates that reducing the error in the initial phase, when the mutual interaction of cyclones is most pronounced, is decisive for improving the accuracy of the final storm position. The contributions along the

storm tracks, especially once the storms have started to diverge, are significantly smaller. Far from the storm tracks the error contributions are almost vanishing (dark blue). These error indicators are used to control the grid adaptation for the adaptive ICON-hex runs discussed in the following section.

4.5 Numerical results

4.5.1 Non-divergent barotropic and shallow-water solutions on uniform grids

Before we discuss the results of model runs on r-adapted grids, we will first discuss how for uniform grids the numerical solutions for our binary TC interaction test case depends on the resolution. For this purpose we consider runs with the ICON-hex shallow-water model on uniform grids with 64^2 ($\delta_{\text{cell}} \approx 72\,\text{km}$) to 1024^2 ($\delta_{\text{cell}} \approx 4.5\,\text{km}$) grid cells and compare the results with the reference solution obtained with the non-divergent barotropic model HiFlow^3 on a uniform grid with $\delta_{\text{dof}} \approx 4.5\,\text{km}$. The cyclone positions $\mathbf{X}(t)$ in these experiments are determined by computing the area-weighted center of the vortex core,

$$\mathbf{X}(t) = \int_{\Omega_R} \mathbf{x}\,\chi(\mathbf{x},t)\mathrm{d}A \Big/ \int_{\Omega_R} \chi(\mathbf{x},t)\mathrm{d}A\ , \tag{4.22}$$

where we use the function χ of Eq. (4.21) to identify the vortex cores. This method allows us to measure the cyclone position with sub-grid precision. The integration region Ω_R is chosen such that it contains only the vortex that is located to the right of the origin in the initial state. Due to the symmetry of the solution the position of the cyclone located originally to the left of the origin is given by $-\mathbf{X}(t)$.

Figure 4.5 displays the cyclone tracks calculated on uniform ICON-hex grids (solid lines) for different resolutions (adapted runs are discussed further below). As expected due to the high sensitivity of the solutions to the initial conditions (cf. Sect. 4.4.3), the cyclone tracks depend strongly on the grid resolution. With increasing resolution the shallow-water ICON-hex tracks converge towards a solution that is very similar to the non-divergent barotropic HiFlow^3 reference track (black). This agreement supports our assumption that the error indicators from HiFlow^3 could be a reasonable approximation for the actual errors arising in the shallow-water runs.

The errors in the final vortex position $\mathbf{X}(T = 96\,\text{h})$ of the shallow-water runs, compared to the reference run, decrease from 690 km for a uniform ICON-hex grid with 64^2 cells to less than 4 km for a uniform grid with 1024^2 cells, an error which is comparable to the cell diameter of this grid, $\delta_{\text{cell}} \approx 4.5\,\text{km}$.

4.5.2 Simulations on r-adapted grids

In the following we present the results of model runs on grids adapted with the methods described in the previous sections. In all of these cases the grid adaptation is based on the error indicators displayed in Fig. 4.4. Furthermore, in all cases the adapted grids are constructed with an area fraction of $b = 1\%$ and a smoothing length of $d = 550\,\text{km}$. This choice of parameters results in well-suited grids similar to the grid shown in Fig. 4.8A, as will be discussed in Sect. 4.5.3. We consider refinement levels γ between 2 and 4, and grids with $n = 64^2$ to $n = 1024^2$ cells.

Using the error in the final cyclone position for a comparison of solutions on adapted and uniform grids turned out to be problematic. When evaluating the accuracy of the predicted cyclone tracks on uniform grids, the error of the final cyclone position $\mathbf{X}(T)$ with

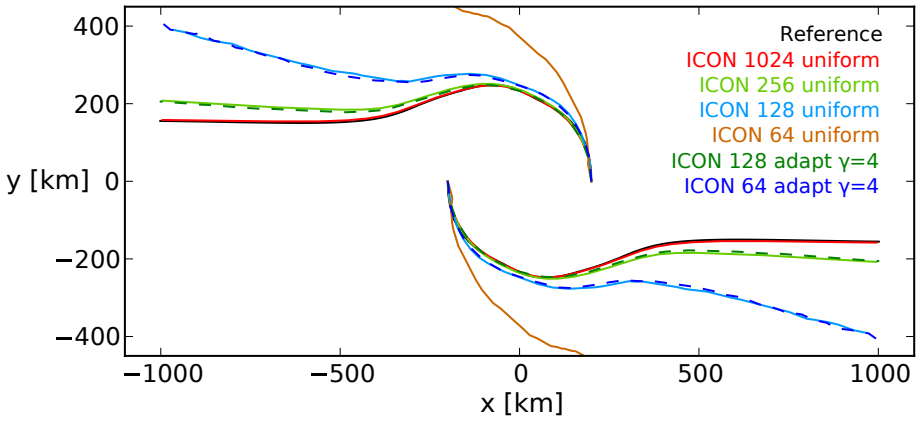

Figure 4.5: Cyclone tracks calculated with the ICON-hex shallow-water model for different resolutions. The numbers displayed in the plot for each line indicate the square root of the number of grid cells used in the model run. The black line is the track for the reference solution of the non-divergent barotropic model HiFlow^3 with $\delta_{\text{dof}} \approx 4.5\,\text{km}$. Tracks for r-adapted ICON-hex runs are shown in dashed lines.

respect to the reference track is an adequate and reliable measure. However, on adapted grids where the grid cells differ in shape and size along the cyclone tracks, we find cases where final vortex positions are relatively close to the correct position, although at earlier times the tracks show significant differences to the reference tracks. To assess the quality of the solution it seems thus more useful to consider the time-averaged position error with respect to the reference run,

$$E_{\text{shw}} := \frac{1}{T}\int_0^T ||\mathbf{X}(t) - \mathbf{X}_{\text{shw}}(t)||dt \ , \tag{4.23}$$

as an error measure. Here $\mathbf{X}_{\text{shw}}(t) \in \Omega$ is the cyclone position at time t (defined analogously to Eq. (4.22)) for the shallow-water reference track calculated on the highest resolved ICON-hex grid with 1024^2 cells (cf. Fig. 4.3). We denote E_{shw} as *mean position error*. All errors presented in the following are meant as mean position errors, unless otherwise stated.

The evaluation of mean position errors for the adapted runs shows that for all refinement levels, the tracks of adaptive runs converge with increasing number of grid cells towards the track of the reference solution (Fig. 4.6). In all cases the mean position errors can be reduced to less than $E_{\text{shw}} \leq 3\,\text{km}$, which is already smaller than the cell diameter of $\delta_{\text{cell}} \approx 4.5\,\text{km}$ in the reference solution. The runs on adapted grids predict cyclone tracks thus comparably accurate as runs on uniform grids. However, for a given maximum error significantly fewer grid cells are required for runs on adaptive grids, compared to the uniform grid runs (black line in Fig. 4.6). To obtain an error of less than $E_{\text{shw}} \leq 3\,\text{km}$, 512^2 grid cells are required on uniform grids. For grids with refinement level $\gamma = 2$, we achieve the same accuracy using only 362^2 grid cells. With $\gamma = 3$, the number of grid cells can be further reduced to 240^2 cells and 222^2 grid cells are sufficient for $\gamma = 4$.

The local resolution of an adapted grid with refinement level γ and n grid cells does not exceed the resolution of a uniform grid with γn cells. Therefore, the best result one can expect for the error of the adaptive run is, that it is close to the error of the uniform grid run using a factor of γ more cells. This is the case for our adaptive runs, as indicated

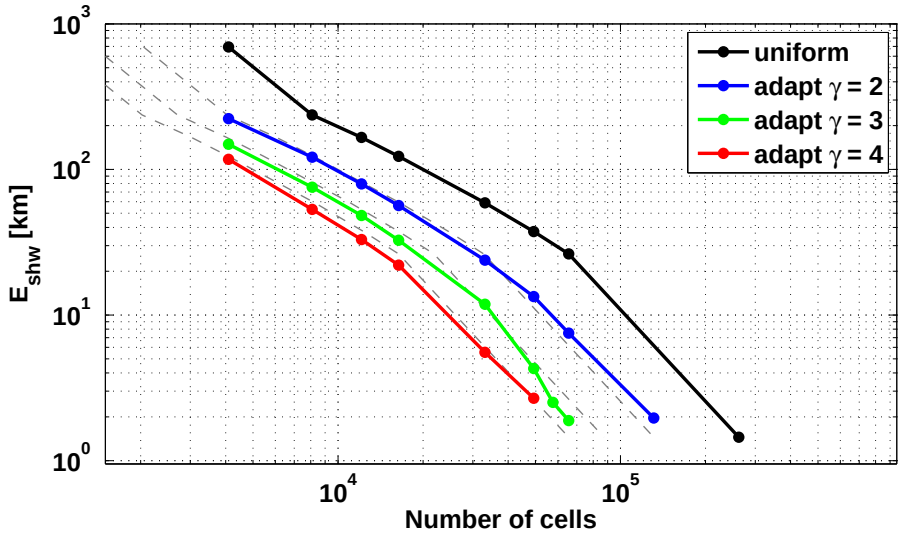

Figure 4.6: Mean position errors of shallow-water solutions with respect to a high-resolution reference run as a function of the number of grid cells $n = N^2$ for adapted grids with $\gamma = 2, 3, 4$. All adapted grids share the parameters $b = 1\%$ and $d = 550\,\mathrm{km}$. The error for uniform grids, $E_{\mathrm{shw}}(n)$, is displayed as a black line. The dashed lines correspond to errors of uniform grids using γn cells, i.e. the best results that can be expected for adapted grids with n cells and $\gamma = 2, 3, 4$ (see text).

by the agreement of colored and dashed lines in Fig. 4.6. An example for this relation between solutions on adaptive and uniform grids is also shown in Fig. 4.5. The cyclone tracks calculated on adapted ICON-hex grids with 64^2 and 128^2 grid cells with a refinement level of $\gamma = 4$ (dashed lines) are very similar to the tracks obtained for uniform grids with 128^2 and 256^2 cells, respectively.

These results can be summarized as follows: Coarser grids can be used outside of the region where the error indicators are large without affecting the accuracy of the track prediction significantly. Grids adapted in this way allow for a substantial reduction of the number of grid cells required to achieve a certain accuracy. However, this approach requires an adequate choice of the grid adaptation parameters and is not possible for arbitrarily large refinement levels, as we will discuss in the next section.

4.5.3 Influence of the grid adaptation parameters on the accuracy in track prediction

The grid adaptation parameters γ (refinement level), b (area fraction), and d (smoothing length) determine, how the DWR error indicators are used to adapt the grid (see Sect. 4.3.3). Only parameter combinations from a certain part of the parameter space lead to adapted grids that allow for accurate track predictions. By means of additional adaptive model runs for a wide range of parameters, we investigate the relations between adaptation parameters, grid quality and the error in the track prediction.

Taking the discussion in the previous section into account, the quality of a solution obtained for a refinement level γ using n grid cells should be assessed by a comparison with the solution on a uniform grid with γn grid cells. In the following, we will therefore use the mean position error with respect to this solution, instead of the high-resolution

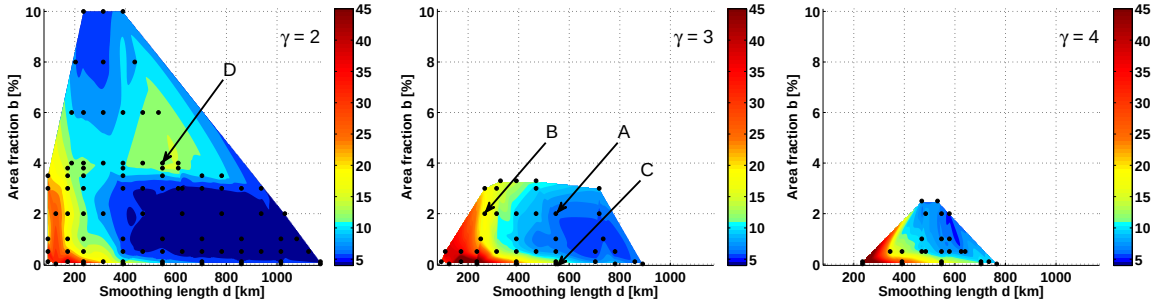

Figure 4.7: Mean position errors $E_\gamma(b, d)$ [km] for $\gamma = 2, 3, 4$ as a function of area fraction b and smoothing length d for adapted grids with 128^2 cells, with red for high and blue for low errors. Black dots represent individual adaptive runs. The values between these runs are obtained by quadratic interpolation. White areas indicate regions, where no grids exist that fulfill the grid duality constraint. The arrows indicate parameter pairs that correspond to the meshes shown in Fig. 4.8A - 4.8D.

reference solution. Analogously to Eq. (4.23) we define

$$E_\gamma(b, d) := \frac{1}{T} \int_0^T ||\mathbf{X}_{\text{adapt}}(t) - \mathbf{X}_{\text{uni}}(t)|| dt \,, \tag{4.24}$$

where $\mathbf{X}_{\text{adapt}}(t)$ and $\mathbf{X}_{\text{uni}}(t)$ denote the position of one of the two cyclones at time t for solutions calculated on an adapted ICON-hex with n cells and a uniform ICON-hex grid with γn cells, respectively.

The evaluation of $E_\gamma(b, d)$ for runs on adapted grids with different parameter combinations shows that for each refinement level $\gamma = 2, 3, 4$ a region in the $b-d$ plane can be found where the error is small (blueish areas in Fig. 4.7). The parameter combination $b = 1\%$ and $d = 550\,\text{km}$ used for the adaptive runs discussed in Sect. 4.5.2 is located in these regions for all considered refinement levels. For the white areas in Fig. 4.7, the parameters lead to adapted grids that do not fulfill the grid duality constraint (see Sect. 4.3.3) and are therefore not suitable for integrations. The usable region in the $b - d$ plane shrinks with increasing γ. For $\gamma = 5$ no valid grid could be found. Within the regions that correspond to valid grids, the error varies strongly. In particular, for small area fractions b and small smoothing lengths d high errors up to $E_\gamma \approx 60\,\text{km}$ result for all three refinement levels. The results displayed in Fig. 4.7 are obtained for 128^2 grid cells. Other numbers of grid cells n lead to similar results. In particular, small errors are found in the same parts of the $b - d$ plane for all grid cell numbers n investigated.

For four examples of (γ, b, d) parameter combinations marked with labels A, B, C, and D in Fig. 4.7, we discuss the properties of the corresponding grids and their influence on the mean position errors $E_\gamma(b, d)$. The cell area distributions for these cases are displayed in Fig. 4.8 for grids with 128^2 cells. The shape and size of the high-resolution regions (dark blue) varies significantly for different parameter combinations. For a quantitative description of the deformation of grid cells we consider also the edge length ratio

$$\Delta l_{\text{hex}}(\mathbf{x}) := \frac{\max\ l_{\text{hex}}(\mathbf{x})}{\min\ l_{\text{hex}}(\mathbf{x})} \,, \tag{4.25}$$

where $l_{\text{hex}}(\mathbf{x})$ describes the edge lengths of the hexagonal cell at point $\mathbf{x}$ (cf. Fig. 4.1). High values of Δl_{hex} indicate strongly deformed cells. Contour lines for Δl_{hex} are included in Fig. 4.8.

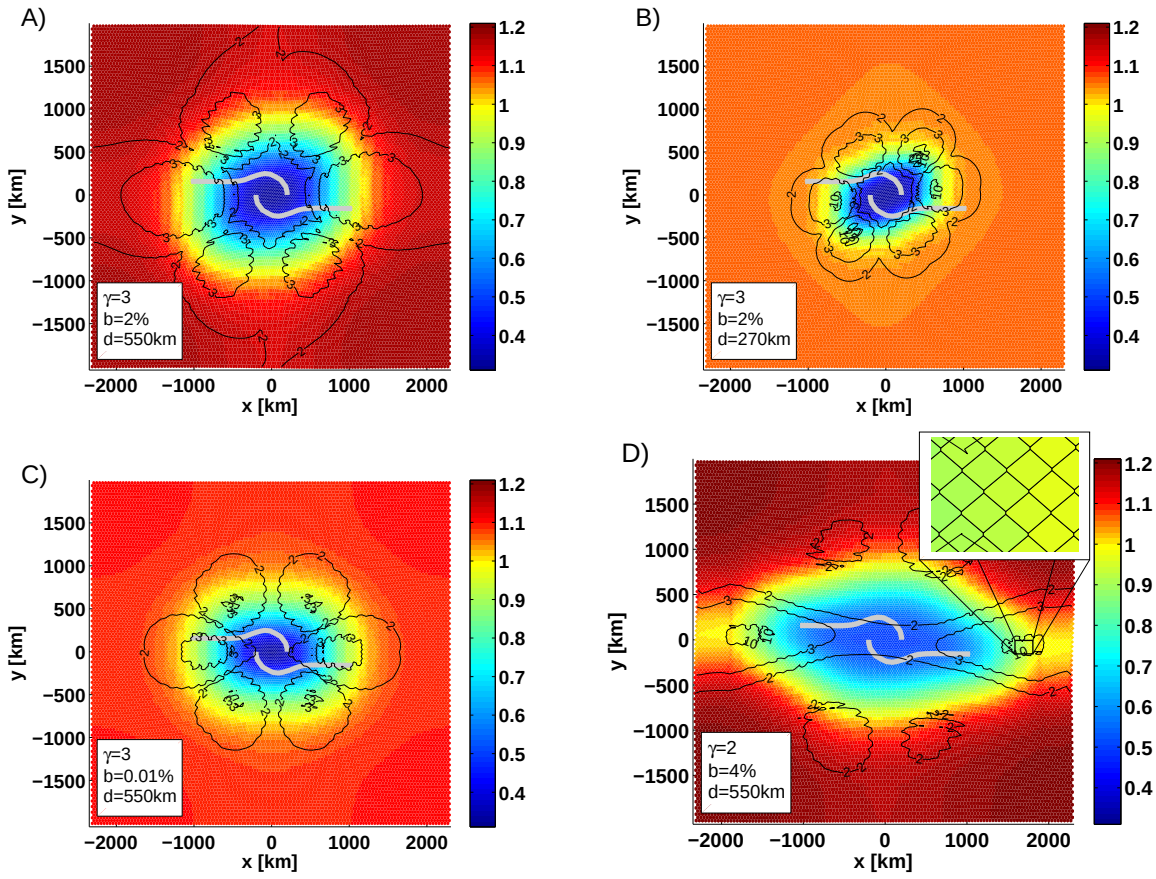

Figure 4.8: Cell area and deformation distributions resulting for different combinations of grid adaptation parameters b, d, γ. The colors indicate the cell areas, with blue for the finest and red for the coarsest cells on meshes with 128^2 grid cells. The gray lines are the shallow-water reference tracks. The black contour lines correspond to $\Delta l_{\mathrm{hex}} = [2, 3, 10, 25]$ and allow for an identification of regions with deformed cells. The inset in D) shows the strongly deformed grid cells in a region with high Δl_{hex}.

In the grid for the parameters combination $\gamma = 3$, $b = 2\%$ and $d = 550\,\mathrm{km}$ (case A in Fig. 4.7) the high-resolution area (dark blue) completely covers the region, in which the initial orbiting of the cyclones takes place and where the largest values for the error indicators are found (Fig. 4.4). This region contains cells with quite regular shapes, which can be inferred by the fact that it is not intersected by the contour lines for Δl_{hex}. Only in the end phase of the model run the cyclones encounter regions where the grid resolution becomes lower and the deformation increases. However, according to the error indicators (Fig. 4.4), the errors in the early phase are much more important for the accuracy of the final cyclone position. This grid leads to a low mean position error of $E_{\gamma=3}(2\%, 550\,\mathrm{km}) \approx 7\,\mathrm{km}$ compared to the corresponding reference solution (cf. Eq. (4.24)).

In case B a smaller smoothing length d and in case C a smaller area fraction b yield grids with smaller high-resolution areas. Also the regions with highly deformed grid cells are located at smaller distances to the origin. In both cases, the cyclones therefore encounter increasing cell sizes and deformed cells already in the initial orbiting phase, earlier than in case A. On both grids the solutions show higher errors than in case A, $E_{\gamma=3}(2\%, 270\,\mathrm{km}) \approx 20\,\mathrm{km}$ for case B and $E_{\gamma=3}(0.01\%, 550\,\mathrm{km}) \approx 16\,\mathrm{km}$ for case C. These increased errors are probably related to a reduced order of differential operators on non-uniform grids (see

[88, 89]). In case A also non-uniform grid regions exist, but they have an influence on the cyclone motion only at later times, so that the impact on the mean position error is much weaker.

The highly deformed cells in cases A, B, C are generated at strong gradients of the cell area distribution. When the smoothing length is reduced further, these gradients are enhanced and the cell deformations become too large to allow for grids fulfilling the grid duality constraint. Also larger refinement levels increase the cell area gradients. For this reason, no valid grids with small errors could be found for $\gamma > 2$ and small smoothing lengths. If b or d is increased from the values of case A, the high-resolution area grows and the high-deformation regions move further away from the origin. In general, the mean position error remains therefore low. However, when the high-resolution area is enlarged, the number of grid points in the rest of the domain decreases and the cell areas grow. If there are too few grid points left, the resulting grid cells outside of the high-resolution area are so strongly deformed that they do not fulfill the grid duality constraint any more. Thus, no valid grids exist for large values of b and d. Also this effect becomes enhanced when γ is increased. This explains why the part of the $b - d$ parameter space leading to valid grids shrinks with increasing γ (Fig. 4.8) and vanishes for $\gamma > 4$.

Even for relatively large values of b and d and within the region of valid grids unfavorable parameter combinations exist, as case D demonstrates. For parameters $b \geq 4\%$ and $d \geq 550\,\mathrm{km}$, we could not construct grids that fulfill the grid duality constraint for the refinement levels $\gamma = 3, 4$. However, for grids with $\gamma = 2$ we find valid adapted grids, for example the one shown in Fig. 4.8D with $b = 4\%$ and $d = 550\,\mathrm{km}$. This grid shows very smooth transitions between coarse and fine resolved grid areas and due to the relatively large value of b the full tracks are contained in the high-resolution region. Therefore, one would expect very accurate solutions. However, compared to Fig. 4.8A, this grid shows a higher error of about $E_{\gamma=2} \approx 14\,\mathrm{km}$, as indicated by the green region in the leftmost panel of Fig. 4.7. The reason for this result is that the high-resolution region spans over a large fraction of the width of the domain and comes relatively close to the domain boundary. This causes a band of strongly deformed cells to spread over the full width of the domain, including the initial orbiting region in the center. The strongest deformations are found where the high-resolution area is closest to the boundary. Here, the hexagonal cells are almost degenerated to quadrangles, as the inset in Fig. 4.8D shows. As in cases B and C, the mean position error is probably increased because the cyclone encounters in a early phase grid regions with deformed cells, where the order of the operators is decreased.

These examples show that too strong grid cell deformations have to be avoided to obtain suitable grids. Deformed cells in regions where the error indicators are large cause an increase in the mean position error that is probably related to the reduced order of the operators on non-uniform grids. In regions where the error indicator is low deformed grid cells should not have a large impact on the track prediction. However, they can also become problematic, if the cell deformation there is so strong that the grid duality constraint cannot be fulfilled any more. These problems can be avoided, when the transition zones between areas of high and low grid resolutions are sufficiently wide and contain enough grid points. In particular, a certain minimum domain size is required to allow for a sufficiently smooth transition from the coarse grid at the domain boundary to high resolution regions in the inner part of the domain. As the grid deformation is stronger for higher refinement levels, the maximum achievable refinement level, for our setup $\gamma = 4$, is thus limited by the domain size.

4.6 Summary and conclusion

Modeling the motion and evolution of tropical cyclones accurately is an important and challenging problem. Interacting processes on a large range of scales need to be represented adequately in the numerical model, so that both a large domain and high resolution are required. Adaptive grid refinement is a promising method to deal with such multiscale problems, as long as high resolution is not required throughout the whole domain. In this case local grid refinement has the potential to reduce the computational effort required to obtain a solution with a given accuracy substantially.

The quality of numerical solutions if often measured by a global error norm. However, in many cases high accuracy in certain properties of the solution is more important. For tropical cyclones mainly the location and intensity of the storm are of interest and the error in these quantities can be used to assess the quality of a solution. By means of the dual-weighted residual method (DWR) it is possible to estimate the contribution of each grid cell (in time and space) to the error in a user-defined quantity, which is formulated as a goal functional and can e.g. be related to the storm position. By increasing the resolution in regions with high error contributions, e.g. by subdividing cells (h-adaptivity) or moving grid points into these regions (r-adaptivity) the error in the goal functional can be minimized.

In this work we have demonstrated for an idealized TC scenario how DWR-based error estimates can be used to generate r-adaptive grids that allow for an efficient prediction of cyclone tracks. ICON-hex, the r-adaptive hexagonal C-grid shallow-water version of the next generation NWP and climate model ICON, was used to perform model runs on these static grids. As a DWR-based error estimator is not yet available for ICON-hex, we computed error information based on the non-divergent barotropic equations using the finite element code HiFlow^3.

The test case considered in this work is an example for the interaction of two tropical cyclones in a barotropic model. In our setup the cyclones orbit each other initially, before they separate and propagate in opposite directions. The numerical solution for this problem depends sensitively on the initial conditions and numerical errors in the initial orbiting phase, as a resolution study using uniform grids has shown. Furthermore, for this test case shallow-water and non-divergent barotropic results converge with increasing resolution towards very similar solutions, which motivated our approach of using error estimates from HiFlow^3 to control the adaptation of ICON-hex grids.

The goal functional chosen for this study, the integral of kinetic energy over the cyclone cores, is strongly correlated with the cyclone positions. The error contributions computed for each cell using this goal functional thus indicate, where the resolution should be increased to minimize the error in the cyclone positions. From these error indicators we estimated the local resolution required to bring the local error below a chosen threshold. Following Semper and Liao [95] an algorithm involving the solution of an Poisson problem was used to move grid points such that the desired local cell sizes were realized. Several parameters influenced this grid adaptation process: The refinement level used to adjust the minimum cell area, the area fraction that determines the part of the domain covered by the smallest grid cells and the smoothing length that controls the minimum width of transition zones between the fine and coarse grid regions.

The results of ICON-hex runs on adapted grids show that for reasonably chosen grid refinement parameters, the number of degrees of freedom (DoFs) can be decreased significantly while maintaining high accuracy in the cyclone track prediction. For these runs the time-averaged error in the cyclone position is determined by the size of the smallest

grid cells and comparable to the error for a uniform grid with the same grid cell size. For a domain size of 4620 km $\times$4000 km we were able to reduce the number of DoFs by a factor of 4 while constraining the mean position error to less than 3 km. Even stronger reductions should be possible for larger domains. These results demonstrate that coarser grids can be used outside of the region where the error indicators are large without loosing precision in the track prediction.

To achieve a high accuracy in the track prediction the parameters controlling the grid adaptation have to be chosen adequately. In particular, our results indicate that it is necessary that a grid with high resolution consisting of cells with nearly constant size and regular shape covers the part of the domain where the initial orbiting of the two cyclones takes place. Grids for which the cell sizes vary too strongly or the deformation of the cells is too pronounced in this region lead to larger errors, which may be related to a reduced order of differential operators on non-uniform grids (see [88]). When the high-resolution area is made too large, grids with strongly deformed cells (e.g. hexagons that are nearly degenerated to quadrangles) result or the grid duality constraint (the circumcenters of the triangles must lie within its triangular boundaries) is not fulfilled any more. These problems arise when not enough grid points are left outside of the high resolution area. For a given maximum error of the solution the ratio of maximum to minimum cell area that can be achieved is thus limited by the size of the domain.

We plan to develop our grid adaptation method further in a way that reduces the number of parameters required to control the adaptation. Similar to the approach of [87], the adaptation should automatically lead to well-suited grids. For this purpose the DWR error information could be used to determine for which grid cells it is important to minimize the deformation. Furthermore, we plan to compare the goal-oriented grid adaptation approach with methods based on the minimization of global norms and methods that use gradient-based criteria to determine in which regions the resolution has to be increased. Such a comparison should prove helpful in assessing whether a higher efficiency for grids adapted with goal-oriented methods justifies the additional effort required to compute DWR-based error information.

The error indicators used to control the grid adaptation in this work were computed with HiFlow^3 using different numerical methods for a different set of equations than in the adaptive runs performed with ICON-hex. Nevertheless, runs on the adapted grids showed the desired high accuracy of the predicted tracks. In future studies it should be investigated if this result is generalizable to other scenarios and different model combinations. This approach could be very useful for complex GCMs, for which the calculation of DWR error information is rather expensive. If it should turn out that computationally cheaper models (e.g. with reduced resolution or simplified physics) can provide sufficiently accurate error indicators, the computational cost of goal-oriented grid adaptation for GCMs could be reduced substantially.

Chapter 5

Conclusions and Outlook

This work dealt with the problem of developing suitable finite difference schemes for r-adaptive grid refinement on the basis of a generalized discretization approach for the equations of geophysical fluid dynamics (GFD). We also discussed applications of such r-adaptive models to investigate geophysical phenomena. In particular, we have proposed the following, to our best knowledge new, approaches:

- a formulation of the invariant equations of GFD that consists in splitting them into topological and metric parts, enabled by the introduction of additional auxiliary prognostic variables;
- a systematic discretization method, in which the discrete scheme descends directly from the choice of the topological meshes and from the discrete metric equations;
- a normal vector reconstruction approach for hexagonal C-grid shallow-water models based on the representation of the Coriolis terms by means of the extrusion;
- a method for goal-oriented grid adaptation, in which the computationally expensive sensitivity analysis and the model runs are not necessarily to be performed by the same model.

We used these methods to derive a hexagonal C-grid discretization of the nonlinear rotating shallow-water equations with goal-oriented grid adaptation, for which we performed the following steps. Applying the systematic discretization method on the linear non-rotating shallow-water equations in topological and metric form, we developed a hexagonal C-grid discretization of these equations with adequate consistency, stability and wave properties on uniform and r-adapted grids. We applied our vector reconstruction approach based on extrusion to obtain the normal vector component required for the discrete hexagonal C-grid scheme of the linear rotating shallow-water equations. An extension toward an hexagonal C-grid scheme for the nonlinear rotating shallow-water equations has been achieved by using methods from literature.

Using our method, we have provided for this model goal-oriented r-adaptivity. By a linear sensitivity analysis, the contribution of each grid cell to the error in a user-defined quantity can be evaluated and the required local resolution to minimize this error can be estimated. As mentioned, the model performing the sensitivity analysis and the model running the experiment are not necessarily the same. Using two different models, we could demonstrate, for the scenario of two interacting tropical cyclones (TC), that the number of grid points required to achieve a certain accuracy in the cyclone track prediction could be substantially reduced.

5.1 Addressing the research questions

Based on the results of this work, we return to the research questions posed in Sect. 1.1:

1.) How can we derive suitable finite difference schemes for r-adaptive grid refinement using a generalized discretization approach?

On the basis of an invariant formulation of the geophysical fluid equations, we split the equations into topological and metric parts by introducing auxiliary prognostic variables. This new set of equations allows a systematic discretization by applying the tools of discrete exterior calculus (DEC). The discrete momentum and continuity equations are represented on purely topological meshes using the concept of chains and cochains. The discrete metric equations are represented by a discrete Hodge-star operator and by an interior product connecting the topological meshes. By the choice of the topological meshes and of the discrete representation of the metric equations, the discrete finite difference scheme follows directly. In particular, both, a triangular and a hexagonal C-grid discretization of the linear non-rotating shallow-water equations, show stability and consistency on uniform and r-adapted grids.

2.) Could such general approach provide new knowledge about the equations of GFD? What practical benefit do we gain in the process of discretization?

Using the invariant set of equations, we have introduced a representation of the Coriolis term by means of exterior calculus, in particular, we employed the concept of extrusion. This provides a geometrical explanation on how the Coriolis force acts on the flow field.

Based on the discrete representation of extrusion, we have introduced a new method for consistent normal vector reconstruction out of neighboring tangential vector components. The weights are determined by the ability of the tangential vector components to contribute to the extrusion. On uniform grids, we have obtained a stable scheme, with proper wave representation, comparable to others from literature, but without imposing similar constraints. This would make the scheme easier to generalize to the three-dimensional case.

3.) What kind of scenarios in geophysical applications profit from grid adaptation? How do we actually adapt the grid to increase the accuracy of model solutions?

For scenarios in which high resolution is not required throughout the entire domain, adaptive grid refinement contributes to an accurate solution while reducing the computational costs. An example of such scenarios is the interaction of two tropical cyclones, in which the cyclones orbit each other initially before they separate and propagate in opposite directions. For an accurate prediction of the cyclone tracks, high resolution is mainly required in the region where the initial orbiting takes place.

When adapting the grid, the automatic optimization of the mesh with respect to some application-specific error measures (goal-oriented adaptivity) is a promising approach. Such error measures (goal functionals), for instance, the error in the track prediction of the TCs, are often more useful in assessing the quality of a numerical solution than global error norms. By a linear sensitivity analysis, the contribution of each grid cell to the error in the goal functional can be estimated and, in turn, the required local resolution to minimize this error. We used for the TC scenario such error estimates to generate r-adaptive grids that efficiently predict the cyclone tracks. Hereby, we innovatively combined two different models with different numerics and complexity; a finite element model provided the error estimates and a finite difference model performed the test runs on the r-adapted grids.

5.2 Outlook

The research questions of this thesis mirror some challenges arising in the process of developing and using models with r-adapted grid refinement. With respect to the available literature, we suggest a new approach for each research question, which may be followed in future research independently from the others. This could lead to a better understanding of finite difference schemes on meshes based on general polytopes and could provide indications on how to reasonably choose geophysical scenarios that profit from r-adaptive grid refinement.

For our formulation of the geophysical fluid equations, consisting in a topological and in a metric part, one may investigate different discrete Hodge-star operators translating into different discrete schemes. The barycentric Hodge-star operator, leading to a barycentric dual mesh, would allow a grid deformation stronger than in case of circumcenter duals. The non-diagonal Hodge-star operator (Galerkin-Hodge) [25, 23], leading to stable schemes in computational electrodynamics (CED), could be used for GFD. How the properties of such discrete schemes would look like and whether some properties present in CED transfer to GFD, for instance, whether the stability of the Galerkin-Hodge would lead to a stable model in GFD, could be content of future studies. Based on the similarity in form of the invariant geophysical fluid equations and of Maxwell's equations it seems possible to generalize our new discretization method toward higher-order schemes by using more than one degree of freedom per edge, face or cell, similarly to the concepts developed for CED by Bossavit [26].

The suggested vector reconstruction approach by using extrusion to describe the Coriolis term should be generalized to non-uniform grids. The similarity with the method suggested by Thuburn et al. [102] on uniform grids underpins our strategy of using geometrical constraints on the equations to derive the weights. Knowing, by an eigenvalue analysis, that those weights have to be antisymmetric with exchange of the contributing edges also on non-uniform grids, the extrusion gives us a strong hint on the properties of the weights. Therefore, a consistent derivation of those antisymmetric weights seems to be achievable but have to be subject of future work.

In this work we used the error indicators computed with the finite element model HiFlow^3 [2] to control the grid adaptation of the ICON-hex model, although both models use different numerical methods for a different set of equations. Nevertheless, runs on the adapted grids showed high accuracy of the predicted cyclone tracks. In future studies it should be investigated whether such results also hold for other scenarios and different model combinations. This approach could be very useful for complex general circulation models (GCMs), for which the calculation of error information is rather expensive. Reasonably accurate error indicators could in fact be provided by computationally cheaper models (e.g. with coarser resolution or simplified physics), abating thus substantially the costs of goal-oriented grid adaptation for GCMs.

Appendix A

Operators of exterior calculus and differential geometry

In this chapter we provide the general definitions and theorems of exterior calculus and differential geometry that are required for a comprehensive derivation of the invariant fluid equations, presented in Appendix B, and for the derivation of the invariant geophysical fluid equations, presented in Chapter 2. The definitions and theorem are taken from Abraham and Marsden [1] and, in Section A.3, of Kambe [60].

A.1 Differential forms

To define differential forms, one usually defines first an exterior algebra. The linear space of k-forms is then extended fiberwise to the tangential bundle $\mathcal{TM}$.

Exterior algebra

Let V be a vector space over $\mathbb{R}$ and V^* its dual space, i.e. the space of all linear maps with $V \to \mathbb{R}$. Then, a k-form on V is a multi-linear and skew-symmetric mapping

$$\omega^k : \underbrace{V \times \cdots \times V}_{k} \to \mathbb{R} \ . \tag{A.1}$$

The space of all k-forms is a real vector space and denoted with $\Lambda^k V^*$.

If $\alpha \in \Lambda^k V^*$ and $\beta \in \Lambda^l V^*$, we define the *exterior* (or *wedge*) *product* $\alpha \wedge \beta \in \Lambda^{k+l}$ by

$$\alpha \wedge \beta = \frac{(k+l)!}{k!l!} \mathbf{A}(\alpha \otimes \beta) \ , \tag{A.2}$$

where $\Lambda^k V^*$ is a tensor with k multi-linear maps, $\otimes$ the tensor product and $\mathbf{A}$ an alternating map, i.e. if two entries of $\mathbf{A}$ are exchanged, the sign changes. This product has the following properties:

Proposition A.1.1. *For $\alpha \in \Lambda^k V^*$, $\beta \in \Lambda^l V^*$ and $\gamma \in \Lambda^m V^*$, we have*

(i) $\alpha \wedge \beta = \mathbf{A}\alpha \wedge \beta = \alpha \wedge \mathbf{A}\beta$,
(ii) $\wedge$ *is bilinear* ,
(iii) $\alpha \wedge \beta = (-1)^{k+l} \beta \wedge \alpha$,
(iv) $\alpha \wedge (\beta \wedge \gamma) = (\alpha \wedge \beta) \wedge \gamma$.

The direct sum of the spaces $\Lambda^k V^* (k = 1, 2, \ldots, n)$, i.e. $\Lambda(V^*) := \otimes_{k=0}^{n} \Lambda^k V^*$, together with its structure as a real vector space and multiplication induced by the wedge product $\wedge$ is called the *exterior algebra* of V^*, or the *Grassmann algebra* of V^*.

Differential forms

We put this structure of the linear algebra fiberwise on the bundle $\mathcal{T}M$. Using the differentiable atlas, the k-forms (see e.g. Eq. (2.3)), can be extended to differential forms on the manifold $\mathcal{M}$. We denote the space of differential k-form with $\Omega^k(\mathcal{M})$.

A.2 Operations on differential forms

Let E be an oriented n-dimensional vector space. The isomorphism $\star : \Lambda^k(E) \to \Lambda^{n-k}(E)$ of the following proposition is called the *Hodge-star operator*, dependent on the metric $\mathbf{g}$ and the volume-form μ.

Volume-form Let $\Omega = dx^1 \wedge \cdots \wedge dx^n \in \Omega^n(\mathbb{R}^n)$ be a standard *volume-form* on $\mathbb{R}^n$ with $\Omega(x) \neq 0 \forall x \in \mathbb{R}^n$. Using the atlas, this can be generalized to a volume-form $\mu \in \Omega^n(\mathcal{M})$ on $\mathcal{M}$ with $\mu(x) \neq 0 \forall x \in \mathcal{M}$.

Hodge-star operator

Proposition A.2.1 (Abraham and Marsden [1])**.** *Let E be an oriented n-dimensional vector space and $\mathbf{g} =<,>\in T_2^0(E)$ a given symmetric and non-degenerate tensor. Let μ be the corresponding volume element of E. Then there exists a unique isomorphism $\star : \Lambda^k(E) \to \Lambda^{n-k}(E)$ satisfying*

$$\bar{\alpha} \wedge \star\bar{\beta} =< \bar{\alpha}, \bar{\beta} > \mu \quad \textit{for} \quad \bar{\alpha}, \bar{\beta} \in \Lambda^k(E) \ . \tag{A.3}$$

If $(\vec{e}_1, ..., \vec{e}_n)$ is a positively oriented $\mathbf{g}$-orthonormal basis of E and $(\vec{e}^1, ..., \vec{e}^n)$ its dual basis, then

$$\star(\vec{e}^{\sigma(1)} \wedge ... \wedge \vec{e}^{\sigma(k)}) = c_{\sigma(1)}...c_{\sigma(k)}\mathrm{sign}(\sigma)(\vec{e}^{\sigma(k+1)} \wedge ... \wedge \vec{e}^{\sigma(k+n)}) \ , \tag{A.4}$$

where $\sigma(1) < ... < \sigma(k)$ and $\sigma(k+1) < ... < \sigma(k+n)$.

Remark. $c_{\sigma(1)}...c_{\sigma(k)}$ is defined in Prop. 6.2.11 in Abraham and Marsden [1]. For the permutation group σ we get $\mathrm{sign}(\sigma) = 1$ for even permutation and $\mathrm{sign}(\sigma) = -1$ for odd permutation.

Proposition A.2.2. *Let E be an oriented n-dimensional vector space, $g =<,>\in T_2^0(E)$ symmetric and nondegenerate of signature s, and μ the associated $\mathbf{g}$-volume of E. The Hodge-star operator satisfies the following, for $\alpha, \beta \in \Lambda^k(E)$:*

(i) $\alpha \wedge \star\beta = \beta \wedge \star\alpha =< \alpha, \beta > \mu$,
(ii) $\star 1 = \mu, \star\mu = (-1)^{\mathrm{Ind(g)}}$,
(iii) $\star\star\,\alpha = (-1)^{\mathrm{Ind(g)}}(-1)^{k(n-k)}\alpha$,
(iv) $< \alpha, \beta >= (-1)^{\mathrm{Ind(g)}} < \star\alpha, \star\beta >$,
where Ind(g) *is the number of minus-ones in the canonical form of $<,>$.*

Example A.2.1. We discuss examples of A.2.1 in $\mathbb{R}^3$ with $c_1 = c_2 = c_3 = 1$:

$$\star\,\vec{e}^1 = \underbrace{\mathrm{sign}(\sigma)}_{=1}(\vec{e}^2 \wedge \vec{e}^3) \ , \tag{A.5}$$

$$\star\,\vec{e}^2 = \underbrace{\mathrm{sign}(\sigma)}_{=1}(\vec{e}^3 \wedge \vec{e}^1) = \underbrace{\mathrm{sign}(\sigma)}_{=-1}(\vec{e}^1 \wedge \vec{e}^3) \ , \tag{A.6}$$

$$\star\,\vec{e}^3 = \underbrace{\mathrm{sign}(\sigma)}_{=1}(\vec{e}^1 \wedge \vec{e}^2) \ . \tag{A.7}$$

The signs $c_1, ..., c_r$ are defined in Proposition 6.2.9, Abraham and Marsden, p. 342. For example, for an Lorenzian manifold we define $c_1 = -1,\ c_2 = c_3 = c_4 = 1$.

Exterior derivative on forms

The following operations are define on differential forms $\Omega(\mathcal{M})$ on manifolds $\mathcal{M}$ and require a differentiable structure of $\mathcal{M}$. First, we define the exterior product.

Theorem A.2.3. *Let $\mathcal{M}$ be a finite-dimensional manifold. Then there is a unique family of mappings $\mathbf{d}^k : \Omega^k(\mathcal{M}) \to \Omega^{k+1}(\mathcal{M})$ ($k = 0, 1, 2, \cdots n$, and U is open in $\mathcal{M}$), which we merely denote by $\mathbf{d}$, called the* **exterior derivative** *on $\mathcal{M}$, such that*

(i) $\mathbf{d}$ *is a $\wedge$-anti-derivation, i.e. $\mathbf{d}$ is $\mathbb{R}$-linear and for $\alpha \in \Omega^k(\mathcal{M})$ and $\beta \in \Omega^l(\mathcal{M})$,*

$$\mathbf{d}(\alpha \wedge \beta) = \mathbf{d}\alpha \wedge \beta + \alpha \wedge (-1)^k \alpha \wedge \mathbf{d}\beta \quad \textit{(product rule)};$$

(ii) *If $f \in \mathcal{F}(\mathcal{M})$, $\mathbf{d}f$ is the total differential of f, i.e. $(\mathbf{d}f)_i = \frac{\partial f}{\partial x^i}$ and $x^i, i = 1, ..., n$ are local coordinates;*
(iii) $\mathbf{d}^2 = \mathbf{d} \circ \mathbf{d} = 0$ *(that is, $\mathbf{d}^{k+1}(U)\mathbf{d}^k(U) = 0$);*
(iv) $\mathbf{d}$ *is a local operator, i.e. $\mathbf{d}$ is natural with respect to restrictions; that is, if $U \subset V \subset \mathcal{M}$ are open and $\alpha \in \Omega^k(V)$, then $\mathbf{d}(\alpha|U) = \mathbf{d}\alpha|U$.*

We find a representation of the exterior derivative $\mathbf{d} : \Lambda^k(\mathcal{M}) \to \Lambda^{k+1}(\mathcal{M})$ of a form $\bar{\alpha} \in \Lambda^k(\mathcal{M})$ in local coordinates in general form:

$$\mathbf{d}\bar{\alpha} = \frac{\partial \alpha_{i_1 ... i_k}}{\partial x^i} dx^i \wedge dx^{i_1} ... \wedge dx^{i_k}, \quad i_1 < ... < i_k \ . \tag{A.8}$$

Be aware of the different notation between $\mathbf{d}$ and d, where $\mathbf{d}$ denote the exterior derivative.

Interior product (contraction) on forms

The interior product, also called contraction, $\mathbf{i}_\mathbf{X}$ on $\mathcal{M}$ is represented by following Definition.

Definition A.2.1. Let $\mathcal{M}$ be a manifold, $\mathbf{X} \in \mathcal{X}(\mathcal{M})$, and $\omega \in \Omega^{k+1}(\mathcal{M})$. Then define $\mathbf{i}_\mathbf{X}\omega \in \Omega^k(\mathcal{M})$ by

$$\mathbf{i}_\mathbf{X}\omega(\mathbf{X}_1, \ldots, \mathbf{X}_k) = \omega(\mathbf{X}, \mathbf{X}_1, \ldots, \mathbf{X}_k) \ . \tag{A.9}$$

If $\omega \in \Omega^0(\mathcal{M})$, we put $\mathbf{i}_\mathbf{X}\omega = 0$. We call $\mathbf{i}_\mathbf{X}\omega$ the *interior product* or *contraction* of $\mathbf{X}$ and ω.

The interior product has the following properties:

Theorem A.2.4. *We have $\mathbf{i}_\mathbf{X} : \Omega^k(\mathcal{M}) \to \Omega^{k-1}(\mathcal{M}), k = 1, \ldots, n$, and if $\alpha \in \Omega^k(\mathcal{M}), \beta \in \Omega^l(\mathcal{M})$ and $f \in \Omega^0(\mathcal{M})$, then*

(i) $\mathbf{i}_\mathbf{X}$ *is a $\wedge$-antiderivation, i.e. $\mathbf{i}_\mathbf{X}$ is $\mathbb{R}$-linear and*
$\mathbf{i}_\mathbf{X}(\alpha \wedge \beta) = (\mathbf{i}_\mathbf{X}\alpha) \wedge \beta + (-1)^k \alpha \wedge (\mathbf{i}_\mathbf{X}\beta)$,
(ii) $\mathbf{i}_{f\mathbf{X}}\alpha = f\mathbf{i}_\mathbf{X}\alpha$,
(iii) $\mathbf{i}_\mathbf{X}\mathbf{d}f = \mathcal{L}_\mathbf{X} f$,
(iv) $\mathcal{L}_\mathbf{X}\alpha = \mathbf{i}_\mathbf{X}\mathbf{d}\alpha + \mathbf{d}\mathbf{i}_\mathbf{X}\alpha$,
(v) $\mathcal{L}_{f\mathbf{X}}\alpha = f\mathcal{L}_\mathbf{X}\alpha + \mathbf{d}f \wedge \mathbf{i}_\mathbf{X}\alpha$.

Lie-derivative

There are different approaches to define the Lie-derivative. The Lie-derivative determines the change of a tensor along a vector field. It is define in either an algebraic or dynamic approach.

Theorem A.2.5. *Let* $\mathbf{X} \in \mathcal{X}^k(\mathcal{M}), \mathbf{t} \in T^r_s(\mathcal{M})$ *be of class* C^k *and* F_λ *be the flow of* $\mathbf{X}$. *Then the* Lie-derivative *is defined by*

$$\frac{d}{d\lambda} F_\lambda^* \mathbf{t} = F_\lambda^* \mathcal{L}_\mathbf{X} \mathbf{t} \ , \tag{A.10}$$

in which λ *is used for the time variable, and in which* * *denotes the pull back.*

Corollary A.2.6. *Let* $\mathbf{X}, \mathbf{Y} \in \mathcal{X}(\mathcal{M})$ *. Then*

$$[\mathcal{L}_\mathbf{X}, \mathbf{i}_\mathbf{Y}] = \mathbf{i}_{[\mathbf{X},\mathbf{Y}]} \qquad \textit{and} \qquad [\mathcal{L}_\mathbf{X}, \mathcal{L}_\mathbf{Y}] = \mathcal{L}_{[\mathbf{X},\mathbf{Y}]} \ , \tag{A.11}$$

and, in particular, $\mathbf{i}_\mathbf{X} \circ \mathcal{L}_\mathbf{X} = \mathcal{L}_\mathbf{X} \circ \mathbf{i}_\mathbf{X}$.

Proposition A.2.7. *Let* $\mathbf{X} \in \mathcal{X}(\mathcal{M})$. *Then* $\mathbf{d}$ *is natural with respect to* $\mathcal{L}_\mathbf{X}$. *That is, for* $\omega \in \Omega(\mathcal{M})^k$ *we have* $\mathcal{L}_\mathbf{X}\omega \in \Omega(\mathcal{M})^k$ *and*

$$\mathbf{d}\mathcal{L}_\mathbf{X}\omega = \mathcal{L}_\mathbf{X}\mathbf{d}\omega \ . \tag{A.12}$$

In $\mathbb{R}^3$ we find with $\alpha = \mathbf{d}x \wedge \mathbf{d}y \wedge \mathbf{d}z$: $\mathbf{d}\mathbf{i}_\mathbf{X}\alpha = \mathbf{d} * \mathbf{X}^\flat = (\mathrm{div}\mathbf{X}^\flat)\mathbf{d}x \wedge \mathbf{d}y \wedge \mathbf{d}z$. (The first equation follows with $\mathbf{i}_\mathbf{X}\mathbf{d}x \wedge \mathbf{d}y \wedge \mathbf{d}z = X^1 dy \wedge dz + X^2 dz \wedge dx + X^3 dx \wedge dy = *\mathbf{X}^\flat$, for the second, see Prop. B.1.1. Because of Cartan's formula (cf. Theorem A.2.4 (iv)) we find a metric free formulation of the divergence:

$$\mathcal{L}_\mathbf{X}\mu = \mathbf{i}_\mathbf{X} \underbrace{\mathbf{d}\mu}_{=0} + \mathbf{d}\mathbf{i}_\mathbf{X}\mu = (\mathrm{div}\mathbf{X})\mu \ . \tag{A.13}$$

General theorems for fluid dynamics

An generalization of Eq. (A.13) is summarized in the following Definition.

Definition A.2.2. Let $(\mathcal{M}, \mu)$ be a volume manifold, i.e. $\mathcal{M}$ is an orientable manifold with a volume-form μ. Let $\mathbf{X}$ be a vector field on $\mathcal{M}$. The unique function $\mathrm{div}_\mu \mathbf{X} \in \mathcal{X}(\mathcal{M})$, such that $\mathcal{L}_\mathbf{X}\mu = (\mathrm{div}_\mu \mathbf{X})\mu$ is called the **divergence** of $\mathbf{X}$. We say $\mathbf{X}$ is **incompressible** (with respect to μ) if $\mathrm{div}_\mu \mathbf{X} = 0$.

Proposition A.2.8. *Let* $(\mathcal{M}, \mu)$ *be a volume manifold and* $\mathbf{X}$ *a vector field on* $\mathcal{M}$.
(i) *If* $f \in \mathcal{F}(\mathcal{M})$ *and* $f(m) \neq 0$ *for all* $m \in \mathcal{M}$, *then*

$$\mathrm{div}_{f\mu}\mathbf{X} = \mathrm{div}_\mu \mathbf{X} + \frac{\mathcal{L}_\mathbf{X} f}{f}. \tag{A.14}$$

(ii) *If* $g \in \mathcal{F}(\mathcal{M})$, *then*

$$\mathrm{div}_\mu g\mathbf{X} = g\mathrm{div}_\mu \mathbf{X} + \mathcal{L}_\mathbf{X} g. \tag{A.15}$$

Change of variable theorems: The change of variable theorem in $\mathbb{R}^n$ states [1] that if ζ is integrable and $f : \mathbb{R}^n \to \mathbb{R}^n$ is a diffeomorphism then $\zeta \circ f$ is integrable with

$$\int_{\mathbb{R}^n} \zeta(x^1, \ldots, x^n) dx^1 \ldots dx^n = \int_{\mathbb{R}^n} |J_\Omega f(x^1, \ldots, x^n)| (\zeta \circ f)(x^1, \ldots, x^n) dx^1 \ldots dx^n \ , \tag{A.16}$$

where $\Omega = dx^1 \wedge \cdots \wedge dx^n$ is the standard volume-form on $\mathbb{R}^n$ and $J_\Omega f$ is the Jacobian determinate of f relative to Ω. With the atlas, this definition can be transfered to the manifold. Therefore, the definition of an integral for n-forms on an n-manifold in Def. 2.2.1 has the following global property:

Theorem A.2.9 (Change of variable theorem)**.** *Suppose $\mathcal{M}$ and $\mathcal{N}$ are oriented n-manifolds and $f : \mathcal{M} \to \mathcal{N}$ is an orientation-preserving diffeomorphism. If $\omega \in \Omega^n(\mathcal{N})$ has compact support, then $f^*\omega \in \Omega^n(\mathcal{M})$ has compact support and*

$$\int_{\mathcal{N}} \omega = \int_{\mathcal{M}} f^*\omega \ , \tag{A.17}$$

where * denotes the pullback of ω by f (cf. Abraham and Marsden [1]).

By the Riesz representation theorem [1], the volume-form μ provides a unique measure $d\mu$. This measure is required in the following transport theorem, which is, in turn, required to derive the invariant fluid equations.

Theorem A.2.10 (Transport theorem with mass density ρ)**.** *Let f be a time dependent smooth function on $\mathcal{M}$. Then, if $\mathcal{W}$ is any (nice) open set of $\mathcal{M}$,*

$$\frac{d}{dt} \int_{\varphi_t(\mathcal{W})} \rho f d\mu = \int_{\varphi_t(\mathcal{W})} \rho \frac{Df}{dt} d\mu \ , \tag{A.18}$$

where $\frac{Df}{dt} = \frac{\partial f}{\partial t} + \mathcal{L}_{\vec{u}} f$ (cf. Abraham and Marsden [1]).

φ_t is the evolution operator that obeys the following relation with the velocity field $\vec{u}$ of the fluid: $\frac{d\varphi_t(x)}{dt} = \vec{u}(\varphi_t(x), t)$.

A.3 Covariant derivative and time dependent vector fields

Covariant derivative (connection) on manifolds

According to Kambe [60], we introduce the connection $\nabla_X Y \in \mathcal{X}(\mathcal{M})$ that describes in every point $p \in \mathcal{M}$ the change of Y in direction of X_p:

Definition A.3.1. A connection on $\mathcal{M}$ is a map $\nabla : \mathcal{X}(\mathcal{M}) \times \mathcal{X}(\mathcal{M}) \to \mathcal{X}(\mathcal{M})$ with:
(i) $\nabla_U(aX + bY) = a\nabla_U X + b\nabla_U Y$,
(ii) $\nabla_{aU+bV} X = a\nabla_U X + b\nabla_V X$,
(iii) $\nabla_U(f(x)X) = (Uf)X + f(x)\nabla_U X$,
where $f(x)$ is a smooth function, $a, b \in \mathbb{R}$, and $Uf = df[U] = U^j \partial_j f$.

Local representation: Using the following local representation of the vector fields

$$X = X^i \partial_i \quad \text{and} \quad Y = X^j \partial_j \ , \tag{A.19}$$

applying the properties of the connection in Def. A.3.1, and defining $\nabla_{\partial_i}\partial_j := \Gamma_{ij}^k \partial_k$, where Γ_{ij}^k are the Christoffel symbols, the local representation of the connection is given by

$$\nabla_X Y = X^i \frac{\partial Y^k}{\partial x^i}\frac{\partial}{\partial x^k} + X^i Y^j \Gamma_{ij}^k \frac{\partial}{\partial x^k} \ . \tag{A.20}$$

The connection is thus defined by its Christoffel symbols, and the Christoffel symbols in turn can be represented with the metric tensor $g = (g_{ij})$ by

$$\Gamma_{ij}^k = \frac{1}{2} g^{ka}(\partial_i g_{ja} + \partial_j g_{ai} - \partial_a g_{ij}) \ . \tag{A.21}$$

Connection one-form In Kampe [60] we find an alternative form of the connection given by

$$(\nabla_X Y)^k \partial_k = \left(X^i \frac{\partial Y^k}{\partial x^i} + X^i Y^j \Gamma_{ij}^k \right) \partial_k = \left(dY^k(X) + \Gamma_{ij}^k Y^j dx^i(X) \right) \partial_k \ , \tag{A.22}$$

where the definitions of one-forms are used to rewrite the local representation. With the definition of a connection one-form $\nabla Y^k(X) := dY^k(X) + \Gamma_{ij}^k Y^j dx^i(X)\partial_k$, one finds the following representation of the connection:

$$(\nabla_X Y) = (\nabla Y)(X) \ . \tag{A.23}$$

The covariant derivative along a curve For a given curve $x(t) \in \mathcal{M}$, where $\mathcal{X}(x(t))$ denotes the vector fields along $x(t)$, we denote the tangent vector at point p with $\dot{x} = \dot{x}^k \partial_k$. Let $Y \in \mathcal{X}(x(t))$ be a tangent vector field along $x(t)$, then we can calculate the change of Y along the curve:

$$\nabla Y(\dot{x}) = \left(dY^k(\dot{x}) + \Gamma_{ij}^k Y^j dx^i(\dot{x}) \right) \partial_k \tag{A.24}$$

$$= \nabla_{\dot{x}} Y = \left(\dot{x}^i \frac{\partial Y^k}{\partial x^i} + \Gamma_{ij}^k Y^j \dot{x}^i \right) \partial_k \tag{A.25}$$

$$= \left(\frac{dY^k}{dt} + \Gamma_{ij}^k Y^j \dot{x}^i \right) \partial_k =: \frac{\nabla Y}{dt}. \tag{A.26}$$

Y is a function of $x(t)$ so that $\frac{dY^k}{dt} = \frac{\partial Y^k}{\partial x^i}\frac{dx^i}{dt}$. This is used from the second to the third line. We call $\frac{\nabla Y}{dt}$ the *covariant derivative* that describes the derivation of Y along the curve $x(t)$ (cf. [60]).

Time dependent vector fields

In most dynamical systems, the velocity fields are time-dependent, i.e. the velocity field $\tilde{X}$ depends on t and on the spatial coordinates, i.e.

$$\tilde{X} := \tilde{X}^i \partial_i = \partial_t + X^a \partial_a \ , \tag{A.27}$$

with $X^0 = 1$, where the index a denotes the spatial components $1, \ldots, n$. Regarding the change of the time dependent vector field $\tilde{Y} = \partial_t + Y^a \partial_a$ along $\tilde{X}$:

$$\nabla_{\tilde{X}} \tilde{Y} = \nabla_{\partial_t}(\partial_t + Y^b \partial_b) + \nabla_{X^a \partial_a}(\partial_t + Y^b \partial_b) \tag{A.28}$$

$$= \nabla_{\partial_t}\partial_t + \nabla_{\partial_t}(Y^b \partial_b) + X^a \nabla_{\partial_a}\partial_t + \nabla_{X^a\partial_a}(Y^b \partial_b) \tag{A.29}$$

$$= \partial_t Y + \nabla_X Y \ , \tag{A.30}$$

where we have used the properties Def. A.3.1 for the derivation. The first term in (A.29) vanishes. With the assumption of a straight time axis, i.e. $\nabla_{\partial_t}\partial_a = 0$ and $\nabla_{\partial_a}\partial_t = 0$, the third term also vanishes. With (iii) of Def. A.3.1 and $\partial_t Y := \frac{\partial Y^a}{\partial t}\partial_a$, the second term follows, where the non-tilded values denotes vectors dependend only on spatial components (cf. [60]).

The flat connection on $\mathbb{R}^n$

For the $\mathbb{R}^n$, all Christoffel symbols are zero, i.e. $\Gamma^k_{ij} = 0 \forall i, j, k$. Thus, we find for the flat connection:

$$\nabla_X Y = X^j \frac{\partial Y^k}{\partial x^j}\frac{\partial}{\partial x^k} = (X \cdot \nabla)Y \ , \tag{A.31}$$

where the last term is written in the notations of vector calculus.

Regarding fluid dynamics, we are usually interested in the covariant derivative along the parameter curve $x(t)$, where we denote the tangential vector $\dot{x} = \vec{u}(x^i)$ as the velocity field. As all Christoffel symbols are zero, we find for the covariant derivative on flat manifolds with Eqn. (A.25) and (A.26):

$$\nabla_{\vec{u}}\vec{u} = \frac{d\vec{u}}{dt} = \frac{\partial \vec{u}}{\partial x^i}\frac{dx^i}{dt} = (\dot{x}^i \frac{\partial}{\partial x^i})\vec{u} = (\vec{u} \cdot \nabla)\vec{u} \ , \tag{A.32}$$

which corresponds to the well known advection term of fluid dynamics.

In the case of time dependent velocity fields $\tilde{u}(t, x^i)$, where $\tilde{u}$ denotes the time dependent and $\vec{u}$ the spatial dependent velocity field, the combination of Eqn. (A.30) with (A.31) or (A.32) reduces the covariant derivative to the total derivative, i.e.

$$\nabla_{\tilde{u}}\tilde{u} = \partial_t \vec{u} + (\vec{u} \cdot \nabla)\vec{u} = \frac{d}{dt}\tilde{u} \ . \tag{A.33}$$

Lie-derivative and connection

The Lie-derivative can by expressed with the Riemannian connection of a manifold $\mathcal{M}$ by

$$\mathcal{L}_u \vec{u}^\flat = (\nabla_{\vec{u}}\vec{u})^\flat + \frac{1}{2}\mathbf{d}(\vec{u}^\flat(\vec{u})) \ , \tag{A.34}$$

where $\flat$ denotes the inverse Riemannian lift that connects vector fields and forms (cf. definition A.4.1). Here, $\vec{u}$ describes again only the spacial components of the velocity field (cf. [1]).

The results of Eqn. (A.32) and (A.33) show that for flat manifolds, for instance $\mathbb{R}^n, n = 2, 3$, the formulation in invariant form corresponds to the equations written in vector calculus. However, the Lie-derivative has the advantage of an invariant and metric-free form.

A.4 Metric dependent definitions and representations

In the following, we represent the abstract formulations from above on a local coordinate system in $\mathbb{R}^n$. We take:
(i) $(\vec{e}_1, \ldots, \vec{e}_n)$ as basic vectors in $V = \mathbb{R}^n$,
(ii) $(\vec{e}^1, \ldots \vec{e}^n)$ as dual basis of the dual vector space V^*, defined by $\vec{e}^i(\vec{e}_j) = \delta^i_j$, and
(iii) the **metric tensor** $\mathbf{g} : V \times V \to \mathbb{R}$, defined by $\mathbf{g} = \sum_{ij} g_{ij}\vec{e}^i \otimes \vec{e}^j$ with the coefficient $g_{ij} =< \vec{e}_i, \vec{e}_j >, i = 1, 2, 3, \ldots, n$.

Flat- and Sharp-Operator

For the derivations of the invariant fluid equations in Chapter B, operators that combine vectors with one-forms are required.

Definition A.4.1. Let V be a finite-dimensional vector space with a real-valued inner product $<,>$. The basis of V is given by $(\vec{e}_1, ..., \vec{e}_n)$. The corresponding dual basis of dual space V^* is $(\vec{e}^1, ..., \vec{e}^n)$, defined by $\vec{e}^i(\vec{e}_j) = \delta^i_j$. There exists an isomorphism, called the *flat* $\flat$, that is given by

$$\flat : \begin{cases} V & \to V^* \\ \vec{v} & \mapsto < \vec{v} \, , \cdot > \, , \end{cases} \tag{A.35}$$

and the inverse of the flat, the *sharp* $\sharp$, given by

$$\sharp : \begin{cases} V^* & \to V \\ < \vec{v} \, , \cdot > & \mapsto \vec{v} \, , \end{cases} \tag{A.36}$$

with $V \ni \vec{v} = \sum_i v^i \vec{e}_i$.

With the above definition we find the following matrix-representation for the flat and sharp maps:

Proposition A.4.1. *The representation of $\flat$ is given with the matrix g_{ij}, i.e. it is a lowering index operation acting on the coefficients of a vector $V \ni \vec{v} = \sum_i v^i \vec{e}_i$ with*

$$(\vec{v}^{\,b})_i = \sum_j g_{ij} v^j \ . \tag{A.37}$$

The resulting coefficients are those of a one-form $V^* \ni \vec{v}^{\flat} = \sum_i (\vec{v}^{\,b})_i \vec{e}^{\,i}$.

Proof. We start with the above definition of the flat operator: $\flat : V \to V^*$; $\vec{v} \mapsto < \vec{v} \, , \cdot > = < \sum_i v^i \vec{e}_i \, , \cdot >$ by applying it on a vector $\vec{v}$:

$$\flat : \vec{v} \mapsto v^1 < \vec{e}_1 \, , \cdot > + \, ... \, + v^n < \vec{e}_n \, , \cdot > \, , \tag{A.38}$$

$$\flat : \vec{v} \mapsto (\vec{v}^{\,b})_1 \vec{e}^{\,1} + \, ... \, + (\vec{v}^{\,b})_n \vec{e}^{\,n} \ . \tag{A.39}$$

Equation (A.38) follows directly from Definition A.4.1. Equation (A.39) follows by defining the dual vector $V^* \ni \vec{v}^{\,b} = \sum_i (\vec{v}^{\,b})_i \vec{e}^{\,i}$ using the dual basis $(\vec{e}^{\,1}, ..., \vec{e}^{\,n})$ defined by the relation $\vec{e}^{\,i}(\vec{e}_j) = \delta^i{}_j$.

We can compare the coefficients by applying both Equations (A.38) and (A.39) on a vector $\vec{e}_j$. Technically, we project the coefficient of both definitions of a one-form onto the basis vector $\vec{e}_j$ and compare both real-valued numbers, i.e.

$$< \sum_i v^i \vec{e}_i \, , \vec{e}_j > = \sum_i v^i < \vec{e}_i \, , \vec{e}_j > = \sum_i v^i g_{ij} \ , \qquad \text{with } g_{ij} := < \vec{e}_i, \vec{e}_j > \, , \tag{A.40}$$

$$\sum_i (\vec{v}^{\,b})_i \vec{e}^{\,i}(\vec{e}_j) = \sum_i (\vec{v}^{\,b})_i \delta^i{}_j = (\vec{v}^{\,b})_j \ . \tag{A.41}$$

A comparison of the coefficients gives $(\vec{v}^{\,\flat})_j = \sum_i v^i g_{ij}$. □

Proposition A.4.2. *The representation of* $\sharp$ *is given with matrix* g^{ij}*, i.e. it is a index raising operation acting on the coefficients of a one-form* $V^* \ni \bar{\alpha} = \sum_i \alpha_i \vec{e}^i$ *with:*

$$(\bar{\alpha}^\sharp)^i = \sum_j g^{ij}\alpha_j \ . \tag{A.42}$$

The resulting coefficients are those of a vector $V \ni \bar{\alpha}^\sharp = \sum_i (\bar{\alpha}^\sharp)^i \vec{e}_i$.

Proof. The $\sharp$ operator of Definition A.4.1, $\sharp : V^* \to V; < \vec{v}, \cdot > \mapsto \vec{v}$, can be written as:

$$\sharp : \quad < \sum_i v^i \vec{e}_i \ , \cdot > = \sum_i v^i < \vec{e}_i \ , \cdot > \mapsto \sum_i v^i \vec{e}_i \ , \tag{A.43}$$

$$\sharp : \quad < \sum_i (\bar{\alpha}^\sharp)^i \vec{e}_i \ , \cdot > = \sum_i (\bar{\alpha}^\sharp)^i < \vec{e}_i \ , \cdot > \mapsto \sum_i (\bar{\alpha}^\sharp)^i \vec{e}_i \ , \tag{A.44}$$

with the identification $V \ni \vec{v} = \bar{\alpha}^\sharp = \sum_i (\bar{\alpha}^\sharp)^i \vec{e}_i$, the notation already used in Proposition A.4.2. We have to compare Eq. (A.44) with a general definition of a one-form $\bar{\alpha} = \sum_i \alpha_i \vec{e}^i$ on which $\sharp$ acts:

$$\sharp : \quad \bar{\alpha} = \sum_i \alpha_i \vec{e}^i \mapsto \bar{\alpha}^\sharp = \sum_i (\bar{\alpha}^\sharp)^i \vec{e}_i \ . \tag{A.45}$$

To compare the relationship between the coefficients α_i and $(\bar{\alpha}^\sharp)^i$, we apply the two different representation of a one-form in Equations (A.44) and (A.45) on a vector $\vec{e}_j$:

$$\bar{\alpha}(\vec{e}_j) = \sum_i \alpha_i \vec{e}^i(\vec{e}_j) = \sum_i \alpha_i \delta^i{}_j = \alpha_j \ , \tag{A.46}$$

$$\sum_i (\bar{\alpha}^\sharp)^i < \vec{e}_i \ , \vec{e}_j > = \sum_i (\bar{\alpha}^\sharp)^i g_{ij} \ . \tag{A.47}$$

Comparing the coefficient leads to the equation $\alpha_j = \sum_i (\bar{\alpha}^\sharp)^i g_{ij}$ and, using the inverse metric g^{ij}, we can reformulate this to

$$\sum_{i'j'} \alpha_j g^{i'j'} = \sum_i \sum_{i'j'} (\bar{\alpha}^\sharp)^i g_{ij} g^{i'j'} = \sum_i \sum_{i'j'} (\bar{\alpha}^\sharp)^i \delta^i{}_{i'} \delta^j{}_{j'} \tag{A.48}$$

$$\Rightarrow \sum_j \alpha_j g^{ij} = (\bar{\alpha}^\sharp)^i \ , \tag{A.49}$$

because $i = i', j = j'$ due to $\mathbb{1} = \delta^i{}_{i'} \delta^j{}_{j'} = \sum_{ii'jj'} g_{ij} g^{i'j'}$. □

Gradient operator

Let $\mathcal{X}(\mathcal{M})$ be the space of smooth vector fields in $\mathcal{M}$. According to Abraham and Marsden [1], we define the gradient operator as following:

Definition A.4.2. Let $\mathcal{M}$ be a pseudo-Riemannian n-manifold with metric $\mathbf{g}$. We call $\mathrm{grad} f := (\mathbf{d}f)^\sharp \in \mathcal{X}(\mathcal{M})$ the **gradient** of the function $f \in \Omega^0(\mathcal{M})$.

By using local coordinates, the gradient of $f \in \Omega^0(\mathbb{R}^n)$ of Definition A.4.2 is given in the following way:

Proposition A.4.3. *In local coordinates with the basis of tangential vectors* $(\frac{\partial}{\partial x^1}, ..., \frac{\partial}{\partial x^n}) \in \mathcal{T}_p(\mathcal{M})$ *for the tangential space and the dual basis* $(dx^1, ..., dx^n) \in \mathcal{T}_p^*(\mathcal{M})$ *for its dual space, the gradient* $(\mathrm{grad} f) \in \mathcal{X}(\mathcal{M})$ *takes the following form:*

$$\mathrm{grad} f = \sum_{i,j} g^{ij} \frac{\partial f}{\partial x^i} \frac{\partial}{\partial x^j} \quad or \quad (\mathrm{grad} f)^i = \sum_j g^{ij} \frac{\partial f}{\partial x^j} \ . \tag{A.50}$$

Proof. Let $\bar{\alpha} \in \mathcal{X}^*(\mathcal{M})$ be given in local coordinates: $\bar{\alpha} = \sum_i \alpha_i dx^i$. Using the operator $\sharp$ of Def. A.4.1 and Proposition A.4.2 gives

$$\sharp(\bar{\alpha}) = \bar{\alpha}^\sharp = \sum_{i,j} \alpha_i g^{ij} \frac{\partial}{\partial x^j} \ ; \quad \bar{\alpha}^\sharp \in \mathcal{X}(\mathcal{M}) \ . \tag{A.51}$$

Set $df = \bar{\alpha} \Rightarrow \sum_i \frac{\partial f}{\partial x^i} dx^i = \sum_i \alpha_i dx^i \Rightarrow \alpha_i = \frac{\partial f}{\partial x^i}$. With definition A.4.2 it follows:

$$(\mathrm{grad} f) = (\mathbf{d}f)^\sharp = \sharp(\mathbf{d}f) = \sum_i \frac{\partial f}{\partial x^i} g^{ij} \frac{\partial}{\partial x^j} \ ; \quad (\mathbf{d}f)^\sharp \in \mathcal{X}(\mathcal{M}) \ , \tag{A.52}$$

which proofs the above representation of the gradient in local coordinates (cf. [1]). □

Appendix B

Derivation of the fluid equations in invariant form

In this chapter we present Euler's equations for ideal fluids in invariant form according to the derivations of Abraham and Marsden [1]. In the following all definitions, theorems, etc. required for this derivation are taken from [1], unless otherwise stated. The aim here is to present this derivation in a concise way. Starting from the principles of mass, momentum and energy conservation, the incompressible and the barotropic fluid equations shall be derived using tools of differential geometry.

B.1 The principle of mass conservation

Let $W \subset \mathcal{M}$ be a subregion of $\mathcal{M}$. Then we assume that the mass of the fluid in W at time $t = 0$ is given by

$$m(W,t) = \int_W \rho_t d\mu \ , \tag{B.1}$$

where $\rho_t(x) \in \mathcal{F}(\mathcal{M})$ describes the mass-density of the fluid at time t and where $d\mu$ is the volume element of the volume-form $\mu \in \Omega^n(\mathcal{M})$ (cf. Sect. (A.2)). $\mathcal{F}(\mathcal{M})$ denotes the space of smooth functions on $\mathcal{M}$.

One of the most important properties of fluid dynamics is the principle of mass conservation, which states that mass is neither created nor destroyed. Thus, the total mass of the fluid at time $t = 0$ occupied in a region W is maintained with time, i.e.

$$\int_{\varphi_t(W)} \rho_t \ d\mu = \int_W \rho_0 \ d\mu \ , \tag{B.2}$$

where φ_t is the evolution operator with respect to the fluid's velocity field $\vec{u}$ defined within the transport theorem A.2.10. Using this transport theorem, one can reformulate (B.2) to

$$\int_W \varphi_t^*(\rho_t \mu) = \int_W \rho_0 \mu \qquad \Rightarrow \qquad \varphi_t^*(\rho_t \mu) = \rho_0 \mu \ , \tag{B.3}$$

using the pullback * (see e.g. [1]) of φ_t, where φ_t^* is a unique map between the fluid density at time 0 and t. Assuming mass conservation with time, we find the relationship:

$$0 = \frac{d}{dt}\varphi_t^*(\rho_t \mu) = \varphi_t^* \left(\mathcal{L}_{\vec{u}}(\rho_t \mu) + \frac{\partial \rho}{\partial t} \right) = \varphi_t^* \left[\left(\mathrm{div}(\rho_t \vec{u}) + \frac{\partial \rho}{\partial t} \right) \mu \right] \ , \tag{B.4}$$

where the Lie-derivative formula of Theorem A.2.5 and Proposition A.2.8 have been used. Thus, the differential form of the *law of conservation of mass* is given by

$$\mathrm{div}(\rho_t \vec{u}) + \frac{\partial \rho}{\partial t} = 0 \ . \tag{B.5}$$

It is interesting to notice that no metric has been required for this derivation, only the volume-form on $\mathcal{M}$.

Continuity equation using exterior calculus

According to an example presented in Abraham and Marsden [1], the divergence operator can be written as introduced in the following Proposition for $\mathbb{R}^3$. A more general definition of the divergence on any manifold $\mathcal{M}$ can be found in Def. A.2.2.

Proposition B.1.1. *Let $\mathcal{M} \subset \mathbb{R}^3$, $\vec{u} \in \mathcal{X}(\mathcal{M})$ and $\rho \in \mathcal{F}(\mathcal{M})$. Then, the divergence operator* div *can be written in the following way:*

$$\mathbf{d} \star (\rho \vec{u})^\flat = \mathrm{div}(\rho \vec{u}) \cdot dx^1 \wedge dx^2 \wedge dx^3 \qquad \textit{or} \tag{B.6}$$

$$\star \mathbf{d} \star (\rho \vec{u})^\flat = \mathrm{div}(\rho \vec{u}) \ , \tag{B.7}$$

with the definitions of $\star$ and $\flat$ from above.

Proof. We proof this statement by comparing the right and the left hand side of Eq. (B.6) in local coordinates. Using the basis $(\vec{e}_1, ..., \vec{e}_3)$ with dual basis $(\vec{e}^1, ..., \vec{e}^3)$ the vector $\vec{u} = \sum_i u^i \vec{e}_i$ is given. By apply the flat operator on $\vec{u}$ one finds

$$(\rho \vec{u})^\flat = \sum_i ((\rho \vec{u})^\flat)_i \vec{e}^i \ , \tag{B.8}$$

according to Proposition A.4.1. Moreover, using local coordinates in $\mathbb{R}^3$, i.e. $\frac{\partial}{\partial x^i}$ and dx^i for $i = 1, 2, 3$, and $g_{ij} = \delta_{ij}$, it follows $((\rho \vec{u})^\flat)_j = \sum_i g_{ij} (\rho u)^i = \rho u^j$, so we can write[1]:

$$(\rho \vec{u})^{\,b} = \rho u^1 dx^1 + \rho u^2 dx^2 + \rho u^3 dx^3 \ . \tag{B.9}$$

Applying the Hodge-star operator $\star$ of Proposition A.2.1 gives

$$\begin{aligned} \star (\rho \vec{u})^{\,b} &= \rho u^1 \star dx^1 + \rho u^2 \star dx^2 + \rho u^3 \star dx^3 && \text{(B.10)} \\ &= \rho u^1 dx^2 \wedge dx^3 - \rho u^2 dx^1 \wedge dx^3 + \rho u^3 dx^1 \wedge dx^2 \ , && \text{(B.11)} \end{aligned}$$

where the results of Example A.2.1 have been used. Finally, we apply the exterior derivation $\mathbf{d}$ of Definition A.8 on Eq. (B.11):

$$\begin{aligned} \mathbf{d} \star (\rho \vec{u})^{\,b} &= \mathbf{d} \left(\rho u^1 dx^2 \wedge dx^3 - \rho u^2 dx^1 \wedge dx^3 + \rho u^3 dx^1 \wedge dx^2 \right) \\ &= \frac{\partial \rho u^1}{\partial x^1} dx^1 \wedge dx^2 \wedge dx^3 - \frac{\partial \rho u^2}{\partial x^2} dx^2 \wedge dx^1 \wedge dx^3 \\ &\quad + \frac{\partial \rho u^3}{\partial x^3} dx^3 \wedge dx^1 \wedge dx^2 && \text{(B.12)} \\ &= \underbrace{\left(\frac{\partial \rho u^1}{\partial x^1} + \frac{\partial \rho u^2}{\partial x^2} + \frac{\partial \rho u^3}{\partial x^3} \right)}_{= \mathrm{div}(\rho \vec{u})} dx^1 \wedge dx^2 \wedge dx^3 \ , && \text{(B.13)} \end{aligned}$$

[1] It remains to investigate the general case of general g_{ij}.

where the wedge products $dx^i \wedge dx^j \wedge dx^k, i \neq j \neq k$, have been permuted once in the second and twice in the third term of Eq. (B.12). All terms with $...dx^i \wedge ... \wedge dx^i... = 0,\ i = 1, 2, 3$, disappear. Using $\star\star\alpha = (\pm)\alpha$ and $\star\mu = \star\left(dx^1 \wedge dx^2 \wedge dx^3\right) = 1$ of Proposition A.2.2, Eq. (B.7) is also verified. □

According to Proposition B.1.1 and by using the volume-form μ, the Hodge-star $\star$ and the exterior derivative $\mathbf{d}$, we may replace in Eq. (B.5) the divergence operator to obtain

$$\begin{aligned} \star\frac{\partial\rho}{\partial t} + \star\star\,\mathbf{d}\star(\rho\vec{u})^\flat = 0\ , \qquad \vec{u} \in \mathcal{M}, \rho \in \mathcal{F}(\mathcal{M})\ , \\ \frac{\partial(\star\rho)}{\partial t} + \mathbf{d}\star(\rho\vec{u})^\flat = 0\ . \end{aligned} \tag{B.14}$$

The continuity equation (B.5) describes the evolution of the density function $\rho \in \Omega^0(\mathbb{R}^3)$, whereas Eq. (B.14) describes the time evolution of the three-form $\star\rho \in \Omega^3(\mathbb{R}^3)$.

Remark. The entropy $s \in \Omega^0(\mathcal{M})$ or tracer equations look very similar to the continuity equation but have an additional source term Λ_s (cf. Blender [17]):

$$\frac{\partial(\star s)}{\partial t} + \mathbf{d}\star(s\vec{u})^\flat = \Lambda_s\ . \tag{B.15}$$

B.2 Principle of Balance of momentum

On the basis of Newton's second law assessing that the rate of change of momentum of a portion of the fluid equals the total force applied to it, Abraham and Marsden [1] derived the momentum equation. We concisely present the major steps of their derivation. Applying this principle on a manifold in $\mathbb{R}^3$ allows to formulate the *balance of momentum*:

$$\frac{d}{dt}\int_{\varphi_t(W)} \rho\vec{u}\ d\mu = \int_{\varphi_t(W)} \rho\vec{b}\ d\mu + \int_{\partial\varphi_t(W)} \widehat{\sigma}\cdot\vec{n}\ da\ , \tag{B.16}$$

where $\varphi_t(W)$ is a volume preserving fluid flow with evolution operator φ_t, where $\vec{b}$ is the body force density, e.g. the gravitational force, where $\widehat{\sigma}$ is the Cauchy stress tensor and where $d\mu$ is the volume element inducing the surface element da.

Applying Gauss' theorem on the second term of the right hand side of Eq. (B.16) and using the change-of-variable formula (A.2.9) for the left hand side lead to the following componentwise equation for $i = 1, 2, 3$:

$$\int_W \frac{d}{dt}\varphi_t^*(\rho u^i\ d\mu) = \int_{\varphi_t(W)} \rho b^i\ d\mu + \int_{\varphi_t(W)} \mathrm{div}(\widehat{\sigma})^i d\mu\ , \tag{B.17}$$

using the vector $\mathrm{div}(\widehat{\sigma}) := (\mathrm{div}(\sigma^{1\mathrm{j}}), \mathrm{div}(\sigma^{2\mathrm{j}}), \mathrm{div}(\sigma^{3\mathrm{j}}))$ that describes componentwise the divergence (cf. [1]). Applying the Lie-derivative of Theorem A.2.5 one gets

$$\begin{aligned} \int_W \varphi_t^*\left[\frac{\partial(\rho u^i)}{\partial t} + (\mathcal{L}_{\vec{u}}\rho)u^i + \rho\mathcal{L}_{\vec{u}}u^i + \rho u^i\mathcal{L}_{\vec{u}}\mu)\right] d\mu = \\ \int_{\varphi_t(W)}\left[\frac{\partial\rho}{\partial t}u^i + \rho\frac{\partial u^i}{\partial t} + (\mathbf{d}\rho\cdot\vec{u})u^i + \rho\mathcal{L}_{\vec{u}}u^i + \rho u^i\mathrm{div}\,\vec{u}\right] d\mu = \int_{\varphi_t(W)} \left(\rho b^i + \mathrm{div}(\widehat{\sigma})^i\right) d\mu\ . \end{aligned} \tag{B.18}$$

The following identities are valid: $\mathcal{L}_{\vec{u}}\mu = \mathrm{div}\,\vec{u}$ (Def. A.2.2), $\mathcal{L}_{\vec{u}}\rho = \mathbf{d}\rho\cdot\vec{u}$ ((iii) of Theorem A.2.4), $\mathbf{d}\rho\cdot\vec{u} + \rho\mathrm{div}\vec{u} = \mathrm{div}(\rho\vec{u})$ ((ii) of Prop. A.2.8), $\frac{\partial\rho}{\partial t} + \mathrm{div}(\rho\vec{u}) = 0$ (conservation

of mass (B.5)) and $\mathcal{L}_{\vec{u}}u^i = (\vec{u}\cdot\nabla)u^i$ according to Eq. (A.32) or discussions further below. Summarizing all term into a vector equation leads to the following differential form of the *law of balance of momentum* for fluids:

$$\frac{\partial\vec{u}}{\partial t} + (\vec{u}\cdot\nabla)\vec{u} = \vec{b} - \frac{1}{\rho}\text{div}\ \widehat{\sigma}\ . \tag{B.19}$$

Assumption of an ideal fluid An ideal fluid is by definition a fluid whose Cauchy stress tensor $\widehat{\sigma}$ is given in terms of a function $p(\vec{x},t)$ called the pressure [1], i.e.

$$\sigma^{ij} = -pg^{ij}\ . \tag{B.20}$$

Then, the momentum equations for an ideal fluid is given by

$$\frac{\partial\vec{u}}{\partial t} + (\vec{u}\cdot\nabla)\vec{u} = \vec{b} - \frac{1}{\rho}\text{grad}\ p\ . \tag{B.21}$$

Let S be any fluid surface in $\mathcal{M}$ with outward unit normal $\vec{n}$. Then, the assumption on $\widehat{\sigma}$ to obtain an ideal fluid means that the force of stress per unit area exerted across a surface element S at x with normal $\vec{n}$ is given by $-p(x,t)\vec{n}$ (cf. [1]).

According to Abraham and Marsden [1], there are some problems with the integral form of the balance of momentum in Eq. (B.16) for general Riemannian manifold $\mathcal{M}$. First, it is not clear what the notion of vector-valued integrals should mean on general $\mathcal{M}$. Second, this integral form is not covariant, i.e. if the coordinates are changed, the balance of momentum changes its appearance. Therefore, in the following differential forms are used to describe the motion of an ideal fluid.

Momentum equation using exterior calculus

We present Abraham and Marsden's [1] derivation of the fluid equations by using differential forms to result in an invariant (covariant) form of the equations. We begin the derivation from the momentum equation (B.21) in vector calculus form.

Let $\vec{u} = \sum_i u^i\vec{e}_i$, $\vec{b} = \sum_i b^i\vec{e}_i \in \mathcal{X}(\mathcal{M})$ with basis $(\vec{e}_1,..,\vec{e}_n)$ of $\mathcal{X}(\mathcal{M})$. The density $\rho(\vec{x},t)$ and the pressure $p(\vec{x},t)$ are smooth functions in $\mathcal{F}(\mathcal{M})$. For the coefficients of Eq. (B.21) in the basis vectors $\{\vec{e}_j\}_{j=1,..,n}$ it follows:

$$\frac{\partial u^j}{\partial t} + (\vec{u}\cdot\nabla)u^j - b^j + \frac{1}{\rho}(\text{grad}\ p)^j = 0\ ; \qquad j = 1,...,n\ . \tag{B.22}$$

We take the flat $\flat$ of these coefficient equations to derive the coefficients of the corresponding one-forms, i.e. $\vec{u}^\flat$ or $\vec{b}^\flat$. Recall that the flat-operator $\flat$ of Definition A.4.1 acts on a vector $\vec{v}\in V$ like

$$\flat : \begin{cases} V \to V^* \\ \vec{v} = \sum_i v^i\vec{e}_i \mapsto \vec{v}^\flat = \sum_i (\vec{v}^\flat)_i\vec{e}^i\ , \end{cases} \tag{B.23}$$

with $(\vec{v}^\flat)_i = \sum_j g_{ij}v^j$ according to Proposition A.4.1. This proposes the derivation of the coefficients for the dual basis vectors $\vec{e}^i$ by simply multiplying the metric-term $\sum_j g_{ij}$ onto the coefficient equations (B.22). This actually relates to a index lowering operation of Proposition A.4.1. We find for the coefficients of the dual vectors $\vec{e}^i$ for $i = 1,...,n$:

$$\begin{aligned} &\frac{\partial(\sum_j g_{ij}u^j)}{\partial t} + (\vec{u}\cdot\nabla)\sum_j g_{ij}u^j - \sum_j g_{ij}b^j + \frac{1}{\rho}\sum_j g_{ij}(\text{grad}\ p)^j = 0\ , \\ &\frac{\partial(\vec{u}^b)_i}{\partial t} + (\vec{u}\cdot\nabla)(\vec{u}^b)_i - (\vec{b}^b)_i + \frac{1}{\rho}\sum_j g_{ij}(\text{grad}\ p)^j = 0\ . \end{aligned} \tag{B.24}$$

The first and the third term of Eq. (B.24) are already coefficients of a dual basis vector and therefore in an invariant form. The following proposition states that the advection term (second term) can be written in terms of a Lie-derivative.

Proposition B.2.1. *The advection term can be written in terms of a Lie-derivative acting on the one-form* $(\vec{u}^{\,b})_i \in \Omega^1(\mathcal{M})$ *by* $(\vec{u}\cdot\nabla)(\vec{u}^{\,b})_i = (\mathcal{L}_{\vec{u}}(\vec{u}^{\,\flat}))_i - \frac{1}{2}\frac{\partial}{\partial x^i}(\vec{u}^{\,\flat}(\vec{u}))$.

To proof this proposition we need the following definition of a Lie-derivative acting on differential forms. Hereby, we take the algebraic definition of the Lie-derivative as introduced in [1]. As shown therein, such algebraic definition is equivalent to the dynamical definition of Theorem A.2.5. We shall give here the coefficient of a Lie-derivative of a one-form in local coordinate, i.e. the tangential vectors $\frac{\partial}{\partial x^1},...,\frac{\partial}{\partial x^n} \in \mathcal{T}_p\mathcal{M}$ and the dual vectors $dx^1,...,dx^n \in \mathcal{T}_p^*\mathcal{M}$:

Definition B.2.1 (Abraham and Marsden [1])**.** The coefficient of a *Lie-derivative* of a one-form $\bar{\alpha}$ with $\bar{\alpha} = \sum_i \alpha_i \vec{e}^{\,i} = \sum_i \alpha_i dx^i$ and $\vec{X} = \sum_i X^i \frac{\partial}{\partial x^i}$ are given by

$$(\mathcal{L}_{\mathbf{X}}\bar{\alpha})_i = \sum_j (X^j \frac{\partial \alpha_i}{\partial x^j} + \alpha_j \frac{\partial X^j}{\partial x^i}) \ . \tag{B.25}$$

With Equation (B.25) we calculate the variation of the coefficient of the one-form $\bar{\alpha}$ along the flow field of $\vec{X}$. It follows $(\mathcal{L}_{\mathbf{X}}\bar{\alpha}) = \sum_i (\mathcal{L}_{\mathbf{X}}\bar{\alpha})_i dx^i$, where $(\mathcal{L}_{\mathbf{X}}\bar{\alpha})$ is also a one-form.

Proof of Proposition B.2.1. We modify the advection term $(\vec{u}\cdot\nabla)(\vec{u}^{\,b})_i$ by adding a zero:

$$(\sum_j u^j \frac{\partial}{\partial x^j})(\vec{u}^{\,\flat})_i + 0 = \underbrace{\sum_j u^j \frac{\partial (\vec{u}^{\,\flat})_i}{\partial x^j} + \sum_j (\vec{u}^{\,\flat})_j \frac{\partial u^j}{\partial x^i}}_{(\mathcal{L}_{\vec{u}}(\vec{u}^{\,\flat}))_i} \underbrace{- \sum_j (\vec{u}^{\,\flat})_j \frac{\partial u^j}{\partial x^i}}_{-\frac{1}{2}\frac{\partial}{\partial x^i}(\vec{u}^{\,\flat}(\vec{u}))} \ . \tag{B.26}$$

Representing $\vec{u} = \sum_i u^i \frac{\partial}{\partial x^i}$ and $\vec{u}^{\,\flat} = \sum_i (\vec{u}^{\,\flat})_i dx^i$ in local coordinates, the coefficients for vectors $u^j = X^j$ and one-forms $(\vec{u}^{\,\flat})_j = \alpha_j$ of Eqn. (B.25) and (B.26) agree. Therefore, the first two term of the right hand side (B.26) can be summarize to $(\mathcal{L}_{\vec{u}}(\vec{u}^{\,\flat}))_i$. The third term in (B.26) can be reformulated as indicated. To see this, we resubstitute $(\vec{u}^{\,\flat})_j = \sum_k g_{jk} u^k$ in Eq. (B.26). g_{ij} in $\mathcal{M}$ shall be constant with respect to partial derivatives $\frac{\partial}{\partial x^i}$. So we can write for the i-th component:

$$-\sum_j (\vec{u}^{\,\flat})_j \frac{\partial u^j}{\partial x^i} = -\sum_{j,k} g_{jk} u^k \frac{\partial u^j}{\partial x^i} = -\frac{1}{2}\frac{\partial (\sum_{j,k} g_{jk} u^j u^k)}{\partial x^i} = -\frac{1}{2}\frac{\partial}{\partial x^i}(\vec{u}^{\,\flat}(\vec{u})) \ , \tag{B.27}$$

with $\vec{u}^{\,\flat}(\vec{u}) = \sum_{j,k} g_{jk} u^j u^k$. □

That the last equality is true is a consequence of the following proposition:

Proposition B.2.2. $\vec{u}^{\,\flat}(\vec{u}) = <\vec{u},\vec{u}> = \sum_{j,k} g_{jk} u^j u^k$.

Proof. If we compare the two definitions of a dual vector (compare proof to Proposition A.4.1) we find the equality of both formulations by the following calculation

$$\vec{u}^\flat(\vec{u}) = \sum_{i,k} (\vec{u}^\flat)_i \vec{e}^i (u^k \vec{e}_k) = \sum_{i,k} (\vec{u}^\flat)_i u^k \underbrace{\vec{e}^i(\vec{e}_k)}_{:=\delta^i{}_k} = \sum_i (\vec{u}^\flat)_i u^i \tag{B.28}$$

$$= \sum_i u^i < \vec{e}_i, \sum_j u^j \vec{e}_j >= \sum_i \sum_j u^j u^i \underbrace{< \vec{e}_i, \vec{e}_j >}_{=g_{ij}} \tag{B.29}$$

$$=< \sum_i u^i \vec{e}_i, \sum_j u^j \vec{e}_j >=< \vec{u}, \vec{u} > \ . \tag{B.30}$$

□

The remaining term in Eq. (B.24) can be written in local form according to Def. A.4.2 and Prop. A.4.3. The j-th component of the gradient is thus given by

$$\frac{1}{\rho} \sum_j g_{ij} \underbrace{(\text{grad } p)^j}_{\sum_k g^{jk} \frac{\partial p}{\partial x^k}} = \frac{1}{\rho} \sum_{j,k} g_{ij} g^{jk} \frac{\partial p}{\partial x^k} = \frac{1}{\rho} \frac{\partial p}{\partial x^i} \ . \tag{B.31}$$

The second equality holds because of the equality $\sum_{j,k} g_{ij} g^{jk} = \delta_i{}^k$ of the metric terms (cf. Abraham and Marsden [1]).

The results of Eq. (B.31) and Prop. B.2.1 allow to reformulate the momentum equation of (B.24) in invariant form. For the i-th component, with $i = 1, ..., n$, we find

$$\frac{\partial (\vec{u}^\flat)_i}{\partial t} + (\mathcal{L}_{\vec{u}} (\vec{u}^\flat))_i - \frac{1}{2} \frac{\partial}{\partial x^i} (\vec{u}^\flat(\vec{u})) - (\vec{b}^\flat)_i + \frac{1}{\rho} \frac{\partial p}{\partial x^i} = 0 \ , \tag{B.32}$$

or, by multiplying these coefficients with the dual basis vectors $dx^i, i = 1, ..., n$, we find

$$\frac{\partial (\sum_i (\vec{u}^\flat)_i dx^i)}{\partial t} + \sum_i (\mathcal{L}_{\vec{u}} (\vec{u}^\flat))_i dx^i - \frac{1}{2} \sum_i \frac{\partial (\vec{u}^\flat(\vec{u}))}{\partial x^i} dx^i - \sum_i (\vec{b}^\flat)_i dx^i + \frac{1}{\rho} \sum_i \frac{\partial p}{\partial x^i} dx^i = 0 \ . \tag{B.33}$$

Be aware that $\vec{u}^\flat(\vec{u}) \in \mathcal{F}(\mathcal{M})$ is a function, i.e. $\vec{u}^\flat(\vec{u}) =< \vec{u}, \vec{u} >= |\vec{u}|^2$ and that for the total derivative of a function $f \in \mathcal{F}(\mathcal{M})$ we write $\mathbf{d}f = \sum_i \frac{\partial f}{\partial x^i} dx^i$. Moreover, the dual vectors $\vec{e}^i$ are represented in local coordinates dx^i. This leads to the invariant formulation of Euler's equations:

$$\boxed{\frac{\partial (\vec{u}^\flat)}{\partial t} + \mathcal{L}_{\vec{u}} (\vec{u}^\flat) - \frac{1}{2} \mathbf{d} (\vec{u}^\flat(\vec{u})) + \frac{1}{\rho} \mathbf{d}p - \vec{b}^\flat = 0 \ .} \tag{B.34}$$

According to property (iii) of Theorem A.2.1 (also called Cartan's magic formula) the Lie-derivative applied to a one-form $\vec{u}^\flat$ may be written as

$$\mathcal{L}_{\vec{u}} (\vec{u}^\flat) = \mathbf{d} \circ \mathbf{i}_{\vec{u}} (\vec{u}^\flat) + \mathbf{i}_{\vec{u}} \circ \mathbf{d} \vec{u}^\flat \ . \tag{B.35}$$

Using $\mathbf{d} \circ \mathbf{i}_{\vec{u}} (\vec{u}^\flat) = \mathbf{d} (\vec{u}^\flat(\vec{u}))$, we find the alternative invariant formulation of Euler's equations:

$$\boxed{\frac{\partial (\vec{u}^\flat)}{\partial t} + \mathbf{i}_{\vec{u}} \circ \mathbf{d} \vec{u}^\flat + \frac{1}{2} \mathbf{d} (\vec{u}^\flat(\vec{u})) + \frac{1}{\rho} \mathbf{d}p - \vec{b}^\flat = 0 \ .} \tag{B.36}$$

This two formulations are equivalent in the continuous case. Whether the one or the other formulation is more suitable for discretization has to be investigated in further studies. In many application there is $\vec{b}^\flat = 0$, thus we assume this in the following.

B.3 Principle of energy-conservation

Regarding the momentum equation (B.34)/(B.36) together with the continuity equation (B.14), the unknowns are $\vec{u}^\flat$ (or its vector proxy $\vec{v}$), ρ and p giving thus $n+2$ scalar unknowns. However, we have only $n+1$ equations. In order to close the system of equations we required an additional constraint.

We present in the following the derivation of Abraham and Marsden [1] to find the closure conditions by assuming energy conservation. For a fluid moving in $\mathcal{M}$ with velocity field $\vec{u}$, the *kinetic energy* of the fluid is given by

$$E_{\text{kin}} = \frac{1}{2}\int_{\mathcal{M}} \rho ||\vec{u}||^2 d\mu \ , \tag{B.37}$$

with $||\vec{u}||^2 =< \vec{u}, \vec{u} >$. The total energy consists in a sum of internal energy E_{int} and the kinetic energy:

$$E_{\text{tot}} = E_{\text{kin}} + E_{\text{int}} \ . \tag{B.38}$$

Case 1) of incompressible flows: The main assumption is that $E_{\text{int}} =$ constant. If no energy is pumped into the system, or if the fluid does not perform work, the kinetic energy E_{kin} should be constant, too, according to Eq. (B.38). There is the following equation [1]:

$$0 = \frac{d}{dt}\left(\frac{1}{2}\int_{\mathcal{M}} \rho ||\vec{u}||^2 d\mu\right) = \int_{\mathcal{M}} (\text{div}(\vec{u}))p\mu \ , \tag{B.39}$$

with the volume-form μ. This has to hold for all conceivable motions. Thus to fulfill this equation we need either

$$\text{div}(\vec{u}) = 0 \qquad \text{or} \qquad p = 0 \tag{B.40}$$

to hold. $p = 0$ is possible but not further regarded. If we require $\text{div}(\vec{u}) = 0$, we regard the case of incompressible fluids with the boundary condition $\mathbf{i}_{\vec{u}}\mu = 0$ on $\partial\mathcal{M}$.

Proof. of B.39: The following equations hold:

$$\mathcal{L}_{\vec{u}}||\vec{u}||^2 \overset{i}{=} \mathcal{L}_{\vec{u}}\left(u^\flat(\vec{u})\right) \overset{ii}{=} \left(\mathcal{L}_{\vec{u}}u^\flat\right)(\vec{u}) \overset{iii}{=} \mathbf{d}\left(u^\flat(\vec{u})\right)(\vec{u}) \ ; \tag{B.41}$$

i) $||\vec{u}||^2 =< \vec{u}, \vec{u} >= u^\flat(\vec{u})$ according to Def. A.4.1 and Prop. B.2.2;
ii) With $u^\flat(\vec{u}) = \mathbf{i_u}u^\flat$ and Corollary A.2.6 it follows: $\mathcal{L}_{\vec{u}}\left(\mathbf{i}_{\vec{u}}u^\flat\right) = \mathbf{i}_{\vec{u}}\left(\mathcal{L}_{\vec{u}}u^\flat\right)$;
iii) Using Eq. (B.35) it follows: $\mathcal{L}_{\vec{u}}\left(u^\flat(\vec{u})\right) = \mathbf{d}\circ\underbrace{\mathbf{i}_{\vec{u}}\left(u^\flat(\vec{u})\right)}_{=0} + \mathbf{i}_{\vec{u}}\circ\mathbf{d}\left(u^\flat(\vec{u})\right) = \mathbf{d}\left(u^\flat(\vec{u})\right)(\vec{u})$.

Therefore, we find for Eq. (B.39):

$$\begin{aligned}
0 &= \frac{d}{dt}\left(\frac{1}{2}\int_{\mathcal{M}} \rho||\vec{u}||^2 d\mu\right) = \frac{1}{2}\int_{\mathcal{M}} \rho\left(\frac{\partial||\vec{u}||^2}{\partial t} + \mathcal{L}_{\vec{u}}||\vec{u}||^2\right) d\mu && \text{(Theorem A.2.10)} \\
&= \int_{\mathcal{M}} \rho\frac{\partial u^\flat}{\partial t}\cdot\vec{u}d\mu + \frac{1}{2}\int_{\mathcal{M}} \rho\left(\mathcal{L}_{\vec{u}}u^\flat\right)\cdot\vec{u}d\mu && \text{(use relation in Eq. (B.41))} \\
&= \int_{\mathcal{M}} \rho\frac{\partial u^\flat}{\partial t}\cdot\vec{u}d\mu + \int_{\mathcal{M}} \rho\left(\mathcal{L}_{\vec{u}}u^\flat\right)\cdot\vec{u}d\mu - \frac{1}{2}\int_{\mathcal{M}} \rho\mathbf{d}\left(u^\flat(\vec{u})\right)\vec{u}d\mu && \text{(replace Eq. (B.34))} \\
&= -\int_{\mathcal{M}} \mathbf{d}p\cdot\vec{u}d\mu \overset{iv}{=} \int_{\mathcal{M}} [(\text{div}(\vec{u}))p\mu - \mathcal{L}_{\vec{u}}(p\mu)] && \text{(with Leibniz rule for } \mathcal{L}) \\
&\overset{v}{=} \int_{\mathcal{M}} [(\text{div}(\vec{u}))p\mu - \mathbf{d}(\mathbf{i}_{\vec{u}}p\mu)] \overset{vi}{=} \int_{\mathcal{M}} (\text{div}(\vec{u}))p\mu && \text{(with boundary } \mathbf{i}_{\vec{u}}\mu = 0);
\end{aligned}$$

iv) Leibniz rule: $\mathcal{L}_{\vec{u}}(p\mu) = \mathcal{L}_{\vec{u}}(p)\mu + p\mathcal{L}_{\vec{u}}\mu = \mathbf{d}p \cdot \vec{u}\mu + p\mathrm{div}_\mu \vec{u}\mu$ with A.2.4 (iii) for the first and Def. A.2.2 for the second term;
v) $\mathcal{L}_{\vec{u}}(p\mu) = \mathbf{d}\mathbf{i}_{\vec{u}}(p\mu) + \mathbf{i}_{\vec{u}}\mathbf{d}(p\mu) = \mathbf{d}(\mathbf{i}_{\vec{u}}p\mu)$ due to $0 = \mathbf{d}(p\mu) \in \Omega^{n+1}(\mathcal{M})$;
vi) Due to Stokes theorem and A.2.4 (i): $\int_{\mathcal{M}} \mathbf{d}(\mathbf{i}_{\vec{u}}p\mu) = \int_{\partial\mathcal{M}}(\mathbf{i}_{\vec{u}}p)\mu + (-1)^0 \int_{\partial\mathcal{M}} p\mathbf{i}_{\vec{u}}\mu = \int_{\partial\mathcal{M}} p\mathbf{i}_{\vec{u}}\mu$ as $p \in \Omega^0$, and thus $0 = \mathbf{i}_{\vec{u}}p$. Setting the boundary condition on $\partial\mathcal{M} : (\vec{u}\cdot\vec{n})da = \mathbf{i}_{\vec{u}}\mu = 0$ (this describes the case where the flux through the boundary is zero), we find the above equality. □

Case 2) of barotropic or ideal isentropic flows: The main assumption is that the internal energy (here not constant) over a region W is a function of the internal energy density per unit mass, denoted with w, and can be written as

$$E_{\mathrm{int}} = \int_W \rho\omega d\mu \ . \tag{B.42}$$

The energy should be balanced such that the rate of change of energy within a region W equals the work done on it:

$$\frac{d}{dt}\left(\int_{\varphi_t(W)} \rho\frac{1}{2}||\vec{u}||^2 d\mu + \rho\omega d\mu\right) = -\int_{\partial\varphi_t(W)} p\vec{u}\cdot\vec{n}da \ . \tag{B.43}$$

Taking the result of Case 1) for the first term on the left, using the transport theorem A.2.10 for the second term on the left, and applying Gauss theorem on the right of Eq. (B.43) lead to

$$-\int_{\mathcal{M}} \mathbf{d}p\cdot\vec{u}d\mu + \int_{\varphi_t(W)} \rho\frac{D\omega}{dt}d\mu = -\int_{\varphi_t(W)} \mathrm{div}(p\vec{u})\cdot d\mu \ . \tag{B.44}$$

According to Prop. A.2.8 (ii), the identity $\mathrm{div}(p\vec{u})\cdot d\mu = \mathbf{d}p\cdot\vec{u}d\mu + p\mathrm{div}_\mu(\vec{u})d\mu$ leads to

$$0 = \int_{\varphi_t(W)} \left(p\mathrm{div}_\mu(\vec{u}) + \rho\frac{D\omega}{dt}\right) d\mu \tag{B.45}$$

$$= p\mathrm{div}_\mu(\vec{u}) + \rho\left(\frac{\partial\omega}{\partial t} + \mathcal{L}_{\vec{u}}\omega\right) \ , \tag{B.46}$$

since W is arbitrary and using Theorem A.2.10 to evaluate $\frac{D\omega}{dt}$.

Barotropic assumptions: The internal energy $\omega = \omega(\rho) \in \Omega^0(\mathcal{M})$ only depends on how much the fluid is compressed. Such fluids are called *ideal isentropic* or *barotropic*. We find with Theorem A.2.4 (iii) and the continuity equation B.5 with Prop. A.2.8 (ii):

$$\begin{aligned} 0 &= p\mathrm{div}_\mu(\vec{u}) + \rho\left(\frac{\partial\omega}{\partial t} + \mathbf{d}\omega\cdot\vec{u}\right) = p\mathrm{div}_\mu(\vec{u}) + \rho\left(\frac{\partial\omega}{\partial\rho}\frac{\partial\rho}{\partial t} + \frac{\partial\omega}{\partial\rho}\mathbf{d}\rho\cdot\vec{u}\right) \\ &= p\mathrm{div}_\mu(\vec{u}) + \rho\frac{\partial\omega}{\partial\rho}\left(-\rho\mathrm{div}_\mu(\vec{u})\right) = \left(p - \rho^2\frac{\partial\omega}{\partial\rho}\right)\mathrm{div}_\mu(\vec{u}) \ . \end{aligned} \tag{B.47}$$

As the value for the divergence $\mathrm{div}_\mu(\vec{u})$ is not restricted, the following identity has to be fulfilled for barotropic flows:

$$p = \rho^2\frac{\partial\omega}{\partial\rho} \ . \tag{B.48}$$

This equation is called an *equation of state*.

A common assumption for barotropic flows is that $p = p(\rho) \in \mathcal{F}(\mathcal{M})$ is a function of the density alone [1]. With this assumption we can find an expression for the internal energy ω by

$$\omega = -\int p d\,(1/\rho)\,. \tag{B.49}$$

This can be found by integrating both sides of Eq. (B.48) over ρ, using the separation of the variables and substitute $\frac{1}{\rho} := \rho \Rightarrow \frac{d(1/\rho)}{d\rho} = -\frac{1}{\rho^2}$, thus

$$\int \frac{p(\rho)}{\rho^2} d\rho = \int \frac{\partial \omega(\rho)}{\partial \rho} d\rho \quad \Rightarrow \quad -\int p d\,(1/\rho) = \int \frac{\partial \omega(\rho)}{\partial \rho} d\rho\,. \tag{B.50}$$

Using the integrand $\mathbf{d}\omega = -p d\,(1/\rho)$ of Eq. (B.49) we find

$$\mathbf{d}(p/\rho) = 1/\rho \mathbf{d}p + p d\,(1/\rho) = 1/\rho \mathbf{d}p - \mathbf{d}\omega \quad \Rightarrow \quad \frac{1}{\rho}\mathbf{d}p = \mathbf{d}\,(\omega + p/\rho) =: \mathbf{d}h\,, \tag{B.51}$$

which can be substituted in the momentum equations (B.34) and (B.36). The quantity $h := \omega + p/\rho$ is called the *enthalpy*.

Comparison to thermodynamics: Let be $\mathbf{d}U = \delta W + \delta Q$, where U denotes the inner energy, W the work done on the fluid and Q the heat added to the fluid (see e.g. [38]). With the assumptions of an isentropic (i.e. adiabatic and reversible) or barotropic flow (see above), where the internal energy depends only on how much the fluid is compressed, $\delta W = -p\mathbf{d}V$, and where no heat is added, $\delta Q = 0$, the following relation holds: $\mathbf{d}U = -p\mathbf{d}V$. This is in agreement with the change in inner energy $\mathbf{d}\omega = -p d\,(1/\rho)$ of Eq. (B.49), as $d\,(1/\rho)$ is equivalent to changes in the volume $\mathbf{d}V$ (recall: lower case letters denote energy density per unit mass).

Using this interpreting, the definition of enthalpy $h := \omega + p/\rho$ equals also those used frequently in thermodynamics [38], $H := U + pV$. For thermodynamical systems, the enthalpy H is a measure for the total energy of the thermodynamical system, including the internal energy as well as the energy that is required to establish the systems volume and its pressure. The change in enthalpy is given by $\mathbf{d}H = \mathbf{d}U + p\mathbf{d}V + \mathbf{d}pV = -p\mathbf{d}V + p\mathbf{d}V + \mathbf{d}pV = V\mathbf{d}p$, which agrees with Eq. (B.51).

B.4 Incompressible and barotropic invariant fluid equations

On the basis of the results of Abraham and Marsden [1] that we presented in detail above, we summarize in the following the fluid equations for incompressible and for barotropic flows. These sets of equations are valid on a general Riemannian manifold $\mathcal{M}$ endowed with a metric $\mathbf{g}$.

B.4.1 Incompressible fluid equations in invariant form

Let the one-form $\vec{u}^\flat \in \Omega^1(\mathcal{M})$ describe the velocity, $\rho, p \in \Omega^0(\mathcal{M})$ describe the density and pressure of the fluid, respectively on a general Riemannian manifold $\mathcal{M}$. Then the incompressible flow is described by the invariant fluid equations:

$$\frac{\partial(\vec{u}^\flat)}{\partial t} + \mathcal{L}_{\vec{u}}(\vec{u}^\flat) - \frac{1}{2}\mathbf{d}(\vec{u}^\flat(\vec{u})) + \frac{1}{\rho}\mathbf{d}p = 0\,, \tag{B.52}$$

$$\frac{\partial(\star\rho)}{\partial t} + \mathbf{d} \star (\rho\vec{u})^\flat = 0\,, \tag{B.53}$$

$$\star\,\mathbf{d} \star (\vec{u})^\flat = 0\,, \tag{B.54}$$

with the initial conditions $\vec{u}(x,0) = \vec{u}_0(x)$ on $\mathcal{M}$ and the boundary condition on $\partial\mathcal{M}$: $(\vec{u}\cdot\vec{n})da = \mathbf{i_u}\mu = \mathbf{0}$.

B.4.2 Barotropic fluid equations in invariant form

Let the one-form $\vec{u}^\flat \in \Omega^1(\mathcal{M})$ describe the velocity, $\rho, p \in \Omega^0(\mathcal{M})$ describe the density and pressure of the fluid, respectively on a general Riemannian manifold $\mathcal{M}$. Moreover, let the inner energy be $\omega = \omega(\rho) \in \Omega^0(\mathcal{M})$ and the pressure be a function of the density, i.e. $p = p(\rho)$. Then the barotropic flow is described by the invariant fluid equations:

$$\frac{\partial(\vec{u}^\flat)}{\partial t} + \mathcal{L}_{\vec{u}}(\vec{u}^\flat) - \frac{1}{2}\mathbf{d}(\vec{u}^\flat(\vec{u})) + \mathbf{d}\,(\omega + p/\rho) = 0\ , \tag{B.55}$$

$$\frac{\partial(\star\rho)}{\partial t} + \mathbf{d}\star(\rho\vec{u})^\flat = 0\ , \tag{B.56}$$

$$p = \rho^2\frac{\partial\omega}{\partial\rho} \qquad \text{(equation of state)}, \tag{B.57}$$

with the initial conditions $\vec{u}(x,0) = \vec{u}_0(x)$ on $\mathcal{M}$ and the boundary conditions $\vec{u}\cdot\vec{n} = 0$ on $\partial\mathcal{M}$.

B.5 Vorticity stream function and conservation properties

On the basis of the momentum equation (B.52) we show conservation of vorticity $\omega = \mathbf{d}\vec{u}^\flat \in \Omega^2(\mathcal{M})$. As the Lie-derivative and the exterior calculus commute (cf. Prop. A.2.7), we derive the following equation:

$$\frac{\partial(\mathbf{d}\vec{u}^\flat)}{\partial t} + \mathcal{L}_{\vec{u}}(\mathbf{d}\vec{u}^\flat) - \frac{1}{2}\mathbf{dd}(\vec{u}^\flat(\vec{u})) + \mathbf{d}\left(\frac{1}{\rho}\right)\wedge\mathbf{d}p + \frac{1}{\rho}\mathbf{dd}p = 0\ . \tag{B.58}$$

All terms with $\mathbf{dd} = 0$ vanish. In case of incompressible or barotropic flows also the fourth term vanishes as either ρ is constant or $\mathbf{dd}(w + p/\rho) = 0$, which leads to the so called *vorticity-stream equation:*

$$\frac{\partial\omega}{\partial t} + \mathcal{L}_{\vec{u}}\omega = 0\ . \tag{B.59}$$

This proves the conservation of vorticity. This fact becomes more clear on a flat manifold. If we present the Lie-derivative by Eq. (A.34) with a connection ∇ of Def. A.3.1 on a flat manifold and if we use Eq. (A.33), then we find $\frac{d}{dt} = \partial_t + \vec{u}\cdot\nabla$ leading to $\frac{d}{dt}\omega = 0$.

Appendix C

Geophysical fluid equations in invariant form

In Appendix C.1, we present the geophysical fluid equations for rotating fluids in vector invariant form according to White et al. [117] and Marshall and Plumb [70].

In Appendix C.2 we introduce an invariant form of the shallow-water equations. This equations are derived on basis of the invariant fluid equations of Appendix B in combination with result of Chapter 2.

C.1 Governing equations in vector invariant form

In this section we present the geophysical fluid equations in vector invariant form according to the derivations of White et al. [117] and Marshall and Plumb [70]. In vector invariant form the equations do not change for different three-dimensional vectors on any coordinate system.

A general vector invariant form of the momentum equation on a rotating frame $\mathcal{R}$ with an angular velocity $\vec{\Omega}$ relative to an inertial frame is given by

$$\frac{D\vec{u}}{Dt} := \left(\frac{\partial}{\partial t} + \vec{u}\cdot\nabla\right)\vec{u} = -2\vec{\Omega}\times\vec{u} - \vec{\Omega}\times(\vec{\Omega}\times\vec{r}) - \nabla\Phi_N - \frac{1}{\rho}\nabla p + \vec{F}\ . \tag{C.1}$$

$\frac{D}{Dt}$ is the material derivative in the rotating frame $\mathcal{R}$ and ∇ the three-dimensional gradient operator. With $\vec{r}$ we denote the position of the fluid parcel relative to any fixed origin on the rotational axis of $\mathcal{R}$, Φ_N is the Newtonian gravitational potential, ρ the density, p the pressure and $\vec{F}$ some other forces. With the continuity equation $\frac{D\rho}{Dt} + \rho\nabla\cdot\vec{u} = 0$ and an additional constraint on energy, for instance, incompressibility $\nabla\cdot\vec{u} = 0$ (cf. Sect. B.3), the system of equations is closed.

The *centrifugal force* $-\vec{\Omega}\times(\vec{\Omega}\times\vec{r}) = \nabla\left(\frac{|\vec{\Omega}|^2 r_\perp^{\,2}}{2}\right)$, where $r_\perp$ is the perpendicular distance of the parcel from the rotation axis, and the Newtonian gravity, $-\nabla\Phi_N$, are usually combined to the *apparent* gravity, $-\nabla\Phi_A$, with $\Phi_A = (\Phi_N - \frac{|\vec{\Omega}|^2 r_\perp^{\,2}}{2})$. Omitting the influence of additional forces, i.e. $\vec{F} = 0$, the momentum equation can be written as

$$\frac{D\vec{u}}{Dt} := \frac{\partial\vec{u}}{\partial t} + \vec{u}\cdot\nabla\vec{u} = -2\vec{\Omega}\times\vec{u} - \nabla\Phi_A - \frac{1}{\rho}\nabla p\ . \tag{C.2}$$

This equation holds irrespective of the coordinate system. The construction of a numerical scheme demands for a representation in a certain coordinate system and a separation into components.

C.1.1 Representation of the vector invariant form

The choice of the coordinate system is an important step in solving the equations numerically. As the vector has to be represented in components, this choice has influence on the complexity of the equations given in vector components. Here, we summaries shortly the properties of the two most frequently used representations.

Spherical representation

With the definition of an apparent gravity potential $\Phi_A = \Phi_N - \frac{|\vec{\Omega}|^2 r_\perp^2}{2}$ one finds surfaces of constant Φ_A. Such surfaces are called geopotentials and are, in general, no spheres. The apparent gravity $-\nabla\Phi_A$ is by definition normal to this surfaces. A separation of Eq. (C.2) into components tangential and perpendicular to the geopotential surfaces is desired, because in such case Φ_A appears only in the terms perpendicular to the geopotentials. As the differences of geopotentials to spheres are sufficiently small, one may apply the *spherical geopotential approximation*, with components of Eq. (C.2) separated tangential and normal to geopotentials, where the geopotentials after the separation are treated as spheres (cf. White et al. [117]).

Using this assumption, the spherical polar coordinates are an adequate coordinate system, where λ describes the longitude, φ the latitude and r the mean earth radius plus distance form earth surface. Then $\Phi_A(r)$ is a function of r only.

Such choice of coordinate system including the spherical geopotential approximation leads to a system of equations that takes the earth's curvature into account.

Cartesian representation

More frequently used is, however, the representation of Eq. (C.2) by a rotating Cartesian frame in $\mathbb{R}^3$. Hereby, the earth's curvature is not taken into account. With such approach, the equations are representation on flat geometry, thus the approximations for a flat geometry introduced in Section A.3 are valid. However, the effect of rotating coordinate system has to be taken into account, as elaborated in the following.

C.1.2 Fluid equations in $\mathbb{R}^3$ on a rotating sphere

We aim for a representation that is mostly used in geophysical science, namely the representation of the fluid equations on a rotating Cartesian frame in $\mathbb{R}^3$. The rotating system leads to additional effects, i.e. the Coriolis force that have to be taken into account. Hereby, we follow in this subsection the argumentation of Marshall and Plumb [70].

The geophysical fluid equations are represented on a rotating Cartesian coordinate system in $\mathbb{R}^3$ that is positioned on the earth surface as following: The local coordinate system is positioned at latitude φ and longitude λ such that the x, y, z direction points eastward, northward and upward, respectively. With respect to spherical coordinates, the line elements are $dx = r\cos\varphi d\lambda, dy = rd\varphi$ and $dz = rdr$, where r is the distance for earth midpoint.

With an earth rotation velocity Ω the rotational vector for this choice of local coordinate system is $\vec{\Omega} = (0, \Omega\cos\varphi, \Omega\sin\varphi)$. With the representation of the velocity $\vec{u} = (u, v, w)$ the Coriolis acceleration reads

$$\vec{\Omega} \times \vec{u} = \begin{pmatrix} \Omega w\cos\varphi - \Omega v\sin\varphi \\ \Omega u\sin\varphi \\ -\Omega u\cos\varphi \end{pmatrix} . \tag{C.3}$$

The vertical components of the Coriolis term act in opposite direction to gravity, however, with negligible strength, as $\Omega u \ll g$. Therefore, we drop its influence. An additional approximation, called the *shallow-atmosphere* approximation, is based on the assumption that the atmosphere is very thin compared to the earth radius a, i.e. $r = a + z \approx a$, where r is the radial distance of the parcel to the origin and z the vertical coordinate of the local coordinate system:
(i) The apparent gravity potential Φ_A of Eq. (C.2) reduces to $\Phi_A^{\mathrm{shw-atm}} = (\Phi_N - \frac{|\vec{\Omega}|^2 a^2 \cos^2\varphi}{2})$;
(ii) Because of the thinness of the atmosphere and ocean, vertical velocity are much less than horizontal velocity. Thus, we omit the term including w in the x-component of the Coriolis-term.

With this assumptions we can approximate the Coriolis term by

$$2\vec{\Omega} \times \vec{u} \approx \begin{pmatrix} -2\Omega v \sin\varphi \\ 2\Omega u \sin\varphi \\ 0 \end{pmatrix} = f\vec{k} \times \vec{u} \,, \tag{C.4}$$

with $\vec{k} = (0, 0, 1)$ and where $f = 2\Omega \sin\varphi$ is known as the *Coriolis parameter*. Both Eq. (C.3) and Eq. (C.4) are component representations in $\mathbb{R}^3$ that can be used for a component wise representation of Eq.(C.2).

C.2 The shallow-water equations

In this section we present a sketch of the derivation for the shallow-water equations according to McWilliams [71] on the basis of the full equations of Eq. (C.2). Then, based on this derivation, we introduce the invariant shallow-water equations, which are also discussed in Chapter 2.

C.2.1 The shallow-water equations in vector calculus

Based on the usual assumptions in order to derive the shallow-water equations, we describe the configuration for a shallow-water flow in this subsection according to McWilliams [71]. Hereby, let the horizontal velocity $\vec{u}$ be depth independent. The fluid layer is of uniform density ρ_0, with an upper free surface p_{up}. The layer has a thickness of $h = H + \eta - B$, with B the bottom elevation, and η the free surface elevation and H the averaged surface depth.

H also characterizes the vertical scale of the motion. The length scale of the characteristic horizontal motion is denoted with L. The equation $\delta = \frac{H}{L} \ll 1$ denotes the fundamental characteristic of shallow-water motion. Thus, the shallow-water equations describe flows where the horizontal scale L is much greater than the mean layer depth H. For this assumption, also the hydrostatic balance approximation (cf. Eq. (C.8)) is justified, which is an important assumption for the following derivation.

The thickness equation in vector calculus: The assumption of a uniform and constant density ρ leads to the incompressibility condition $\mathrm{div}(\vec{u}) = 0$. This can be seen as following: $\rho = \text{const.} \Leftrightarrow \frac{\partial \rho}{\partial t} = 0$ and $\nabla\rho = 0$. Based on the continuity equation (B.5) we find

$$\frac{\partial \rho}{\partial t} + \rho \mathrm{div}(\vec{u}) + \vec{u}\,\nabla\rho = 0 \Leftrightarrow \mathrm{div}(\vec{u}) = 0 \,. \tag{C.5}$$

The degenerated continuity equation $\mathrm{div}(\vec{u}) = 0$ can be formulated independently of the height by vertical integration. Assuming $\frac{\partial}{\partial z}\vec{u}_{\mathrm{hor}} = 0$ and a flat bottom topography, $B = 0$,

the integration over each water column gives

$$0 = \int_0^h \left(\nabla_{\mathrm{hor}} \cdot (\vec{u}_{\mathrm{hor}}) + \frac{\partial u_z}{\partial z} \right) dz = h \nabla_{\mathrm{hor}} \cdot (\vec{u}_{\mathrm{hor}}) + u_z|_h - u_z|_0 \ , \tag{C.6}$$

where we use the notation $\vec{u}_{\mathrm{hor}} = (u_x, u_y)$ and $\nabla_{\mathrm{hor}} = (\partial_x, \partial_y)$. By imposing kinematic boundary conditions on (i) the lower boundary by $u_z|_0 = 0$, and (ii) on the free surface at height h by $u_z|_h = \frac{dh}{dt} = \frac{\partial h}{\partial t} + \vec{u}_{\mathrm{hor}} \nabla_{\mathrm{hor}} h$ there follows

$$\frac{\partial h}{\partial t} + \nabla_{\mathrm{hor}} \cdot (h \vec{u}_{\mathrm{hor}}) = 0 \ , \tag{C.7}$$

which is called the *height* or *thickness equation*. This equation is also valid for non-flat bottom topography with $B \neq 0$ (cf. McWilliams [71]).

The height independent momentum equation in vector calculus: Let the total pressure p be described by the function $p(x, y, z, t) = -g\rho z + \delta p(x, y, z, t)$. The scale analysis for shallow flows with $\delta = \frac{H}{L} \ll 1$ (cf. Pedlowsky [77]) reveals that the vertical pressure variation δp can be neglected leading to

$$\frac{\partial p}{\partial z} = -g\rho + O(\delta^2) \ . \tag{C.8}$$

This balance between the vertical pressure gradient and the buoyancy force is called the *hydrostatic approximation*.

The pressure at the height z is determined by the water column over that point and by the constant pressure at the surface $p_{up} = p(x, y, h, t)$. This can by found by integrating Eq. (C.8) from z to the free surface h with constant density $\rho = \rho_0$:

$$\int_z^h \frac{\partial p}{\partial z} dz = p(x, y, h, t) - p(x, y, z, t) = -\int_z^h g\rho_0 dz = -\rho_0 g (h - z) \ , \tag{C.9}$$

$$p(x, y, z, t) = p_{up} + \rho_0 g (h - z) \ . \tag{C.10}$$

Based on this function for the pressure, we calculate the horizontal gradient, $\frac{1}{\rho_0} \nabla_{\mathrm{hor}} p$, and find

$$\frac{1}{\rho} \frac{\partial p}{\partial x} = g \frac{\partial h}{\partial x} \ , \qquad \frac{1}{\rho} \frac{\partial p}{\partial y} = g \frac{\partial h}{\partial y} \ . \tag{C.11}$$

As p_{up} is constant, we find that the horizontal partial derivatives are independent of z and only dependent on the absolute water depth h.

The typical vertical velocity is at most of the order of $W \leq O(\delta U)$, where W is the typical vertical and U the typical horizontal scale of velocity [71]. Omitting the vertical velocity, the horizontal momentum equation is independent of the height z and given by

$$\frac{\partial \vec{u}_{\mathrm{hor}}}{\partial t} + \vec{u}_{\mathrm{hor}} \cdot \nabla_{\mathrm{hor}} \vec{u}_{\mathrm{hor}} = -f \vec{k} \times \vec{u}_{\mathrm{hor}} - g \nabla_{\mathrm{hor}} h \ . \tag{C.12}$$

We use the shallow atmosphere approximation for the Coriolis term in Eq. (C.2) with the Coriolis parameter $f = 2\Omega \sin \varphi$. In contrast to Eq. (C.2), the gravitational acceleration $\nabla \Phi_A$ is caused by the weight of the water column, which in turn causes a pressure at height z, i.e. $\Phi_A \approx gz$. Therefore, the pressure term takes over the role of gravity in this formulation.

C.2.2 The shallow-water equations in invariant form

On the basis of the results of the previous section, we derive the shallow-water equations in invariant form. To our best knowledge there exists no such formulation for the shallow-water equations in the literature. Therefore, we include this derivation in the present section.

The invariant form of Euler's equation in Eq. (B.4) allows for a representation of the equations on any Riemannian manifold $\mathcal{M}$ by the choice of the coordinate representation, for instance, the spherical coordinates (r, ϑ, φ) or Cartesian coordinate (x, y, z). Hereby, the earth rotating, i.e. the fact of an rotating Coordinate system, has to be included to represent the Coriolis effect adequately.

The general formulation of the Lie-derivative allows for time dependent coordinates and vector fields (cf. Section A.3). Thus, the time dependency of the invariant equations is contains in the choice of an adequate coordinate representation. In order to apply the shallow-atmosphere approximation of Section C.1.2, we use the therein introduced rotating Cartesian frame to represent the invariant equations. Under this prerequisites, we derive the following invariant shallow-water equations.

The thickness equation in invariant form: Analogously to Proposition B.1.1 the divergence in two dimensions can be written using operators of exterior calculus by $\mathrm{div}_{\mathrm{hor}}(\rho\vec{v}_{\mathrm{hor}}) = \star\mathbf{d}\star(\rho\vec{v}^{\flat})$ for any vector field $\vec{v}_{\mathrm{hor}} = (v_x, v_y) \in \mathcal{X}(\mathcal{M})$, as the following calculation shows. Let the vector $\rho\vec{v}$ be represented as one-form by $(\rho\vec{v})^{\flat} = \rho v_x dx + \rho v_y dy \in \Omega^1(\mathcal{M})$, then

$$\star(\rho\vec{v})^{\flat} = \star(\rho v_x dx + \rho v_y dy) = \rho v_x dy - \rho v_y dx \ , \tag{C.13}$$

$$\mathbf{d}\star(\rho\vec{v})^{\flat} = \frac{\partial \rho v_x}{\partial x} dx \wedge dy - \frac{\partial \rho v_y}{\partial y} dy \wedge dx = \left(\frac{\partial \rho v_x}{\partial x} + \frac{\partial \rho v_y}{\partial y} \right) dx \wedge dy \ . \tag{C.14}$$

With $\star(dx \wedge dy) = 1$ we find the horizontal divergence, analogously to ∇_{hor}, which leads to the following thickness equation

$$\frac{\partial \star h}{\partial t} + \mathbf{d}\star(h\vec{u}_{\mathrm{hor}})^{\flat} = 0 \ . \tag{C.15}$$

The momentum equation in invariant form: Let us regard the momentum equation of the incompressible fluid equations of Eq. (B.52) for a vector field $\vec{u}^{\flat} = u_x dx + u_y dy + u_z dz$ in three dimensions. As shown in the previous section, the momentum equation in vector calculus can be formulated such to be independent of the height z.

To find an analogous representation of the invariant momentum equation, we represent the flow with the two-dimensional one-form $\vec{u}^{\flat}_{\mathrm{hor}} = u_x dx + u_y dy \in \Omega^1(\mathcal{M})$, whereas the vertical velocity u_z is neglected because it is small compared to the horizontal velocity. This assumption is valid with the shallow-atmosphere approximation (cf. Sect. C.1.2). Using this assumption, we find an expression for the Coriolis term in exterior calculus with $f\vec{k} \times \vec{u}_{\mathrm{hor}} = \mathbf{i}_{\vec{u}_{\mathrm{hor}}} f$ (this identity is given in the proof to Theorem 2.3.1), where the two-form $f_{\mathrm{cor}} = f_C dx \wedge dy \in \Omega(\mathcal{M})$ describes the Coriolis effect in the horizontal direction taking the earth rotation into account.

As the vector component u_z is neglected, the Lie-derivative $\mathcal{L}$ of Def. B.2.1 acting on $\vec{u}^{\flat}_{\mathrm{hor}}$ only accounts for terms in the horizontal direction. Using the gradient operator of Prop. (A.4.3) and the hydrostatic approximation (C.11) the horizontal momentum equation in invariant form on a two-dimensional manifolds $\mathcal{M}$ is given by

$$\frac{\partial(\vec{u}^{\flat}_{\mathrm{hor}})}{\partial t} + \mathcal{L}_{\vec{u}_{\mathrm{hor}}}(\vec{u}^{\flat}_{\mathrm{hor}}) - \frac{1}{2}\mathbf{d}(\vec{u}^{\flat}_{\mathrm{hor}}(\vec{u}_{\mathrm{hor}})) + \mathbf{i}_{\vec{u}_{\mathrm{hor}}} \circ f + g\mathbf{d}h = 0 \ . \tag{C.16}$$

Using Cartan's formula (B.35) and exploiting the linearity of the interior product, we find

$$\frac{\partial(\vec{u}_{\rm hor}^{\,\flat})}{\partial t} + (\mathbf{i}_{\vec{u}_{\rm hor}} \circ (\mathbf{d}\vec{u}_{\rm hor}^{\,\flat} + f)) + \frac{1}{2}\mathbf{d}(\vec{u}_{\rm hor}^{\,\flat}(\vec{u}_{\rm hor})) + g\mathbf{d}h = 0 \ . \tag{C.17}$$

On a flat manifold, the term $\mathcal{L}_{\vec{u}_{\rm hor}}(\vec{u}_{\rm hor}^{\,\flat}) - \frac{1}{2}\mathbf{d}(\vec{u}_{\rm hor}^{\,\flat}(\vec{u}_{\rm hor}))$ reduces to the conventional advection term $\vec{u}_{\rm hor} \cdot \nabla_{\rm hor}\vec{u}_{\rm hor}$ according to Prop. B.2.1 and Eq. (A.34).

Summary: Let be $\mathcal{M}$ a two-dimensional manifold on a rotating frame, $\vec{u}_{\rm hor}^{\,\flat} \in \Omega^1(\mathcal{M})$ the velocity one-form and $h \in \Omega^0(\mathcal{M})$ the surface height function. Then, the rotating shallow-water equations in invariant form are given by

$$\frac{\partial(\vec{u}_{\rm hor}^{\,\flat})}{\partial t} + (\mathbf{i}_{\vec{u}_{\rm hor}} \circ (\mathbf{d}\vec{u}_{\rm hor}^{\,\flat} + f)) + \frac{1}{2}\mathbf{d}(\vec{u}_{\rm hor}^{\,\flat}(\vec{u}_{\rm hor})) + g\mathbf{d}h = 0 \ , \tag{C.18}$$

$$\frac{\partial \star h}{\partial t} + \mathbf{d} \star (h\vec{u}_{\rm hor})^{\flat} = 0 \ , \tag{C.19}$$

$$\star\, \mathbf{d} \star (\vec{u}_{\rm hor})^{\flat} = 0 \ , \tag{C.20}$$

with the initial conditions $\vec{u}_{\rm hor}(x,0) = \vec{u}_{{\rm hor},0}(x)$ on $\mathcal{M}$ and the boundary condition on $\partial\mathcal{M} : (\vec{u}_{\rm hor} \cdot \vec{n})da = \mathbf{i}_{\vec{u}_{\rm hor}}\mu = 0$.

Bibliography

[1] R. Abraham, J. E. Marsden, and T. Ratiu. *Manifolds, Tensor Analysis, and Applications*, volume 2. Addison-Wesley, 1983.

[2] H. Anzt, W. Augustin, M. Baumann, H. Bockelmann, T. Gengenbach, T. Hahn, V. Heuveline, E. Ketelaer, D. Lukarski, A. Otzen, S. Ritterbusch, B. Rocker, S. Ronnås, M. Schick, C. Subramanian, J.-P. Weiss, and F. Wilhelm. Hiflow3 - a flexible and hardware-aware parallel finite element package. In *Proceedings of the 9th Workshop on Parallel/High-Performance Object-Oriented Scientific Computing*, POOSC '10, pages 4:1–4:6. ACM, 2010.

[3] A. Arakawa and V. R. Lamb. A potential enstrophy and energy conserving scheme for the shallow water equations. *Monthly Weather Review*, 109(1):18–36, 1981.

[4] D. N. Arnold, R. S. Falk, and R. Winther. Finite element exterior calculus, homological techniques, and applications. *ACTA NUMERICA*, 15:1–155, 2006.

[5] V. Arnold. *Mathematical Methods of Classical Mechanics, Second Edition*. Springer US, New York, 1989.

[6] D. P. Bacon, N. N. Ahmad, Z. Boybeyi, T. J. Dunn, M. S. Hall, P. C. S. Lee, R. A. Sarma, M. D. Turner, K. T. Waight, S. H. Young, and J. W. Zack. A dynamically adapting weather and dispersion model: The operational multiscale environment model with grid adaptivity (omega). *Mon. Wea. Rev.*, 128(7):2044–2076, July 2000.

[7] W. Bangerth and R. Rannacher. *Adaptive Finite Element Methods for Differential Equations*. Birkhäuser Verlag, 2003.

[8] S. R. M. Barros and C. I. Garcia. A global semi-implicit semi-lagrangian shallow-water model on locally refined grids. *Mon. Wea. Rev.*, 132(1):53–65, Jan. 2004.

[9] W. Bauer, M. Baumann, L. Scheck, A. Gassmann, V. Heuveline, and S. Jones. Simulation of tropical-cyclone-like vortices in shallow-water icon-hex using goal-oriented r-adaptivity. *Submitted to Theoretical and Computational Fluid Dynamics (TCFD)*, 2012.

[10] M. Baumann. *Numerical Simulation of Tropical Cyclones using Goal-Oriented Adaptivity*. PhD thesis, Karlsruhe Institute of Technology (KIT), Engineering Mathematics and Computing Lab (EMCL), 2011.

[11] M. Baumann and V. Heuveline. Evaluation of Different Strategies for Goal Oriented Adaptivity in CFD – Part I: The Stationary Case. EMCL Preprint Series, 2010.

[12] M. Beckers, H. J. H. Clercx, G. J. F. van Heijst, and R. Verzicco. Dipole formation by two interacting shielded monopoles in a stratified fluid. *Phys. Fluids*, 14(2):704–720, 2002.

[13] J. Behrens. *Adaptive atmospheric modeling key techniques in grid generation, data structures, and numerical operations with applications*. Springer-Verlag, Berlin; New York, 2006.

[14] J. Behrens and M. Bader. Efficiency considerations in triangular adaptive mesh refinement. *Philosophical Transactions of the Royal Society - Series A: Mathematical, Physical and Engineering Sciences*, 367(1907):4577–4589, 2009.

[15] J. Behrens, N. Rakowsky, W. Hiller, D. Handorf, M. Lauter, J. Papke, and K. Dethloff. amatos: Parallel adaptive mesh generator for atmospheric and oceanic simulation. *Ocean Modelling*, 10(1-2):171–183, 2005.

[16] C. H. Bishop and A. J. Thorpe. Potential vorticity and the electrostatics analogy: Quasi-geostrophic theory. *Q.J.R. Meteorol. Soc.*, 120(517):713–731, 1994.

[17] R. Blender. Eulerian velocity reconstruction in ideal atmospheric dynamics using potential vorticity and potential temperature. *Journal of Physics A: Mathematical and General*, 38(28):6419, 2005.

[18] L. Bonaventura and T. Ringler. Analysis of discrete shallow-water models on geodesic delaunay grids with c-type staggering. *Monthly Weather Review*, 133(8):2351–2373, 2005.

[19] A. Bossavit. Computational electromagnetism and geometry (2): Network constitutive laws. *The Japan Society of Applied Electromagnetics and Mechanics*, 7(3):294–301, 1999.

[20] A. Bossavit. Computational electromagnetism and geometry (3): Convergence. *The Japan Society of Applied Electromagnetics and Mechanics*, 7(4):401–408, 1999.

[21] A. Bossavit. Computational electromagnetism and geometry: Building a finite-dimensional 'maxwell's house'. (1): Network equations. *The Japan Society of Applied Electromagnetics and Mechanics*, 7(2):150–159, 1999.

[22] A. Bossavit. Computational electromagnetism and geometry (4): From degrees of freedom to fields. *The Japan Society of Applied Electromagnetics and Mechanics*, 8(1):102–109, 2000.

[23] A. Bossavit. Computational electromagnetism and geometry (5): The 'galerkin hodge'. *The Japan Society of Applied Electromagnetics and Mechanics*, 8(2):203–209, 2000.

[24] A. Bossavit. Computational electromagnetism and geometry (6): Some questions and answers. *The Japan Society of Applied Electromagnetics and Mechanics*, 8(3):372–377, 2000.

[25] A. Bossavit. 'Generalized finite differences' in computational electromagnetics. *Progress In Electromagnetics Research (PIER)*, 32:45–64, 2001.

[26] A. Bossavit. Generating whitney forms of polynomial degree one and higher. *IEEE Transactions on Magnetics*, 38(2):341–344, 2002.

[27] A. Bossavit. Extrusion, contraction: their discretization via whitney forms. *The International Journal for Computation and Mathematics in the Electrical and Electronic Engineering*, 22(2):470–480, 2003.

[28] A. Bossavit. Force-related nuts and bolts in the discretization toolkit for electromagnetics. *Magnetics, IEEE Transactions on*, 44(6):1158 –1161, june 2008.

[29] Z. Boybeyi, N. N. Ahmad, D. P. Bacon, T. J. Dunn, M. S. Hall, P. C. S. Lee, R. A. Sarma, and T. R. Wait. Evaluation of the operational multiscale environment model with grid adaptivity against the european tracer experiment. *J. Appl. Meteor.*, 40(9):1541–1558, Sept. 2001.

[30] S. Brand. Interaction of binary tropical cyclones of the western north pacific ocean. *Journal of Applied Meteorology*, 9:433–441, 1970.

[31] Q. Chen, M. Gunzburger, and T. Ringler. A scale-invariant formulation of the anticipated potential vorticity method. *Mon. Wea. Rev.*, 139:2614–2629, Apr. 2011.

[32] M. Desbrun, A. N. Hirani, M. Leok, and J. E. Marsden. Discrete exterior calculus. *42nd IEEE International Conference on Decision and Control IEEE Cat No03CH37475*, 2003:53, 2005.

[33] M. Desbrun, E. Kanso, and Y. Tong. Discrete differential forms for computational modeling. In *ACM SIGGRAPH 2005 Courses*, SIGGRAPH '05, New York, NY, USA, 2005. ACM.

[34] D. G. Dritschel and D. W. Waugh. Quantification of the inelastic interaction of unequal vortices in two-dimensional vortex dynamics. *Phys. Fluids*, 4A:1737–1744, 1992.

[35] K. Emanuel. Tropical cyclones. *Annual Review of Earth and Planetary Sciences*, 31(1):75–104, 2003.

[36] K. Eriksson, D. Estep, P. Hansbo, and C. Johnson. Introduction to adaptive methods for differential equations. *Acta Numerica*, 4:105–158, 1995.

[37] T. O. Espelid, J. Berntsen, and K. Barthel. Conservation of energy for schemes applied to the propagation of shallow-water inertia-gravity waves in regions with varying depth. *International Journal for Numerical Methods in Engineering*, 49(12):1521–1545, 2000.

[38] E. Fermi. *Thermodynamics*. Dover Publications, 1956.

[39] A. Fournier, M. A. Taylor, and J. J. Tribbia. The spectral element atmosphere model (seam): High-resolution parallel computation and localized resolution of regional dynamics. *Mon. Wea. Rev.*, 132(3):726–748, Mar. 2004.

[40] S. Fujiwhara. The natural tendency towards symmetry of motion and its application as a principle of motion. *Quart. J. Roy. Meteor. Soc.*, 47:287–293, 1921.

[41] S. Fujiwhara. On the growth and decay of vortical systems. *Quart. J. Roy. Meteor. Soc.*, 49:75–104, 1923.

[42] S. Fujiwhara. Short note on the behaviour of two vortices. *Proc. Phys. Math. Soc. Japan, Ser. 3*, 13:106–110, 1931.

[43] A. Gassmann. Inspection of hexagonal and triangular c-grid discretizations of the shallow water equations. *Journal of Computational Physics*, 230(7):2706–2721, Apr. 2011.

[44] M. Giorgetta, T. Hundertmark, P. Korn, S. Reich, and M. Restelli. Conservative space and time regularizations for the icon model. Technical report, Berichte zur Erdsystemforschung, Report 67, MPI for Meteorology, Hamburg, 2009.

[45] F. X. Giraldo and T. Warburton. A nodal triangle-based spectral element method for the shallow water equations on the sphere. *J. Comput. Phys.*, 207:129–150, July 2005.

[46] D. A. Ham, S. C. Kramer, G. S. Stelling, and J. Pietrzak. The symmetry and stability of unstructured mesh c-grid shallow water models under the influence of coriolis. *Ocean Modelling*, 16(12):47–60, 2007.

[47] A. Hatcher. *Algebraic Topology*. Cambridge University Press, 2002.

[48] R. Heikes and D. A. Randall. Numerical integration of the shallow-water equations on a twisted icosahedral grid. part i: Basic design and results of tests. *Mon. Wea. Rev.*, 123(6):1862–1880, June 1995.

[49] R. Heikes and D. A. Randall. Numerical integration of the shallow-water equations on a twisted icosahedral grid. part ii. a detailed description of the grid and an analysis of numerical accuracy. *Mon. Wea. Rev.*, 123(6):1881–1887, June 1995.

[50] T. Heinze. *An Adaptive Shallow Water Model on the Sphere*. Phd thesis, University of Bremen, Germany, 2009.

[51] F. Herbert. The physics of potential vorticity. *Meteorologische Zeitschrift*, 16(3):243–254, 2007.

[52] H. Heumann and R. Hiptmair. Eulerian and semi-lagrangian methods for convection-diffusion for differential forms. *Discrete and Continuous Dynamical Systems*, 29(4):1471–1495, 2011.

[53] R. Hiptmair. Finite elements in computational electromagnetism. In *Acta Numer.*, volume 11, pages 237–339. 2002.

[54] A. N. Hirani. *Discrete exterior calculus*. PhD thesis, Pasadena, CA, USA, 2003. AAI3086864.

[55] G. J. Holland. Tropical cyclone motion: Environmental interaction plus a beta effect. *J. Atmos. Sci.*, 40(2):328–342, Feb. 1983.

[56] G. J. Holland and G. S. Dietachmayer. On the interaction of tropical-cyclone-scale vortices. iii. continuous barotropic vortices. *Quart. J. Roy. Meteor. Soc.*, 119:1381–1398, 1993.

[57] C. Jablonowski, M. Herzog, J. E. Penner, R. C. Oehmke, Q. F. Stout, B. van Leer, and K. G. Powell. Block-structured adaptive grids on the sphere: Advection experiments. *Mon. Wea. Rev.*, 134(12):3691–3713, Dec. 2006.

[58] C. Jablonowski and D. L. Williamson. A baroclinic instability test case for atmospheric model dynamical cores. *Q.J.R. Meteorol. Soc.*, 132(621C):2943–2975, 2006.

[59] J. D. Jarrell, S. Brand, and D. S. Nicklin. An analysis of western north pacific tropical cyclone forecast errors. *Mon. Wea. Rev.*, 106:925–937, 1978.

[60] T. Kambe. Geometrical theory of fluid flows and dynamical systems. *Fluid Dynamics Research*, 30(6):331 – 378, 2002.

[61] R. Klein, S. Vater, E. Paeschke, and D. Ruprecht. *Asymptotic Methods in Fluid Mechanics: Survey and Recent Advances*, volume 523. Springer Vienna, 2011.

[62] O. Kleptsova, J. Pietrzak, and G. Stelling. On the accurate and stable reconstruction of tangential velocities in c-grid ocean models. *Ocean Modelling*, 28(13):118 – 126, 2009.

[63] M. Lander and G. J. Holland. On the interaction of tropical-cyclone-scale vortices. i: Observations. *Quart. J. Roy. Meteor. Soc.*, 119:1347–1361, 1993.

[64] M. Läuter, D. Handorf, N. Rakowsky, J. Behrens, S. Frickenhaus, M. Best, K. Dethloff, and W. Hiller. A parallel adaptive barotropic model of the atmosphere. *Journal of Computational Physics*, 223(2):609–628, 2007.

[65] D. Y. Le Roux and B. Pouliot. Analysis of numerically induced oscillations in two-dimensional finite-element shallow-water models part ii: Free planetary waves. *SIAM J. Sci. Comput.*, 30(4):1971–1991, May 2008.

[66] D. Y. Le Roux, V. Rostand, and B. Pouliot. Analysis of numerically induced oscillations in 2d finite-element shallow-water models part i: Inertia-gravity waves. *SIAM J. Sci. Comput.*, 29(1):331–360, Jan. 2007.

[67] R. J. Leveque. *Finite Volume Methods for Hyperbolic Problems*. Cambridge University Press, Cambridge, 2002.

[68] G. Liao and D. Anderson. A new approach to grid generation. *Applicable Analysis: An International Journal*, 44(3):285–298, 1992.

[69] G. Liao, G. de la Pena, and G. Liao. A deformation method for moving grid generation. *Proceedings, 8th International Meshing Roundtable*, South Lake Tahoe, CA, U.S.A.:pp.155–162, October 1999.

[70] J. Marshall and R. Plumb. *Atmosphere, ocean and climate dynamics: an introductory text*, volume International Geophysics, volume 93. Academic Press, 2007.

[71] J. C. McWilliams. *Fundamentals of Geophysical Fluid Dynamics*. Cambridge University Press, New York, 2006.

[72] M. V. Melander, J. C. McWilliams, and N. J. Zabusky. Symmetric vortex merger in two dimensions: causes and conditions. *J. Fluid Mech.*, 195:303–340, 1988.

[73] J. Molinari and D. Vollaro. Rapid intensification of a sheared tropical storm. *Mon. Wea. Rev.*, 138(10):3869–3885, June 2010.

[74] J. Moser. On the volume elements on a manifold. *Transactions of the American Mathematical Society*, 120(2):pp. 286–294, 1965.

[75] P. Mullen, A. McKenzie, D. Pavlov, L. Durant, Y. Tong, E. Kanso, J. Marsden, and M. Desbrun. Discrete lie advection of differential forms. *Foundations of Computational Mathematics*, 11:131–149, 2011.

[76] S. Ničković, M. B. Gavrilov, and I. A. Tošić. Geostrophic adjustment on hexagonal grids. *Mon. Wea. Rev.*, 130(3):668–683, Mar. 2002.

[77] J. Pedlosky. *Geophysical fluid dynamics / Joseph Pedlosky.* Springer Verlag, New York :, 1979.

[78] B. Perot. Conservation properties of unstructured staggered mesh schemes. *Journal of Computational Physics*, 159(1):58–89, Mar. 2000.

[79] J. Perot, D. Vidovic, and P. Wesseling. Mimetic reconstruction of vectors. In D. N. Arnold, P. B. Bochev, R. B. Lehoucq, R. A. Nicolaides, and M. Shashkov, editors, *Compatible Spatial Discretizations*, volume 142 of *The IMA Volumes in Mathematics and its Applications*, pages 173–188. Springer New York, 2006.

[80] P.-O. Persson. Mesh size functions for implicit geometries and pde-based gradient limiting. *Eng. with Comput.*, 22:95–109, August 2006.

[81] R. Prieto, B. D. McNoldy, S. R. Fulton, and W. H. Schubert. A classification of binary tropical cyclone–like vortex interactions. *Mon. Wea. Rev.*, 131:2656–2666, 2003.

[82] F. Rauser, P. Korn, and J. Marotzke. Predicting goal error evolution from near-initial-information: A learning algorithm. *Journal of Computational Physics*, 230(19):7284–7299, 2011.

[83] F. Rauser, J. Riehme, K. Leppkes, P. Korn, and U. Naumann. On the use of discrete adjoints in goal error estimation for shallow water equations. *Procedia Computer Science*, 1(1):107–115, 2010. ICCS 2010.

[84] P. Raviart and J. Thomas. A mixed finite element method for 2-nd order elliptic problems. In I. Galligani and E. Magenes, editors, *Mathematical Aspects of Finite Element Methods*, volume 606 of *Lecture Notes in Mathematics*, pages 292–315. Springer Berlin / Heidelberg, 1977.

[85] S. Reich. Linearly implicit time stepping methods for numerical weather prediction. *BIT Numerical Mathematics*, 46:607–616, 2006.

[86] S. Reich, N. Wood, and A. Staniforth. Semi-implicit methods, nonlinear balance, and regularized equations. *Atmospheric Science Letters*, 8(1):1–6, 2007.

[87] T. Ringler, L. Ju, and M. Gunzburger. A multiresolution method for climate system modeling: application of spherical centroidal voronoi tessellations. *Ocean Dynamics*, 58(5-6):475–498, 2008.

[88] T. D. Ringler, D. Jacobsen, M. Gunzburger, L. Ju, M. Duda, and W. Skamarock. Exploring a multi-resolution modeling approach within the shallow-water equations. *Mon. Wea. Rev.*, 139:3348–3368, May 2011.

[89] T. D. Ringler, J. Thuburn, J. B. Klemp, and W. C. Skamarock. A unified approach to energy conservation and potential vorticity dynamics for arbitrarily-structured c-grids. *J. Comput. Phys.*, 229:3065–3090, May 2010.

[90] P. Rípodas, A. Gassmann, J. Förstner, D. Majewski, M. Giorgetta, P. Korn, L. Kornblueh, H. Wan, G. Zängl, L. Bonaventura, and T. Heinze. Icosahedral shallow water model (icoswm): results of shallow water test cases and sensitivity to model parameters. *Geoscientific Model Development*, 2(2):231–251, 2009.

[91] E. A. Ritchie and G. J. Holland. On the interaction of two tropical cyclone scale vortices. ii: Discrete vortex patches. *Quart. J. Roy. Meteor. Soc.*, 119:1363–1379, 1993.

[92] V. Rostand, D. Y. Le Roux, and G. Carey. Kernel analysis of the discretized finite difference and finite element shallow-water models. *SIAM J. Sci. Comput.*, 31(1):531–556, Oct. 2008.

[93] F. Schieweck. A-stable discontinuous galerkin-petrov time discretization of higher order. *Journal of Numerical Mathematics*, 18(1):25–57, 04 2010.

[94] T. Schneider, I. M. Held, and S. T. Garner. Boundary effects in potential vorticity dynamics. *J. Atmos. Sci.*, 60(8):1024–1040, Apr. 2003.

[95] B. Semper and G. Liao. A moving grid finite-element method using grid deformation. *Numerical Methods for Partial Differential Equations*, 11:603–615, 1995.

[96] S.-E. Shin, J.-Y. Han, and J.-J. Baik. On the critical separation distance of binary vortices in a nondivergent barotropic atmosphere. *Journal of the Meteorological Society of Japan*, 84(5):853–869, 2006.

[97] R. K. Smith, W. Ulrich, and G. Dietachmayer. A numerical study of tropical cyclone motion using a barotropic model. I: The role of vortex asymmetries. *Quart. J. Roy. Meteor. Soc.*, 116(492):337–362, 1990.

[98] A. St-Cyr, C. Jablonowski, J. M. Dennis, H. M. Tufo, and S. J. Thomas. A comparison of two shallow-water models with nonconforming adaptive grids. *Mon. Wea. Rev.*, 136(6):1898–1922, June 2008.

[99] A. Staniforth, N. Wood, and S. Reich. A time-staggered semi-lagrangian discretization of the rotating shallow-water equations. *Quarterly Journal of the Royal Meteorological Society*, 132(621C):3107–3116, 2006.

[100] A. J. Thorpe and C. H. Bishop. Potential vorticity and the electrostatics analogy: Ertelrossby formulation. *Q.J.R. Meteorol. Soc.*, 121(526):1477–1495, 1995.

[101] J. Thuburn. Numerical wave propagation on the hexagonal c-grid. *J. Comput. Phys.*, 227:5836–5858, May 2008.

[102] J. Thuburn, T. D. Ringler, W. C. Skamarock, and J. B. Klemp. Numerical representation of geostrophic modes on arbitrarily structured c-grids. *J. Comput. Phys.*, 228:8321–8335, December 2009.

[103] H. Tomita, M. Satoh, and K. Goto. An optimization of the icosahedral grid modified by spring dynamics. *Journal of Computational Physics*, 183(1):307–331, 2002.

[104] H. Tomita, M. Tsugawa, M. Satoh, and K. Goto. Shallow water model on a modified icosahedral geodesic grid by using spring dynamics. *Journal of Computational Physics*, 174(2):579–613, Dec. 2001.

[105] T. Torsvik, O. Thiem, and J. Berntsen. Stability analysis of geostrophic adjustment on hexagonal grids for regions with variable depth. *Mon. Wea. Rev.*, 133(11):3335–3344, Nov. 2005.

[106] S. Valcke and J. Verron. Interactions of baroclinic isolated vortices: The dominant effect of shielding. *J. Phys. Oceanogr.*, 27(4):524–541, Apr. 1997.

[107] E. L. Wachspress. Barycentric coordinates for polytopes. *Computers & Mathematics with Applications*, 61(11):3319 – 3321, 2011.

[108] R. L. Walko and R. Avissar. The ocean–land–atmosphere model (olam). part i: Shallow-water tests. *Mon. Wea. Rev.*, 136(11):4033–4044, Nov. 2008.

[109] R. L. Walko and R. Avissar. The ocean–land–atmosphere model (olam). part ii: Formulation and tests of the nonhydrostatic dynamic core. *Mon. Wea. Rev.*, 136(11):4045–4062, Nov. 2008.

[110] R. L. Walko and R. Avissar. A direct method for constructing refined regions in unstructured conforming triangular-hexagonal computational grids: Application to olam. *Mon. Wea. Rev.*, 139:3923–3937, July 2011.

[111] R. Walters, E. Hanert, J. Pietrzak, and D. Le Roux. Comparison of unstructured, staggered grid methods for the shallow water equations. *Ocean Modelling*, 28(13):106–117, 2009.

[112] H. Wan. *Developing and testing a hydrostatic atmospheric dynamical core on triangular grids*. PhD thesis, Reports on Earth System Science at International Max Planck Research School, Hamburg, 2009.

[113] B. Wang, G. Zhao, and O. Fringer. Reconstruction of vector fields for semi-lagrangian advection on unstructured, staggered grids. *Ocean Modelling*, 40(1):52–71, 2011.

[114] J. Warren, S. Schaefer, A. Hirani, and M. Desbrun. Barycentric coordinates for convex sets. *Advances in Computational Mathematics*, 27(3):319–338, Oct. 2007.

[115] H. Weller and H. G. Weller. A high-order arbitrarily unstructured finite-volume model of the global atmosphere: Tests solving the shallow-water equations. *International Journal for Numerical Methods in Fluids*, 56(8):1589–1596, 2008.

[116] H. Weller, H. G. Weller, and A. Fournier. Voronoi, delaunay, and block-structured mesh refinement for solution of the shallow-water equations on the sphere. *Mon. Wea. Rev.*, 137(12):4208–4224, Dec. 2009.

[117] A. A. White, B. J. Hoskins, I. Roulstone, and A. Staniforth. Consistent approximate models of the global atmosphere: shallow, deep, hydrostatic, quasi-hydrostatic and non-hydrostatic. *Quarterly Journal of the Royal Meteorological Society*, 131(609):2081–2107, 2005.

[118] D. L. Williamson, J. B. Drake, J. J. Hack, R. Jakob, and P. N. Swarztrauber. A standard test set for numerical approximations to the shallow water equations in spherical geometry. *Journal of Computational Physics*, 102(1):211–224, Sept. 1992.

[119] S. O. Wilson. Differential forms, fluids, and finite models. *Proceedings of the American Mathematical Society*, 9939:1–8, 2011.

[120] J. Wloka. *Partial differential equations*. Cambridge Univ. Pr., Cambridge, engl. ed., reprinted edition, 1992.

Acknowledgements

I would like to thank my supervisor Almut Gassmann for her support, giving me the opportunity to work on this exciting and challenging topic, while having the possibility to develop and to follow my own ideas. Moreover, I wish to thank my supervisor Jörn Behrens for his guidance, his supportive and encouraging advices.

I appreciated being part of the ICON development group and I would like to thank all group members for their encouragement. Special thanks to Leonidas Linardakis for interesting and fruitful discussions and his support with the manuscript. Moreover, I deeply thank Tobias Hundertmark and Marco Restelli for providing important parts of the model source code and for their assistance and patience.

I thank Connie Kampmann and Antje Weitz for their administrative and emotional support. Thanks to the Max Planck Institute and its staff for providing an efficient and a comfortable working environment. I thank the Priority Program SPP 1276 "MetStroem: Multiple Scales in Fluid Mechanics and Meteorology" of the German Research Foundation (DFG) which financed my doctoral research.

Special thanks to Peter Düben, Francesca Guglielmo, Laura Niederdrenk, Ronny Petrik and Florian Rauser for proof reading and helpful revision comments.

I would like to thank all my friends and colleagues and all who supported me throughout the last years. Special thanks go to Laura and Rosi for a constant fresh air and coffee supply that proved to be enormously important for the forthcoming of my writings. Thanks to Ronny for his help and for being a perfect office mate. Thanks to Florian and Cafe Alibi for their support to sustain the Berlin 2008 MetStroem summer-school marathon and to Florian, Peter and Lorenzo for a great time in Los Angeles in 2010.

I deeply thank my parents Marianne and Rudolf, my siblings Anita, Renate and Klaus and all my family for their constant encouragement and love. Finally, I would like to thank Francesca for her patience and her tremendous support.



ISSN 1614-1199